Parameters of evolved stars in nearby star-forming dwarf galaxies

A dissertation submitted to the University of Manchester
for the degree of Master of Science by Research
in the Faculty of Science and Engineering

2016

By
James Bamber
School of Physics and Astronomy

Contents

Abstract **16**

Declaration **17**

Copyright **18**

Acknowledgements **19**

1 Introduction **21**

1.1 Motivation 21
1.2 The life cycle of an intermediate mass star 22
1.2.1 Star formation 22
1.2.2 Main sequence 23
1.2.3 Red giant branch 24
1.2.4 Horizontal branch 26
1.2.5 Asymptotic giant branch 26
1.2.6 Stellar remnants 28
1.3 Factors affecting stellar surface abundances 29
1.3.1 Dredge-up 29
1.3.2 Additional metal production processes 34
1.4 Mass loss from AGB stars 36
1.4.1 Mass loss 36
1.4.2 Drivers of mass loss 37

1.4.3 Dust 39
1.4.4 Metallicity and dust production 45
1.5 Dwarf galaxies 46
1.5.1 Determining star-formation histories 46
1.5.2 Chemical enrichment of a galaxy 47
1.5.3 Determining galactic metallicities 48
1.6 Galaxies of interest 50
1.6.1 Sextans B 52
1.6.2 Sextans A 53
1.6.3 IC 1613 54
1.6.4 Sagittarius Dwarf Irregular 54
1.6.5 Pegasus Dwarf Irregular 55
1.6.6 Wolf-Lundmark-Melotte 56
1.6.7 NGC 6822 57
1.6.8 LGS 3 58
1.6.9 Phoenix 58
1.6.10 Leo A 59
1.6.11 Andromeda IX 60
1.6.12 NGC 185 60
1.6.13 NGC 147 61
1.7 Personal objectives 62

2 Observations and data **65**
2.1 Photometry 65
2.1.1 Data reduction 70
2.1.2 Matching sources 70
2.1.3 Spectral energy distributions 75
2.1.4 Reliability 79
2.2 H–R Diagrams 80

2.2.1 Sextans B 81
2.2.2 Sextans A 83
2.2.3 IC 1613 85
2.2.4 Sag DIG 86
2.2.5 Peg DIG 88
2.2.6 WLM 89
2.2.7 NGC 6822 90
2.2.8 LGS 3 91
2.2.9 Phoenix 92
2.2.10 Leo A 94
2.2.11 And IX 95
2.2.12 NGC 185 95
2.2.13 NGC 147 96
2.2.14 Poor results 97

3 The IR excess **99**

3.1 Filter-fit profiles 99
3.1.1 Sextans B 100
3.1.2 Sextans A 101
3.1.3 IC 1613 102
3.1.4 Sag DIG 102
3.1.5 Peg DIG 102
3.1.6 WLM 107
3.1.7 NGC 6822 107
3.1.8 LGS 3 107
3.1.9 Phoenix 113
3.1.10 Leo A 113
3.1.11 And IX 115
3.1.12 NGC 185 118

3.1.13 NGC 147 118
3.2 Searching for an IR excess 121
3.2.1 Sextans B 123
3.2.2 Sextans A 126
3.2.3 IC 1613 126
3.2.4 Sag DIG 128
3.2.5 Peg DIG 128
3.2.6 WLM 130
3.2.7 LGS 3 130
3.2.8 Phoenix 133
3.2.9 Leo A 133
3.2.10 And IX 134
3.2.11 NGC 185 134
3.2.12 NGC 147 134

4 Isochrones **141**
4.1 Introduction to isochrones 141
4.2 Selection of an isochrone set 143
4.3 Isochrone fitting 143
4.3.1 Sextans B 148
4.3.2 Sextans A 149
4.3.3 IC 1613 150
4.3.4 Sag DIG 151
4.3.5 Peg DIG 152
4.3.6 WLM 153
4.3.7 NGC 6822 154
4.3.8 LGS 3 154
4.3.9 Phoenix 155
4.3.10 Leo A 157

4.3.11 And IX . . . 158
4.3.12 NGC 185 . . . 160
4.3.13 NGC 147 . . . 161

5 Discussion **163**

5.1 Quantification of uncertainties . . . 163
5.1.1 Galaxy parameters and systematic uncertainties . . . 167
5.1.2 Systematic uncertainties . . . 170
5.1.3 Sextans B . . . 170
5.1.4 Sextans A . . . 171
5.1.5 Sag DIG . . . 173
5.1.6 Peg DIG . . . 174
5.1.7 WLM . . . 174
5.1.8 NGC 6822 . . . 174
5.1.9 LGS 3 . . . 177
5.1.10 Phoenix . . . 179
5.1.11 Leo A . . . 179
5.1.12 And IX . . . 179
5.1.13 NGC 185 . . . 181
5.1.14 NGC 147 . . . 184
5.2 An analysis of supergiants . . . 185
5.2.1 Blue supergiants . . . 185
5.2.2 Red supergiants . . . 187
5.3 Determining the typical stellar population of a Local Group dIrr galaxy . . . 190
5.4 Properties of dusty objects . . . 191
5.4.1 Analysis of individual objects . . . 194
5.5 Variability . . . 200
5.5.1 Pulsation amplitude versus IR excess . . . 201

5.5.2 Dust production rate versus IR excess 204
5.5.3 Identification of matched variables 208
5.6 Identification of carbon stars 214
5.6.1 IC 1613 214
5.6.2 Sag DIG 214
5.6.3 Peg DIG 217
5.6.4 WLM 218
5.6.5 NGC 6822 219
5.6.6 NGC 185 220
5.6.7 NGC 147 221
5.7 Constraints on carbon star formation 222
5.7.1 Less-luminous carbon stars 223
5.7.2 Mass constraints 223
5.8 Further research 233

6 Conclusion **237**

BIBLIOGRAPHY **240**

This thesis contains 47365 words.

List of Tables

1.1 List of galaxies studied in this project, including several of their parameters. 51

1.2 Description of the stellar populations of WLM. 56

2.1 Studies that produced the photometry used in this work, and the filters used in their observations. 66

2.2 Table displaying the order and tolerance used when matching objects between catalogs. 73

2.3 Specifications of filters used to produce input photometry. 76

4.1 List of parameters used to produce each isochrone. 145

5.1 Overview of the temperatures and luminosities of the RGB tips for the sampled dIrrs. 167

5.2 Comparison between spectroscopically determined and SED fit temperatures for BSGs in IC 1613 and WLM. 186

5.3 Comparison between spectroscopically determined and SED fit temperatures for RSGs in NGC 6822. 187

5.4 Summary of the positions and classifications of 29 3σ objects highlighted in Figure 5.21. 195

6.1 Table presenting new estimates of the distance to several dIrrs. . . 238

6.2 Table presenting new estimates of the metallicity of several dIrrs. 238

List of Figures

1.1 Simple H–R diagram depicting post-AGB evolution. 25
1.2 Internal structure of an AGB star. 27
1.3 Depiction of the IR excess. 43

2.1 An example of an offset seen when matching sources from two catalogs. 71
2.2 An example of how the matching tolerance is determined. 72
2.3 H–R diagrams for Sextans B. 82
2.4 Plot showing the positions of two groups of objects in Sex B. . . . 83
2.5 Plot showing the radial distribution of two populations in Sex B. . 84
2.6 H–R diagrams for Sextans A. 85
2.7 H–R diagrams for IC 1613. 86
2.8 H–R diagrams for Sag DIG. 87
2.9 H–R diagrams for Peg DIG. 88
2.10 H–R diagrams for WLM 89
2.11 H–R diagrams for NGC 6822. 91
2.12 H–R diagrams for LGS 3. 92
2.13 H–R diagrams for Phoenix. 93
2.14 H–R diagrams for Leo A. 94
2.15 H–R diagrams for And IX. 96
2.16 H–R diagram for NGC 185. 97
2.17 H–R diagram for NGC 147. 97

3.1 Filter-fit profiles for Sextans B. 100

3.2 Filter-fit profiles for Sextans A. 101

3.3 Filter-fit profiles for IC 1613. 103

3.4 Filter-fit profiles for Sag DIG. 104

3.5 Filter-fit profiles for Peg DIG. 105

3.6 Recalculated filter-fit profiles for Peg DIG. 106

3.7 Filter-fit profiles for WLM. 108

3.8 Recalculated filter-fit profiles for WLM. 109

3.9 Filter-fit profiles for NGC 6822. 110

3.10 Recalculated filter-fit profiles for NGC 6822. 111

3.11 Filter-fit profiles for LGS 3. 112

3.12 Recalculated filter-fit profiles for LGS 3. 114

3.13 Filter-fit profiles for Phoenix. 115

3.14 Filter-fit profiles for Leo A. 116

3.15 Filter-fit profiles for And IX. 118

3.16 Recalculated filter-fit profiles for And IX. 120

3.17 Filter-fit profiles for NGC 185. 120

3.18 Filter-fit profiles for NGC 147. 121

3.19 Explanation of the colour scale in the following Figures. 123

3.20 H–R diagram showing the IR excess of objects in Sextans B. . . . 124

3.21 H–R diagrams showing the IR excess of objects in Sextans A. . . 125

3.22 H–R diagrams showing the IR excess of objects in IC 1613. 127

3.23 H–R diagram showing the IR excess of objects in Sag DIG. 128

3.24 H–R diagrams showing the IR excess of objects in Peg DIG. . . . 129

3.25 H–R diagrams showing the IR excess of objects in WLM. 131

3.26 H–R diagrams showing the IR excess of objects in LGS 3. 132

3.27 H–R diagrams showing the IR excess of objects in Phoenix. 135

3.28 H–R diagram showing the IR excess of objects in Leo A. 136

3.29 H–R diagram showing the IR excess of objects in And IX. 137

3.30 H–R diagram showing the IR excess of objects in NGC 185. 138
3.31 H–R diagram showing the IR excess of objects in NGC 147. 139

4.1 An example of three isochrones. 142
4.2 H–R diagram and isochrones of Sextans B. 148
4.3 H–R diagram and isochrones of Sextans A. 149
4.4 H–R diagram and isochrones of IC 1613. 150
4.5 H–R diagram and isochrones of Sag DIG. 151
4.6 H–R diagram and isochrone of Peg DIG. 152
4.7 H–R diagram and isochrones of WLM. 153
4.8 H–R diagram and isochrones of NGC 6822. 155
4.9 H–R diagram and isochrone of LGS 3. 156
4.10 H–R diagram and isochrones of Phoenix. 157
4.11 H–R diagram and isochrones of Leo A. 158
4.12 H–R diagram and isochrones of And IX. 159
4.13 H–R diagram and isochrones of NGC 185. 160
4.14 H–R diagram and isochrones of NGC 147. 161

5.1 RGB tip luminosity histogram of IC 1613. 164
5.2 An example of two isochrones with markedly different metallicities. 165
5.3 RGB tip temperature histogram of IC 1613. 166
5.4 Plot relating L_{RGB} for each of the galaxies in this sample to their bulk metallicity. 168
5.5 Comparison of SED- and theoretically-derived RGB tip luminosities. 169
5.6 Luminosity and temperature histograms of the RGB tip of Sextans B. 171
5.7 Luminosity and temperature histograms of the RGB tip of Sextans A. 172
5.8 Luminosity and temperature histograms of the RGB tip of Sag DIG. 173
5.9 Luminosity and temperature histograms of the RGB tip of Peg DIG. 175

5.10 Luminosity and temperature histograms of the RGB tip of WLM. 176
5.11 Luminosity and temperature histograms of the RGB tip of NGC 6822. 177
5.12 Luminosity and temperature histograms of the RGB tip of LGS 3. 178
5.13 Luminosity and temperature histograms of the RGB tip of Phoenix. 180
5.14 Luminosity and temperature histograms of the RGB tip of Leo A. 181
5.15 Luminosity and temperature histograms of the RGB tip of And IX. 182
5.16 Luminosity and temperature histograms of the RGB tip of NGC 185. 183
5.17 Luminosity and temperature histograms of the RGB tip of NGC 147. 184
5.18 Plot relating $T_{SED} - T_{spec}$ to [Fe/H] for RSGs in NGC 6822. . . . 189
5.19 An H–R diagram showing the typical dIrr population. 191
5.20 H-R diagram showing dusty AGB candidates for 12 of the 13 galaxies in the sample. 192
5.21 H-R diagram highlighting objects for which a further analysis was carried out. 194
5.22 Plot showing the relationship between the IR excess and variability amplitude for objects in Sex A and Sex B. 202
5.23 Plot showing the relationship between the IR excess and variability amplitude for objects in IC 1613. 203
5.24 Plot showing the relationship between the IR excess and variability amplitude for objects in NGC 185 and NGC 147. 204
5.25 Plot showing the relationship between the IR excess and dust production rate for x-AGB stars in Sex A and Sex B. 205
5.26 Plot showing the relationship between the IR excess and dust production rate for x-AGB stars in IC 1613. 206
5.27 Plot showing the relationship between the IR excess and dust production rate for x-AGB stars in NGC 185 and NGC 147. 207

5.28 H–R diagram highlighting variable objects in Sex B. 208
5.29 H–R diagram highlighting variable objects in Sex A. 209
5.30 H–R diagram highlighting variable objects in IC 1613. 209
5.31 H–R diagram highlighting variable objects in Sag DIG. 210
5.32 H–R diagram highlighting variable objects in Peg DIG. 211
5.33 H–R diagram highlighting variable objects in LGS 3. 211
5.34 H–R diagram highlighting variable objects in Leo A. 212
5.35 H–R diagram highlighting variable objects in And IX. 212
5.36 H–R diagram highlighting variable objects in NGC 185. 213
5.37 H–R diagram highlighting variable objects in NGC 147. 213
5.38 H–R diagram highlighting carbon stars in IC 1613. 215
5.39 H–R diagram highlighting carbon stars in Sag DIG. 216
5.40 H–R diagram highlighting carbon stars in Peg DIG. 217
5.41 H–R diagram highlighting carbon stars in WLM. 218
5.42 H–R diagram highlighting carbon stars in NGC 6822. 220
5.43 H–R diagram highlighting carbon stars in NGC 185. 221
5.44 H–R diagram highlighting carbon stars in NGC 147. 222
5.45 Histogram showing the luminosity distribution of all carbon stars. 225
5.46 Histogram showing the mass distribution of all carbon stars. . . . 226
5.47 Histograms showing the luminosity and mass distribution of carbon stars in IC 1613. 228
5.48 Histograms showing the luminosity and mass distribution of carbon stars in NGC 6822. 229
5.49 Histograms showing the different luminosity distributions of C and O stars in NGC 6822. 230
5.50 Histograms showing the luminosity and mass distribution of carbon stars in NGC 185. 231
5.51 Histograms showing the luminosity and mass distribution of carbon stars in NGC 147. 232

The University of Manchester

ABSTRACT OF DISSERTATION submitted by James Bamber
for the Degree of Master of Science by Research and entitled
"Parameters of evolved stars in nearby star-forming dwarf galaxies"
September 2016

The resolved stellar populations of a sample of 13 nearby (< 1.5 Mpc) dwarf irregular galaxies were investigated. Spectral energy distributions were produced using multi-wavelength photometry from literature data. These were used to calculate the temperature and luminosity of evolved stars in each galaxy, which were statistically separated from foreground and background objects using Hertzsprung–Russell diagrams.

Systematic uncertainties in temperature and luminosity were calculated for typical objects in each galaxy. A comparison was carried out between the SED-derived temperatures from this study and the spectroscopically-determined temperatures of a limited sample of supergiants. Comparison with stellar evolution models allowed for new estimates of distance and [Fe/H] to be calculated for several of these galaxies, with distance estimates differing up to $\sim 10\%$ compared with literature values. However, these parameters and the systematic uncertainties are correlated. Mid-IR photometry was used to measure the IR excess of evolved stars in the 3.6 and 4.5 μm bands, being tracers of carbon-rich dust. It was found that the IR excess can be used to separate the AGB from the RGB on an H–R diagram, although no correlation was found with the limited available variability data.

The luminosity distribution of known carbon stars in these galaxies was investigated, and used to produce tentative limits on the range of initial masses at which carbon stars can form. The minimum mass of 1.4 $M_\odot$ is greater than theoretically calculated values at the range of metallicities found in dwarf irregular galaxies, although this may be in part attributable to systematic uncertainties in the conversion of luminosity to initial mass. The upper limit of $3.5 - 5.0$ $M_\odot$ was more difficult to define, as relatively few stars are found in this mass range, but it remains comparable to literature values (Marigo and Girardi 2007; Fishlock et al. 2014; Ventura et al. 2016). The mass distribution of carbon stars was found to peak at ~ 2 $M_\odot$. Further studies using *JWST* will likely constrain these values further, and allow far more-precise spectra and photometry to be obtained.

Declaration

No portion of the work referred to in this dissertation has been submitted in support of an application for another degree or qualification of this or any other university or other institution of learning.

Copyright

Acknowledgements

I would like to thank my supervisor, Iain McDonald, for the invaluable help and guidance he has provided over the course of the year, and for having the willpower to profread this thesis.

I would also like to thank everyone I've had the pleasure of meeting at JBCA, particularly to the postgraduate community, who have made me feel incredibly welcome, and Ant and Bob for the technical support. I cannot fail to mention the remainder of the 2015 MSc intake. From the Radio Astronomy study sessions, to the games of *D&D* (which I promise we will finish one day), thank you for being excellent sources of advice, listeners of complaints, and all-round great people.

Finally, I would like to thank Elena, my diaspora of friends, and my family. Without their help and support, none of this would have been possible.

Chapter 1

Introduction

1.1 Motivation

Asymptotic Giant Branch (AGB) stars are one of the key drivers of chemical evolution in the Universe, therefore an integral part of the process leading to planetary formation and ultimately life. AGB stars represent the final stages of life for stars with low to intermediate initial mass (between 0.8 and 8 $M_{\odot}$; Karakas and Lattanzio 2014).

A crucial parameter of AGB evolution is metallicity: the percentage of elements other than hydrogen or helium (synthesised in the Big Bang). Typical metallicities for Population I stars in our Galaxy are up to $Z = 0.01 - 0.02$, meaning the evolution of stars with this chemical composition can be presented with a degree of confidence. Less well understood, however, are the lifecycles and internal mechanisms of metal-poor stars, such as those found in the early Universe. Although galaxies at high redshift will contain these metal-poor stars, they are found at distances at which telescopes cannot define individual stars within them.

Fortunately, sources of metal-poor stars exist nearby. Dwarf galaxies in the

Local Group appear to have had quiet star-formation histories compared to their larger neighbours (Tolstoy et al. 2009). This results in a lower average metallicity than that of other galaxy types. This, coupled with their relatively close proximity, means their AGB stars are excellent candidates for studies aiming to understand both stellar and chemical evolution in the early Universe. Surveys such as DUSTiNGS (DUST in Nearby Galaxies with *Spitzer*) have begun investigating these metal-poor AGB stars, with aims such as determining the relationship between metallicity and dust production, and understanding the influence of metallicity on the period–luminosity relationship (Boyer et al. 2015a,b).

1.2 The life cycle of an intermediate mass star

This section will discuss the generalised evolution of stars of mass 0.8 $M_\odot < M <$ 8 $M_\odot$. Many of the stages and processes present in this section can vary (sometimes in duration, sometimes existentially) with metallicity. We are assuming solar metallicity ($Z \sim 0.015$; Asplund et al. 2009) for the following stages unless otherwise stated.

Before beginning, it is worth noting that all phases of stellar evolution occur more quickly in metal-poor stars. Lower metallicities allow the core to heat faster, due to a lower opacity. For example, this allows hydrogen shell burning to occur much faster, bringing forward the end of the red giant branch (RGB) stage (Karakas and Lattanzio 2014).

1.2.1 Star formation

Stars form from molecular clouds within the interstellar medium (ISM), with masses of order $10^3 - 10^6$ $M_\odot$. These dense, cool clouds allow molecules to form, including H_2. These clouds form multiple clumps, which may proceed to gravitationally collapse and form the core of a new star. These clumps continue to accrete matter until their centres attain the pressures and temperatures required for hydrogen fusion. They are now known as protostars.

Protostars continue to contract and heat up, increasing the efficiency of hydrogen fusion and hence the core's radiative output. A disk that surrounds the protostar at this time may go on to form planets (Goodwin 2013).

If any stars > 10 $M_\odot$ form, the radiation output becomes great enough to either dissipate the entire molecular cloud (via radiation pressure), or sufficiently ionise it to an extent where stars can no longer be formed (Herwig 2013).

1.2.2 Main sequence

Once the dominant energy production mechanism has become hydrogen fusion, the star can be considered on the main sequence. A main-sequence (MS) star has stable hydrogen fusion occurring in its core, and is in hydrostatic equilibrium. Radiation pressure pushes any local gas and dust away from the new star (Herwig 2013). This is by far the longest stage of a star's life with sustained fusion, with a duration of $\sim 10^{10}$ yrs for a 1 $M_\odot$ star, with notable variation in duration, depending on the star's mass and metallicity.

There are two different processes in which hydrogen is fused into helium:

- For stars with $M < 1.5$ $M_\odot$, energy is mostly generated via the proton-proton chain. This is where $^1_1$H nuclei are directly fused (via various intermediary isotopes) into $^4_2$He. There are four possible paths this reaction chain can take, all resulting in helium nuclei, and often returning hydrogen as a by-product.

- For stars with a mass of $M > 1.5\ \mathrm{M}_{\odot}$, energy is mostly generated via the CNO cycle, again fusing ${}^{1}_{1}$H nuclei to produce ${}^{4}_{2}$He but using various carbon, nitrogen, and oxygen nuclei as catalysts (depending on the exact chain). As the cycle progresses, the relative abundance of C, N, and O in the core will change, which becomes important in the latter stages of the star's life if it passes through the AGB (Karakas and Lattanzio 2014; Section 1.3.1.3).

1.2.3 Red giant branch

Once the hydrogen fuel in the star's core begins to dwindle, energy output slowly decreases, and the subsequent cooling causes a contraction of the outer layers of the star. This results in an increase of temperature and pressure in the stellar interior. Hydrogen burning becomes possible in a shell around the predominately helium core. The ignition of this shell establishes a new hydrostatic equilibrium, with the outer layers of the star expanding and cooling. The stellar radius is now an order of magnitude greater than during the main sequence. The star has entered the Red Giant Branch (RGB; Herwig 2013).

The hydrogen-burning shell moves outwards as it depletes fuel, further increasing the temperature and pressure of the core, which becomes degenerate as it contracts for stars with a mass of $M < 2\ \mathrm{M}_{\odot}$. Due to changing hydrogen abundances, the efficiency of fusion changes when the H-burning shell expands and reaches the former radius of the convective shell. The star's expansion slows and produces the RGB "bump" seen on the Hertzsprung–Russell (H–R) diagram (Riello et al. 2003). The RGB bump is very useful in the isochrone fitting process for constraining parameters of the stellar population.

An important chemical mixing process occurs during the RGB stage, known as the "first dredge-up" (FDU; Herwig 2013); see Section 1.3.1.1.

1.2.3.1 RGB tip

An RGB star expands and brightens to a peak luminosity, visible on the H–R diagram as the "RGB tip" — shown in Figure 1.1 (Karttunen 2007). Temperatures in the core increase to the point where helium burning can occur. This reaction occurs quickly: in the case of $0.8\ \mathrm{M}_\odot < M < 2\ \mathrm{M}_\odot$ stars, the core can entirely ignite in the space of minutes (known as the "helium flash"). Helium burning occurs via the triple-α process, in which three ${}^{4}_{2}\mathrm{He}$ nuclei fuse to form ${}^{12}_{6}\mathrm{C}$.

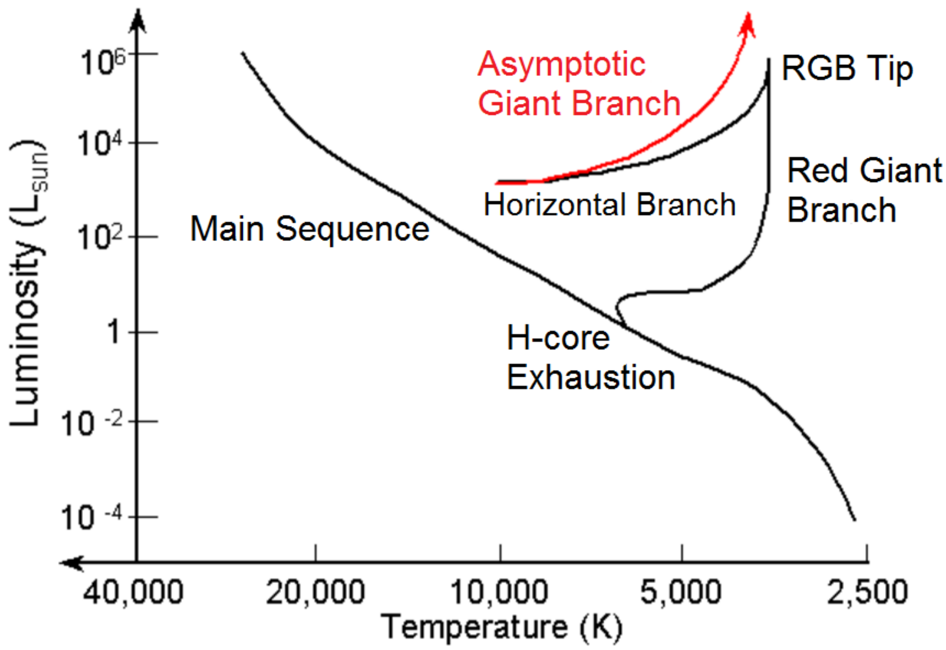

Figure 1.1: Reproduced from Pogge (2015). A Hertzsprung-Russell diagram displaying a schematic of post-main sequence evolution. The RGB tip is the most-luminous part of the red giant branch, occurring immediately before the star's migration to the horizontal branch.

1.2.4 Horizontal branch

With the advent of helium core burning, stars of mass $\lesssim 0.9$ $M_\odot$ (i.e. old metal-poor stars) are considered part of the horizontal branch (HB). The energy liberated from He burning is absorbed by outer layers of the star, and causes vast changes in stellar structure. Overall luminosity decreases by nearly two orders of magnitude during this stage. The star's chemical composition starts to change significantly at this point due to products of the triple-α process (although this is not yet measurable at the surface). Additionally, the effective temperature of the star rises, as can be seen with the migration "bluewards", in Figure 1.1. This horizontal movement on the H–R diagram provides the name of this stage of stellar evolution (Karttunen 2007).

It was noticed that in globular clusters, there is a range of temperatures in the horizontal branch containing few stars. This is due to its intersection with the instability strip, a region of pulsating stars caused by the presence of He III in the stellar photosphere. Stars on the horizontal branch evolving through this region become RR Lyrae variables, with periods of between 0.8 and 1.2 days (Gautschy and Saio 1996; AAVSO 2012). Following further increases in temperature, the star returns to the horizontal branch.

1.2.5 Asymptotic giant branch

The helium-burning core rapidly runs out of fuel, and again contracts. This increase in pressure allows the helium burning to move from the core into a new shell. This is situated between the hydrogen-burning shell and the once again inert core, analogous to the main-sequence–RGB transition. This structure is displayed in Figure 1.2. It joins a branch of the H–R diagram very close to the RGB, known as the asymptotic giant branch (AGB). This is because it asymptotically approaches the RGB on the H–R diagram, an important point as the two branches can be difficult to distinguish. At this point, the star's luminosity increases, and its outer layers expand and cool further. Despite the relatively few stars in this branch (due to its short duration), AGB stars emit up to 70% of a galaxy's luminosity in near-IR bands (Herwig 2013; Karakas and Lattanzio 2014). An accurate calibration of the evolution of these stars can therefore be used to reproduce the observed properties of unresolved populations in distant galaxies (Maraston et al. 2006).

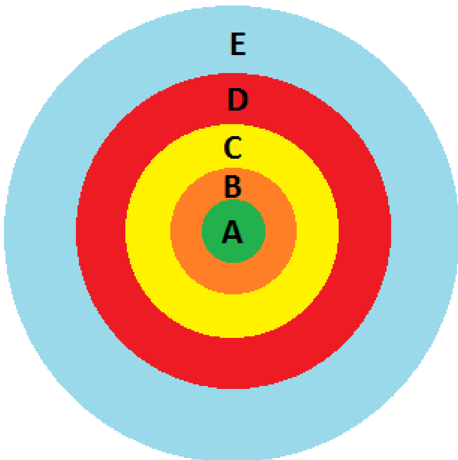

Figure 1.2: A diagram detailing the internal structure of an AGB star. The relative width of layers are not to scale. **A**: Inert CO core. **B**: Helium-burning shell. This layer only exists intermittently in later phases of the AGB. **C**: Intershell zone, composed primarily of helium. **D**: Hydrogen-burning shell. **E**: Convective envelope (predominantly hydrogen).

Many important processes take place in a star of this type, including mass loss, stellar pulsation, multiple channels of production for elements heavier than iron, and the resulting transfer of metals from the stellar interior to its outer layers (Section 1.3.1).

1.2.5.1 Post-AGB stage

When the stellar wind has removed sufficient material from the convective envelope, pressure decreases to a level where fusion of both hydrogen and helium are no longer sustainable. The core contracts, and most remaining layers of material are sloughed off, leaving a small star with thin hydrogen- and helium-burning shells. The remaining core rapidly increases in temperature over the next $10^3 - 10^5$ years (faster for high-mass stars; Karttunen 2007). This compares to an MS lifetime of $\sim 10^{10}$ years, and $\sim 10^7$ years for the AGB for a solar-mass star. In most cases, this occurs fast enough for the ionisation of the ejected material, forming a planetary nebula.

The post-AGB stage can be analysed to find a number of parameters about the former star. If not already known, an estimate of the mass can be determined using its luminosity (Bloecker 1995). If the former mass has already been determined, it is possible to determine the initial–final mass relation, and the efficiency with which mass has been lost. There may be a metallicity dependence in this relation, which, if true, could indicate a metallicity dependence in $\dot{M}$ (Section 1.4.3; Kalirai et al. 2004).

1.2.6 Stellar remnants

The white dwarf is the remaining stellar core, discussed in the previous section, which ceases all fusion after the post-AGB stage. Stars in the initial mass range $0.08\ \mathrm{M}_\odot < M < 8\ \mathrm{M}_\odot$ (at solar metallicity) will end their lives as white dwarfs (Karakas and Lattanzio 2014); the mass of the remaining stellar core will not be greater than the Chandrasekhar limit ($\sim 1.4\ \mathrm{M}_\odot$), so collapse to a neutron star is not possible.

A young white dwarf has a surface temperature of $10^4 - 10^5$ K, although this is dependent on the initial mass of the star. All of this energy is provided by cooling, as fusion has ceased. Typical radii are on the order of 0.01 $R_{\odot}$, comparable to the radius of the Earth, demonstrating the significant density of these objects (Koester 2013).

The composition of the degenerate matter that forms the white dwarf is dependent on the nuclear processes the star formerly sustained. Stars with an initial mass $\lesssim 7$ $M_{\odot}$ will be composed of mostly CO, as elements heavier than this have not been synthesised. Stars with a mass greater than this will produce an O-Ne white dwarf, with the neon produced from carbon burning (Karakas and Lattanzio 2014).

These stellar remnants will gradually cool and traverse the "white dwarf cooling track" on the H–R diagram, ultimately forming an object known as a black dwarf. The timescales involved in the cooling process are currently a matter of debate, although all estimates provide an answer significantly greater than the current age of the Universe. No black dwarfs have yet been observed as they are not yet predicted to exist (Mestel and Ruderman 1967).

1.3 Factors affecting stellar surface abundances

Metallicity both determines, and is determined by, numerous features and processes within AGB stars.

1.3.1 Dredge-up

Dredge-up processes distribute metals and helium synthesised in the stellar core throughout the star. These occur in two or three distinct periods, depending on the stellar mass.

1.3.1.1 First dredge-up (FDU)

This chemical mixing process occurs during the red giant branch. It is a result of the significant structural changes caused by the start of hydrogen shell burning. This is the first major change of chemical composition of the outer regions of the star, destroying the records of the initial abundance of several isotopes.

The dredged-up material added to the convective envelope is still H-rich, with some added He and CNO cycle products, as it is the product of only partial H burning. He burning has not yet begun in the RGB star. The overall change in metallicity is minimal, with the helium fraction in the convective envelope only increasing by approximately 3%. The overall depth and efficiency of the FDU is seemingly dependent on stellar mass and initial metallicity (Karakas and Lattanzio 2014).

1.3.1.2 Second dredge-up (SDU)

The second dredge-up occurs only in early AGB stars > 4 $M_{\odot}$, and its effects appear to be the same regardless of metallicity and mass. It begins when the convective currents of the outer regions expand into the stellar interior. This process increases He abundance in outer regions by around 10%, and the abundance of ^{14}N and ^{23}Na. The surface ^{16}O is also depleted as part of this process (Boothroyd and Sackmann 1999; Karakas and Lattanzio 2014).

1.3.1.3 Third dredge-up (TDU)

The third dredge-up occurs in TP-AGB (thermally pulsing AGB) stars, and supplies a significant proportion of the metals found in the interstellar medium and planetary nebulae.

The helium-burning shell of the early-AGB is quickly extinguished; it is a much faster reaction than hydrogen burning so fuel is more readily depleted. A new helium shell will ignite periodically once appropriate pressures, temperatures, and helium "ash" (from the hydrogen shell) have accumulated in a region. Similar to the helium core ignition at the end of the RGB stage, this process causes rapid expansion and structural change of the star, to the extent that the hydrogen-burning shell ceases fusion. This jump in volume and luminosity is known as a "thermal pulse". Following this pulse, hydrogen shell burning is re-established and the rate of helium burning decreases, allowing the star to return to a "normal" luminosity. These pulses will reoccur every $10^3 - 10^4$ years, whenever helium fusion begins again. With the beginning of these pulses, the star is known as a thermally pulsing AGB star (Herwig 2013). Convective mixing during these thermal pulses cycles material from the core, causing the TDU.

A key uncertainty is at which mass the TDU can begin at. Wallerstein and Knapp (1998) suggest from observation that this should be at 1.5 $M_\odot$ (for metallicities seen in the Milky Way (MW)). However, theoretical models suggest that it is not possible at this mass without some convective overshoot (see Section 1.3.1.4; Herwig 2000; Kamath et al. 2012).

Carbon abundance in the outer layers of the star increases during the TDU. Stars with a greater initial percentage of oxygen (higher metallicity) require a greater number, or more efficient, dredge-up events to gain a C/O ratio greater than unity; indeed the majority of stars in the current era never reach carbon star status. However, as metallicity in previous eras was lower, carbon stars may have been more common in the past. Evidence for this exists in the fact that carbon stars are still seen in higher relative abundances in modern metal-poor galaxies, for example, dwarf spheroidals (McDonald et al. 2012a; Boyer et al. 2015a).

There appears to be a "metallicity ceiling" (i.e. highest initial metallicity) for C star formation of [Fe/H] ≈ 0.3 (Boyer et al. 2013), although this has been disputed by Karakas (2014), who argues that helium abundance is also a significant factor in carbon star formation. There is also a mass constraint on carbon stars. Lower-mass stars have weaker thermal pulses, dredging up less carbon (Karakas et al. 2002). For higher-mass stars, the CNO cycle is the dominant fusion process, cycling carbon through various isotopes of nitrogen and oxygen, and reducing the final C/O ratio (Lattanzio et al. 1996).

1.3.1.4 Mixing processes

The following processes have been suggested as contributing to the mixing processes in AGB stars, including dredge-ups. The presence and fractional contribution of each process in different stars is a matter of debate due to the clear difficulties in observing these events.

- Convective overshoot — the heat of fusion travels further out than expected, meaning the convective envelope mixes with the burning shells more efficiently than predicted in 1D models. It is a theory developed after higher abundances of various metals were seen in the convective envelope than these models predicted. Models that omit this have a less efficient TDU, so do not produce carbon stars (Herwig 2000).

- Thermohaline mixing — although this is a convective process originally developed from observations in saltwater, an analogous process is predicted to occur within stars. It allows for high density material to sit upon a low density envelope, with high density "fingers" penetrating downwards. These "fingers" can then mix with the surrounding material (Karakas and Lattanzio 2014).

- Extra mixing — for stars < 1.3 $M_{\odot}$, there is also some evidence for extra mixing processes (Lind et al. 2009). In particular, the measured ratios of certain isotopes of O and Al in pre-solar grains appear too high to have only occurred with known convective mixing processes (Busso et al. 2010; Palmerini et al. 2011). This extra mixing is expected to be slow and non-convective. However, other non-mixing solutions have been proposed as causes of this isotope ratio, such as a nearby supernova enriching the pre-solar cloud with ^{26}Al shortly before its collapse and development into the current solar system (Gritschneder et al. 2011). Additionally, a decreasing O-abundance towards the late RGB cannot be explained by current mixing models (Johnson and Pilachowski 2012).

The efficiency of these processes are poorly understood. Attempts are being made to constrain the parameters by understanding which stars undergo each of these mixing processes, e.g. Karakas and Lattanzio (2014).

Convective processes are frequently modelled using Mixing Length Theory. A major uncertainty in many models is the value and physical significance of the mixing length parameter, α. It is generally calculated based on solar values for mass, metallicity, and structure. As these parameters are likely considerably different in AGB stars, models should take this into consideration (Karakas and Lattanzio 2014). Lebzelter and Wood (2007) suggest that a varying value for α throughout the star may be more appropriate. This would have the effect of reducing the temperature gradient of the convective envelope and producing an overall higher luminosity. It may also impact the efficiency of HBB (Ventura and D'Antona 2005; Section 1.3.2.4).

1.3.2 Additional metal production processes

1.3.2.1 The s-process

The s-process (or slow neutron-capture process) is a mechanism in which heavy nuclei are synthesised via the addition of a neutron, predominately occurring in AGB stars. The process can also occur in massive stars, though these objects are rare. In this process it is assumed that the β-decay that may follow a neutron capture event always occurs before further neutron capture, due to the relative speed of these processes in the conditions within the star. β-decay can be ignored in extremely high neutron-density environments, such as supernovae, allowing different nuclides to be produced. This is known as the r-process (or rapid neutron capture process; Wallerstein et al. 1997).

The s-process allows the synthesis of elements heavier than iron, and it is estimated that around half of heavy metals are produced this way. Iron is considered to be the starting point of the s-process, and it appears that it can produce stable nuclides as heavy as ^{209}Bi. The path of this process branches, caused by variation in temperature and pressure (Wallerstein et al. 1997).

A current unknown in this process is how its efficiency is affected by processes such as dredge-up and hot bottom burning. These both affect the relative abundances of various nuclei, and therefore the number density of free neutrons (Lugaro et al. 2012).

1.3.2.2 The α-process

The α-process is the addition of a $^4_2$He nucleus (or α particle) to a more massive nuclide. The α-process does not generally make a great contribution to a star's energy output (ignoring the more specific triple-α process), nor the abundance of various nuclides (Burbidge et al. 1957).

Unlike the s-process, this does not produce heavy metals, i.e. those heavier than iron. Characteristic nuclei produced from this process are known as α-elements, and are often expressed as a logarithmic ratio compared to a star's iron content, [α/Fe].

1.3.2.3 Proton ingestion episodes (PIEs)

Metal-poor stars of $\sim 1\,\mathrm{M}_\odot$ may undergo proton ingestion episodes (PIEs) during the helium flash. The rapid burning during this flash results in powerful convective currents that drag hydrogen into close proximity to the core. This can initiate a second, smaller flash (Karakas and Lattanzio 2014).

Some models that suggest that PIEs lead to nucleosynthesis events. As the protons arrive in a region with significant quantities of ^{12}C, it is expected that ^{13}C is produced, which is as an excellent neutron source. The rapid production of ^{13}C in the second flash can provide a peak of 10^{15} neutrons cm^{-3}. Although the density is too low to be considered part of the r-process, it is greater than that required for the s-process. Models including this so called "i-process" are a reasonable fit to observations, although major uncertainties remain, such as the exact formation of this "^{13}C pocket", and the specific process this neutron capture follows (Bertolli et al. 2013).

1.3.2.4 Hot bottom burning (HBB)

Hot bottom burning (HBB) is a process that occurs in stars with mass $\gtrsim 3$ M$_\odot$. Convective currents develop near the base of the convective envelope, cycling very close to the H-burning shell. Temperatures near this base can reach 5×10^6 K, allowing nuclear processes such as the CNO cycle, the Ne-Na cycle, and potentially the Mg-Al chain (Ventura and D'Antona 2005; Karakas and Lattanzio 2014). This temperature is predicted to climb further in the lowest metallicity

AGB models. The processes involved in HBB can deplete much of the carbon that arrives as part of the TDU, and may prevent the star from becoming carbon-rich. The efficiency of HBB is affected significantly by the mass of the star, due to variation in convection and pressure (Scalo et al. 1975; Boothroyd et al. 1993). The initial mass at which HBB is expected to begin may also be affected by metallicity (Ventura et al. 2013).

1.4 Mass loss from AGB stars

1.4.1 Mass loss

Mass loss starts to become significant during the AGB stage. The following equation, although determined in 1975, is still considered an excellent method of calculating mass loss for a given star on the RGB or early AGB (Reimers 1975):

$$\dot{M} = 4 \times 10^{-13} \cdot \eta_R \frac{LR}{M} \ [\mathrm{M}_\odot \, \mathrm{yr}^{-1}], \tag{1.1}$$

where luminosity, L, stellar radius, R, and stellar mass, M, are given in solar units and $\eta_R \simeq 0.477$ (McDonald and Zijlstra 2015). This equation can be applied to the Sun during giant branch evolution. Assuming an unchanged mass (before significant mass loss), a value for $\dot{M}$ of $\sim 10^{-8}$ $\mathrm{M}_\odot$ yr^{-1} is calculated for the RGB tip, and $\sim 10^{-7}$ $\mathrm{M}_\odot$ yr^{-1} for the AGB.

As stars progress through the AGB, luminosity gradually increases as the hydrogen- and helium-burning shells move outwards and increase in volume. The gradual increase in radius and loss of mass further accelerate the increase in $\dot{M}$. Thermal pulses (Section 1.3.1.3) also contribute significantly to mass loss, as L and R likely undergo significant increases at these times (Herwig 2013).

Following Equation 1.1, it becomes clear that more-massive stars transition away from the branch more quickly. Despite their higher mass, the related and significant increases in radius and luminosity at the AGB tip cause a higher $\dot{M}$.

For nearby (< 50 kpc), bright stars, mass loss is usually measured indirectly by detecting the strength of molecular spectral lines, particularly CO (with $\dot{M}$ obtained from the integrated flux of the line, and velocity from the width). These are then fit into a radiative transfer model, which can provide a reasonable estimate of mass loss given the velocity of CO. Using this method, mass loss can be detected down to a rate of 10^{-9} $M_{\odot}$ yr^{-1} (Groenewegen 2014; McDonald et al. 2016). Other methods must be used to measure mass loss for stars further away from the observer, or for those with a lower mass-loss rate. An example of this is radiative transfer fitting of circumstellar dust (see Section 1.4.3; Schöier et al. 2002).

1.4.2 Drivers of mass loss

Possible drivers of mass loss include magnetic activity, pulsations, binary interactions, and radiation pressure on dust (Section 1.4.3).

1.4.2.1 Magnetic activity

Low-frequency oscillations in the star's magnetic field may provide additional energy to the stellar wind via the chromosphere, driving mass loss. This is likely to be more important in the RGB and early-AGB stages, reducing in influence as the thermally pulsing stage begins. Mass loss at this stage is driven by the heating of material in the chromosphere via magnetic reconnection (detectable by an Hα line with a "blue wing"), which grants material sufficient velocity to escape from the star (Dupree et al. 1984; McDonald and van Loon 2007).

Observations of magnetic fields in space are carried out by measuring circular polarisation. In AGB stars, this is achieved by observing maser polarisation from SiO, H_2O, and OH. Observations suggest that the field has a flux proportionality between R^{-1} and R^{-2}; additional data is required to constrain this. Findings are consistent with a field in the form of a dipole shape, with large-scale structure to drive stellar winds. It has been suggested that this field makes a significant contribution to mass loss for early AGB stars (Falceta-Gonçalves and Jatenco-Pereira 2002), i.e. before the thermally pulsing stage, although models show that this cannot be the only driver. The origin of the field is also unclear, with possible mechanisms including convective dynamos (similar to the process in the Sun), and interactions with a circumstellar disc in the case of binary stars (Vlemmings 2014; Schröder and Cuntz 2005).

1.4.2.2 Pulsation

Pulsations are significant in AGB stars, and arguably upper-RGB stars (such as the OGLE small amplitude red giants (OSARG stars) detected in the LMC; Soszynski et al. 2004). These provide kinetic energy to the dust and gas in the outer layers of the star, contributing to the stellar wind (McDonald et al. 2014).

There are two significant descriptions of pulsation for AGB stars: low-frequency harmonic oscillations of the stellar surface, which occur every $20 - 800$ days (Ita et al. 2004); and more powerful nuclear-driven thermal pulses of the stellar interior, generally seen every $10^3 - 10^4$ years during the TDU (Section 1.3.1.3; Iben 1975).

The surface pulsations occur because internal convective cells have a similar sound-crossing time to harmonic oscillations. The star enters forced harmonic oscillation causing significant pulsation of the star. However, it is unclear how exactly these pulsations become harmonic. It has not been determined whether they are driven, or randomly generated (Wood 2000). An important driver of this may be the κ mechanism. Here, surface pulsations occur when compressions from below ionise a layer of H into H^+, releasing electrons. The electrons absorb photons, causing the layer to store energy for longer than the layers around it. As the layer warms, it expands outward, increasing the radius and luminosity of the star. As the layer cools, opacity lowers again and the star begins to contract to its original radius (Hansen et al. 2012; McDonald et al. 2014).

1.4.2.3 Binary interactions

When a star in a binary system evolves to the AGB and expands, its radius may approach the limits of its Roche lobe. Material that remains inside the Roche lobe remains bound to the star that it originated from, while material that strays beyond it may fall under the gravitational influence of the stellar companion. If an AGB star (or its wind) expands beyond its Roche lobe radius, mass begins to systematically transfer from the AGB to its companion (Carroll and Ostlie 2007). A dust disc may also be present around the companion star or the entire binary system, forming due to the collimation of the AGB star's stellar wind, which may obscure the system, and cause a greater IR excess than expected (Kervella et al. 2015). Mass loss will continue via this process until the AGB star's radius (or wind) remains within the Roche lobe (Carroll and Ostlie 2007).

1.4.3 Dust

At the apex of pulsation (for both the long period pulsations and the occasional thermal pulses), the outer layers of the star expand and therefore cool, eventually reaching a temperature where molecules can form. This is determined from the appearance of molecular lines in the stellar spectrum (in optical and IR bands; Habing and Olofsson 2003). Multiple lines become visible at this point, the most significant of which is CO. CO is important as carbon and oxygen are the most abundant metals in most stars, and due to its high disassociation energy (~ 11 eV) it is one of the first molecules to form. It is often possible to infer the relative abundances of numerous other metals from the strength of the CO line (Le Bertre 1997).

As the star expands and cools further, larger molecules can be formed during the pulsations. These molecules are more likely to clump together due to their size, eventually forming μm-sized grains considered as dust (Habing 1996; Norris et al. 2012). The dust increases the opacity of the star, changing the shape of the star's spectral energy distribution (i.e. more flux is radiated at longer wavelengths). The type of dust produced depends on the chemistry of the star, and will be explored in the following sections.

1.4.3.1 Why is dust important?

Dust is an interesting product of AGB stars for the following reasons:

- AGB stars are an important distributor of metals, being one of the major drivers of the chemical make-up of a galaxy (Wallerstein et al. 1997). These newly synthesized elements are often bound in molecules and expelled as dust. This chemistry can impact the chemical make-up of future solar systems, as well as their formation (dust may affect the Jeans length and initial mass functions; Walch et al. 2011). Cooling in the ISM is also affected; cooling via metal ions is the dominant cooling mechanism in the ISM, despite being only a fractional component (Draine 2010).

- The energy balance and eventual fate of an AGB star is dependent on dust. Stellar opacity can vary depending on the species of molecules produced in circumstellar dust; higher opacity increases mass loss and accelerates the death of the star (Woitke 2006).

- Dust is currently the best tracer we have to detect mass loss in individual stars that are too distant for spectroscopy (Section 1.4.3.5).

1.4.3.2 How dust drives mass loss

After its production in the circumstellar envelope, dust is driven by radiation pressure, and ejected from the star. The velocity of the dust grain decreases as it travels, as it transfers a fraction of its momentum to the surrounding gas (the velocity of which increases). The difference between these two values is known as the drift velocity. This dust and gas are both ejected from the star (considered the stellar wind), leading to increased AGB mass loss (Willson 2000). Models of radiation-driven mass loss provide close matches to the observed values (Decin et al. 2010; Höfner 2008, 2011; Norris et al. 2012). Major uncertainties exist in our understanding of this process, such as how significant the drift velocity is, and whether radiation pressure is the only driver.

1.4.3.3 Oxygen-rich stars

Oxygen-rich stars have a C/O ratio of < 1 (a typical AGB star has a value of ~ 0.4 before the TDU begins). It is more difficult for metal-rich stars to become carbon stars, so all AGB stars remain oxygen-rich in metal-rich regions (Boyer et al. 2013, although Karakas (2014) suggests that helium abundance may also be a factor; Section 1.3.1.3). Additionally, stars $\gtrsim 3$ $M_\odot$ destroy carbon during HBB, and remain O-rich (Section 1.3.2.4).

As a result of this C/O ratio, the chemistry occurring in the outer layers of the star produces molecules based on oxygen, which condense into silicate dust grains that increase in size with metallicity (Dell'Agli et al. 2014). Frequently encountered molecules in oxygen-rich stars include (in increasing complexity; Cherchneff 2012; Molster et al. 2002; Blommaert et al. 2007; Jones et al. 2012; Kemper et al. 2002; McDonald et al. 2010a):

- CO and CO_2
- Metal oxides, i.e., TiO, VO (and ZrO in S stars, where C/O $\sim$ 1)
- H_2O
- Al_2O
- Al_2O_3

A well-known spectral feature produced by dust is found at 9.5 $-$ 10 μm, caused by magnesium and iron-rich silicates (such as olivines; Lebzelter et al. 2006), but with a notable contribution from alumina dust (Jones et al. 2014).

Magnesium-rich grains form closer to the star, with iron-rich grains condensing further away (Bladh and Höfner 2012). This is due to the high opacities of iron-based silicates compared to magnesium, causing ferrous molecules to evaporate at higher fluxes.

Amorphous iron does not show spectral features, but increases the strength of the IR excess. The IR excess is a reddening of the star due to absorption of light by dust in optical bands, and re-emission in the IR, caused by dust (Figure 1.3; Meyer et al. 1997).

At later stages, the stellar wind increases in strength, and becomes known as the superwind. In larger AGB stars (of around 8 $M_\odot$), this reaches $\dot{M} \approx 10^{-4}$ $M_\odot$ yr^{-1}. This ushers in the end of the AGB stage (Owocki 2013). The strength of the superwind, and age at which it occurs is depends on the levels

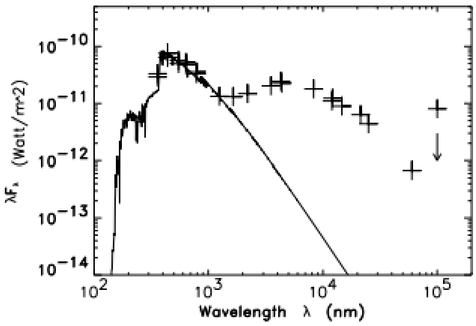

Figure 1.3: Reproduced from Maas et al. (2005). A typical observation of an IR excess. Discrepancy between observed data points and non-reddened model can clearly be seen.

of dust production in the outer regions of the circumstellar envelope (Section 1.4.3.2; McDonald et al. 2013).

Lagadec and Zijlstra (2008) predict that, for an oxygen-rich star, the superwind is triggered when luminosity reaches the following point (assuming dust fraction scales with metallicity and is proportional to the dust-to-gas mass ratio):

$$L_{OSW} = 10^4 \left(\frac{Z}{Z_\odot} \right)^{-4/3} L_\odot. \tag{1.2}$$

This occurs when the fractional composition of silicate grains in the circumstellar envelope is great enough that radiation pressure is sufficiently influential to cause significant mass loss.

1.4.3.4 Carbon-rich stars

An AGB star is considered carbon-rich when it has a C/O ratio > 1; most carbon stars achieve this during the TDU (Section 1.3.1.3). All oxygen is locked away in CO, leaving carbon as the most abundant remaining metal, and dominant driver of molecule production.

It is worth noting that there are other circumstances in which a star may become carbon-rich. "Extrinsic" carbon stars are non-AGB (typically MS) stars that accrete material from a carbon-rich AGB binary companion (Section 1.4.2.3). The outer atmosphere of the non-AGB star can become carbon-rich before leaving the main sequence. These are considered "non-classical" carbon stars (McClure 1985). Additionally, some stars are born carbon-rich. Carbon-enhanced metal poor (CEMP) stars can be found in the Galactic halo, where they appear to have formed. This means that they must have formed in an oxygen-depleted environment, although the exact details of this are a matter of debate (Aoki et al. 2007). These two types of stars are not of interest to this study, and the terminology "carbon star" will refer only to carbon-rich AGB stars (unless otherwise stated).

Carbon stars have significantly different chemistry than those with oxygen-dominated envelopes. Completely different molecules are seen, such as (Cherchneff 2012):

- CH, CN, HCN, and C_2H_2
- Polycyclic aromatic hydrocarbons, i.e. molecules containing multiple benzene rings
- Carbides, e.g. SiC and TiC

Mass loss may behave differently in carbon stars. Due to the presence of amorphous carbon and carbon-rich dust, stellar opacity is higher than in oxygen-rich AGB stars. Radiative transfer modelling suggests that this increases the strength of stellar winds (due to the stronger effects of radiation pressure) and may therefore increase mass loss, shortening the life span of the AGB star (Woitke 2006).

In carbon stars, a superwind may begin when the fraction of free carbon is 10% greater than that of oxygen (Lagadec and Zijlstra 2008). This carbon allows the formation of "sooty" grains, increasing opacity and the effects of radiation pressure. Therefore, this is likely to begin at a lower luminosity than the superwind of an equivalent-mass oxygen-rich star. Factors that also need to be taken into consideration in this model, however, are the effects of increasing radius and pulsation strength, caused by an increased metallicity from dredge-up.

1.4.3.5 Detection

The dust-production rate of a star is determined by analysing its IR colour. The strength of IR excess flux is proportional to the amount of dust in the circumstellar envelope. It is assumed that dust driven into the ISM via stellar winds dissipates relatively quickly, so it does not linger in the stellar vicinity, meaning the excess is dependent only on recent dust production (the last $\sim 100 - 1000$ years). Beyond this point, the dust cools, fading in mid-IR bands and joining the ISM (McDonald et al. 2012a).

Emission spectra of the dust can be analysed to determine its composition. Spectral energy distributions for individual stars can be determined out to the Mpc range (Local Group) but we have no idea of the expansion velocities of the winds of metal-poor stars at this range (McDonald et al. 2011).

1.4.4 Metallicity and dust production

In general, metal-poor stars are expected to produce less dust, as they lack the raw material to do so. This appears to be the case for oxygen-rich AGB stars. However, this does not appear to be true for C stars, due to the enhanced production possible with the carbon-based chemistry in their outer layers (as a lower fraction of dredged-up carbon is bound in CO; Sloan et al. 2012). Indeed, preliminary results from the DUSTiNGS survey have suggested that there is little correlation between metallicity and dust production in C stars (at least above [Fe/H] $= -2.2$ dex; Boyer et al. 2015b). Investigating this relationship was one of the key goals of the DUSTiNGS project.

Current objectives in this area include:

- Examining the interplay between dust production and pulsation
- Improving estimates of dust-production rates and dust composition
- Assessing metallicity's influence on the period–luminosity relationship
- Selecting targets for studying dust mineralogy with the *James Webb Space Telescope*

1.5 Dwarf galaxies

Dwarf galaxies are likely the predominant form of galaxy in the Universe (assuming our Local Group is typical). They are difficult to detect in more distant galaxy clusters due to their small angular size and low luminosity, evidenced by the fact that dwarf companion galaxies to the MW are still being found regularly, e.g. Crater 2 (Torrealba et al. 2016). There are various types, including dwarf spheroidals, spirals, ellipticals, and irregulars, mirroring their larger counterparts (van den Bergh 2000; Simon and Geha 2007).

1.5.1 Determining star-formation histories

Determination of the star-formation histories (SFHs) of dwarf galaxies has been achieved by producing colour-magnitude diagrams (CMDs). These CMDs can be used in conjunction with computational models to determine the age of various stellar populations and hence calculate a galaxy's SFH. These have shown that dwarf spheroidal (dSph) galaxies generally had rapid star formation greater than 10 Gyr ago (equivalent to $z = 2$), but have been broadly quiescent since shortly after reionization (although there is significant variation). On the other hand, dwarf irregulars (dIrr) only formed $\sim 30\%$ of their stars during this period, with an increased star-formation rate in the past 6 Gyr ($z = 1$), with little variation in the Local Group (Tolstoy et al. 2009). The cause of this is debated, but a leading hypothesis states that interstellar gas is shocked when falling into the Local Group potential (as the galaxy's velocity becomes greater than the speed of sound of the X-ray halo composing the intergalactic medium), encouraging the development of new stars. This may be part of a process in which they will ultimately evolve into dSph galaxies (Grebel et al. 2003).

However, this SFH may be biased due to the more-probable detection of young, bright stars, and a lack of data for fainter, extended regions. Overall, results suggest that star-formation efficiency is reduced for low-mass galaxies, and that this effect is more significant at earlier times (Weisz et al. 2014). It is worth noting these explanations of SFHs do not take into account interactions with larger galaxies. Gravitational interactions with these could cause distortions within a dwarf galaxy, inducing star formation that could not occur otherwise.

1.5.2 Chemical enrichment of a galaxy

Throughout a galaxy, different elements are produced on different timescales. For example, in Type II supernovae, a wide variety of elements are produced. These SNe are less frequent at current times, as the massive stars that produce them have become less common. Type Ia SNe (caused by accretion onto a white dwarf star) have become the dominant form of supernova in the modern Universe, and produce mostly iron. Elements synthesised in AGB stars are also distributed over these longer time periods. The abundance of Fe to other metals increases over time due to the SNe Ia contribution. An [α/Fe] "knee" is visible when various elemental abundances are plotted, demonstrating the era when dominant nucleosynthesis products change (Wheeler et al. 1989; Bensby et al. 2004). Measuring the abundances of elements in a galaxy can inform us of its SFH. This is often known as "galactic archaeology" (Tolstoy et al. 2009).

There remain major uncertainties, however, in determining SFHs in this manner, particularly in dwarf galaxies, which as discussed tend to have a lower than expected metallicity. A possible explanation for this is that high velocity SNe ejecta (including the metals produced within) are more likely to be lost from dwarf galaxies due to their shallower potential wells. In addition, galactic winds are more likely to strip the galaxy of its ISM. These factors could reduce both a galaxy's metallicity and star-formation efficiency (Nomoto et al. 2013).

1.5.3 Determining galactic metallicities

Determining the metallicity of galaxies is not a simple process, and involves numerous methods; none are perfect but some become more advantageous than others at certain distances.

1.5.3.1 Stellar spectroscopy

One useful metallicity determination method is stellar spectroscopy. The strength of spectral lines in the outer atmospheres of a sample of RGB and AGB stars can be used to determine the overall metallicity of a galaxy (Kirby et al. 2008). As this requires spectra of individual stars to be acquired, it can only be performed for the brightest stars in nearby galaxies, so can only be used extensively within the Local Group.

Iron abundance is the preferred measure of metallicity as it is the heaviest abundant metal, with hundreds of well-documented lines in optical wavelengths.

As a result, metallicities are often provided using the [Fe/H] logarithmic ratio. However, dwarf galaxies tend to be at such a distance that only the brightest stars can be individually resolved. Giant stars are excellent candidates for this due to their intrinsic brightness (Kirby et al. 2008). However, these stars must have a temperature $\gtrsim$ 4000 K, or molecular lines will obscure the atomic transitions. As the brightest stars are of a relatively young age compared to that of the galaxy, and have an enhanced metallicity from the third dredge-up and fusion processes (although iron abundance is unchanged), the calculated metallicity can be over-estimated and therefore a misrepresentation of the overall galactic metallicity. A similar problem is encountered when attempting to measure the spectra of OBA stars. These stars are very young, so have an intrinsic higher metallicity than most other stars in the galaxy.

1.5.3.2 Spectroscopy of the ISM

For more distant galaxies a similar process to stellar spectroscopy can be used. The strength of spectral lines detected in the ISM is used as the indicator, rather than that of the stars themselves. Iron is generally depleted from the gas phase of these regions, so lighter elements are used, (often those produced as a result of the α-process). The considerable range of temperatures encountered in the ISM makes the choice of carrier difficult. This means a different ratio must be calculated (i.e. not including Fe) which may not be directly relatable to the values determined via stellar spectroscopy. Often, molecular recombination lines of OH, detectable at radio wavelengths, can be used for neutral gas, although optical forbidden lines can be used for hot plasma. This allows for a calculation of oxygen abundance for the ISM (Pilyugin 2001). Metallicities of the ISM are not likely to be a good representation of the metallicity of the entire galaxy (similar to the abundances calculated from AGB spectra). In addition, the galaxy's ratio of [α/Fe] will change over time as iron is more readily produced than oxygen at modern times.

1.5.3.3 Isochrones

Stellar evolution tracks have been produced based on nearby globular clusters, with the following parameters known for each of the stars within: age, metallicity (Z), helium content (Y), [α/Fe], and interstellar reddening ($E(B-V)$). For distant galaxies ($>$ 400 kpc), where stellar spectra cannot be taken, these evolutionary tracks can be used to produce an isochrone, a snapshot of the current stellar population modelled with the given parameters. These parameters can be adjusted to match the isochrone with with various observed features, e.g. Dotter et al. (2008); McDonald et al. (2009). The adjusted parameters of this inferred method suffer from substantial correlation, causing more complete degeneracies than the spectroscopic method and rendering it less reliable. Adjusting different parameters can provide the same result for isochrone fitting, meaning it must be used with caution.

1.6 Galaxies of interest

This Section provides a brief description of the dIrr galaxies covered by this study for which usable photometry and H–R diagrams were returned. Particular emphasis is placed on stellar populations and their chemical properties. A galaxy must fulfil the following criteria for it to be included:

- Dwarf irregular galaxy
- Recent star formation
- Within 1.5 Mpc
- Has sufficient photometry

An initial analysis was carried out on several more galaxies, but they were not included in this list as they did not yield usable results. Data from DUSTiNGS was used in 12 of the 13 galaxies listed below. In addition to providing excellent photometry in mid-IR bands (their 3.6 and 4.5 μm data goes down to 21 mag), Boyer et al. (2015a) provided AGB star candidates based on their variability (using data from previous epochs). The number of AGB candidates (with over a 2σ certainty) identified by this study for each galaxy are reported below.

Table 1.1 contains an overview of the distance, average metallicity, average reddening and mass (in stars) of each these galaxies.

Table 1.1: List of galaxies to be studied in this project in descending order of interest, based on their metallicity, star-formation history, distance, and stellar mass. Provided values are from Tables 2, 4, and 5 in McConnachie (2012) and references therein, unless otherwise stated. Values for [Fe/H] and $E(B-V)$ are mean values for the galaxy, as these values may vary across the galaxy's extent. Additional references: (1) Bellazzini et al. (2014a); (2) Miller et al. (2001); (3) Tikhonov et al. (2005)

Galaxy	Distance (kpc)		[Fe/H] (dex)		$E(B-V)$ (mag)	$M_\star$ (10^6 $M_\odot$)
Sextans B	1426	20	–1.4[1]	—	0.031	52
Sextans A	1432	53	–1.85	—	0.045	44
IC 1613	755	42	–1.6	0.2	0.025	100
Sag DIG	1067	88	–2.1	0.2	0.124	3.5
Peg DIG	920	30	–1.4	0.2	0.068	6.6
WLM	933	34	–1.27	0.04	0.038	43
NGC 6822	459	17	–1	0.5	0.231	100
LGS 3	650[2]	25	–1.5[2]	0.3[2]	0.04	0.96
Phoenix	415	19	–1.37	0.2	0.016	0.77
Leo A	798	44	–1.4	0.2	0.021	6
And IX	766	25	–2.2	0.2	0.075	0.15

Galaxy	Distance (kpc)		[Fe/H] (dex)		$E(B-V)$ (mag)	$M_\star$ (10^6 M$_\odot$)
NGC 185	617	26	–1.3	0.1	0.184	68
NGC 147	676	28	–1.1	0.1	0.172	62
Aquarius	1072	39	–1.3	0.2	0.051	1.6
NGC 3109	1300	48	–1.84	0.2	0.067	76
IC 10	794	44	–1.28	—	1.568	86
NGC 55	1932	107	–1.25[3]	—	0.013	2200
UGCA 438	2188	121	–1.68	0.19	0.015	17
Antlia	1349	62	–1.6	0.1	0.079	1.3

1.6.1 Sextans B

Sextans B (often shortened to Sex B) is a galaxy visible just above the equatorial plane (Bellazzini et al. 2014a). It is a member of the loose group of dwarf galaxies known as the "NGC 3109 Association" (Tully et al. 2006), with a distance of $\sim$ 1400 kpc, verified by both measurements of Cepheids and the RGB. This likely puts the galaxy just over the edge of the Local Group (Sakai et al. 1997). Studies of motion within the galaxy suggest that it is composed of $\sim$ 90% dark matter (Bellazzini et al. 2014a).

The galaxy contains at least three star clusters (Bellazzini et al. 2014a; Sharina et al. 2005), and at least three stellar populations. The youngest population has an age $\leq$ 1 Gyr, and may still be forming stars in the present era. This population has [Fe/H] $= -1.3$ dex (Tosi et al. 1991). A slightly older population ($\sim$ 2 Gyr) exists, including a large globular cluster, with [Fe/H] $= -1.35$ dex and [α/Fe] $= 0.1$ dex (Sharina et al. 2007). The bulk of the stars in this galaxy are from a much older population of age $\leq$ 13 Gyr, with [Fe/H] $= -1.6$ dex (Bellazzini et al. 2014a).

The galaxy contains many Cepheid variables, four of which have periods between 11.1 and 25.1 days (Sandage and Carlson 1984). There are at least 5 PNe, for which chemical abundances have been measured (Magrini et al. 2005b). There is also a population of RSGs, with variability below 0.8 mag (Sandage and Carlson 1985). 35 variable AGB candidates were reported by Boyer et al. (2015a).

1.6.2 Sextans A

Sextans A (shortened to Sex A) lies just below the equatorial boundary, so is just in the southern hemisphere. Similar to Sextans B, Sextans A is a member of the NGC 3109 association, and is at a similar distance ($\sim$ 1400 kpc), so is again likely just over the boundary of the Local Group (Sakai et al. 1996). It is composed of $\sim$ 90% dark matter (Bellazzini et al. 2014a).

Two very recent star-formation regions can be seen, active within the past 50 Myr (Bianchi et al. 2012). The overall young stellar population ($\leq$ 2 Gyr) has [Fe/H] $= -0.99$ dex and [α/Fe] $= -0.11$ dex (Kaufer et al. 2004). There is an overall increase in metallicity amongst the underlying population towards the galactic centre, with [Fe/H] $= -2.2$ dex for the $\sim$ 14 Gyr population around the edges of the galaxy, and [Fe/H] $= -1.4$ dex for the more evolved 11 Gyr population towards the centre (Battaglia et al. 2011). For the galaxy as a whole, [Fe/H] $= -1.9$ dex (Battaglia et al. 2011).

There are many short-period Cepheids which have been studied in detail to constrain the distance to the galaxy (Dolphin et al. 2003). Only one planetary nebula has been found (Magrini et al. 2005b), and RSGs have a similar variability to those in Sex B, $<$ 0.8 mag (Sandage and Carlson 1985). 28 variable AGB candidates were reported by Boyer et al. (2015a).

1.6.3 IC 1613

IC 1613 is a well-studied dwarf irregular galaxy. Its high galactic latitude means it only experiences low reddening and, coupled with its relative proximity (~ 750 kpc; Dolphin et al. 2001), it is an attractive target for observation compared to other nearby dwarfs.

The galaxy contains several stellar populations. A very young population ($<$ 10 Myr) has been detected, with [Fe/H] $= -0.85 \pm 0.25$ dex. Additionally, there is a slightly older population of age 10 Myr – 1 Gyr, with [Fe/H] $= -1.0 \pm 0.3$ dex. A population of intermediate age ($1 - 8$ Gyr) comprises the majority of the stars of the galaxy, and has a lower metallicity, [Fe/H] $= -1.35 \pm 0.3$ dex. Finally, a small, old population ($>$ 10 Gyr) exists, with [Fe/H] $= -2.0 \pm 0.5$ dex (Cole et al. 1999).

There are no known globular clusters in this galaxy. Many Cepheids have been recorded, with a very tight period–luminosity relation (Freedman et al. 2009). There are two or three PNe (Mateo 1998; Magrini et al. 2005a), and at least one WR star from the young population (Mateo 1998; Cole et al. 1999). 52 variable AGB candidates were reported by Boyer et al. (2015a).

1.6.4 Sagittarius Dwarf Irregular

The Sagittarius Dwarf Irregular (or Sag DIG) is a fairly poorly studied galaxy in the southern sky. It is at a distance of 1.06 Mpc (Karachentsev et al. 1999), and is thought to be the most distant member of the Local Group from the barycentre (van den Bergh 2000).

The galaxy is comprised of multiple stellar populations (Gullieuszik et al. 2007; Momany et al. 2005). A recently ($<$ 100 Myr) formed population is present, with [Fe/H] $= -1.6 \pm 0.3$ dex, which may be the most-metal-poor young population in the Local Group. The underlying stellar population is 1 – 10 Gyr old, with the bulk likely formed 4 – 8 Gyr ago, and with [Fe/H] ~ -2.2 dex. There is also an ancient population (> 10 Gyr), again of lower metallicity (Gullieuszik et al. 2007). 8 variable AGB candidates were reported by Boyer et al. (2015a). Momany et al. (2002) identified a population of supergiants.

1.6.5 Pegasus Dwarf Irregular

The Pegasus Dwarf Irregular (or Peg DIG) is visible in the northern sky. There have been significant disagreements regarding the distance to this galaxy, with estimates ranging from 170 kpc to 1.75 Mpc. This upper limit was calculated due to the misidentification of a group of variables as Cepheids. Estimates from the RGB tip suggest a distance of $0.90 - 0.95$ Mpc (Aparicio et al. 1997b; Kniazev et al. 2009; Lee 1995). Due to its distance and motion, it is likely a member of the Local Group (Lee 1995), and a member of the M31 subgroup, i.e. a dwarf belonging to Andromeda (Kniazev et al. 2009). The Kniazev et al. (2009) paper also suggests a composition of $\sim 60\%$ dark matter.

Only one region of very-recent star formation (< 10 Myr) can be detected, an ionised region around a B star (Aparicio and Gallart 1995). The remainder of the young (< 0.5 Gyr) population exists in two clumps, with [Fe/H] $= -1.3$ dex (Gallagher et al. 1998). Due to the SFH of this galaxy, it is deemed unlikely that the intermediate age population, forming the bulk of the stellar population of this galaxy (and forming $2 - 4$ Gyr ago), is significantly more metal-poor; a value of [Fe/H] $= -1.4$ dex was used for this work (Gallagher et al. 1998; McConnachie et al. 2005).

One PN has been discovered in this galaxy (Jacoby and Lesser 1981). At least 20 Cepheids have been discovered with periods between 0.6 and 15.3 days

(Meschin et al. 2008), and there are at least two RSGs from the younger stellar population (Britavskiy et al. 2015). 15 variable AGB candidates were reported by Boyer et al. (2015a).

1.6.6 Wolf-Lundmark-Melotte

Wolf-Lundmark-Melotte (or WLM) is an isolated (Leaman et al. 2012) dwarf irregular in the southern sky, named after its discoverers. It is at a distance of $\sim$ 950 kpc (derived from Cepheid measurements; Gieren et al. 2008), and is composed of 90 – 95% dark matter.

WLM possesses a brighter GC than expected for the galaxy's size, containing a population of stars with [Fe/H] $= -1.96 \pm 0.3$ dex, and [α/Fe] $= 0.3$ dex. This GC accounts for 17 – 31% of the metal-poor stars within WLM, and an age of 13 Gyr has been assumed (Larsen et al. 2014). A summary of the remaining populations and their metallicity are given in Table 1.2.

Table 1.2: Populations and their associated metallicities for the dwarf irregular galaxy WLM. Data is from Dolphin (2000).

Age of population	[Fe/H]	Uncertainty
0 – 1 Gyr	–1.08	0.18
1 – 2.5 Gyr	–1.13	0.16
2.5 – 5 Gyr	–1.20	0.14
5 – 7 Gyr	–1.25	0.13
7 – 9 Gyr	–1.34	0.14
9 – 12 Gyr	–2.18	0.28

The significant star formation that has recently occurred in this galaxy means there is a large population of RSG stars. These are of interest as WLM is the most-metal-poor galaxy known undergoing this magnitude of star formation in the Local Group, allowing the chemical dependence of RSGs to be probed. A number of RSGs in this galaxy undergo significant variation, changing from spectral type M2.5 I to K5 I (Levesque 2013). One PN has been found in this galaxy (Magrini et al. 2005b), and the period–luminosity relation of its Cepheids have been studied in great detail in Tammann et al. (2011). 37 variable AGB candidates were reported by Boyer et al. (2015a).

1.6.7 NGC 6822

NGC 6822 is a galaxy in the southern sky, which appears to be a close analogue of the SMC. Its low galactic latitude means that it suffers from significant reddening, and a higher population of foreground objects, posing challenges for observational studies (Veljanoski et al. 2015). It lies at a distance of $\sim$ 450 kpc (Górski et al. 2011), and is one of the closest galaxies investigated in this study. Additionally, it is the most massive galaxy included (McConnachie 2012). This has allowed it to hold onto more gas over its lifetime, resulting in more star formation and a higher metallicity (Tolstoy et al. 2001).

The bulk of the stars in this galaxy are from an intermediate age population ($1 - 9$ Gyr), with a smooth distribution of ages. The mean metallicity of this population is [Fe/H] $= -0.9$ dex. There is a tiny population of stars older than this, perhaps dating to the first era of star formation within the galaxy (Tolstoy et al. 2001). Star formation in the past Gyr has been sporadic, with RSG studies suggesting a metallicity of [Fe/H] $= -0.5$ dex for these recently formed stars (Bianchi and Efremova 2006; Patrick et al. 2015). Perhaps due to its size, NGC 6822 contains eight globular clusters, considered unusual for a dwarf galaxy. An in-depth estimate of metallicities for seven of these GCs can be found in Veljanoski et al. (2015).

There are 26 planetary nebula candidates in this galaxy (García-Rojas et al.

2016). Chemical analyses of 11 of the galaxy's RSGs have been carried out in Patrick et al. (2015). In-depth analysis of 16 long-period Cepheids (10-100 days) have been carried out, used to determine distances (Madore et al. 2009). This galaxy was not covered by the DUSTiNGS survey.

1.6.8 LGS 3

LGS 3 (also known as the Pisces Dwarf) is visible in the northern sky. A distance of 650 kpc has been calculated (Miller et al. 2001), and studies of its motion suggest it is composed of 95% dark matter (Aparicio et al. 1997a) and a member of the Andromeda subgroup (van den Bergh 2000).

Stars of all ages are present within this galaxy, following the initial era of star formation 12 Gyr ago (Aparicio et al. 1997a). The bulk of the star formation (85%) appears to have occurred early on, $9 - 12$ Gyr ago, and peaking at 11.5 Gyr (Hidalgo et al. 2011). The metallicity of this older population is [Fe/H] $= -1.5 \pm 0.3$ dex. The younger stars (< 1 Gyr) are generally found towards the centre of the galaxy, where the SFR has been more consistent. These typically have a metallicity of [Fe/H] $= -1$ dex (Miller et al. 2001). Five variable AGB candidates were reported by Boyer et al. (2015a).

1.6.9 Phoenix

Phoenix is a dwarf galaxy in the southern sky, previously misidentified as a globular cluster. It has a distance of ~ 400 kpc (Martínez-Delgado et al. 1999b).

There has been disagreement over the mean metallicity of Phoenix. Martínez-Delgado et al. (1999b) determined [Fe/H] $= -1.37$ dex, but studies by Held et al. (1999) and Hidalgo et al. (2009) provide the more consistent values of –1.81 and

–1.87 dex respectively. The SFH of this galaxy can be split into three epochs. Around 50% of the stars formed before 10.5 Gyr ago, with an additional 35% before 6 Gyr. The final 15% have formed since this point, with a burst of star formation in the past 150 Myr (Hidalgo et al. 2009; Martínez-Delgado et al. 1999b).

It is unlikely that this galaxy contains GCs due to its small size (Mateo 1998). There is at least one PN, for which chemical abundances have been derived (Saviane et al. 2009), and at least one RSG (Britavskiy et al. 2015). Eleven variable AGB candidates were reported by Boyer et al. (2015a).

1.6.10 Leo A

Leo A (also known as Leo III) is a dwarf irregular in the northern sky, at a distance of $\sim$ 800 kpc (Bernard et al. 2013; Dolphin et al. 2002). An analysis of the structure and chemical composition of the galaxy suggests that it may be a relic of the early Universe, similar to the kinds of objects that merged to form larger galaxies such as the MW (Cole et al. 2007). It is likely $> 80\%$ dark matter (Brown et al. 2007).

The stellar population of the galaxy is primarily of a young to intermediate age, with a younger mean age than that of most other dwarf irregulars. Around 90% of its star formation has occurred in the past 8 Gyr, increasing to a peak around 3 Gyr ago. From this point, star formation has decreased, ignoring a spike around 500 Myr ago. There is a tiny, ancient population that formed > 10 Gyr ago, meaning the galaxy may have formed before or during the era of reionization. Metallicity appears to have remained constant throughout much of its lifetime, at [Fe/H] $= -1.4$ dex (Cole et al. 2007).

Over 156 Cepheids have been detected in this galaxy (Bernard et al. 2013). They are of particular interest as their relative abundance allows for good tests of the P–L relation in low-metallicity conditions. One planetary nebula has been discovered in this galaxy (Magrini et al. 2003). Five variable AGB candidates were reported by Boyer et al. (2015a).

1.6.11 Andromeda IX

Andromeda IX (or And IX) is a satellite of the Andromeda Galaxy, discovered by the *Sloan Digital Sky Survey*, and first presented by Zucker et al. (2004). At the time of its discovery it had lowest surface brightness of any galaxy ever found. It lies at a distance of $\sim$ 750 kpc (Harbeck et al. 2005), and contains either a less dense or more extended DM halo than would be expected for a galaxy of its size (Collins et al. 2010).

The galaxy appears to be extremely metal-poor, with only limited star formation ever having occurred. There is no evidence for an intermediate age population; most stars are ancient (>10 Gyr), with a small level of recent star formation in the past Gyr. The galaxy has a metallicity (averaged over all populations) of [Fe/H] $= -2.2$ dex (Collins et al. 2010). Eight variable AGB candidates were reported by Boyer et al. (2015a).

1.6.12 NGC 185

NGC 185 is a satellite galaxy of Andromeda, at a distance of $\sim$ 600 kpc (McConnachie 2012). Within the inner two half-light radii of the galaxy, it is composed of $40-50\%$ dark matter (De Rijcke et al. 2006). The galaxy likely contains an active galactic nucleus (AGN), which if true would make it the closest AGN to Earth (Ho et al. 1997). However, this claim has been disputed (Martins et al. 2012).

The majority of the stars in this galaxy have an age of > 10 Gyr (Martínez-Delgado and Aparicio 1998), and it has an average metallicity of [Fe/H] $= -1.08$ dex (Crnojević et al. 2014). Recent (< 1 Gyr) star formation appears to only have occurred in its most central regions (Martínez-Delgado et al. 1999a). Between six and nine globular clusters are associated with this galaxy (Sharina et al. 2006; Veljanoski et al. 2013), with metallicity information available for the six discussed by Sharina et al. (2006).

Up to five PNe have been discovered in this galaxy, and these are systematically brighter than those seen in the nearby NGC 147 galaxy (Corradi et al. 2005). This is likely due to the fact that it has had more star formation in the past 3 Gyr, meaning a greater proportion of current PNe were formed from larger stars. 73 variable AGB candidates were reported by Boyer et al. (2015a).

1.6.13 NGC 147

NGC 147 is a satellite of Andromeda, and a similar (albeit more massive) galaxy to NGC 185, with which it forms a pair. It is at a distance of ~ 680 kpc (McConnachie 2012), and $40-50\%$ of its mass within two half-light radii is composed of dark matter (Conn et al. 2012).

The galaxy's overall metallicity is slightly higher than that of NGC 185, with [Fe/H] $= -0.96$ dex (Crnojević et al. 2014). This is likely because more star formation has occurred within the galaxy over its lifetime, as it retained more ISM due to its higher mass. Between three and four globular clusters are associated with this galaxy (Sharina et al. 2006; Veljanoski et al. 2013), with metallicity information for the three confirmed provided by Sharina et al. (2006). Up to nine PNe have been detected in this galaxy (Corradi et al. 2005). 94 variable AGB candidates were reported by Boyer et al. (2015a).

1.7 Personal objectives

As part of the DUSTiNGS survey, several hundred sources were seen in nearby dwarf irregular galaxies that are candidate dust-producing, mass-losing AGB stars. The aim of this project is to produce an SED for each of resolvable star in the target galaxies, using multi-wavelength photometry from literature data. This will enable dust-producing stars to be distinguished from contaminating objects, such as background galaxies. In addition, effective temperatures and luminosities will be measured, allowing placement on the H–R diagram. The IR excess of each of these objects will be determined by analysing the flux in 3.6 and 4.5 μm bands. Finally, known carbon stars will be identified based on literature, and an analysis carried out upon them using the parameters determined in this work.

Chapter 2 details the photometry collated from the literature, and the process used to match between catalogs. The SED-fitting code is then described, followed by the H–R diagrams for each galaxy. Chapter 3 contains an analysis of the filters used to produce the H–R diagrams, and the need to remove some of them to produce more accurate SEDs is discussed. Following this, an estimate of the IR excess is calculated in 3.6 and 4.5 μm bands (and in some cases additional values in 5.8 and 8.0 μm bands). Chapter 4 provides an analysis of the stellar populations of the dIrrs using isochrones. New estimates of metallicity are suggested for the general stellar population of several galaxies. In Chapter 5, the RGB tip of each galaxy is characterized, and related to metallicity. SED-determined values of temperature are compared to spectroscopically-determined literature values for supergiants. The "typical" stellar population of a dIrr is determined by combining

H–R diagrams for each galaxy in the sample. The overall dusty AGB population is discussed and compared to the work of Boyer et al. (2015a), particularly relating to variability. Carbon stars are then identified by comparison with literature, and their parameters analysed. Chapter 6 details the conclusions of this work.

Chapter 2

Observations and data

2.1 Photometry

A list of photometry obtained for individual galaxies in this study is presented in Table 2.1. All photometry was obtained from the *VizieR* database, excluding that from the INT Wide Field Survey and VHS, which were obtained from their own respective databases.

A significant source of data that was not used in this project is the *Hubble Space Telescope* (*HST*). This is due to the telescope's point spread function. The excellent optical photometry from the *HST*'s Wide Field Camera 3 resolves a point source to $\sim$ 0.1". This compares to $\sim$ 1" for ground-based optical telescopes, or $\sim$ 2" for the *Spitzer Space Telescope* (*Spitzer*), corresponding to a difference in area up to a factor of 400. Difficulties arise when trying to match optical photometry from *HST* to, for example, mid-IR photometry from *Spitzer*, as many objects which appear to be point sources to the *HST* are blended in the *Spitzer* data. Therefore, for ease of source matching between wavelengths, no *HST* photometry was used in this work.

Table 2.1: List of galaxies studied in the project, listing the sources of the photometry and filters these used. Note: objects do not necessarily appear in each filter in each catalog. Details of the filters used can be seen in Table 2.3. Boyer et al. (2009) also contained observations in [3.6] and [4.5] bands in addition to [5.8] and [8.0], but were not used due to the superior quality of the more-recent DUSTiNGS observations.

Galaxy	Telescope	Study	Filters
Sextans B	LBT	Bellazzini et al. (2014b)	g, r
	INT	INT Wide Field Survey	g, i, r
	UKIRT	UKIDSS	Strömgren y, J, H, K
	Spitzer	DUSTiNGS; Boyer et al. (2015b)	[3.6], [4.5]
Sextans A	LBT	Bellazzini et al. (2014b)	g, r
	VISTA	VHS	Strömgren y, J, H, K
	Spitzer	DUSTiNGS; Boyer et al. (2015b)	[3.6], [4.5]
	Spitzer	Boyer et al. (2009)	[5.8], [8.0]
IC 1613	Warsaw Telescope	Udalski et al. (2001)	V, I
	UKIRT	Sibbons et al. (2015)	J, H, K
	Spitzer	DUSTiNGS; Boyer et al. (2015b)	[3.6], [4.5]
	Spitzer	Boyer et al. (2009)	[5.8], [8.0]
Sag DIG	VLT	Beccari et al. (2014)	V, I

Galaxy	Telescope	Study	Filters
	Spitzer	DUSTiNGS; Boyer et al. (2015b)	[3.6], [4.5]
Peg DIG	SDSS 2.5 m	SDSS-3	u, g, r, i, z
	UKIRT	UKIDSS	Strömgren y, J, H, K
	Spitzer	DUSTiNGS; Boyer et al. (2015b)	[3.6], [4.5]
	Spitzer	Boyer et al. (2009)	[5.8], [8.0]
WLM	Kitt Peak & Cerro Tololo	Massey et al. (2007)	U, B, V, R, I
	Spitzer	DUSTiNGS; Boyer et al. (2015b)	[3.6], [4.5]
	Spitzer	Boyer et al. (2009)	[5.8], [8.0]
NGC 6822	Kitt Peak & Cerro Tololo	Massey et al. (2007)	U, B, V, R, I
	UKIRT	Sibbons et al. (2012)	J, H, K
LGS 3	SDSS 2.5 m	SDSS-3	u, g, r, i, z
	Spitzer	DUSTiNGS; Boyer et al. (2015b)	[3.6], [4.5]
	Spitzer	Boyer et al. (2009)	[5.8], [8.0]
Phoenix	Kitt Peak & Cerro Tololo	Massey et al. (2007)	U, B, V, R, I
	VLT	Battaglia et al. (2012)	V, I
	VISTA	VHS	Strömgren y, J, H, K
	Spitzer	DUSTiNGS; Boyer et al. (2015b)	[3.6], [4.5]

Galaxy	Telescope	Study	Filters
	Spitzer	Boyer et al. (2009)	[5.8], [8.0]
Leo A	Subaru	Stonkutė et al. (2014)	B, V, I
	Spitzer	DUSTiNGS; Boyer et al. (2015b)	[3.6], [4.5]
And IX	USNO	Zacharias et al. (2004)	B, V, R, J, H, K
	SDSS 2.5 m	SDSS-3	u, g, r, i, z
	Spitzer	DUSTiNGS; Boyer et al. (2015b)	[3.6], [4.5]
NGC 185	NOT	Nowotny et al. (2003)	V, Gunn i
	Spitzer	DUSTiNGS; Boyer et al. (2015b)	[3.6], [4.5]
NGC 147	NOT	Nowotny et al. (2003)	V, Gunn i
	Spitzer	DUSTiNGS; Boyer et al. (2015b)	[3.6], [4.5]
Aquarius	USNO	Zacharias et al. (2004)	B, V, R, J, H, K
	Spitzer	DUSTiNGS; Boyer et al. (2015b)	[3.6], [4.5]
NGC 3109	Various	Monet et al. (2003)	B, R, I
	USNO	Zacharias et al. (2004)	B, V, R, J, H, K
IC 10	Kitt Peak & Cerro Tololo	Massey et al. (2007)	U, B, V, R, I
	Spitzer	DUSTiNGS; Boyer et al. (2015b)	[3.6], [4.5]
NGC 55	USNO	Zacharias et al. (2004)	B, V, R, J, H, K

Galaxy	Telescope	Study	Filters
	Spitzer	Williams and Bonanos (2016)	[3.6], [4.5], [5.8], [8.0]
UGCA 438	USNO	Zacharias et al. (2004)	B, V, R, J, H, K
	VISTA	VIKING	z, Y, J, H, K
Antlia	USNO	Zacharias et al. (2004)	B, V, R, J, H, K
	Spitzer	DUSTiNGS; Boyer et al. (2015b)	[3.6], [4.5]

2.1.1 Data reduction

A number of datasets contained multiple measured apparent magnitudes for the same object for the same filter. Averaging these values reduces the size of the datasets, and the errors in the magnitude (particularly for variable stars), both of which are advantageous when processing the data.

To achieve this, all magnitudes for the selected filter were converted into flux (using an arbitrary but consistent zero point), averaged, and converted back to magnitudes. The errors on the initial magnitudes were propagated by preserving their fraction of the the initial magnitude during the flux conversion, i.e. $\sigma_F = F \times 10^{\sigma_M - M}$, where M is magnitude, F is the same value in flux, and σ represents the error.

The flux errors were then added in quadrature and divided by their number, to find their average value. The ratio of average flux error to average flux was similarly preserved when converting back into magnitudes. The flux errors were also used to calculate the weighted average of other values that required reduction as part of this process, such as the error in RA and DEC.

2.1.2 Matching sources

In order to compare magnitudes of objects in different bands, allowing SED fitting to take place, objects were first matched between various catalogs based on their position, providing magnitudes in a wide range of bands. For each of the detected objects in catalog A, the angular distance to each object in catalog B was calculated, and the coordinates of the object in B with the minimum angular separation returned. Objects were considered matched if this minimum angular separation was found to be below an arbitrary value (for this first cycle), typically taken to be 0.001°. A combined data file was compiled, with one entry for each matched object, and entries for each unmatched object.

Following this, systematic errors in the coordinate systems of the photometry could be determined. Plotting the discrepancy in right ascension and declination for each of the matched objects displays any overall offset, caused by each survey using a slightly different frame of reference for assigning coordinates. An example of this can clearly be seen in Figure 2.1. Two catalogs using the same coordinate system would produce a plot with scatter centred on zero. Two catalogs with a systematic offset would show scatter around a different point. This offset is determined by eye. Any offsets are then added to each value in the second catalog, effectively removing this discrepancy for the next run of the matching algorithm.

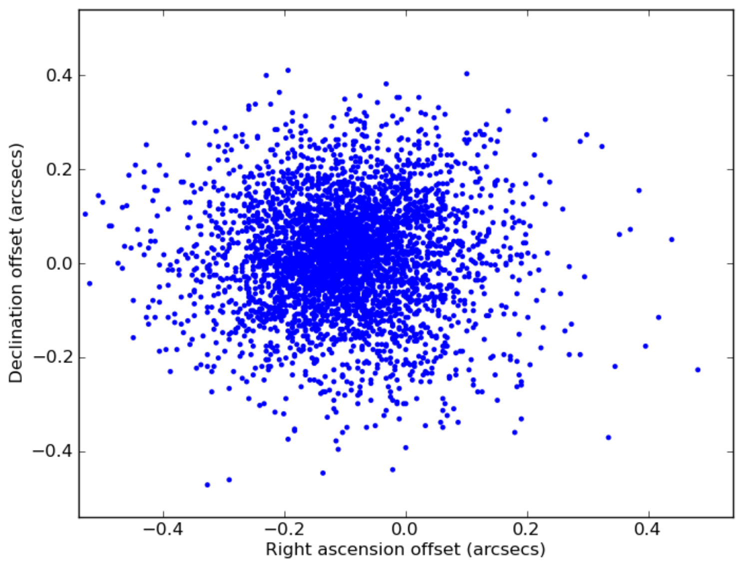

Figure 2.1: An example of an offset seen when matching sources from two catalogs. This particular example is matching objects imaged in near-IR bands to those in mid-IR. Scatter is centred around a point approximately 0.1" left of centre, which must be corrected for in the RA of the second catalog. There does not appear to be a significant offset in declination.

After the second round of matching, a more accurate tolerance (below which sources are considered matched) can be determined. The angular distances between matched sources are cumulatively plotted, starting at the minimum value. A typical example of this can be seen in Figure 2.2. Following the initial slope, a more-horizontal region can be seen. Sources with an angular separation below this discontinuity are considered strong matches, whereas those above are not considered true matches. The point of discontinuity is taken as the new tolerance, and typically has a value below 0.5". This limit is added to the matching algorithm and it is run once more.

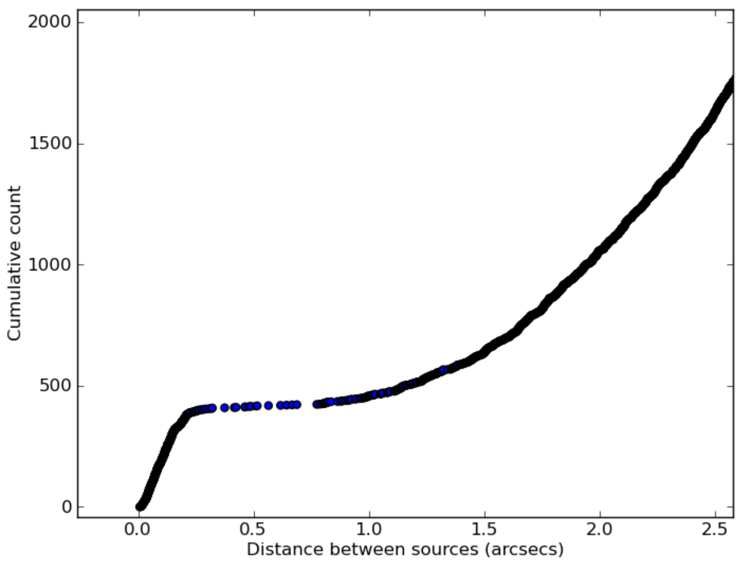

Figure 2.2: This plot demonstrates how the tolerance, below which sources are considered matched, is determined. The gradient of the line flattens significantly at around 0.2", suggesting that source with an angular separation above this point are not true matches.

Additional datasets can be added to the matched catalogue by repeating the above processes. This results in a combined catalog containing photometry in various bands matched for each object, allowing for further analysis. The order in which catalogs were matched, and the tolerances used to achieve this, are displayed in Table 2.2.

Table 2.2: Table displaying how various catalogs were matched. For each galaxy, the catalog with rank 1 was taken as the frame of reference to which all other catalogs were mapped. Catalogs with ranks above this number were matched with all preceding catalogs using the listed tolerance. Note, mid-IR data from Boyer et al. (2009) was matched only to DUSTiNGS data, as it similarly came from *Spitzer*.

Galaxy	Catalog Rank	Source	Tolerance (arcsecs)
Sex B	1	Bellazzini et al. (2014b)	—
	2	UKIDSS	0.4
	2	DUSTiNGS	0.5
	3	INT	0.3
Sex A	1	Bellazzini et al. (2014b)	—
	2	DUSTiNGS	0.4
	3	VISTA	0.5
	—	Boyer et al. (2009)	0.4
IC 1613	1	DUSTiNGS	—
	2	Udalski et al. (2001)	0.5
	3	Sibbons et al. (2015)	0.4
	—	Boyer et al. (2009)	0.4
Sag DIG	1	Beccari et al. (2014)	—
	2	DUSTiNGS	0.35
Peg DIG	1	DUSTiNGS	—
	2	UKIDSS	0.35
	3	SDSS-3	0.45
	—	Boyer et al. (2009)	0.4
WLM	1	DUSTiNGS	—
	2	Massey et al. (2007)	0.6
	—	Boyer et al. (2009)	0.5

Galaxy	Catalog Rank	Source	Tolerance (arcsecs)
NGC 6822	1	Sibbons et al. (2012)	—
	2	Massey et al. (2007)	0.55
LGS 3	1	DUSTiNGS	—
	2	SDSS-3	0.35
	—	Boyer et al. (2009)	0.45
Phoenix	1	Battaglia et al. (2012)	—
	2	DUSTiNGS	0.5
	3	VISTA	0.5
	3	Massey et al. (2007)	0.5
	—	Boyer et al. (2009)	0.4
Leo A	1	Stonkutė et al. (2014)	—
	2	DUSTiNGS	0.45
And IX	1	DUSTiNGS	—
	2	SDSS-3	0.5
	3	Zacharias et al. (2004)	0.75
NGC 185	1	DUSTiNGS	—
	2	Nowotny et al. (2003)	0.6
NGC 147	1	DUSTiNGS	—
	2	Nowotny et al. (2003)	0.75
Aquarius	1	DUSTiNGS	—
	2	Zacharias et al. (2004)	0.45
NGC 3109	1	Monet et al. (2003)	—
	2	Zacharias et al. (2004)	0.3
IC 10	1	DUSTiNGS	—
	2	Massey et al. (2007)	0.35
NGC 55	1	Williams and Bonanos (2016)	—
	2	Zacharias et al. (2004)	0.7

Galaxy	Catalog Rank	Source	Tolerance (arcsecs)
UGCA 438	1	VIKING	—
	2	Zacharias et al. (2004)	0.5
Antlia	1	DUSTiNGS	—
	2	Zacharias et al. (2004)	0.5

2.1.3 Spectral energy distributions

After the compilation of the catalogues, spectral energy distributions (SEDs) were produced, using the GETSED code first demonstrated in McDonald et al. (2009), and improved upon in McDonald et al. (2012b). Below is a brief discussion of the processes undertaken by the code.

In order to calculate the temperature and luminosities of the sources in the target galaxy, a number of fixed parameters were required for the model. These were: the distance to the galaxy, metallicity, reddening (caused by the ISM in the direction of the galaxy), and the model mass of the star. The first three of these parameters were taken from existing literature (typically McConnachie 2012), and collated in Table 1.1. The final parameter, stellar mass, was set at 1 $M_{\odot}$, although this could be adjusted later by the code. This is a good estimate for the typical mass of the red, luminous stars that this study aimed to identify (and is only used to determine $\log(g)$ of the comparison model, providing a small impact on the result).

To achieve this, the magnitudes of the input photometry are first converted into flux (in Janskys), using zero points defined by each filter. A breakdown of the zero point and central wavelength of each filter can be seen in Table 2.3. These are then matched to a blackbody, which provides first-order approximations of temperature, $T_{\rm eff}$, and luminosity, L, using best fits to the curve's shape. Only filters that used a wavelength < 5 μm were used to fit to the blackbody as, beyond this point, stellar flux is significantly impacted by dust surrounding the star (although model fluxes are still returned for these filters). This is a first-order estimate of the SED. Note that many galaxies lack reliable photometry in near-IR bands (i.e. J, H and K). Although this reduces the accuracy of output T and L, this is less significant than missing optical or mid-IR photometry, as the general shape of the SED can still be inferred. For stars with $L > 2500$ L$_\odot$, an improved estimate of mass is calculated at this point, using $M = (L/2500\mathrm{L}_\odot)^{2/3}$ M$_\odot$. Following this, a value for the star's surface gravity, $\log(g)$, is obtained using the following equation:

$$\log(g) = -10.6113 + \log(M) + 4\log(T_{\mathrm{eff}}) - \log(L), \tag{2.1}$$

where M is an estimate for the star's mass (a user defined input parameter discussed above; McDonald 2009).

Table 2.3: Specifications of filters used to produce input photometry.

Filter	Central λ (nm)	Zero Point (Jy)
u	354.3	3631
U	365	1884
B	440.7	4063
g	477	3631
V	553.7	3636
r	623.1	3631
R	700	2875
i	762.5	3631
Gunn i	786	2427
I	880	2241

Filter	Central λ (nm)	Zero Point (Jy)
z	913.4	3631
Strömgren y	1021	3631
J	1250	1594
H	1650	1024
K	2200	666.7
[3.6]	3600	280.9
[4.5]	4500	179.7
[5.8]	5800	115
[8.0]	8000	64.13

Following this, model spectra were selected from a three-dimensional grid, based on the value of log(g), $T_{\rm eff}$, and [Fe/H]. These spectra were pre-computed using the BT-Settl code, first described in Allard et al. (2003) with the current version from Allard et al. (2012). The BT-Settl code produces synthetic model stellar atmospheres, based on atomic and molecular data. To do so, it requires an input value for g, as well as metallicity, which can be further defined by specifying α-enrichment. From these models, spectra are produced. Uncertainties in the model spectra, for example, due to the molecular composition of the stellar atmosphere, are considered to be much lower than the uncertainties in the observed photometric data, so the code's limitations do not impact the resulting SEDs significantly for the majority of objects. This code was chosen in preference to other model spectra codes, such as the Marcs code (Gustafsson et al. 1975, 2008), due to the finer grid spacing and grid completeness in the $4000 - 6000$ K range (McDonald et al. 2012b).

The BT-Settl spectral models are used to better constrain the temperature of the observed object. A second-order temperature estimate is derived by comparing the observed photometry to the interpolated grid of model spectra at

256 K intervals, starting with the first-order estimate from the blackbody fitting process. An error estimate is calculated by comparing the observed and the combined model fluxes for varying [Fe/H] and $\log(g)$, and the minimum value of σ is returned via χ^2 analysis.

Reddening is taken into account at this point, using the input parameter discussed above. Adjusted values of flux are calculated using:

$$\frac{A_\lambda}{E(B-V)} = 1.248\lambda^{-1.75-(\lambda-1)/1.3} \tag{2.2}$$

for $\lambda < 1\mu$m, and

$$\frac{A_\lambda}{E(B-V)} = 1.248\lambda^{-1.75} \tag{2.3}$$

for $\lambda > 1\mu$m, where A_λ represents extinction, and $E(B-V)$ takes its usual meaning.

Subsequently, $\log(g)$ is recalculated using this best fit value of $T_{\rm eff}$ (along with a recalculated L, via the Stefan-Boltzmann law), and a refined grid of model spectra is returned, using a halved grid spacing. This entire process is repeated several more times, calculating a value of $T_{\rm eff}$ down to a precision of 1 K. This will also provide a good constraint of L.

Once complete, the code outputs the final values for each object's $T_{\rm eff}$ and L. This allows for the production of an H–R diagram, including all objects in the field of view. In order to improve this diagram, only sources which appear in more than one catalog (i.e. only those that were matched to an object in at least one other dataset) had their SEDs calculated. A wider range of observed wavelengths, and hence more data points, provides more reliable results.

2.1.4 Reliability

There are several factors that reduce the reliability of these results for AGB stars. The first occurs for dust-forming stars. The spectral models do not take this dust into account, meaning estimates of $T_{\rm eff}$ and L become more unreliable for stars with $T_{\rm eff} \lesssim 3500$ K, when dust production becomes prevalent.

Additionally, our photometry may be unreliable for variable stars. Some of our photometry contains the average magnitude of objects from multiple epochs (for example, that from DUSTiNGS; Boyer et al. 2015b), in an attempt to reduce the impact of variability and obtain a mean value of flux. However, this was not possible in all studies in all galaxies. The most severe case of this would occur for an object detected at its photometric maximum at short λ in catalog A, that is then matched with its photometric minimum at short λ in catalog B. The mismatch in flux would make it more likely that an incorrect $T_{\rm eff}$ and L are determined. Additionally, models assume that all stars are oxygen-rich: there are small differences in the SED of a carbon-rich star. Atmospheres that are not in local thermodynamic equilibrium (LTE), such as variable and chromospherically-heated stars, also pose uncertainties, as the code assumes an LTE atmosphere.

Finally, the integrated flux from a binary system causes clear problems, especially if the stellar atmospheres are interacting, or if the stars are of a similar luminosity. Other problems may arise from stellar blending (when flux from two non-binary stars cannot be resolved into two objects, artificially increasing calculated luminosity), and background nebulosity.

Uncertainties from the photometry are likely much greater than the differences from the different codes, so the choice of model atmosphere (i.e. MARCS or BT-SETTL) is not of great importance (McDonald et al. 2012b). This is likely the greatest cause uncertainty for the majority of stars included in this study.

The importance of photometry in a wide range of bands should also be discussed at this point. In order to produce an accurate temperature, the SED fitter requires well-sampled Wien and Rayleigh–Jeans tails. Without this information, temperatures can be systematically over or underestimated. In order to be fit well, objects with $T \gtrsim 6000$ K require photometry shorter than V band (although these objects are not of particular interest to this work), and objects with $T \lesssim 3000$ K require photometry longer than K band.

2.2 H–R Diagrams

Below are displayed H–R diagrams for the 13 dwarf irregular galaxies for which data was of sufficient quality to discern structure. A list of the photometric sources and filters therein can be seen in Table 2.1.

Many vertical artefacts in the plots are the result of poor-quality photometry that has caused the SED fitter to become trapped in a local minimum. Where possible, this photometry was then removed for subsequent iterations of the plots, reducing or removing these artefacts. Additionally, in some cases, specific filters (typically those at UV wavelengths) have been excluded from the SED fitting procedure following an analysis carried out in Section 3.1. New H–R diagrams were produced following these exclusions.

Also present in the data are objects that are not part of the target galaxy, such as foreground stars and background galaxies. These may fall outside the range of temperatures and luminosities displayed in the plots below (as the SED fitter may class them at temperatures or luminosities beyond the region displayed), but often a population of red objects can be seen to the right of the RGB, likely dusty or redshifted background galaxies. We cannot rule out the possibility that some of these objects may lie amongst the RGB and AGB stars. To reduce the likelihood of this, some of the displayed plots limit data to the within the target galaxy's maximum radius. The population of red galaxies is reduced by this process, as is the probability of the presence of other contaminating objects within the RGB and AGB. Any objects that fall into these regions that are visible through or in front of the target galaxy cannot be removed by this method.

The finalised H–R diagrams were used in other sections of this work, such as the search for dusty sources in Section 3.2, and fitting isochrones in Chapter 4.

2.2.1 Sextans B

H–R diagrams can be seen for this galaxy in Figure 2.3. Plot (a), which uses data from all four catalogs, has clear vertical bands. It was found that by removing two photometry sources (optical from the INT, and the near-IR UKIDSS data), these effects could be reduced, which can be seen in (b). Two groups of objects are visible. Due to its proximity to the galactic centre, the left group (in the grey box in Figure 2.3 (c)) is likely the RGB within Sextans B. The right group is more likely external sources which are almost completely excluded when reducing data to within 3' of the galactic centre, visible in Figure 2.3 (c).

To test this, the positions of objects from each of the two groups were plotted in Figure 2.4, coloured by their membership. The sampled regions can be seen in Figure 2.3 (b). The two groups were best separated below 3000 $L_{\odot}$, so only objects below this limit are shown. It can be clearly seen in Figure 2.4 that the galaxy is defined well by the grey points (so most likely AGB and RGB stars in Sex B), with the other objects in a fairly even distribution, though much less

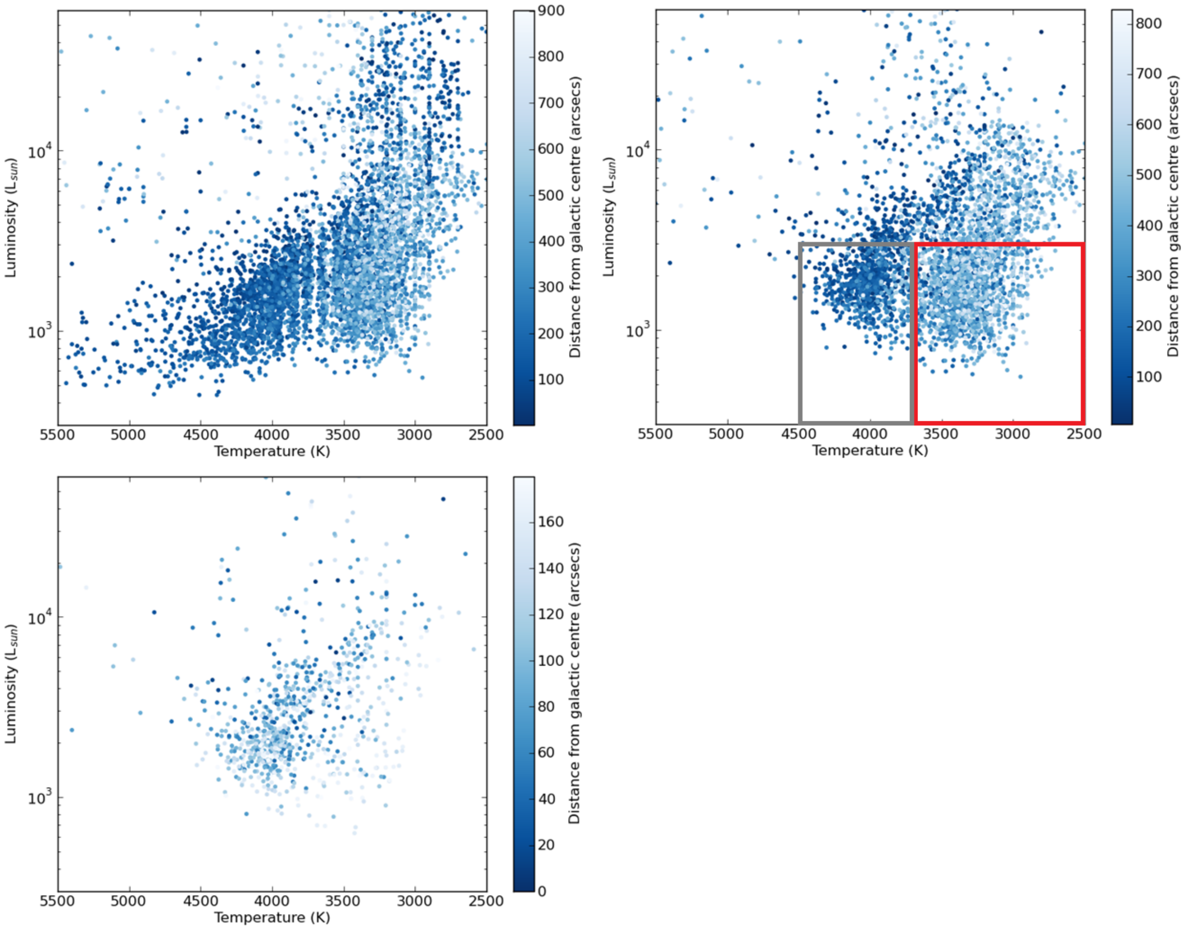

Figure 2.3: H–R diagrams for Sextans B. *Top:* (a) Using data from all four sources; (b) Using data only from Bellazzini et al. (2014b) and DUSTiNGS. Objects within the red and grey boxes are respectively the red and grey points in Figures 2.4 and 2.5. *Bottom:* (c) Using data from Bellazzini et al. (2014b) and DUSTiNGS and limiting data to within 3' of the galactic centre.

common in the central regions of the galaxy, which may be affected by photometric crowding. This is illustrated well in Figure 2.5, a cumulative plot of the two groups. More than 80% of the grey points are within 3' of the galactic centre, with a notable drop off after this point. The red points appear to have no relation to galactic radius other than the lack of objects $\lesssim 0.5$'. This implies that the red objects are predominantly, if not entirely, background galaxies.

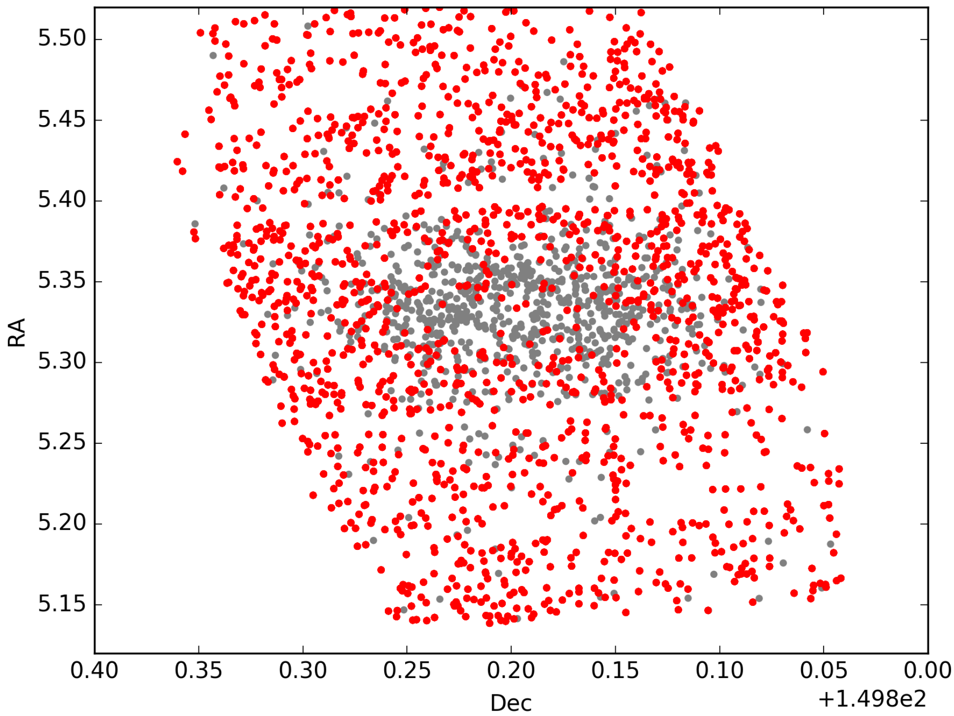

Figure 2.4: Plot showing the position on the sky of objects from the two populations selected in Figure 2.3.

2.2.2 Sextans A

H–R diagrams can be seen for this galaxy in Figure 2.6. Plot (a), which uses data from all catalogs, has clear vertical bands, similar to Sextans B. Again, near-IR sky survey photometry was removed, resulting in (b). The two groups of objects are visible once more, but they are less clearly separated by their distance from the galactic centre. Limiting data to sources within 5' of the galactic centre (in (c)) reduces the number of sources in the right group, but by a far smaller fraction than in Sextans B. It is possible that this is caused by background galaxies again, but due to the more diffuse nature of this galaxy (McConnachie 2012), they remain visible through the bulk of its stellar mass.

The position of the hotter group, best seen in (c), is broadly similar to that of

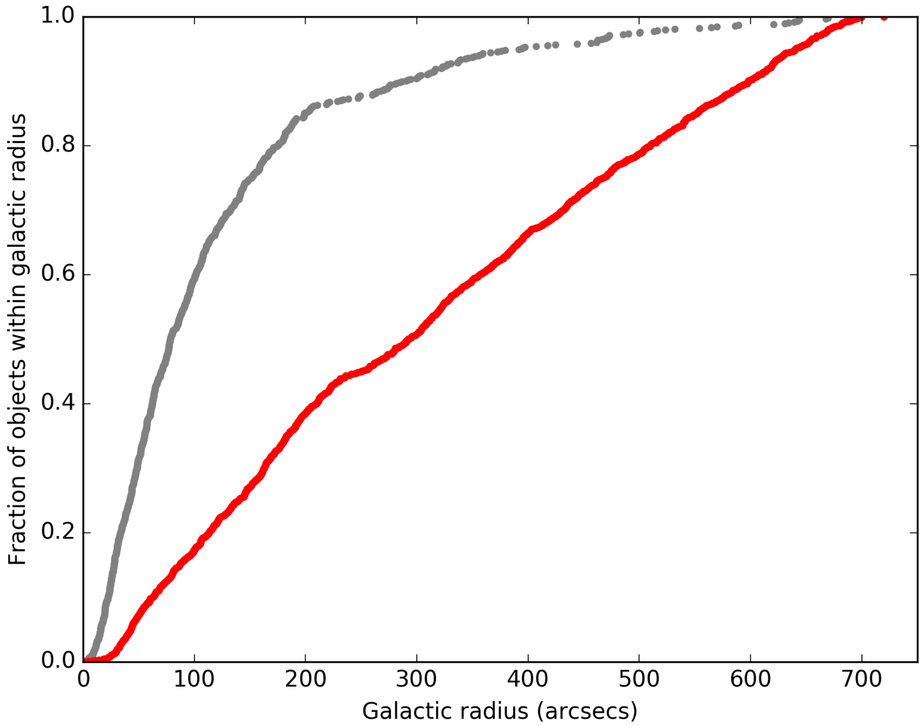

Figure 2.5: Plot showing the fraction of objects in each of the two populations within a given radius in Sex B. Colours are as in Figures 2.3 and 2.4.

the RGB tip in Sextans B ($\sim$ 4100 K, 2000 $L_\odot$), so it is a reasonable assumption that it is the same feature. It appears slightly more luminous and hotter than in Sextans B, which may be due to the lower overall metallicity of the galaxy. It is much more difficult to discern the AGB in this galaxy, although it may be visible as a band moving to the right above the RGB tip. Another explanation could be that more AGB stars are carbon-rich or dusty, shifting them to cooler temperatures and making them more difficult to separate from the background scatter.

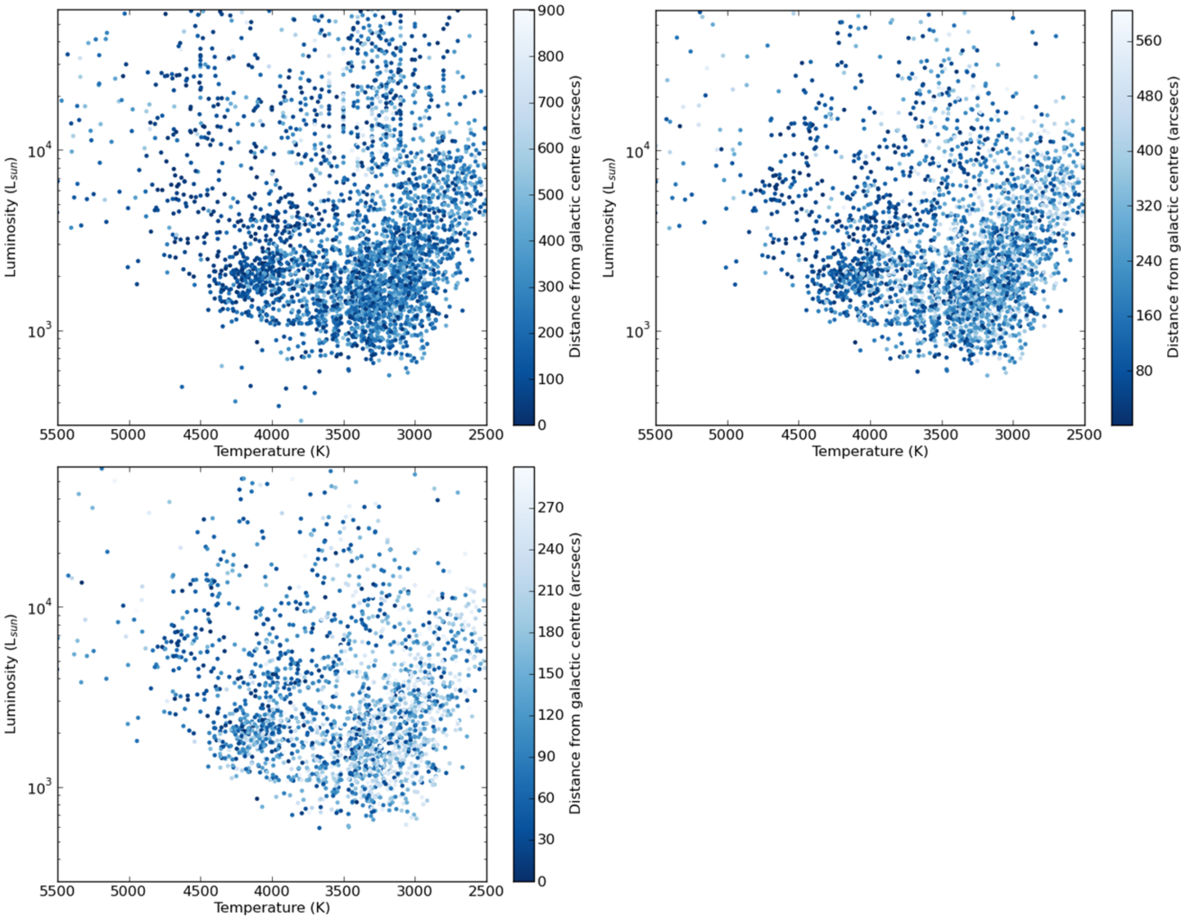

Figure 2.6: H–R diagrams for Sextans A. *Top:* (a) Using data from all three sources; (b) Using data only from Bellazzini et al. (2014b), DUSTiNGS, and Boyer et al. (2009). *Bottom:* (c) Using data from Bellazzini et al. (2014b), DUSTiNGS, and Boyer et al. (2009), and limiting data to within 5' of the galactic centre.

2.2.3 IC 1613

H–R diagrams can be seen for IC 1613 in Figure 2.7. Much more of the RGB is visible in this diagram compared with that in the Sextans galaxies. This is due to the relative proximity of the target galaxy. The edges of the RGB are very well defined. Also visible is the AGB tip, visible above and to the right of the RGB tip (found at $\sim$ 4000 K, $\sim$ 2000 $L_{\odot}$). The prevalence of more-distant sources towards the centre of the RGB implies that many objects towards the centre of the galaxy suffer from blending, causing the scatter beyond this point.

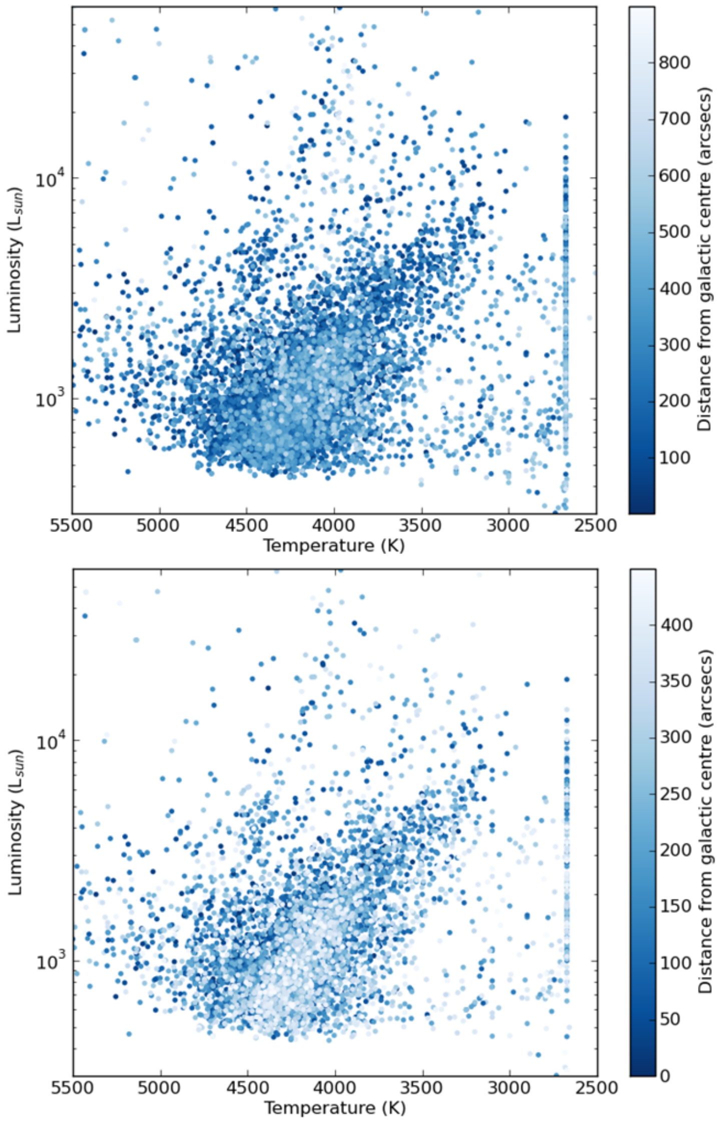

Figure 2.7: H–R diagrams for IC 1613. (a) Using data from all four sources with no limit on the position of objects; (b) Limiting data to within 7.5' of the galactic centre.

2.2.4 Sag DIG

Very little structure, if any, can be discerned in the first two H–R diagrams for this galaxy (Figure 2.8 (a) and (b)). However, following an analysis in Section 3.1.4, two populations can be defined. Those with a full excess in I, ($F_{obs}/F_{model} < 1$; Figure 2.8 (c)) produce an H–R diagram similar to those seen for other galaxies,

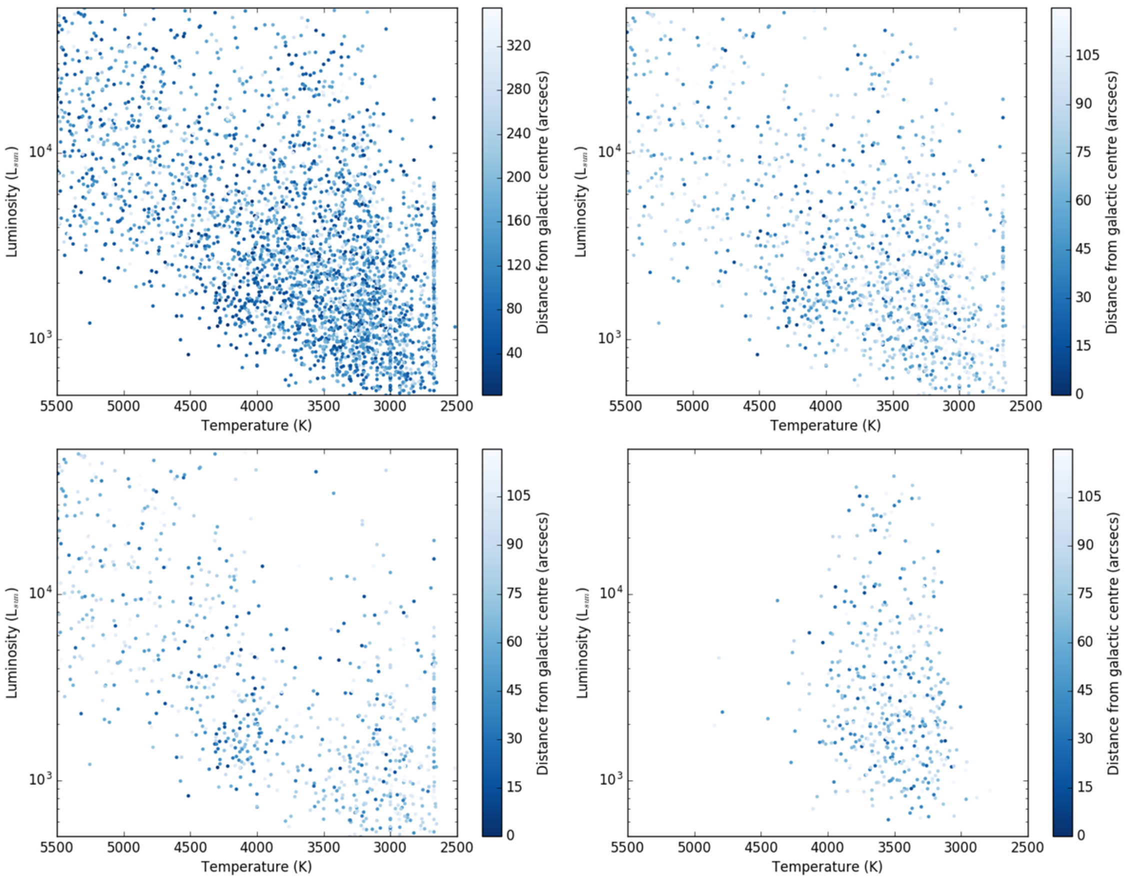

Figure 2.8: H–R diagrams for Sag DIG. *Top:*(a) Using data from all three sources with no limit on the position of objects; (b) Limiting data to within 2' of the galactic centre. *Bottom:* See Figure 3.4; (c) $F_{obs}/F_{model} < 1$ in I; (d) $F_{obs}/F_{model} > 1$ in I.

with a sparse RGB visible (centred on $\sim$ 4200 K, 1500 L$_{\odot}$). A number of foreground stars are visible in towards the top left of the image. The other population in (d), with $F_{obs}/F_{model} > 1$, is likely composed of foreground red dwarfs due to their temperature, distribution on the H–R diagram, and lower peak luminosity in I in Figure 2.8. Their detection in this galaxy is perhaps due to the deep VLT optical photometry. The diagram from (c) is used for analysis of this galaxy in the remainder of this work.

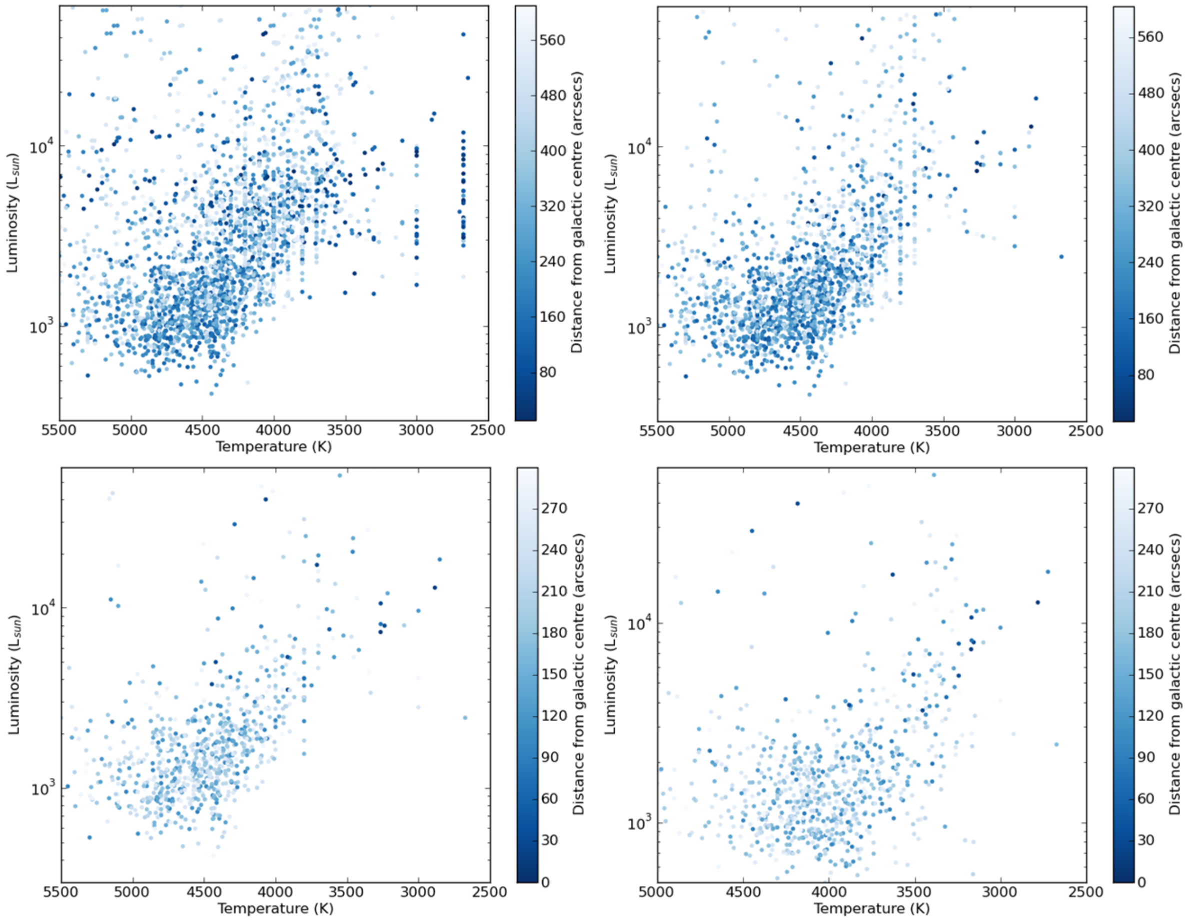

Figure 2.9: H–R diagrams for Peg DIG. *Top:* (a) Using data from all four sources; (b) Using data only from SDSS-3, DUSTiNGS, and Boyer et al. (2009). *Bottom:* (c) Using data only from SDSS-3, DUSTiNGS, and Boyer et al. (2009), and limiting data to within 6' of the galactic centre; (d) Using data only from SDSS-3, DUSTiNGS, and Boyer et al. (2009) (excluding the u filter), and limiting data to within 6' of the galactic centre.

2.2.5 Peg DIG

Note that for Peg DIG, the SDSS photometry suffers from significant crowding, excluding objects within ~ 2.3' of the galactic centre.

Using all photometry, the RGB tip is clearly visible in Figure 2.9 (a), as well as some of the AGB, although this is largely obscured by vertical artefacts. Removing the UKIDSS photometry reduces some of these in (b), and restricting objects to within 6' from the galactic centre removes more in (c). Remaining is a well defined RGB, with a clear boundary, and a number of AGB candidates. Removing the u filter (due to its poor SED fit; Section 3.1) shifts the RGB, modelling it as cooler and less luminous, leaving the tip centred on 4000 K. It also increases the spread of points amongst the RGB.

2.2.6 WLM

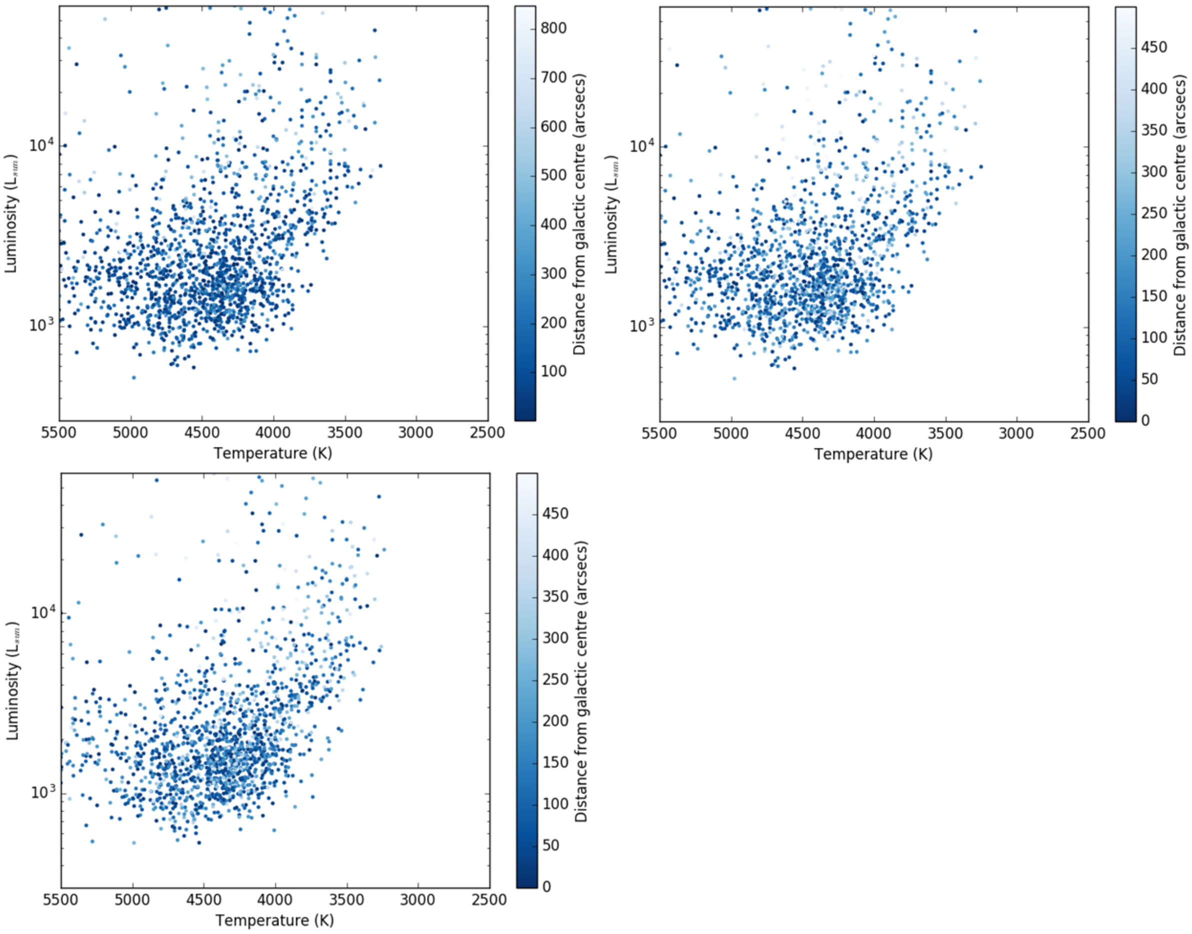

Figure 2.10: H–R diagrams for WLM. *Top*: (a) Using data from all three catalogs; (b) Restricting data to within 8' of the galactic centre. *Bottom*: (c) Restricting data to within 8' of the galactic centre and excluding data from the U band.

A photometric sensitivity cut-off may be visible in Figure 2.10 (a), with the approximately diagonal line rising to the top right of the image, still clear when data is restricted to the galactic centre (Figure (b)). Additionally, very few objects can be seen cooler than 3400 K. It is highly unlikely that this could have been caused by other factors, as background galaxies would almost be guaranteed to appear. An RGB tip is visible ($\sim$ 4300 K, 1500 $L_{\odot}$), and rising almost diagonally from this there appears to be an AGB, although objects may be missing due to the photometry limitations. The removal of U band data causes the RGB to shift to a lower range of T and L (Figure 2.10 (c)).

2.2.7 NGC 6822

Clear structure and many data points are visible in the H–R diagram of this galaxy (Figure 2.11), perhaps due to its size and relative proximity compared to other dIrrs. This is better resolved in (b), where data points have been restricted in location. The removal of U band data in (c) appears to have had little effect on the H–R diagram.

There is far more scatter to the left of the RGB than the right; this is likely due to the photometry obtained for this galaxy. No archival data could be found in mid-IR bands (such as that from *Spitzer*), which may systematically shift data points to higher temperatures, and cause the completeness issues seen below 3500 K. Additionally, problems may have arisen from the unreliability of the Massey et al. (2007) photometry (Section 3.2.8). However, as no other optical photometry of a comparable depth was available, this proved difficult to test. Much of this scatter may also be caused by contamination from foreground stars, as NGC 6822 lies close to the Galactic plane (Sibbons et al. 2012).

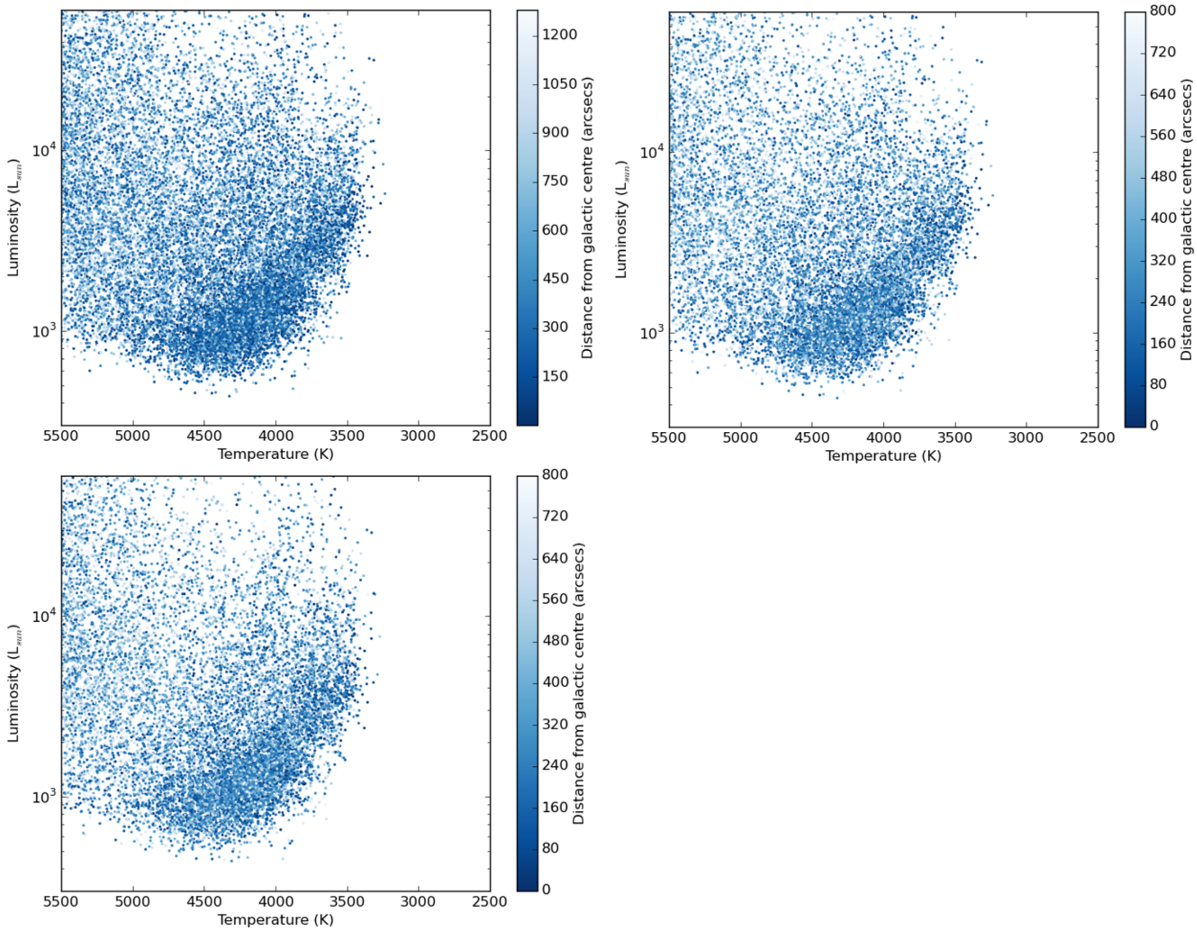

Figure 2.11: H–R diagrams for NGC 6822. *Top*: (a) Using data from both sources; (b) Restricting data to within 13' of the galactic centre. *Bottom*: (c) Excluding U band data.

2.2.8 LGS 3

Some structure can be made out on the H–R diagrams for this galaxy (Figure 2.12), but there are too few data points to define the RGB tip with confidence. The removal of u band data (Figure 2.12 (c)) appears to have removed some of the vertical artefacts, and on average lowered T and L. Deeper optical and near-IR photometry would likely constrain data points more readily and reduce scatter (as only catalogs from sky surveys could be found to match to the DUSTiNGS data). This large scatter in data points also suggests that poor photometry is the limiting factor in this galaxy.

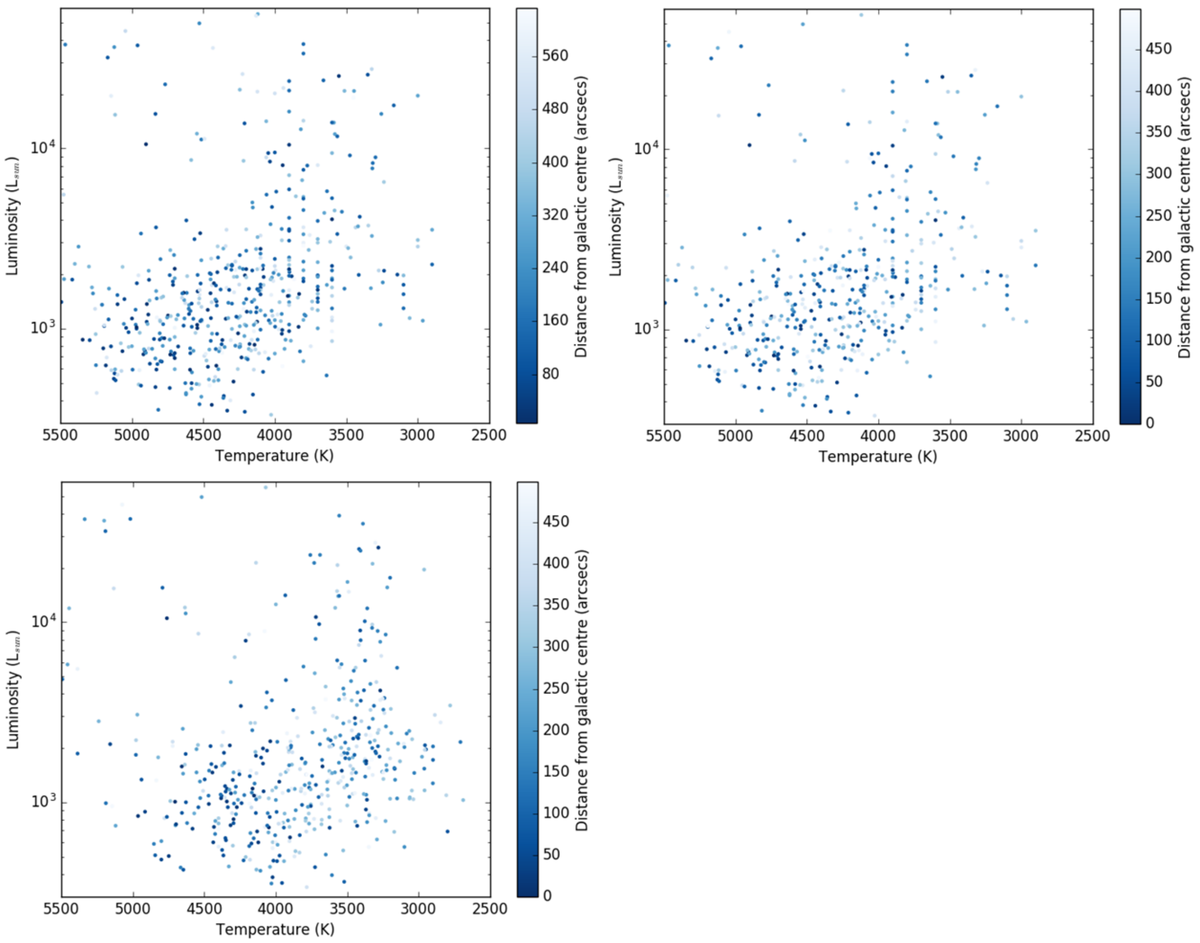

Figure 2.12: H–R diagrams for LGS 3. *Top*: (a) Using data from all three sources; (b) Restricting data to within 120" of the galactic centre. *Bottom*: Removing u band data.

2.2.9 Phoenix

The relative proximity of this galaxy compared to some others in this study means it is possible to see much further down the RGB (although this is not visible in Figure 2.13 (a)–(c) due to consistency in the scales used compared to the other galaxies). This is likely due to the excellent VLT photometry from Battaglia et al. (2012). Limits on the RGB are clearly defined, with the RGB tip in (c) at 4000 K and 2000 $L_\odot$. Scatter is reduced in (b) when data is restricted to around the galactic centre. Data from UKIDSS and Massey et al. (2007) were removed

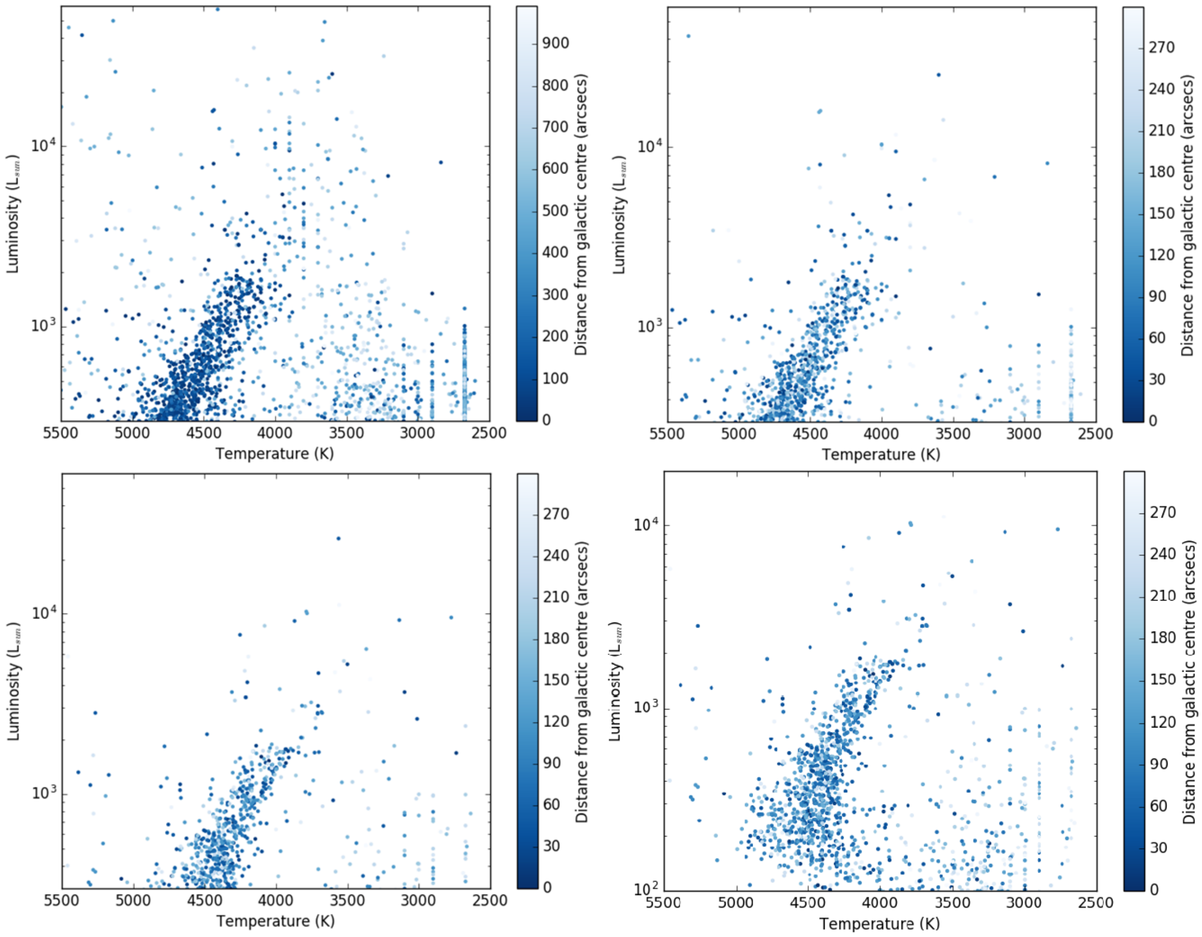

Figure 2.13: H–R diagrams for the Phoenix Dwarf galaxy. *Top*: (a) Using data from all five sources; (b) Restricting data to within 5' of the galactic centre. *Bottom*: (c) Restricting data to within 5' of the galactic centre and excluding data from UKIDSS and Massey et al. (2007); (d) As in Figure (c), with an adjusted range of luminosities displayed to demonstrate the resolved extent of the RGB.

following an analysis of the IR excess (Section 3.2). Figure (c) shows that this caused a systematic reduction in T by around 300 K, more apparent at the lower range of displayed luminosities. Figure (d) shows the full extent of the resolved RGB.

2.2.10 Leo A

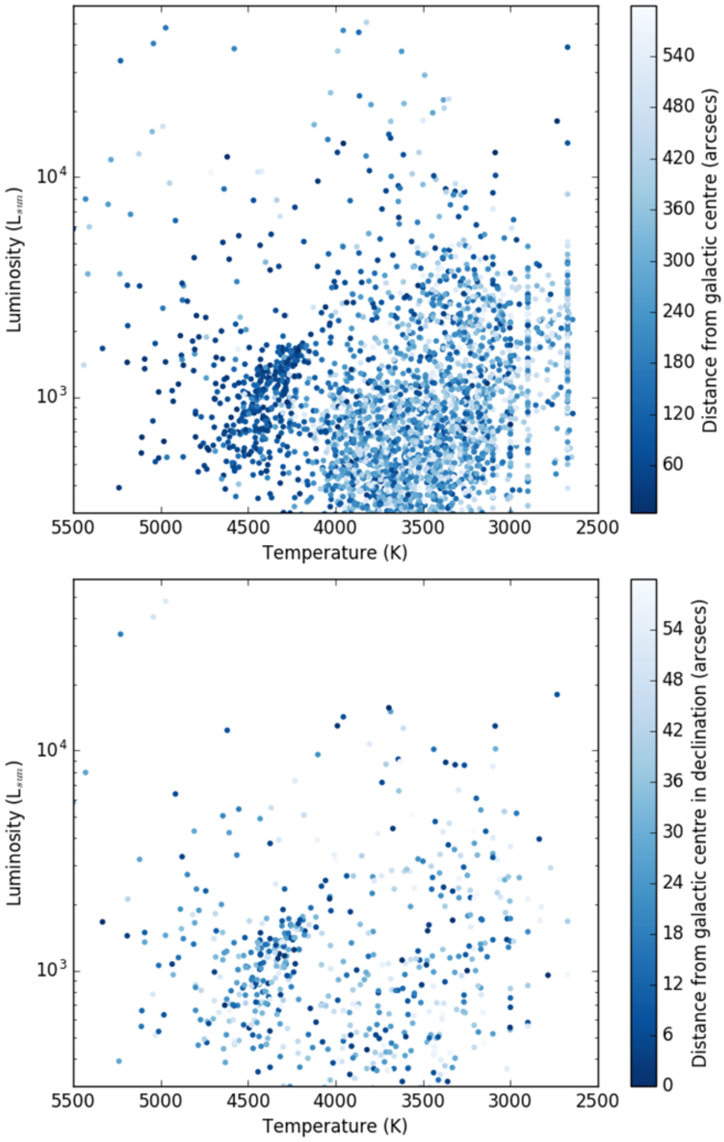

Figure 2.14: H–R diagrams for the Leo A Dwarf galaxy. (a) Using data from both sources; (b) Restricting data to within 5' of the galactic centre, and 100" from the galactic centre in declination.

This galaxy appears almost horizontal on the sky in the equatorial coordinate system. For this reason, the field of view was reduced for Figure 2.14 (b) by first restricting to points within 6' of the galactic centre, then restricting the remaining points in declination to within 100". This method allowed for a better reduction of background galaxies without impacting objects in the galaxy itself.

A sparsely populated RGB is visible in Figure 2.14, with the tip at 4100 K and 2000 $L_{\odot}$. These objects appear very close to the galactic centre, more obvious with the colour disparity in Figure (a). A small AGB population appears to continue onwards from this, ascending to the right of the diagram.

2.2.11 And IX

Figure 2.15 (a) shows that there is a clear RGB in the H–R diagram of this galaxy. However, there are vertical artefacts in the data, which are not removed when the Zacharias et al. (2004) catalog is not included (Fig (b)). Much of the scatter is reduced in Fig (c), when data is limited to points within 5' from the galactic centre to exclude background galaxies. Many points reduce in T in (d) (following the exclusion of u band data), and there is a further reduction in vertical artefacts. An RGB tip is visible in (d), with a potential AGB population extending almost vertically above this point. However, it is difficult to define the centre of the RGB tip due to the large scatter of points.

2.2.12 NGC 185

Note that for NGC 185, the DUSTiNGS photometry suffers from significant crowding, excluding objects within $\sim$ 0.8' of the galactic centre.

The RGB is clearly visible in Figure 2.16, although the precise location of the RGB tip is difficult to define visually. An AGB can be seen ascending to the top right. Although there are small vertical artefacts present, the well-defined edges of the RGB suggests that several foreground objects may be visible in the upper-left corner of the image. Similar to IC 1613, the presence of many distant points

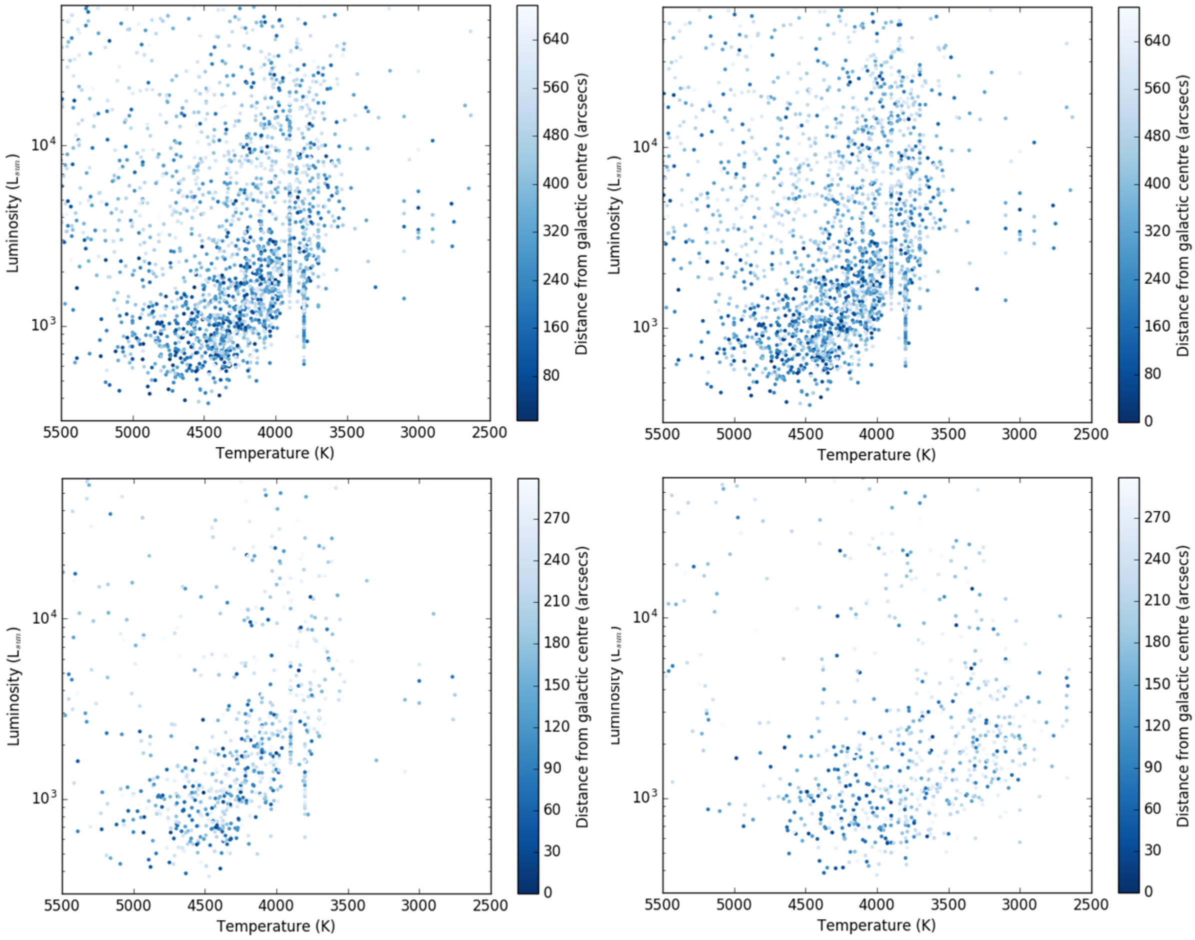

Figure 2.15: H–R diagrams for And IX. *Top:* (a) Using data from all three sources; (b) Using data only from SDSS-3 and DUSTiNGS. *Bottom:* (c) Using data from all three sources and limiting data to within 5' of the galactic centre; (d) Excluding data from u band.

towards the centre of the RGB implies that some stellar blending is occurring.

2.2.13 NGC 147

Figure 2.17 displays a very similar H–R diagram to NGC 185, which is expected as the photometry came from the same studies. The primary difference is that NGC 147 has a slightly hotter AGB region. This is likely due to the lower metallicity of the galaxy (Table 1.1). Again, there is evidence for stellar blending from the stratification of the colour of the RGB.

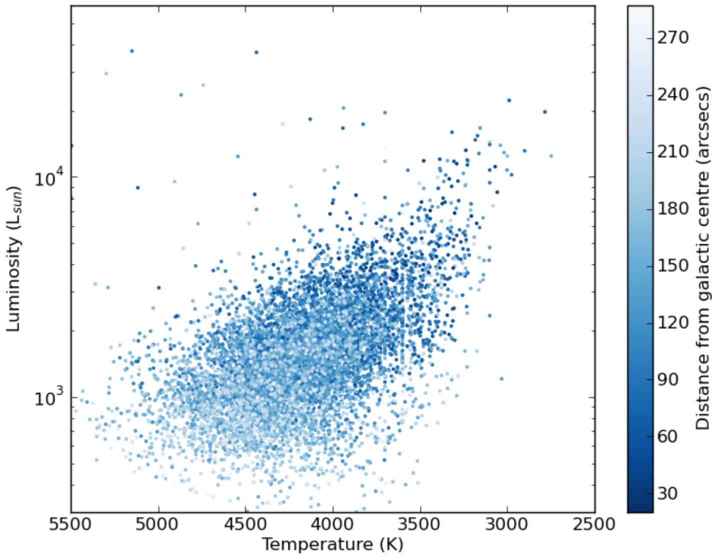

Figure 2.16: H–R diagram for NGC 185. Only one plot is displayed, as one of the source datasets only covers the galactic centre.

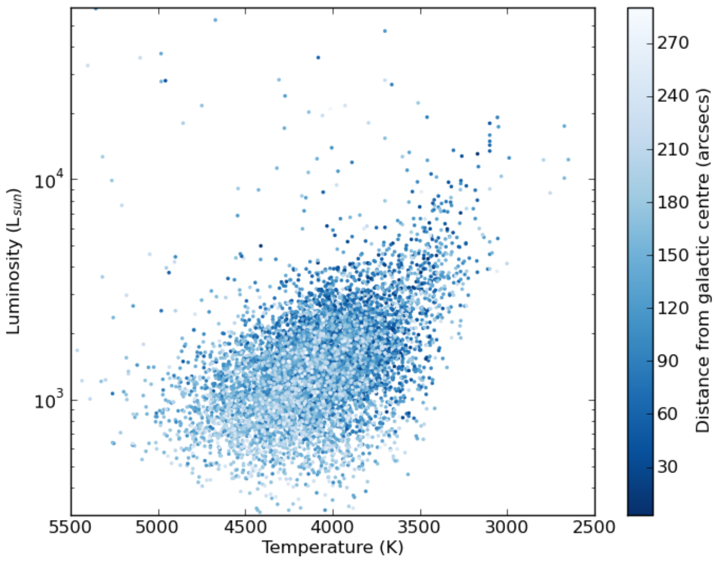

Figure 2.17: H–R diagram for NGC 147. Only one plot is displayed, as one of the source datasets only covers the galactic centre.

2.2.14 Poor results

The following galaxies yielded no useful results, i.e. the RGB could not be resolved. This was often due to the fact that only low-quality photometry could be obtained:

- Aquarius
- NGC 3109
- IC 10
- NGC 55
- UGCA 438
- Antlia

Additionally, the following galaxies had such poor available data (typically only as part of all-sky surveys), that SED fitting was not attempted:

- IC 5152
- GR 8
- Leo P
- UGCA 92

Chapter 3

The IR excess

3.1 Filter-fit profiles

The GETSED code (Section 2.1.3) returns a model flux for each input filter. The ratio of observed to modelled flux was plotted against the modelled luminosity of each source to produce a filter-fit profile. For well-modelled objects, it would be expected that data in these profiles should be centred on unity, with perhaps an increasing F_{obs}/F_{model} for dusty stars towards mid-IR wavelengths, where the IR excess becomes apparent. Modelling can be considered more successful in a filter with less scatter, as scatter derives from uncertainties in observations. An incorrect zero point or transmission function will cause scatter around a point offset from unity.

Poor modelling, indicated by high scatter in these filter-fit profiles, can occur if the originating study has used an incorrect zero point, or simply that the filter uses a wavelength range that is difficult to calibrate. These poorly modelled filters were removed, and the GETSED code rerun, allowing for a re-analysis of the other filters, which often had a reduced scatter due to a better-fit SED. This also allowed for a more-accurate H–R diagram to be produced, as recalculated temperatures and luminosities from the new SEDs may differ significantly from the original values (Section 2.2).

Below is an analysis of the filters for each of the 13 galaxies which presented usable results in Chapter 2.

3.1.1 Sextans B

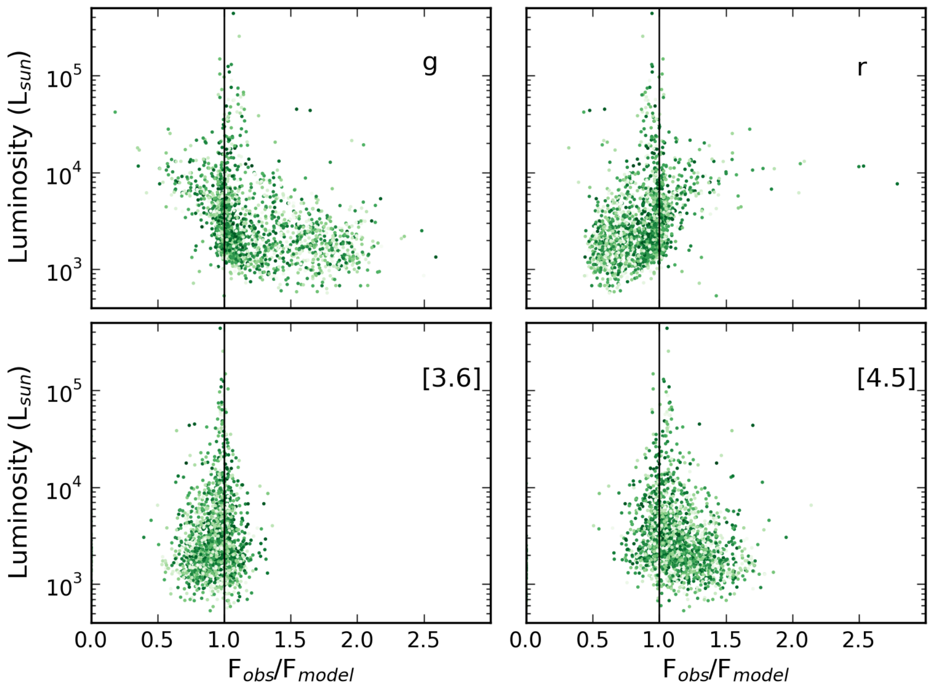

Figure 3.1: Filter-fit profiles for Sextans B. Darker colour indicates a closer proximity to the galactic centre. A line has been placed through $F_{obs}/F_{model} = 1$ to better display how scatter is distributed.

Filter-fit profiles for this galaxy are displayed in Figure 3.1. Scatter can be seen to the right of unity in the g filter, and to the left in the r filter, indicating colour correction in the source data. These points have been poorly fitted. Their paler colour indicates, however, that many are at high galactic radius, and are therefore more likely distant background galaxies. Indeed, checking the positions of these objects confirms that the majority are far from the bulk of stars in this galaxy, strongly implying they are background objects. Other than these, scatter in all filters appears roughly where expected.

3.1.2 Sextans A

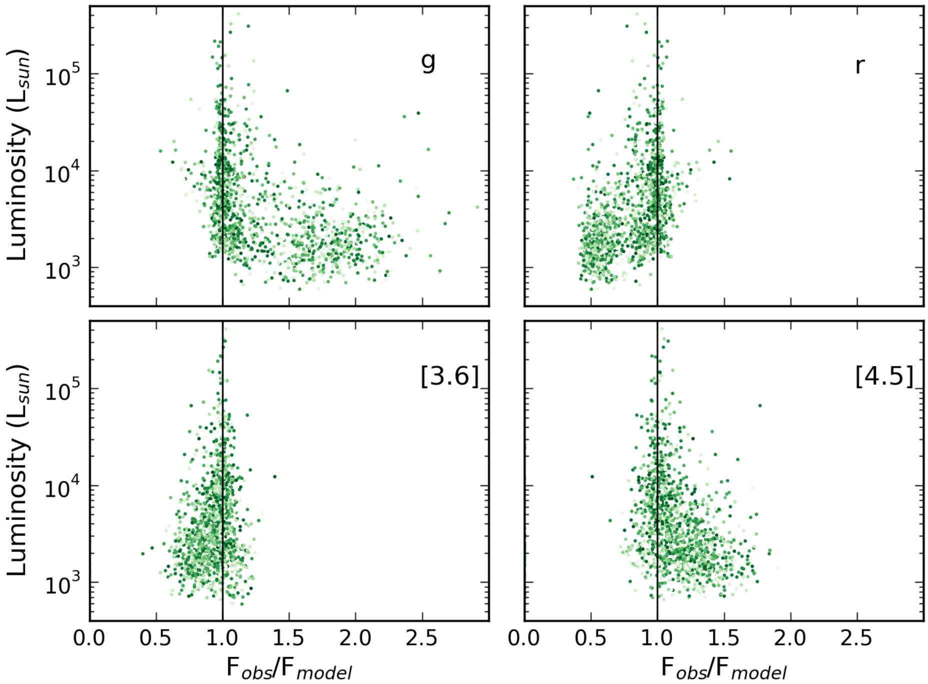

Figure 3.2: Filter-fit profiles for Sextans A. Darker colour indicates a closer proximity to the galactic centre. A line has been placed through $F_{obs}/F_{model} = 1$ to better display how scatter is distributed.

The appearance of the filter-fit profiles from Sextans A (Figure 3.2) appear very similar to those in Sextans B. Poorly fitted objects in g and r bands are, however, more separated from the central scatter than in the other galaxy. Once again, it was determined that these poorly fitted objects are most likely background galaxies due to their distribution relative to Sextans A.

3.1.3 IC 1613

In general, fits for IC 1613 are fairly tightly constrained around unity (Figure 3.3). An examination of some of the points with $F_{obs}/F_{model} < 1$ in I band shows that most of these objects correspondingly have $F_{obs}/F_{model} > 1$ in mid-IR bands. The [3.6] filter shows what appears to be two populations of red objects. The SEDs of the more-luminous group show that these are AGB stars, likely the predominant intermediate-age population. Some objects in the less-luminous group have poorly fit SEDs, suggesting they are background galaxies. However, they have a broadly even spatial distribution (including the galactic centre), meaning it is unlikely that they are all background galaxies. The remaining objects in this group are likely AGB stars from the ancient stellar population.

3.1.4 Sag DIG

Despite the lack of structure in this galaxy's H–R diagrams (Figure 2.8), Figure 3.4 shows filters that seem relatively well calibrated, with low levels of scatter and centred on unity. Some background galaxies are visible in the I filter. It also appears that there is some splitting in the profiles of V and I bands, with two groups of objects visible around unity. H–R diagrams of the two groups can be seen in Section 2.2.4, where it is shown that the group with $F_{obs}/F_{model} < 1$ in I is the population we are interested in, with the other likely foreground red dwarfs.

3.1.5 Peg DIG

Examining the filters for Peg DIG (Figure 3.5) shows that scatter is significant for this galaxy, most pronounced in the u band. This could be due to a number of reasons. The SED-fitting code models UV filters particularly poorly for giant branch stars, as small inaccuracies in modelling molecular absorption significantly affect UV flux in model spectra. Many of these stars have substantial UV excesses

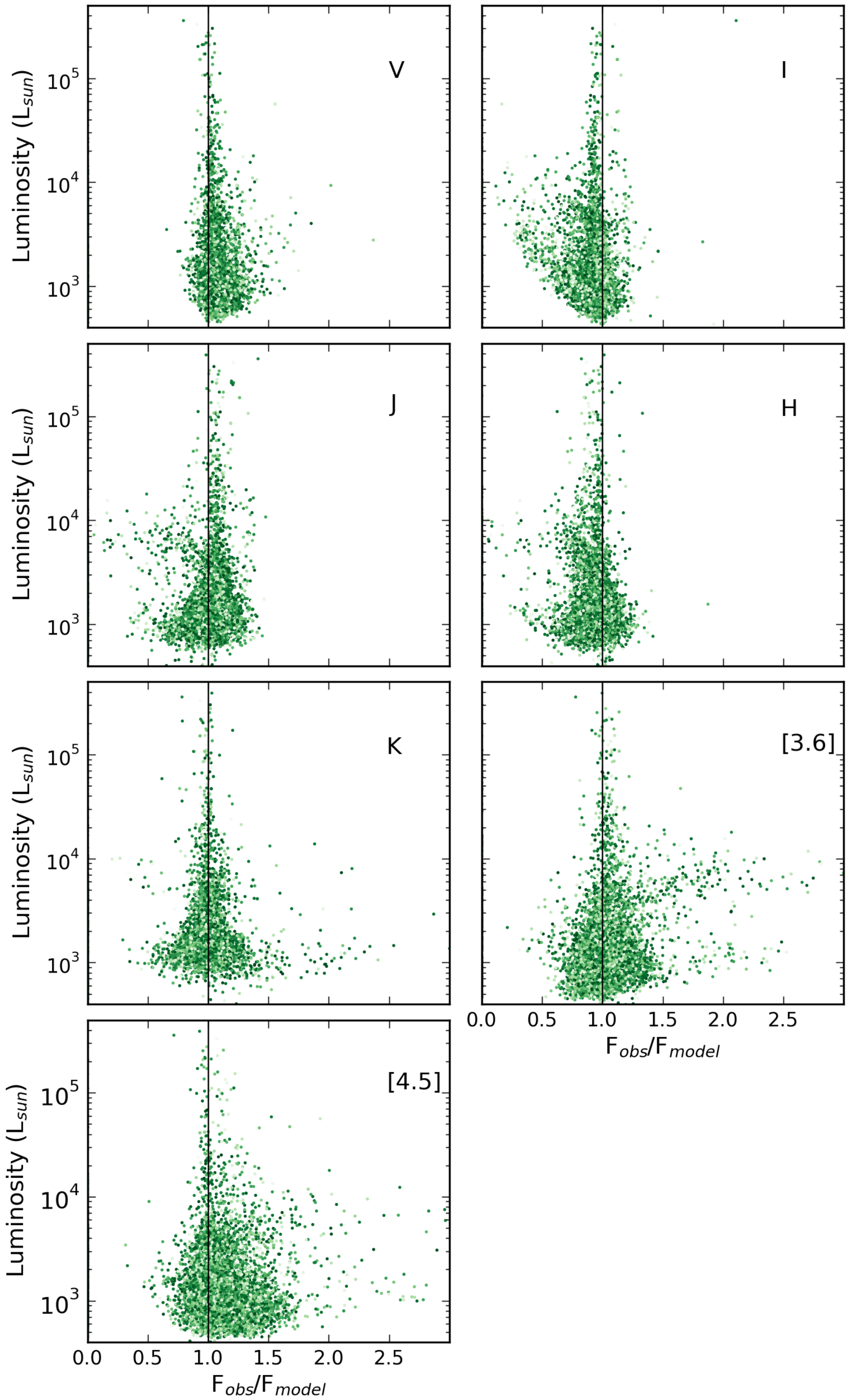

Figure 3.3: Filter-fit profiles for IC 1613. Darker colour indicates a closer proximity to the galactic centre. A line has been placed through $F_{obs}/F_{model} = 1$ to better display how scatter is distributed.

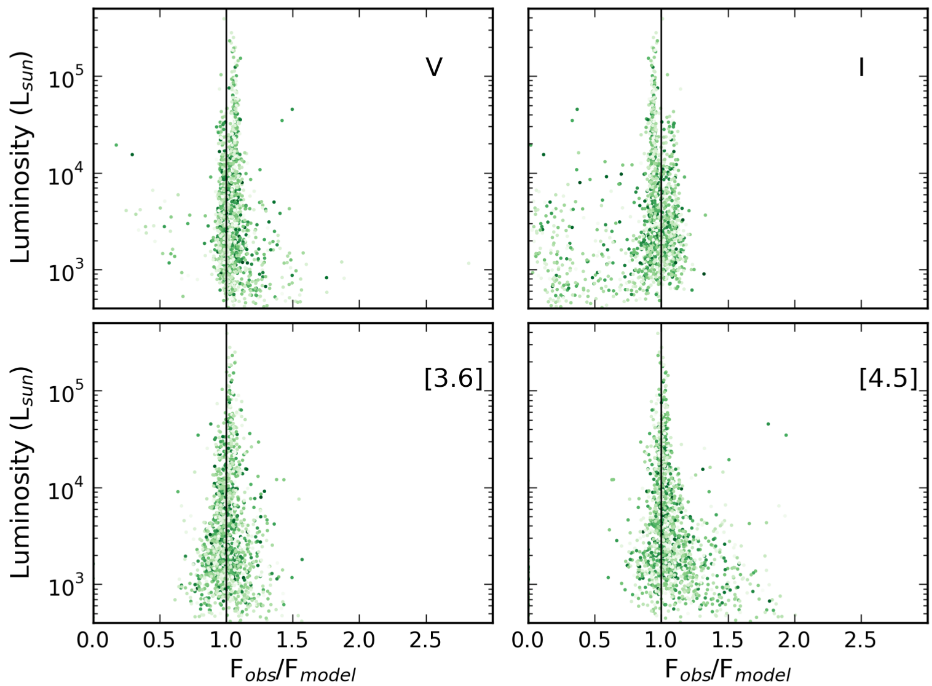

Figure 3.4: Filter-fit profiles for Sag DIG. Darker colour indicates a closer proximity to the galactic centre. A line has been placed through $F_{obs}/F_{model} = 1$ to better display how scatter is distributed.

due to an abundance of spectral lines and magnetic activity. Additionally, the u band may have been systematically poorly modelled, depending on the atmospheric corrections applied in the originating study (as atmospheric transmission has a strong wavelength dependency in this filter). A poorly modelled filter can affect the reliability of the remainder of the SED, so could be the cause of the scatter seen in the other filters. SEDs were recalculated excluding the u filter.

Figure 3.6 shows the result of this. Although scatter is still present, there has been a significant improvement, reducing to levels comparable to the previous galaxies. The centring on unity is better achieved. As all temperatures and luminosities were recalculated, a new H–R diagram was produced, which is shown in Figure 2.9 (d).

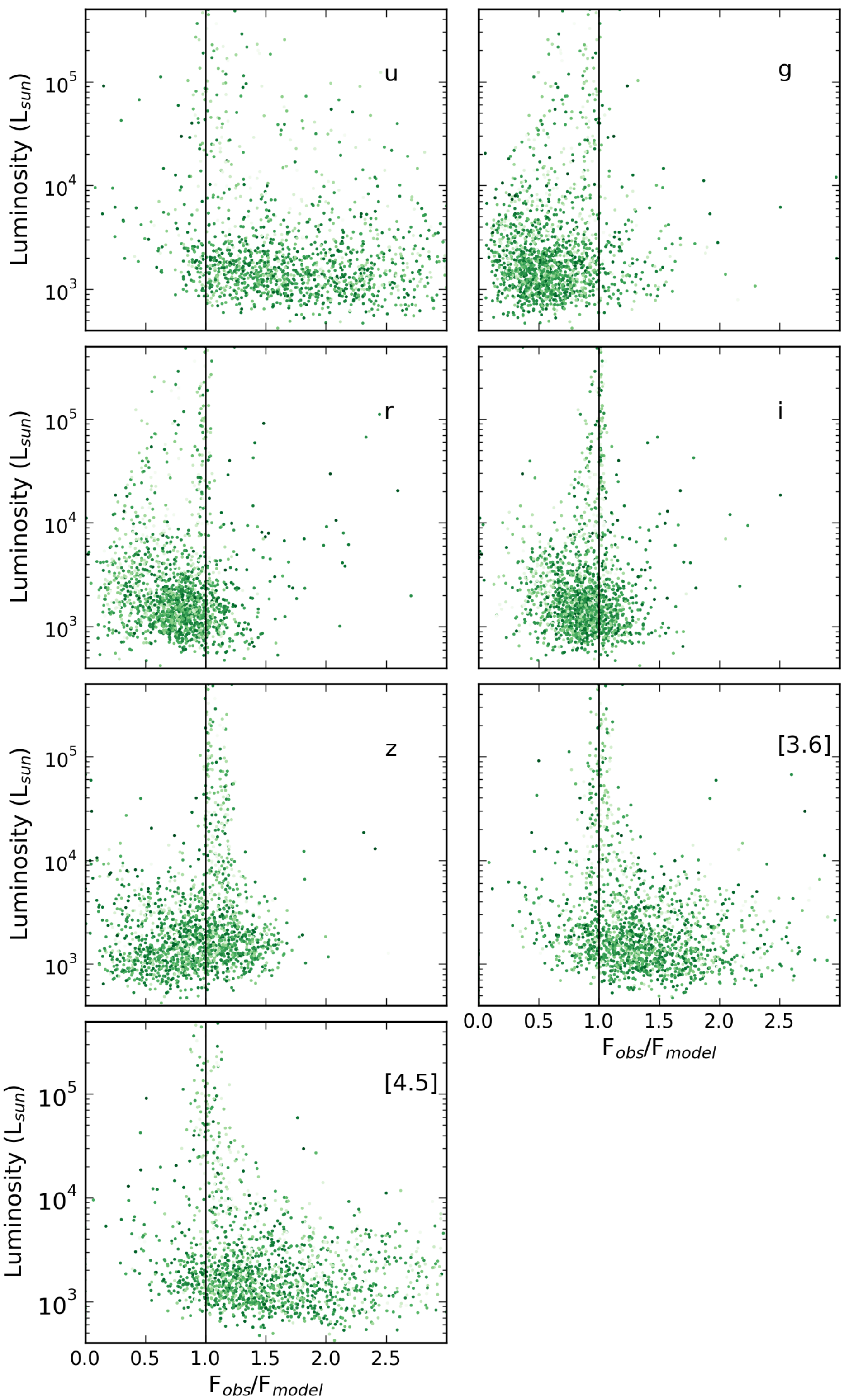

Figure 3.5: Filter-fit profiles for Peg DIG. Darker colour indicates a closer proximity to the galactic centre. A line has been placed through $F_{obs}/F_{model} = 1$ to better display how scatter is distributed.

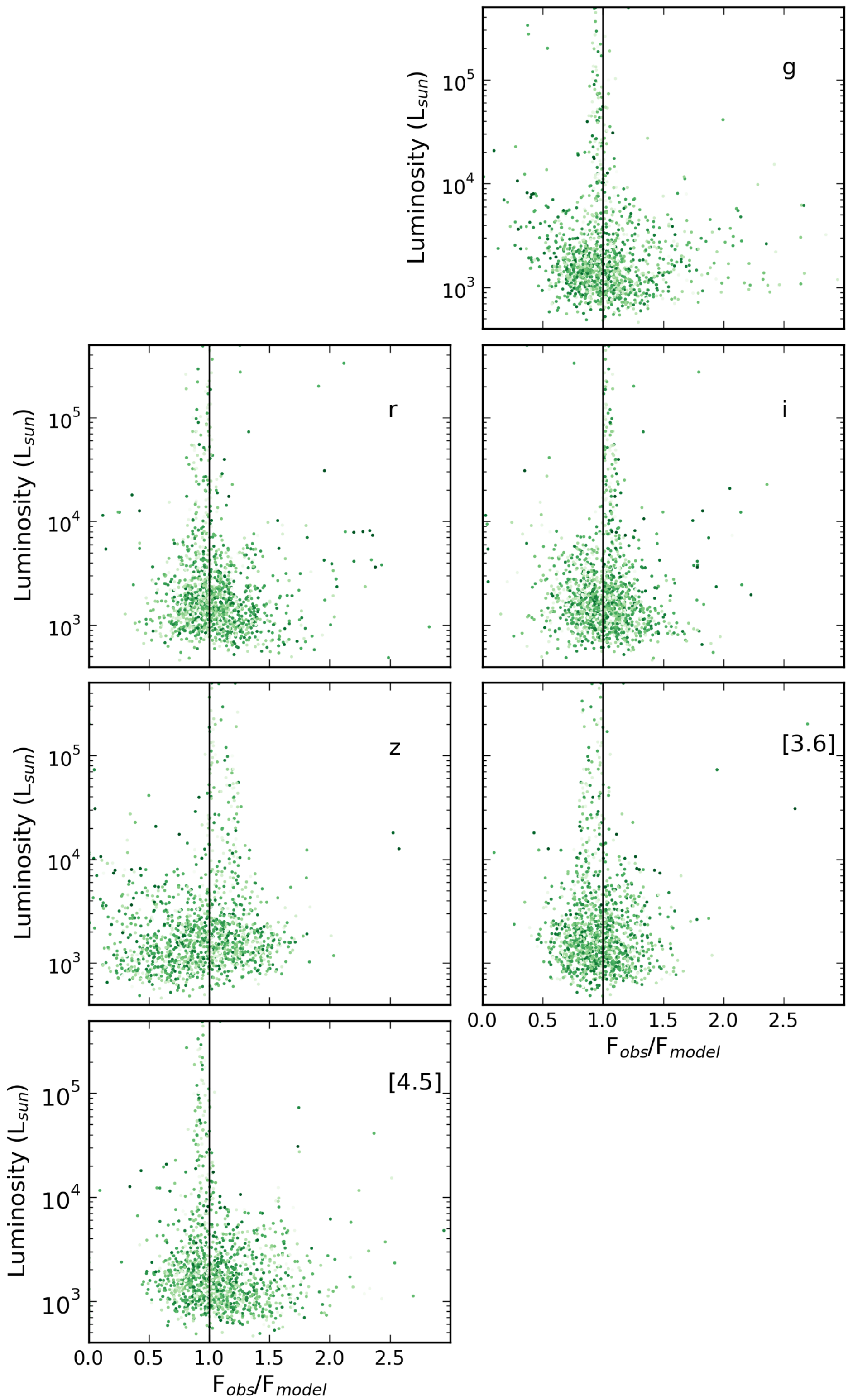

Figure 3.6: Recalculated filter-fit profiles for Peg DIG, excluding u band. Darker colour indicates a closer proximity to the galactic centre. A line has been placed through $F_{obs}/F_{model} = 1$ to better display how scatter is distributed.

3.1.6 WLM

The filter-fit profiles for this galaxy can be seen in Figure 3.7. The lack of data in V and I bands is immediately obvious. Again there is a notable scatter in many of these bands, more so in U (which covers a similar range of wavelengths to u). SEDs were again calculated omitting the U filter.

Figure 3.8 contains these newly calculated filter-fit profiles. The exclusion of U has caused a small but noticeable reduction in scatter in the remaining filters. Again, an H–R diagram was produced from the new SEDs (Figure 2.10 (c)).

3.1.7 NGC 6822

Considering the number of objects identified for this galaxy (Figure 3.9), filter-fit profiles remain mostly well constrained, with the exception of the U filter. The dark colour of the points in the scatter shows that many of these objects are close to the galactic centre, so unlikely to be background galaxies. They are most likely affected by stellar blending in U, as it has the poorest seeing and largest point spread function (PSF). SEDs were recalculated without this filter, shown in Figure 3.10. Small improvements are seen for the fits of points in all filters but B band, where blending effects are still present. This may also be due to its role as the shortest wavelength filter. However, this scatter in B is still reduced compared with U in the previous SED iteration. H band in particular has been fitted very precisely. An updated H–R diagram is presented in Figure 2.11.

3.1.8 LGS 3

Despite the lack of data points available for this galaxy, filter-fit profiles can still be analysed to an extent (Figure 3.11). Scatter is significant, particularly at the ends of the wavelength range (u, g, [3.6], [4.5]). The u filter has the most scatter, with an association with unity difficult to establish. SEDs were recalculated

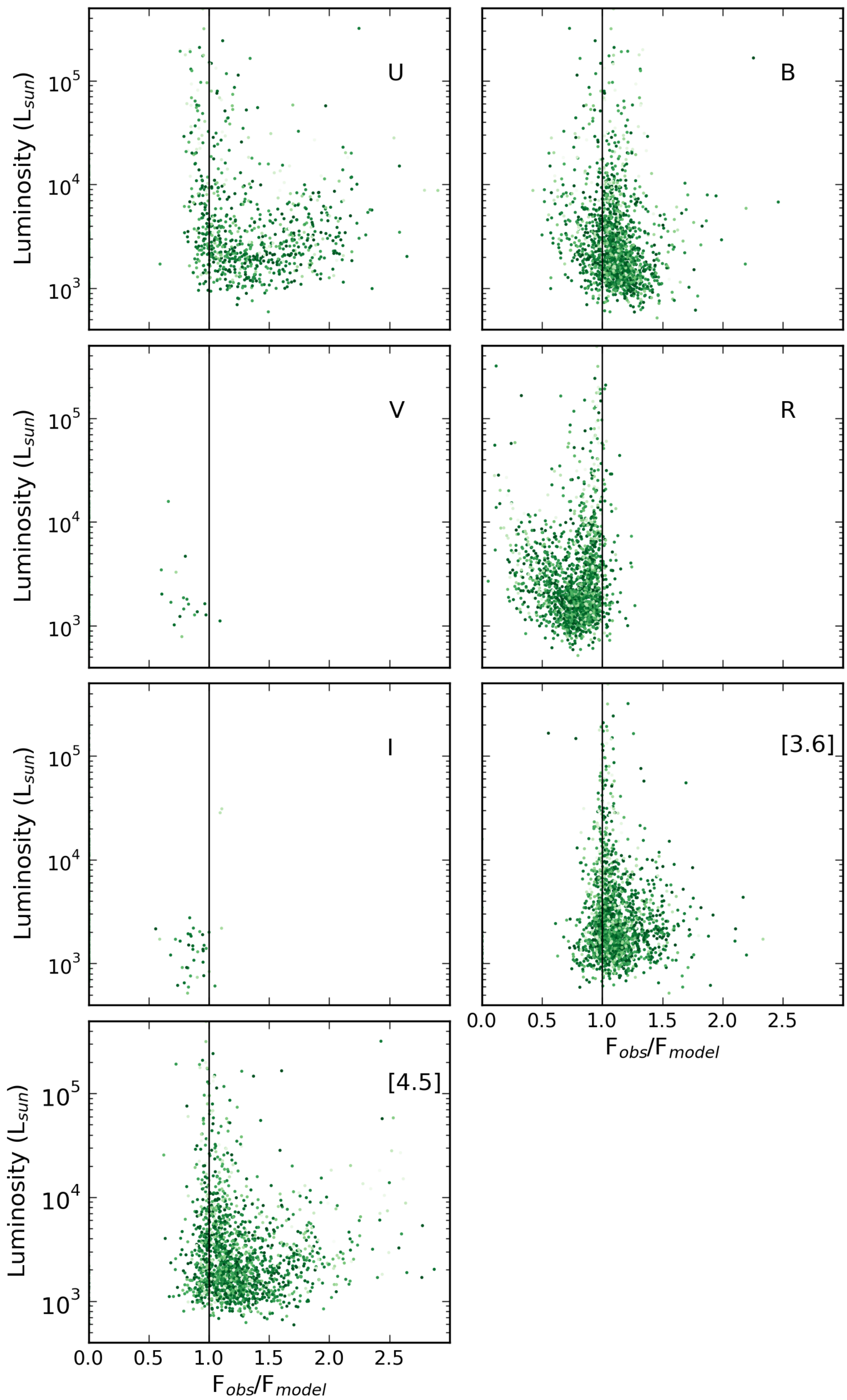

Figure 3.7: Filter-fit profiles for WLM. Darker colour indicates a closer proximity to the galactic centre. A line has been placed through $F_{obs}/F_{model} = 1$ to better display how scatter is distributed.

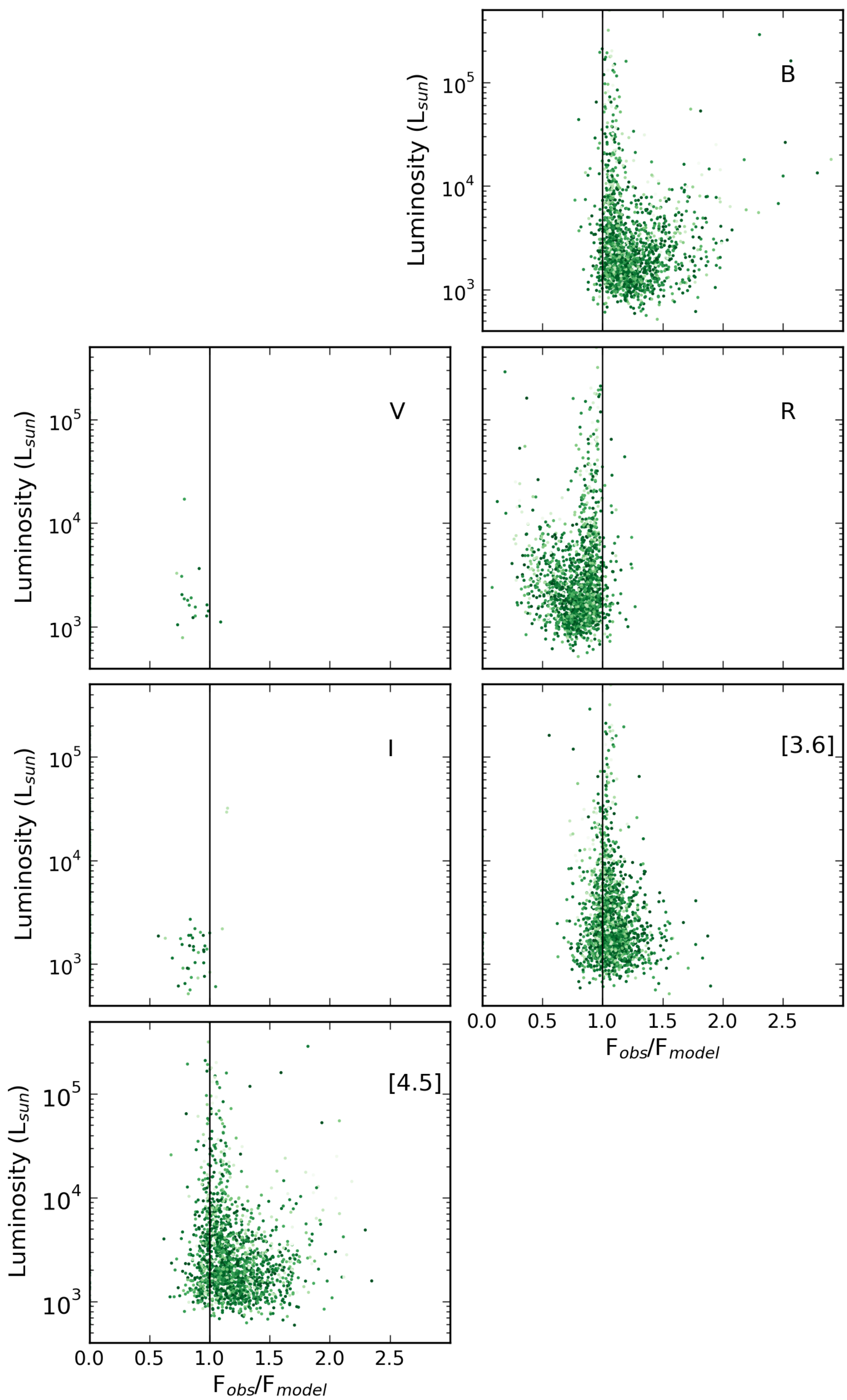

Figure 3.8: Recalculated filter-fit profiles for WLM, excluding U band. Darker colour indicates a closer proximity to the galactic centre. A line has been placed through $F_{obs}/F_{model} = 1$ to better display how scatter is distributed.

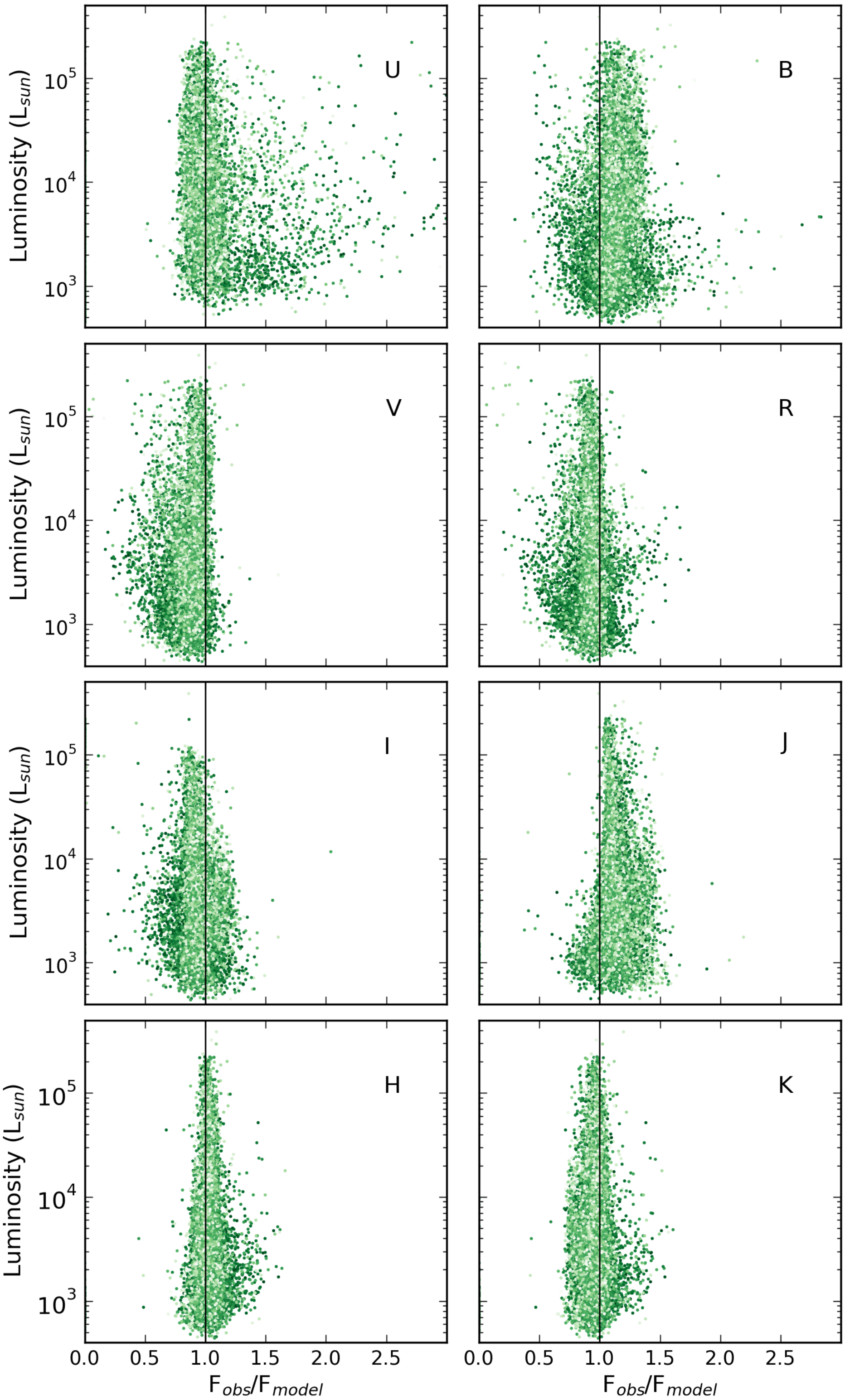

Figure 3.9: Filter-fit profiles for NGC 6822. Darker colour indicates a closer proximity to the galactic centre. A line has been placed through $F_{obs}/F_{model} = 1$ to better display how scatter is distributed.

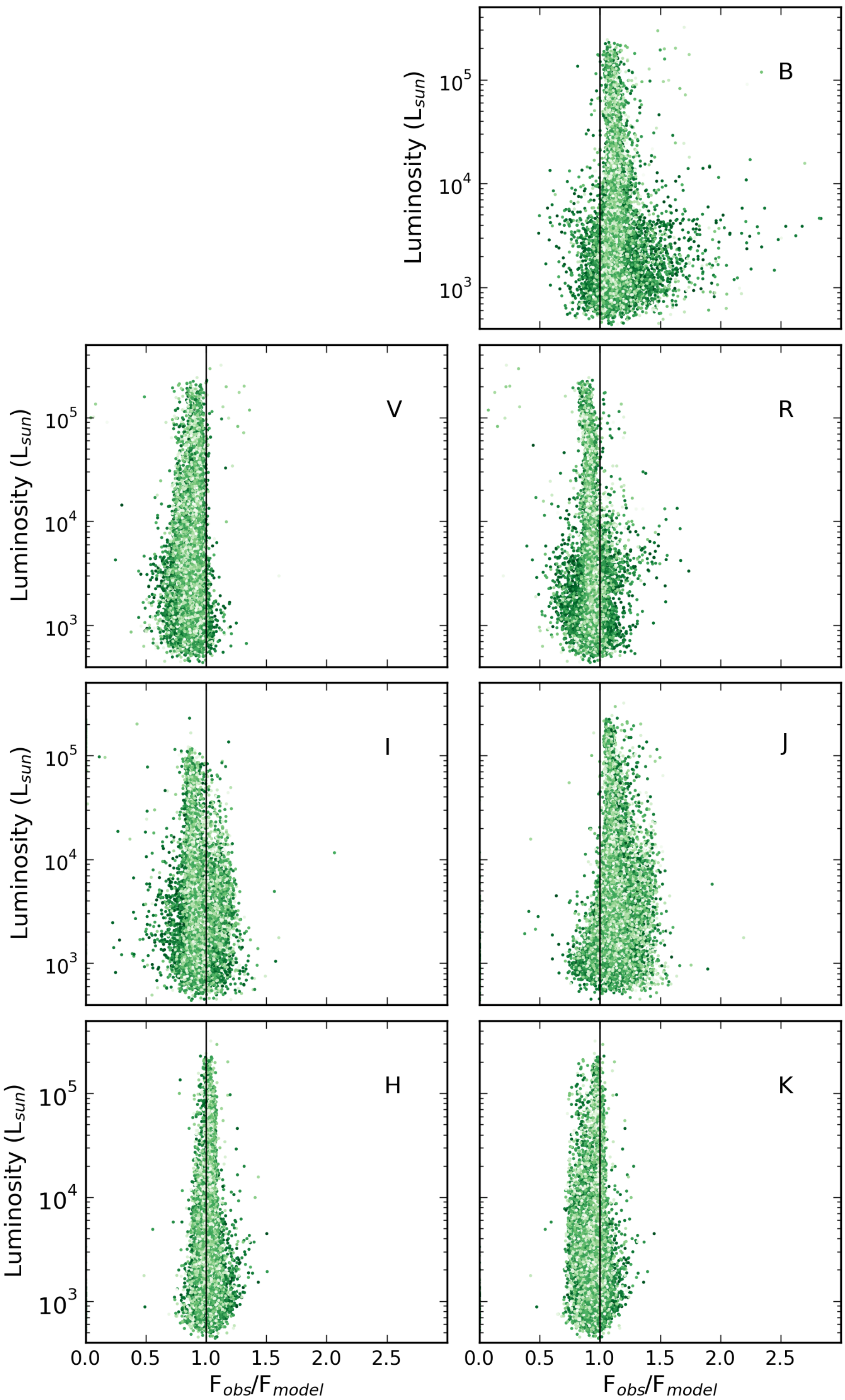

Figure 3.10: Recalculated filter-fit profiles for NGC 6822, excluding U band. Darker colour indicates a closer proximity to the galactic centre. A line has been placed through $F_{obs}/F_{model} = 1$ to better display how scatter is distributed.

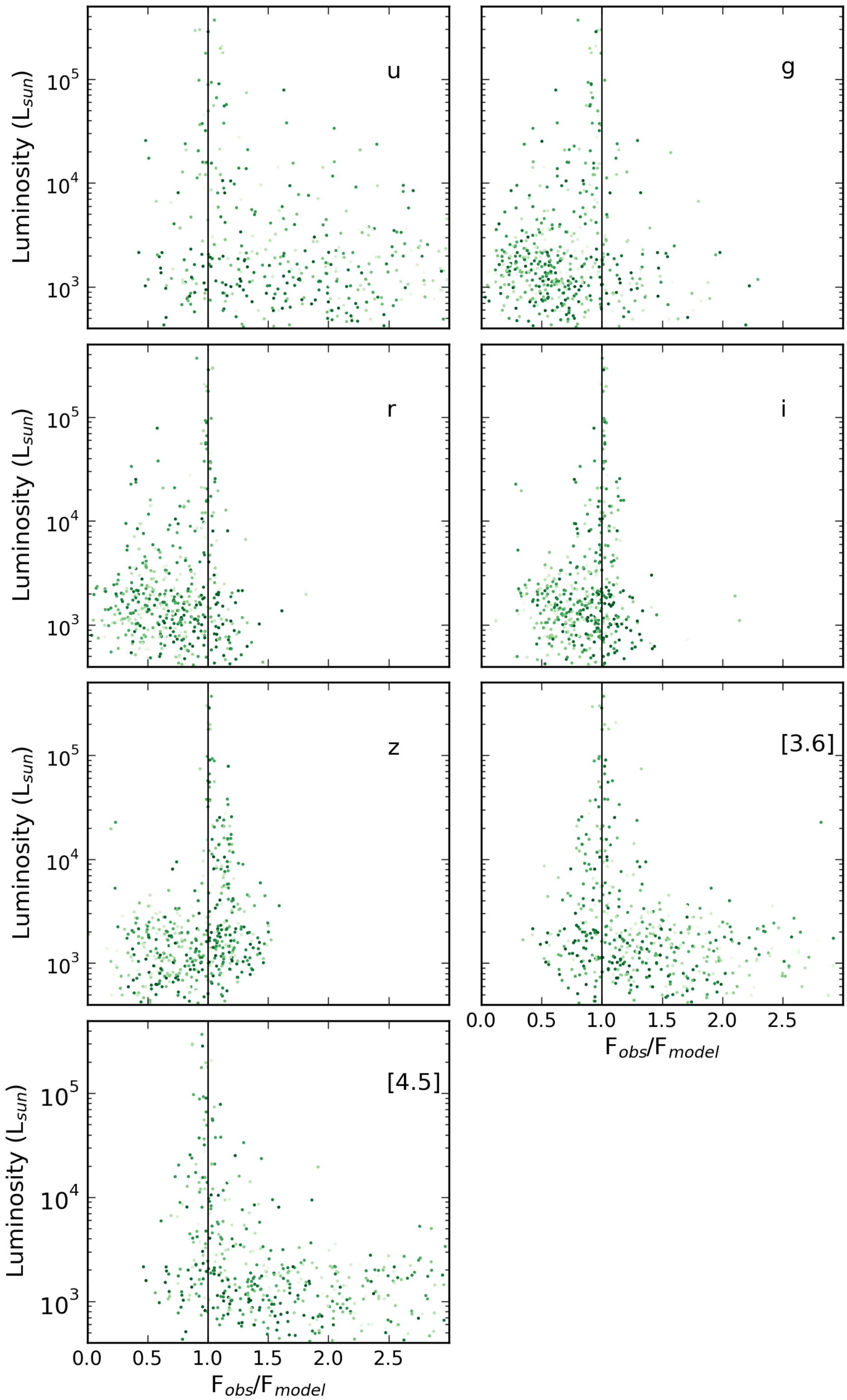

Figure 3.11: Filter-fit profiles for LGS 3. Darker colour indicates a closer proximity to the galactic centre. A line has been placed through $F_{obs}/F_{model} = 1$ to better display how scatter is distributed.

without this filter. It can be seen in Figure 3.12 that this provides a significant reduction in scatter in the filter-fit profiles, although interestingly not in the new H–R diagram, the main impact on which is a shift in temperature (Figure 2.12 (c)).

3.1.9 Phoenix

Figure 3.13 displays profiles for the available filters for the Phoenix galaxy. Note the different scale used to display luminosity in these plots compared to the other displayed galaxies. The proximity of this galaxy, and the deep photometry that is available allowed for the detection of fainter sources than in other galaxies in the sample.

Profiles are well constrained, particularly for objects $\gtrsim 1000$ $L_\odot$. It was determined that the scatter to the left of the plot in I is likely from background galaxies, due to the distance of the points from the galactic centre and their position on the sky. Scatter in V and I appears centred around points slightly offset from unity.

3.1.10 Leo A

Figure 3.14 contains scatter in many filters, but the majority these points are far from the galactic centre, suggesting that they are background galaxies. Indeed, comparing this with the H–R diagrams in Figure 2.14 appears to confirm this. The remainder of the objects appear very well constrained, though in some cases the scatter appears to be around points slightly offset from unity.

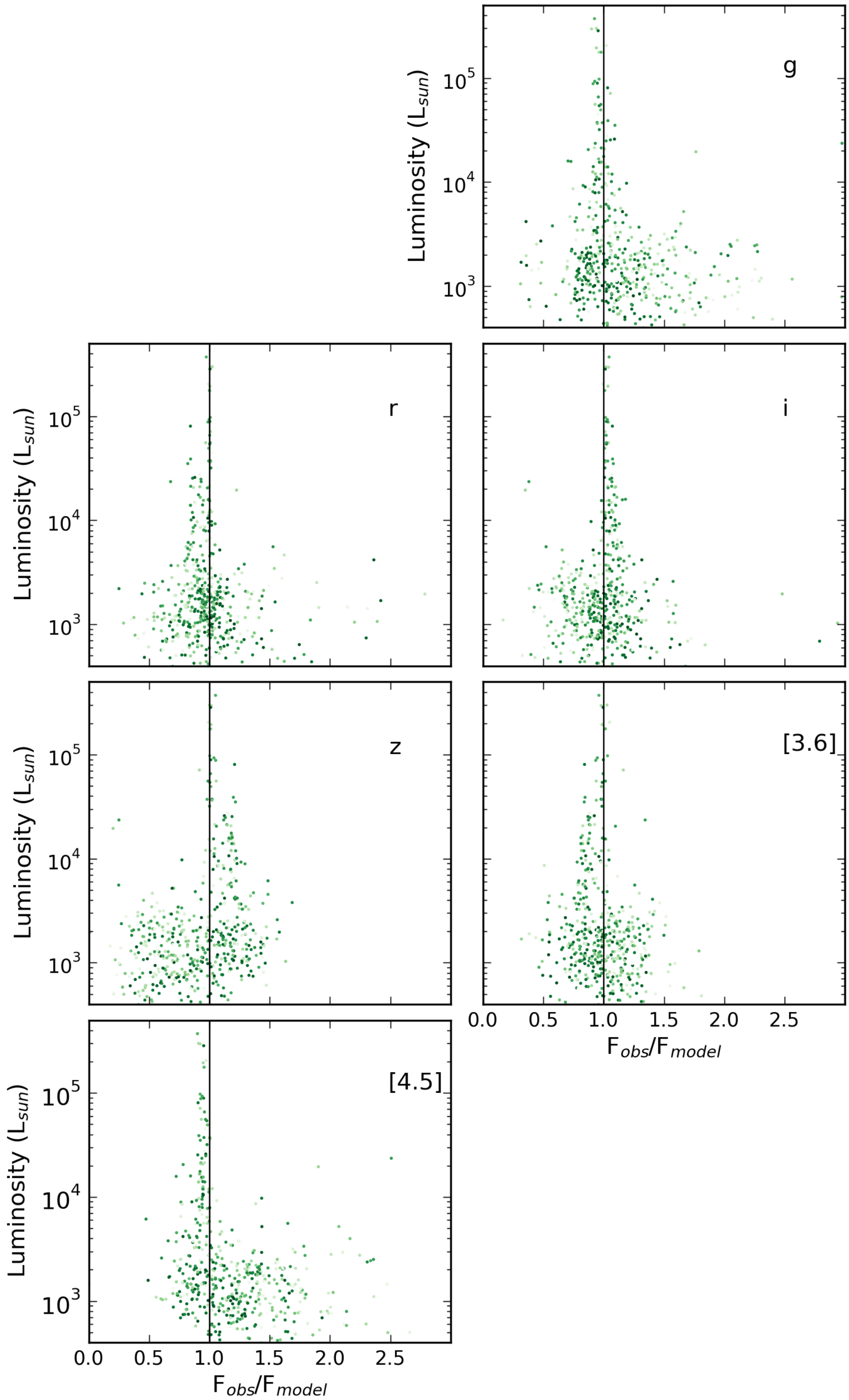

Figure 3.12: Recalculated filter-fit profiles for LGS 3, excluding u band. Darker colour indicates a closer proximity to the galactic centre. A line has been placed through $F_{obs}/F_{model} = 1$ to better display how scatter is distributed.

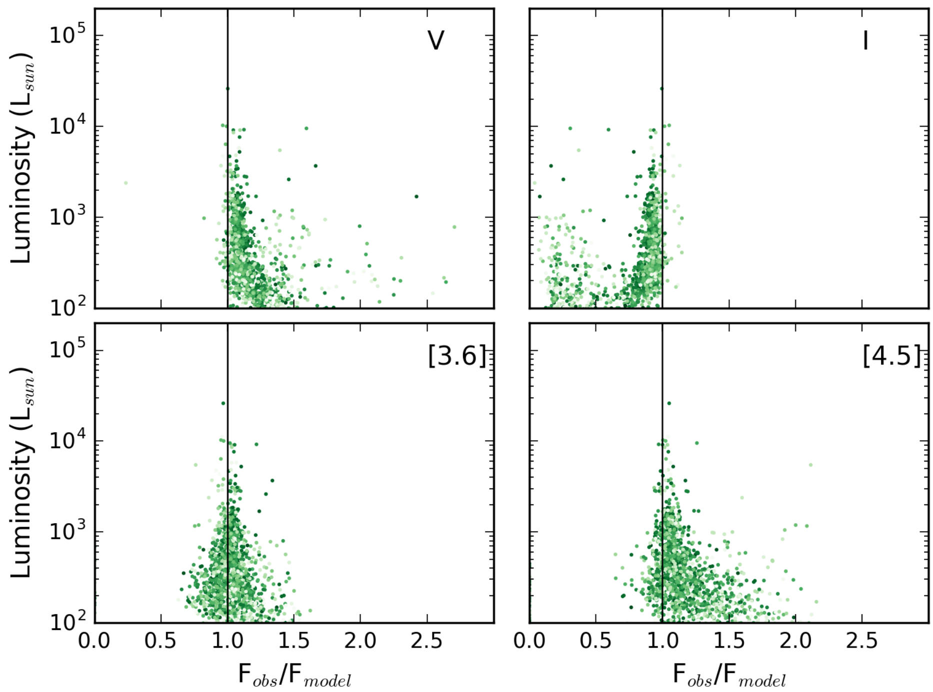

Figure 3.13: Filter-fit profiles for Phoenix. Darker colour indicates a closer proximity to the galactic centre. A line has been placed through $F_{obs}/F_{model} = 1$ to better display how scatter is distributed. Note the different range of luminosities displayed here compared to other galaxies in this Section.

3.1.11 And IX

Figure 3.15 immediately demonstrates the lack of data available in near-IR (JHK) bands, and the significant scatter in u. SEDs were recalculated excluding this filter.

The recalculated SEDs demonstrate significant improvements in the filter-fit profiles, displayed in Figure 3.16. Scatter is reduced across all filters, with the most notable improvement in near-IR bands, where many more points become visible. The cut-off of these filters is clearly demonstrated (at around 20,000 $L_{\odot}$). A recalculated H–R diagram is presented in Figure 2.15.

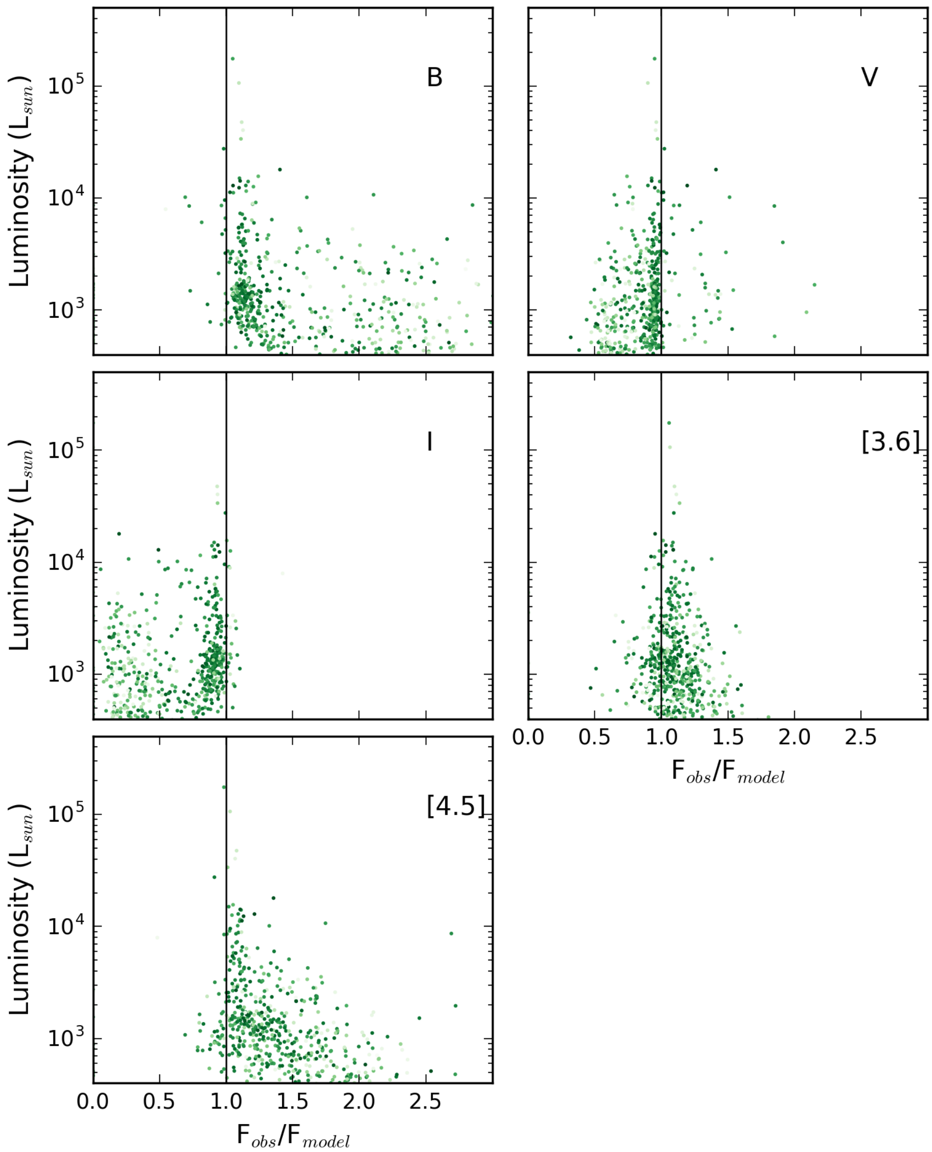

Figure 3.14: Filter-fit profiles for Leo A. Darker colour indicates a closer proximity to the galactic centre. A line has been placed through $F_{obs}/F_{model} = 1$ to better display how scatter is distributed.

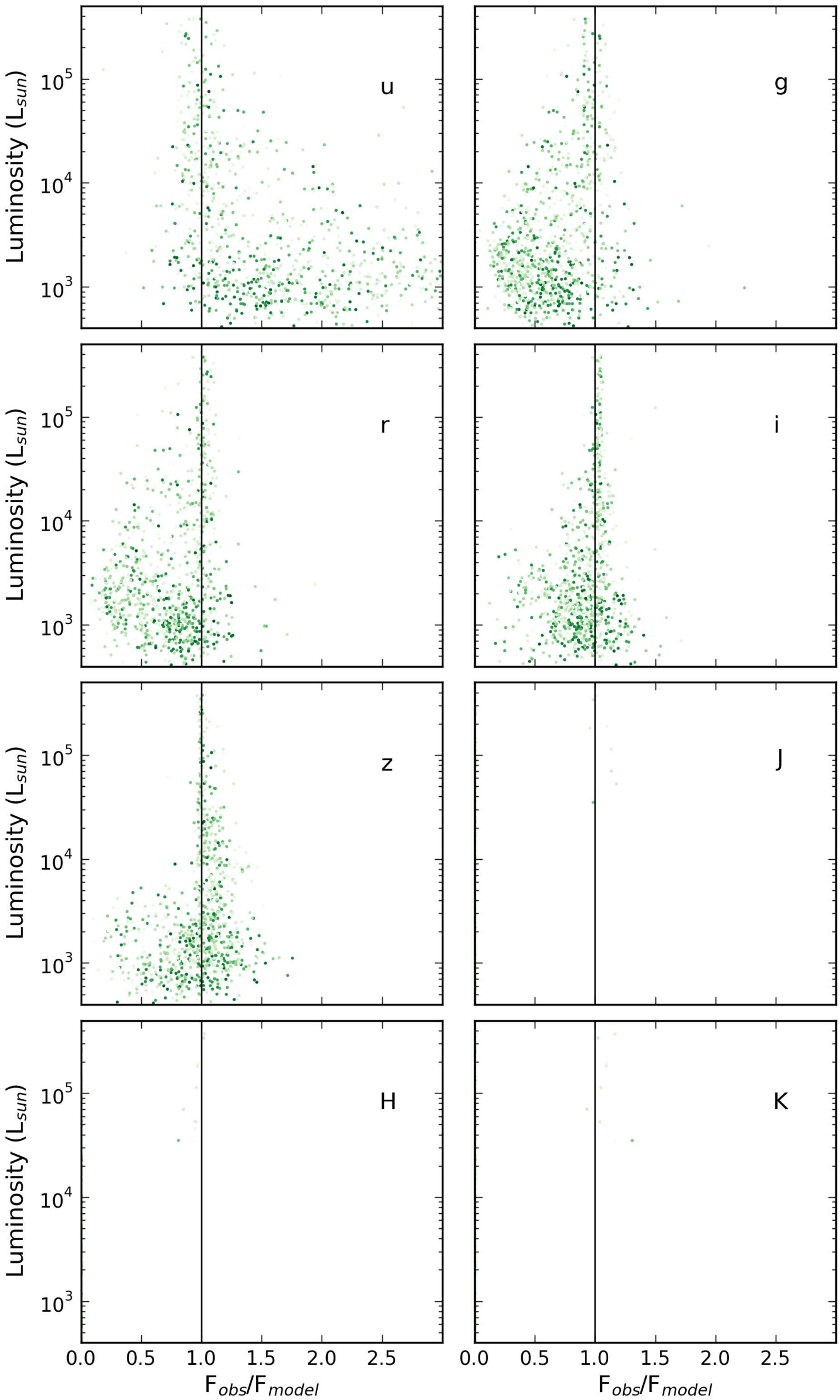
u
g
r
i
z
J
H
K
Luminosity (L_{sun})
10^3
10^4
10^5
0.0
0.5
1.0
1.5
2.0
2.5
F_{obs}/F_{model}

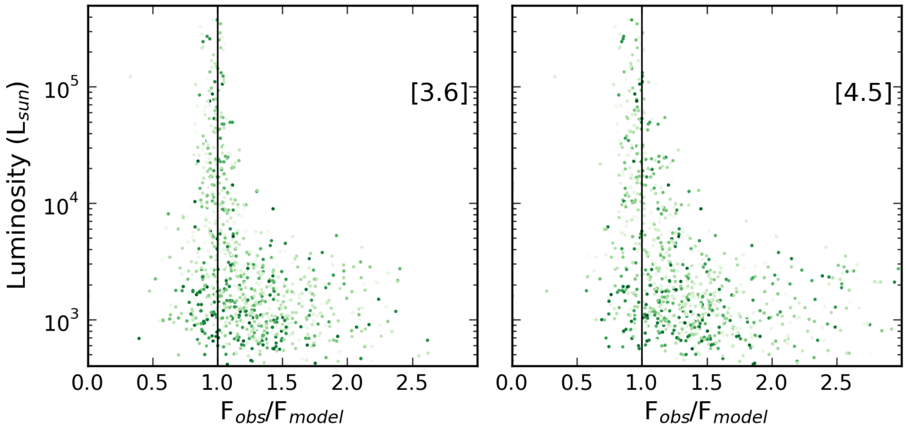

Figure 3.15: Filter-fit profiles for And IX. Darker colour indicates a closer proximity to the galactic centre. A line has been placed through $F_{obs}/F_{model} = 1$ to better display how scatter is distributed.

3.1.12 NGC 185

From Figure 3.17, we can see that all filter-fit profiles for NGC 185 are consistent in their levels of scatter. There is a fairly tight distribution around unity, although the presence of dark points around the edges of the profiles implies that stellar blending has been an issue for this galaxy.

3.1.13 NGC 147

As expected, the filter-fit profiles for NGC 147 are almost identical to NGC 185, as data came from the same studies. The analysis of that galaxy equally applies to this one, including the presence of stellar blending.

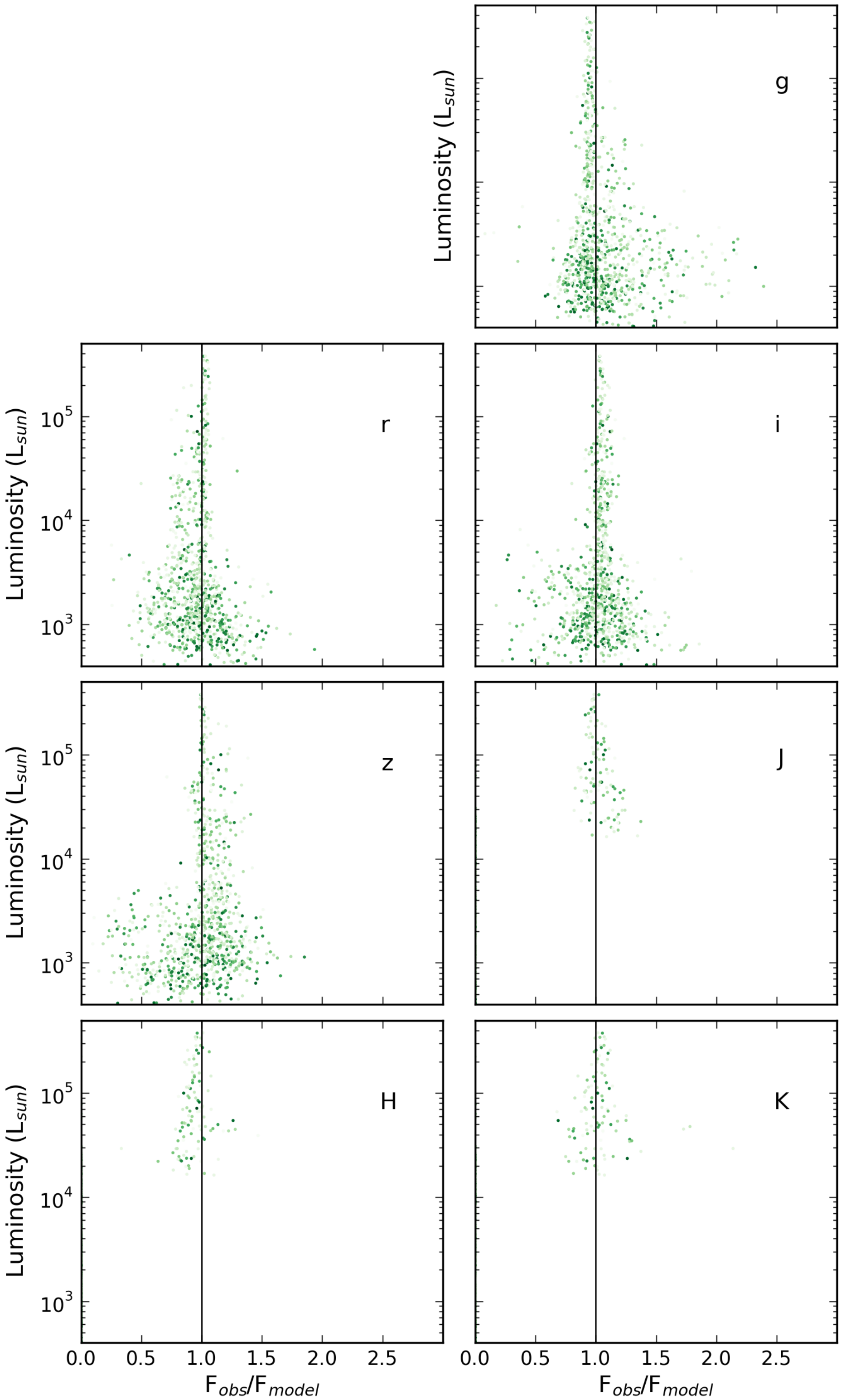
g
r
i
z
J
H
K
Luminosity (L_{sun})
10^5
10^4
10^3
0.0 0.5 1.0 1.5 2.0 2.5
F_{obs}/F_{model}

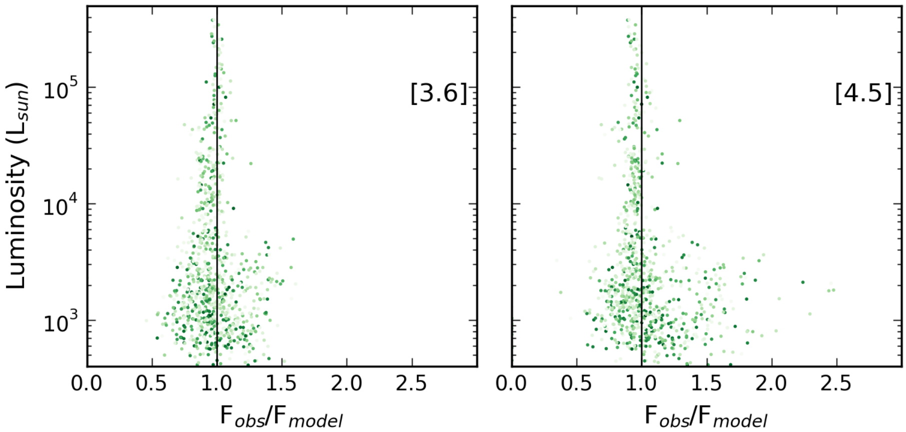

Figure 3.16: Recalculated filter-fit profiles for AndIX, excluding u band. Darker colour indicates a closer proximity to the galactic centre. A line has been placed through $F_{obs}/F_{model} = 1$ to better display how scatter is distributed.

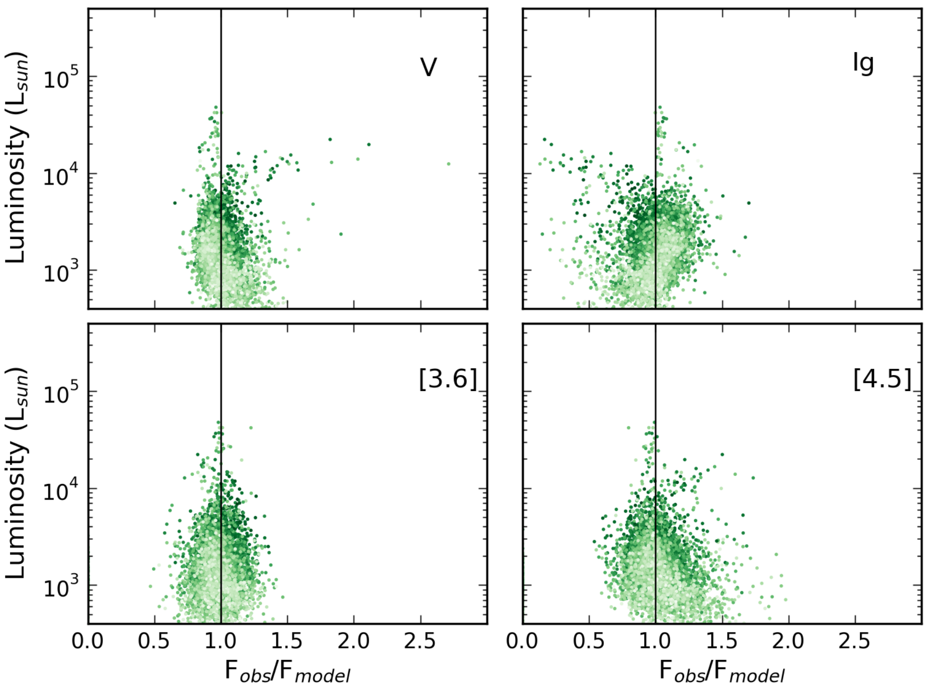

Figure 3.17: Filter-fit profiles for NGC 185. Darker colour indicates a closer proximity to the galactic centre. A line has been placed through $F_{obs}/F_{model} = 1$ to better display how scatter is distributed.

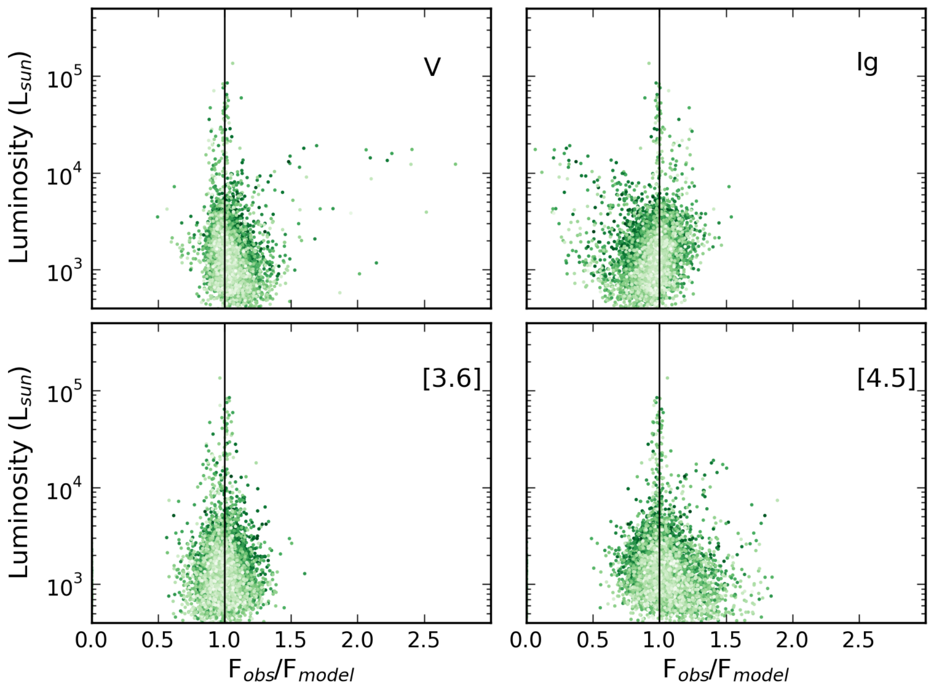

Figure 3.18: Filter-fit profiles for NGC 147. Darker colour indicates a closer proximity to the galactic centre. A line has been placed through $F_{obs}/F_{model} = 1$ to better display how scatter is distributed.

3.2 Searching for an IR excess

Objects with a significant IR excess (see Section 1.4.3.3) are of importance to this project, as they may be dusty AGB stars. These objects are expected to be amongst the coolest and most-luminous AGB stars, so would be visible at the upper limit of the AGB in our H–R diagrams. The IR excess (particularly from carbon-rich dust) would be detectable in mid-IR bands, such as those used in the DUSTiNGS survey. The average of F_{obs}/F_{model} for each point in [3.6] and [4.5] bands was calculated, providing an estimate of the IR excess for each star.

The final H–R diagrams from Section 2.2 were reproduced for each galaxy, and coloured using this averaged IR excess parameter and its relation to the observational scatter of the IR excess for the galaxy, σ. The scatter was calculated by sorting all points with a value for IR excess in the range $3000 < T < 5500$ K, and $300 < L < 6000$ $L_{\odot}$, (i.e. the range of points visible in the H–R diagrams based on the final versions from Section 2.2, and excluding poorly fitted points < 3000 K). Galaxies with significant background galaxy contamination had the region containing most of these removed. This was to avoid skewing the deviation by using data that is of no interest to the study. Typically, there was an area of low density between this region and the population of RGB/AGB stars, allowing for identification by eye.

Following the sorting, the central 68.3% of values for the IR-excess were found (similar to the standard deviation but reducing the impact of outliers in this non-Gaussian distribution), and the upper and lower limits of the range calculated. Half of this range was defined as the deviation, σ. The median of this range was also recorded. A dataset with many well-fit points would have its scatter centred around a median very close to unity. However, systematic offsets in the photometry may return data with scattered centred on a different point. Calculating deviation via this method allows for the detection of dusty objects in data that suffers from this type of offset. Objects with an IR excess within 1σ of the median are coloured grey. Above this value, objects transition through red towards black, and below this transition towards dark blue. Dusty AGB stars are modelled with an IR excess greater than unity, so would appear as a cluster of red objects from the RGB to the brightest and coolest points of the AGB in the H–R diagrams. However, other sources such as post-AGB objects and dusty galaxies may also be modelled with a similar IR-excess, so appear as the same colour on the H–R diagram. An illustration of how colour is related to σ and the median is shown in Figure 3.19.

With good photometry, the RGB tip should be well-modelled, so appear grey in the following plots. Mass loss normally remains comparatively low at this stage

Figure 3.19: Figure showing how colour varies with relation to the median (Med) and σ in the following H–R diagrams.

of stellar evolution, with negligible amounts of dust present, allowing for the photometry to be fit well to the models. The colour of the RGB tip can therefore be used as an indicator of the quality and reliability of the data for each galaxy.

For several galaxies, F_{obs}/F_{model} was calculated for [5.0] and [8.0] bands, allowing for similar plots to be produced using the average of these values as an IR excess. However, a significantly diminished number of objects possessed data in these filters, primarily due the fact that less flux is produced at these wavelengths (despite the IR excess). The values of σ and the median from the [3.6] and [4.5] plots were used to colour the data points here, due to their reduced number and bias towards a high IR excess.

These H–R diagrams are discussed below for 12 of the 13 galaxies for which results were presented in Chapter 2; an IR excess could not be determined for NGC 6822 as it lacks available photometry in mid-IR wavelengths. Due to the method in which the median and σ were calculated, points are plotted in order of increasing IR-excess, meaning many blue points are obscured by the bulk of the stellar population, while red points are more prominent.

3.2.1 Sextans B

The RGB population appears to have little IR excess, with expected scatter around unity (Figure 3.20). However, there is a very red population of stars at the cool side of the RGB tip. These may be part of the population of background

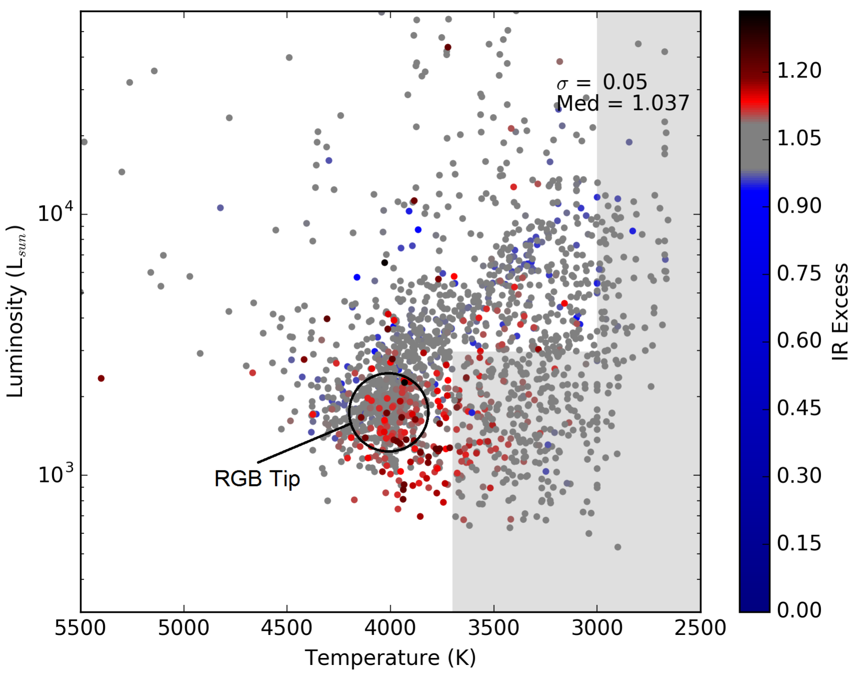

Figure 3.20: H–R diagram of the stellar population of Sex B, coloured by the [3.6] and [4.5] IR excess of each point. Regions shaded grey were excluded from the statistical analysis of this galaxy. The region containing the majority of the background galaxies has been removed. Blue objects emit less mid-IR flux than expected, while red objects emit more. The approximate location of the RGB tip is indicated.

galaxies, but this seems unlikely, as they appear with an approximately even spatial distribution across the galaxy. Another possibility is that they are the result of stellar blending. There are several red objects in the region where AGB stars would be expected, but amongst a significant scatter of well-fit (grey) and over-estimated (blue) points, meaning it is difficult say with confidence if they are dusty AGB stars. The median is close to unity, and with the low σ, this suggests that most of the excess is real.

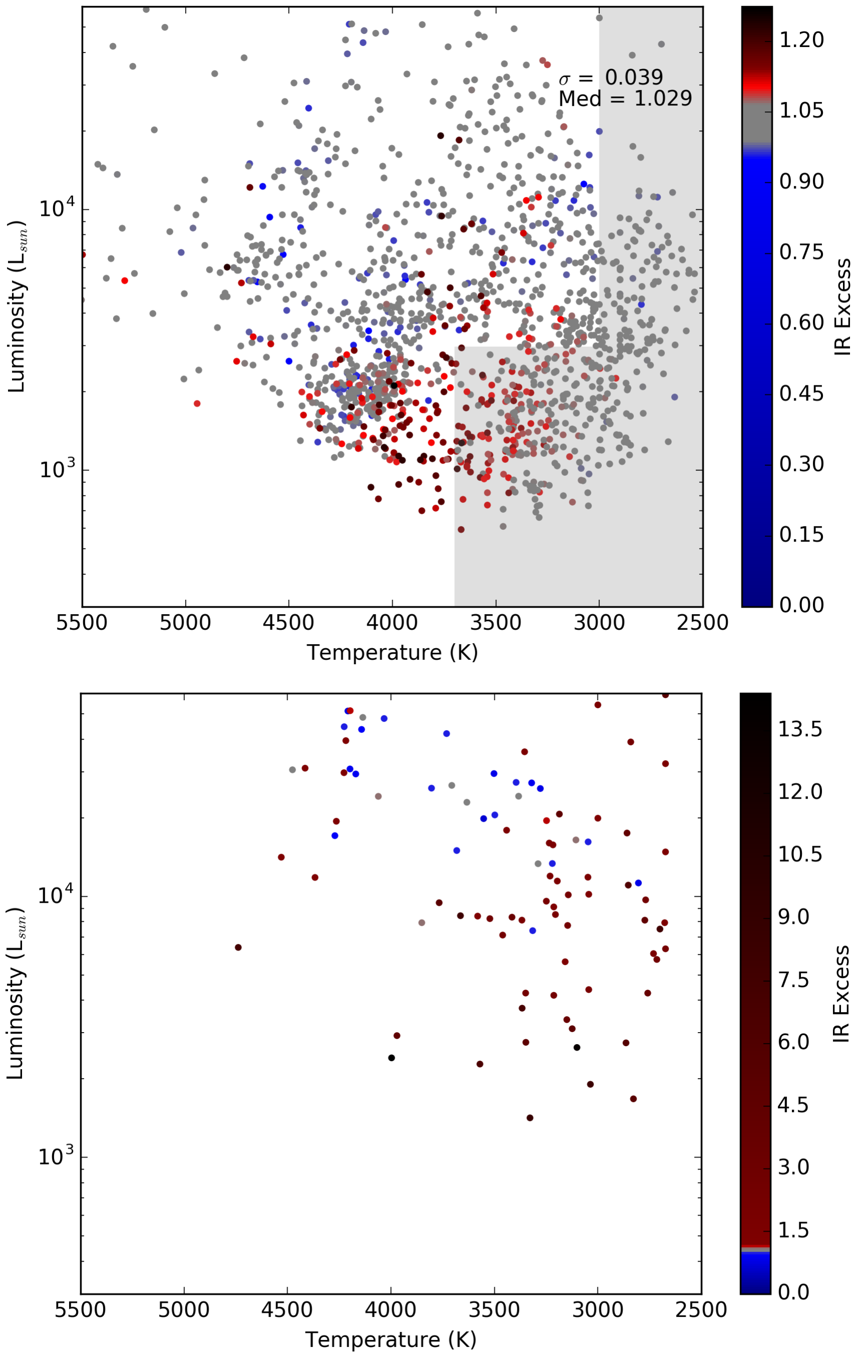

Figure 3.21: H–R diagram of the stellar population of Sex A, coloured by the IR excess of each point. Regions shaded grey were excluded from the statistical analysis of this galaxy. Blue objects emit less mid-IR flux than expected, while red objects emit more. *Top*: (a) IR excess calculated from [3.6] and [4.5]. *Bottom*: (b) IR excess calculated from [5.8] and [8.0].

3.2.2 Sextans A

The RGB tip appears to be well fit (grey) overall, (Figure 3.21 (a)) but the very red objects seen for Sex B are once again present, which is to be expected considering the photometry is from the same source. Again, these have an even distribution across the field of view. There is evidence for an increasing IR excess towards the top right of the diagram, more pronounced compared to the natural scatter than in Sex B. Again, the low σ suggests this scatter is real. Figure 3.21 (b) includes [5.8] and [8.0] data, and highlights objects that may be dusty AGB stars, as well as many blue objects above 10^4 L$_\odot$ that appear to have been poorly modelled.

3.2.3 IC 1613

Figure 3.22 (a) shows a grey RGB tip, with a population of red objects at its centre. Similar to the red objects seen in Sex A and Sex B, they are distributed evenly across the galaxy. This is likely a consequence of the way points were sorted before plotting, with high-IR excess objects plotted last. Some of these points remain visible in (b). The red objects in (b) do not appear to reduce in density around the RGB tip, implying they are AGB stars. There is a very red population where dusty AGB stars would be expected ($\sim$ 3250 K, 6000 L$_\odot$), increasing with T and L and visible with both sets of filters. However, the IR excess in many of these stars is greater than would be expected, particularly notable in (b). Another group of AGB stars are present in the centre of the RGB, likely from the ancient stellar population. At a similar range of luminosities, but cooler temperatures, are the background galaxies discussed in Section 3.1.3. Many of these objects are in the minimum-temperature band (i.e. the temperature assigned to all objects with a calculated temperature below a certain value), becoming indistinguishable from the coolest AGB stars at higher L. Values for the IR excess are significantly

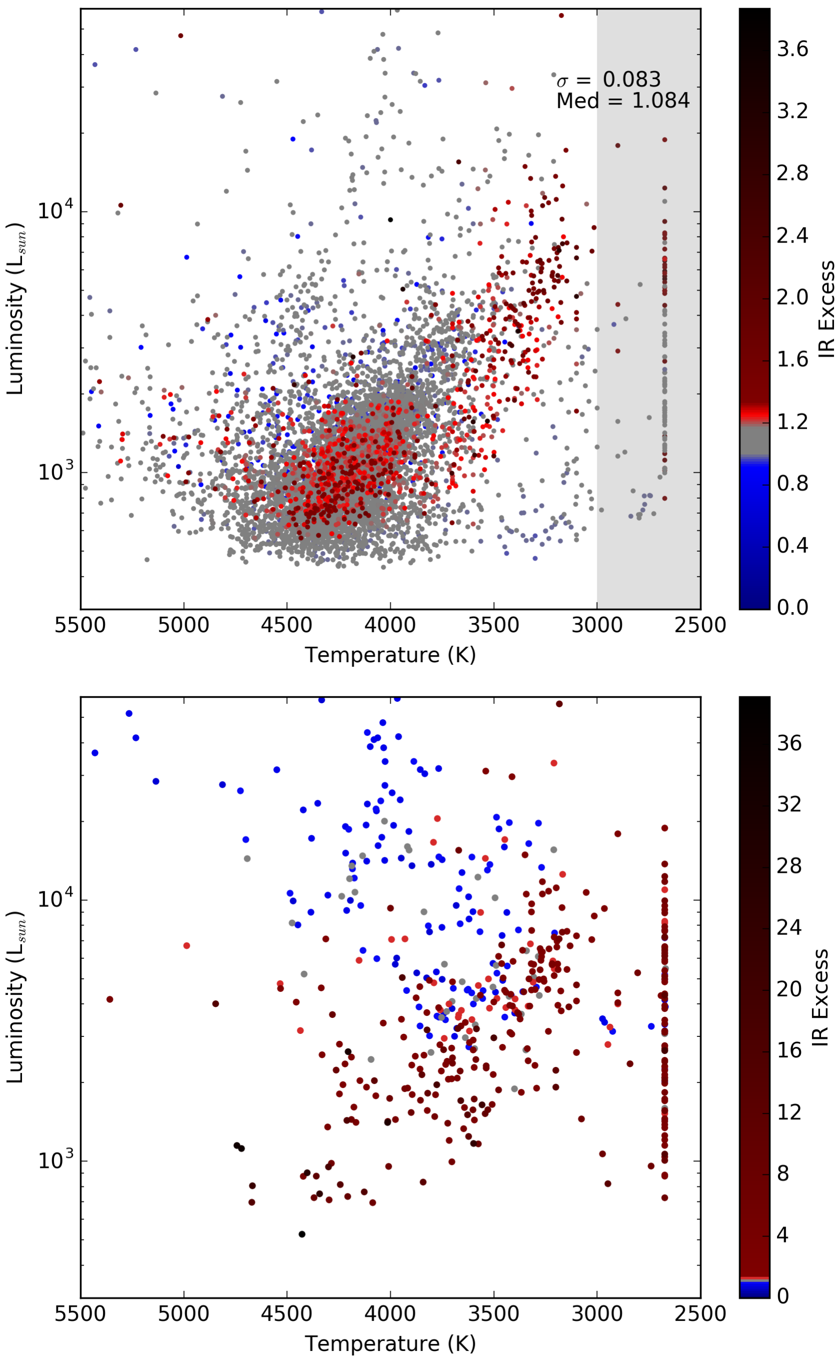

Figure 3.22: H–R diagram of the stellar population of IC 1613, coloured by the IR excess of each point. Regions shaded grey were excluded from the statistical analysis of this galaxy. Blue objects emit less mid-IR flux than expected, while red objects emit more. *Top*: (a) IR excess calculated from [3.6] and [4.5]. *Bottom*: (b) IR excess calculated from [5.8] and [8.0].

greater in this galaxy than in any other in this sample.

3.2.4 Sag DIG

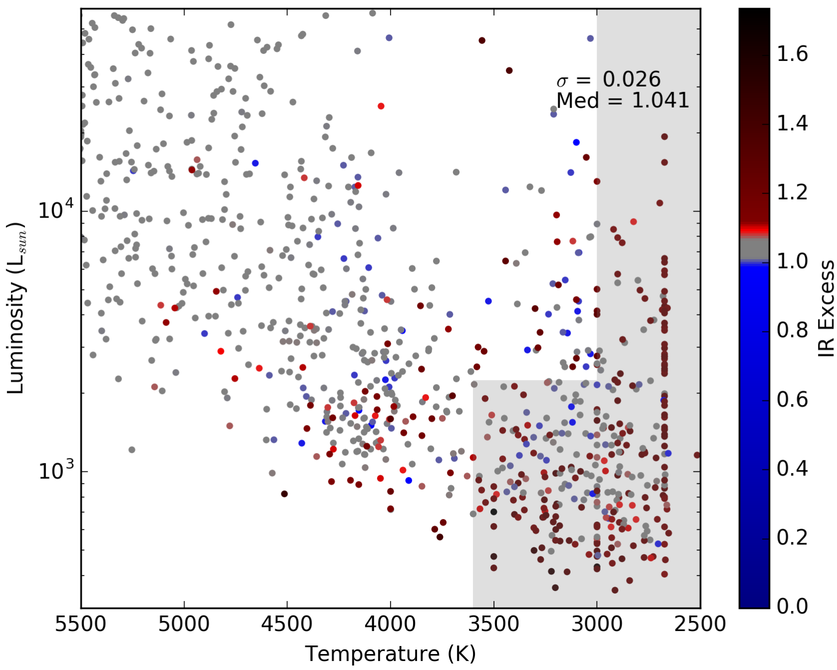

Figure 3.23: H–R diagram of the stellar population of Sag DIG, coloured by the [3.6] and [4.5] IR excess of each point. Regions shaded grey were excluded from the statistical analysis of this galaxy. Blue objects emit less mid-IR flux than expected, while red objects emit more.

Figure 3.23 shows a broadly grey RGB tip, with the majority of the scatter caused by the low σ. The IR excess increases towards the region where dusty AGB stars are expected, suggesting that a number of these objects have been detected.

3.2.5 Peg DIG

Figure 3.24 (a) contains a broadly grey RGB tip, and there is some evidence for an increased IR excess amongst the natural scatter towards the dusty AGB

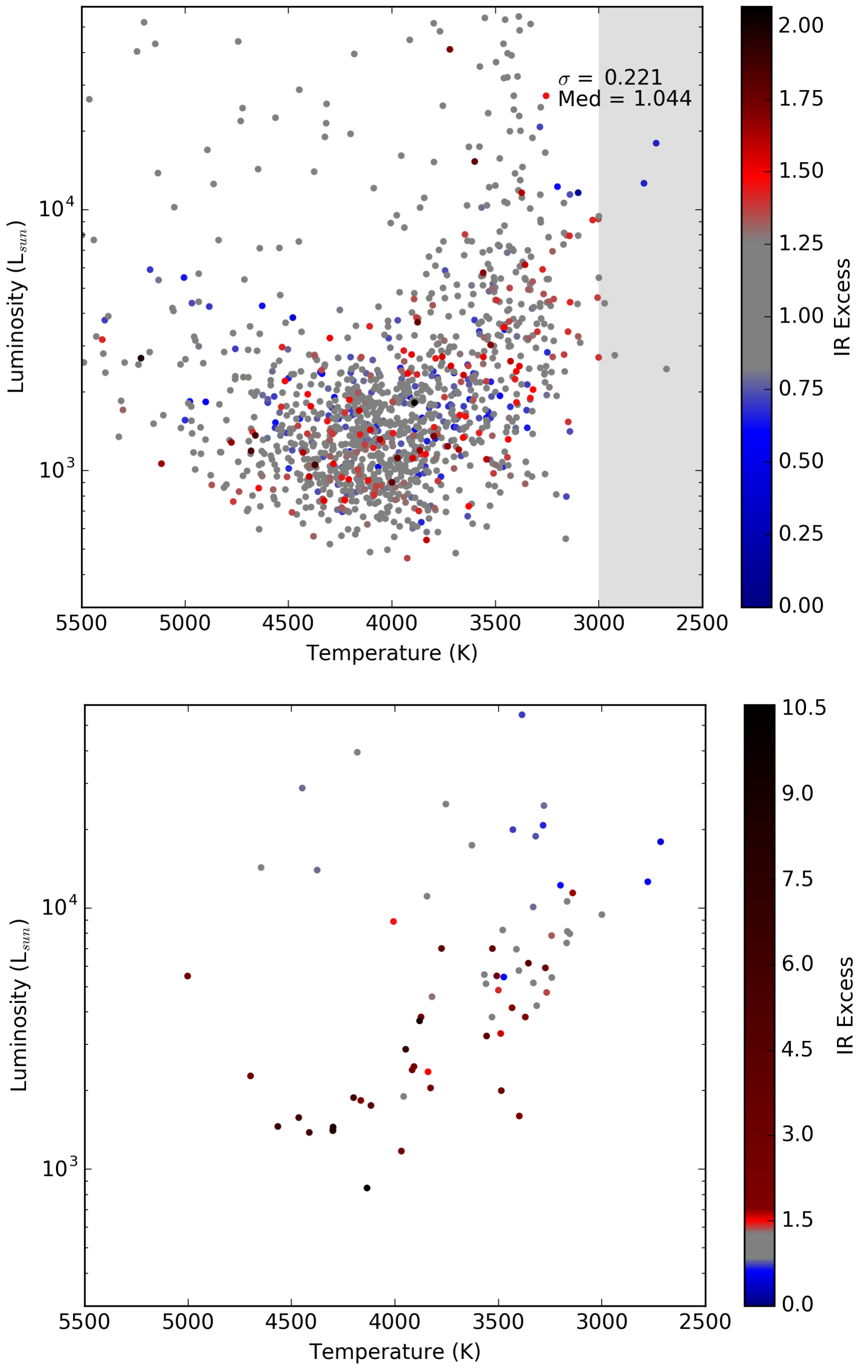

Figure 3.24: H–R diagram of the stellar population of Peg DIG, coloured by the IR excess of each point. Regions shaded grey were excluded from the statistical analysis of this galaxy. Blue objects emit less mid-IR flux than expected, while red objects emit more. *Top*: (a) IR excess calculated from [3.6] and [4.5]. *Bottom*: (b) IR excess calculated from [5.8] and [8.0].

region, also visible in (b). This is hard to verify, however, due to the natural scatter and high σ. The optical data may be the cause of this, as it is from an all-sky survey, so lacks depth. Another possibility is the asymmetry in the scatter of low-confidence *Spitzer* objects. $5\sigma_{Spitzer}$ objects recorded as $4\sigma_{Spitzer}$ objects will not be included, but $4\sigma_{Spitzer}$ recorded as $5\sigma_{Spitzer}$ will be, causing a systematic bias.

3.2.6 WLM

Figure 3.25 (a) shows that there is significant scatter of the IR excess for this galaxy, meaning it is not possible to determine the presence of dusty AGB candidates from this data. The position of the median demonstrates the problems with this photometry. There appears to be more blue than red points towards the region where dusty AGB stars would be expected, also visible in (b). Some of these may have been foreground objects, although when combined with the high value of σ and the scatter in the RGB, they imply that there is a problem with the photometry. This may be in part due to the Massey et al. (2007) photometry, discussed in more detail in Section 3.2.8. Alternatively, it may be related to the clear photometric cut-off.

3.2.7 LGS 3

The lack of SED-fit objects, and broad distribution of T and L for LGS 3 makes it difficult to discern much detail from Figure 3.26 (a) and (b). There are several red points in the region where dusty AGB stars would be present, but amongst a scatter of grey and blue points. Their excess is not visible in (b). The high σ shows the unreliability of this data. Similarly to Peg DIG, this is likely caused by the fact that optical data originates from a comparatively shallow all-sky survey.

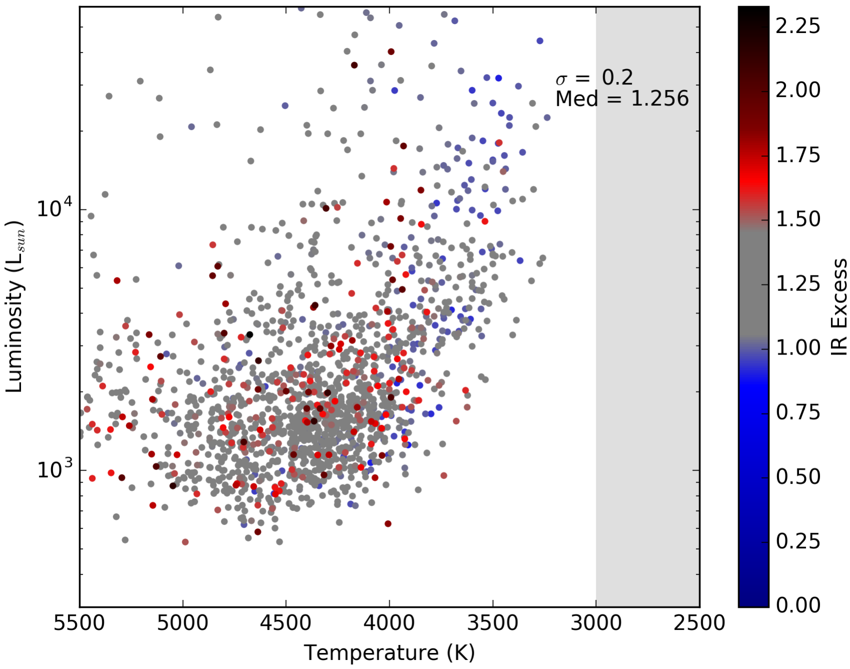

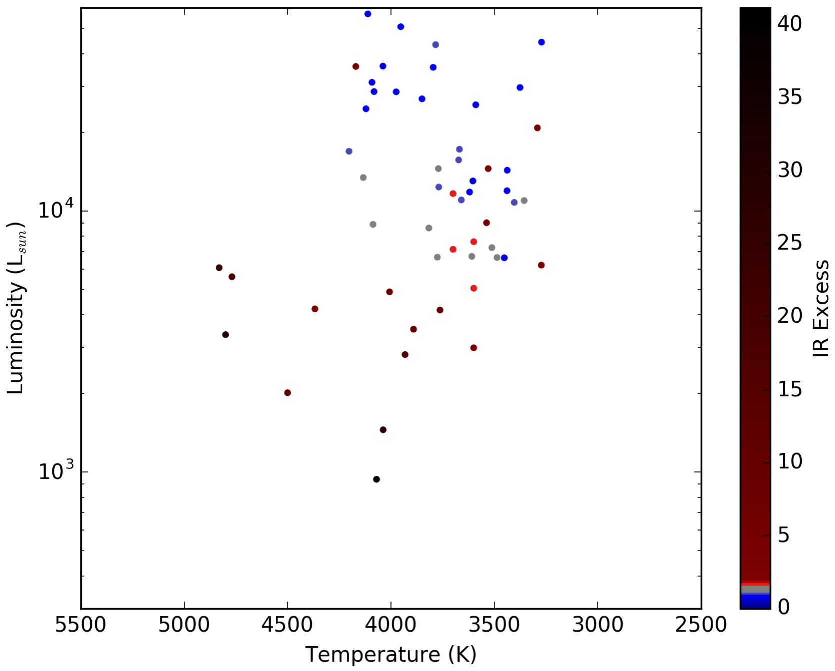

Figure 3.25: H–R diagram of the stellar population of WLM, coloured by the IR excess of each point. Regions shaded grey were excluded from the statistical analysis of this galaxy. Blue objects emit less mid-IR flux than expected, while red objects emit more. *Top*: (a) IR excess calculated from [3.6] and [4.5]. *Bottom*: (b) IR excess calculated from [5.8] and [8.0].

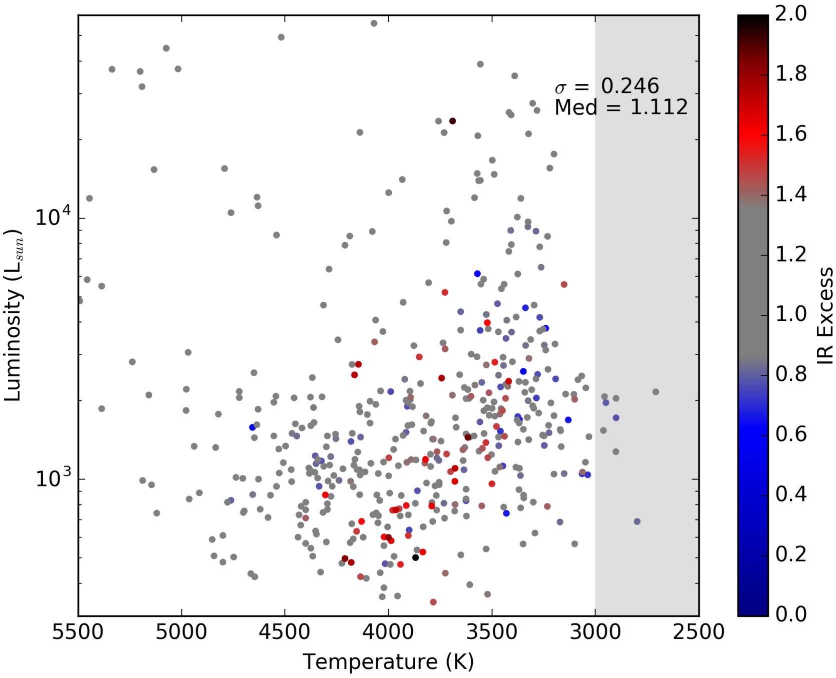

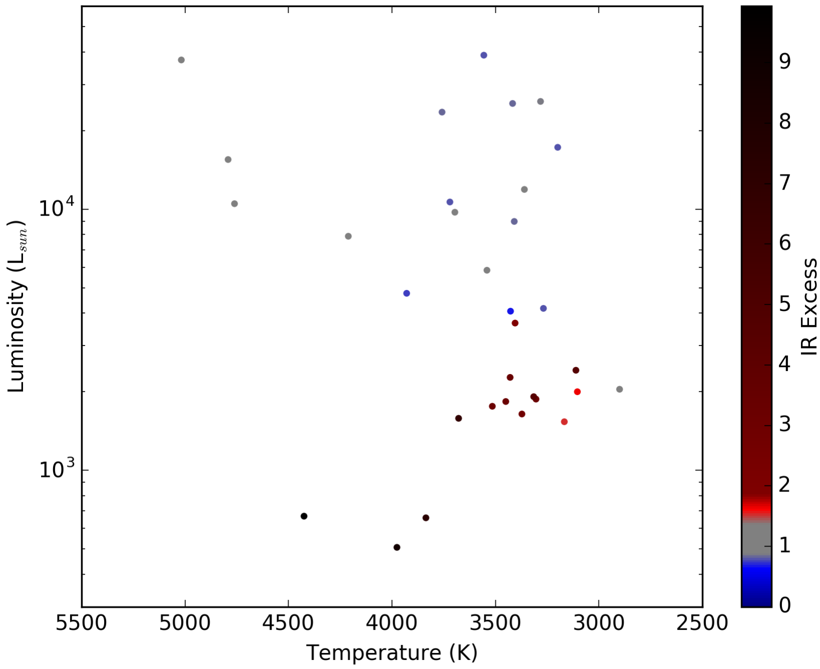

Figure 3.26: H–R diagram of the stellar population of LGS 3, coloured by the IR excess of each point. Regions shaded grey were excluded from the statistical analysis of this galaxy. Blue objects emit less mid-IR flux than expected, while red objects emit more. *Top*: (a) IR excess calculated from [3.6] and [4.5]. *Bottom*: (b) IR excess calculated from [5.8] and [8.0].

3.2.8 Phoenix

The first attempt at producing Figure 3.27 used all photometry available for Phoenix in Table 2.1. It displayed significant scatter, with $\sigma \sim 0.11$. It was found that when the data from Massey et al. (2007) and VISTA were removed, this scatter diminished considerably (each contributing a factor of ~ 2), to the values displayed in the current version of Figure 3.27. This also raises questions about the reliability of the Massey et al. (2007) photometry, and the affect this may have had on the calculated IR excess of other galaxies. This was perhaps caused by the relatively poor seeing quality in the images.

Due to the tight fit the stars in Phoenix showed in T and L, the IR excess of the RGB tip remains well-constrained. As Figure 3.27 shows, σ remains fairly low in this galaxy, suggesting that the red points in the dusty AGB region are significant. The position of the median reinforces the quality of the photometry, and the reliability of the data. Phoenix appears to have very few luminous, dusty AGB stars compared to other galaxies in the sample, with only a few objects with a demonstrable IR excess in both (a) and (b) above 2000 $L_\odot$. This is likely due to the low mass of the galaxy (McConnachie 2012). There are a significant number of red objects in the RGB in (b), some of which are at luminosities lower than expected for a dusty AGB star (McDonald et al. 2012b). This is likely due to poor data collected towards the photometric sensitivity limit.

3.2.9 Leo A

Figure 3.28 shows a grey RGB tip, with a fairly high σ. Leo A may contain a small dusty AGB poopulation, although it is difficult to differentiate it from the remaining background galaxies and natural scatter. This also shows that there is a group of very red objects on the lower right side of the RGB tip, similar to those seen in Sex A and B.

3.2.10 And IX

Figure 3.29 shows little evidence for a dusty AGB population in And IX, possibly due to the reasonably high value of σ, and low number of data points. There is a large amount of scatter over the RGB tip and AGB populations.

3.2.11 NGC 185

NGC 185 has a low value of σ, making it likely that the scatter of red objects at 10^4 $L_\odot$ in Figure 3.30 are at least not a statistical coincidence. There is also a very red population of objects towards the lower right of the diagram, similar to that seen in Sex A and B (which also had low σ). The field of view for this galaxy is very close to the galactic centre, again making it unlikely that these objects are background galaxies.

3.2.12 NGC 147

Similar to NGC 185, NGC 147 has a population of red objects where dusty AGB stars are expected, although there is a smaller population here, and it appears that a number of them have fallen into a local minima for T during SED fitting. Again, the red population is visible in the lower right of the diagram.

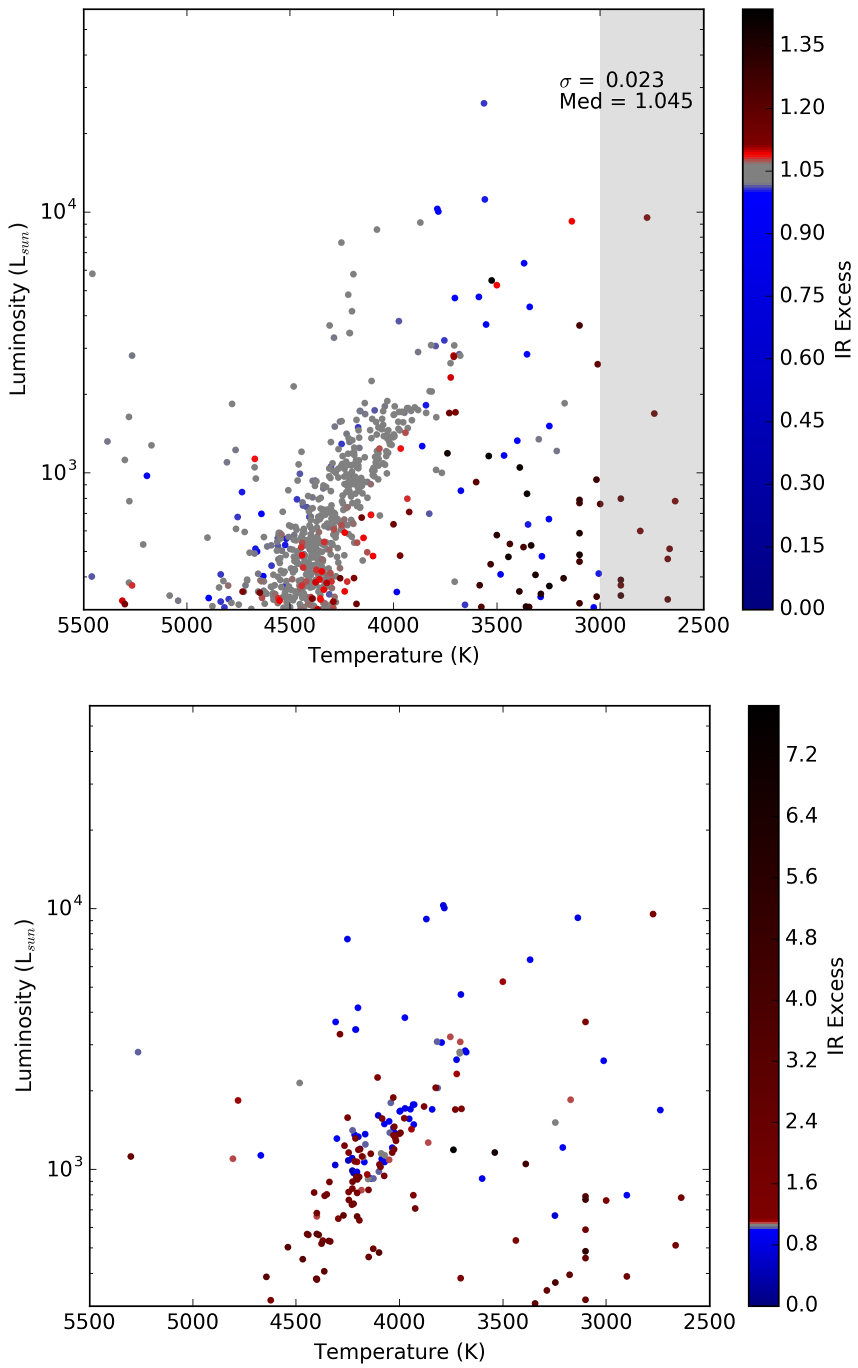

Figure 3.27: H–R diagram of the stellar population of Phoenix, coloured by the IR excess of each point. Regions shaded grey were excluded from the statistical analysis of this galaxy. Blue objects emit less mid-IR flux than expected, while red objects emit more. *Top*: (a) IR excess calculated from [3.6] and [4.5]. *Bottom*: (b) IR excess calculated from [5.8] and [8.0].

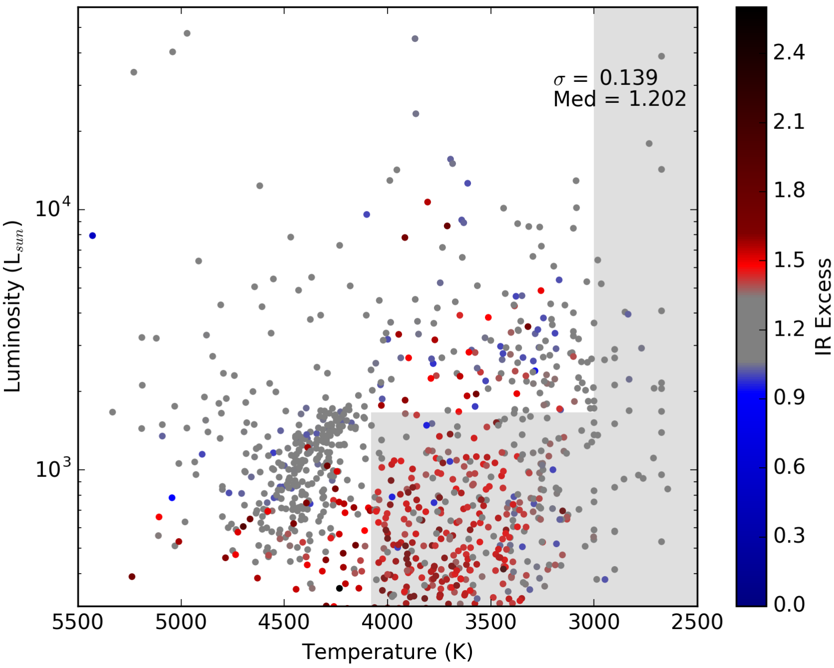

Figure 3.28: H–R diagram of the stellar population of Leo A, coloured by the [3.6] and [4.5] IR excess of each point. Regions shaded grey were excluded from the statistical analysis of this galaxy. Blue objects emit less mid-IR flux than expected, while red objects emit more.

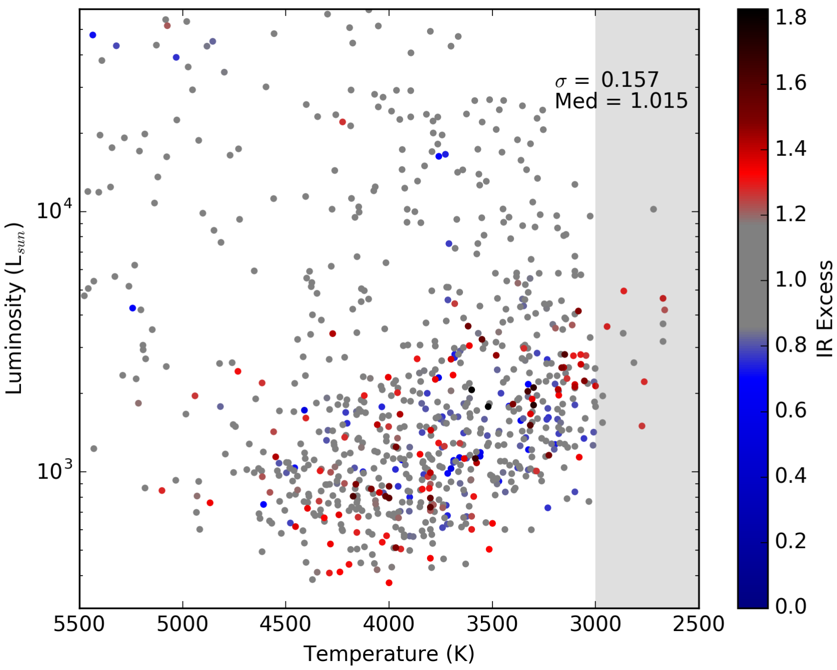

Figure 3.29: H–R diagram of the stellar population of And IX, coloured by the [3.6] and [4.5] IR excess of each point. Regions shaded grey were excluded from the statistical analysis of this galaxy. Blue objects emit less mid-IR flux than expected, while red objects emit more.

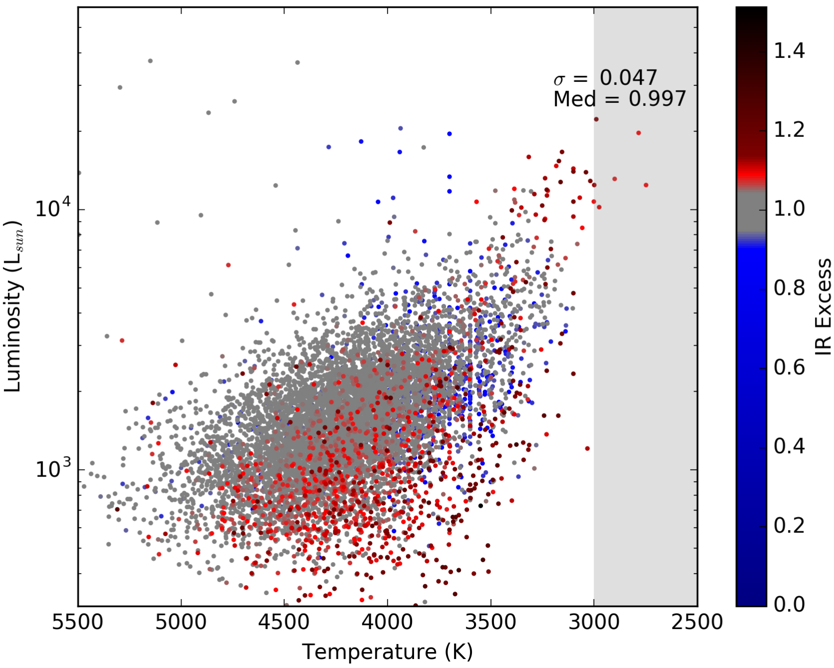

Figure 3.30: H–R diagram of the stellar population of NGC 185, coloured by the [3.6] and [4.5] IR excess of each point. Regions shaded grey were excluded from the statistical analysis of this galaxy. Blue objects emit less mid-IR flux than expected, while red objects emit more.

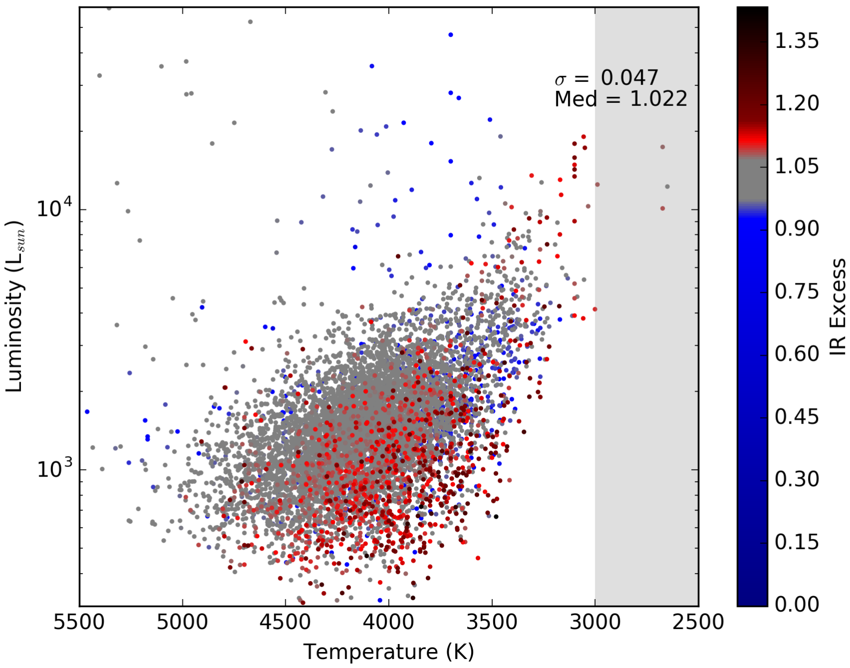

Figure 3.31: H–R diagram of the stellar population of NGC 147, coloured by the [3.6] and [4.5] IR excess of each point. Regions shaded grey were excluded from the statistical analysis of this galaxy. Blue objects emit less mid-IR flux than expected, while red objects emit more.

Chapter 4

Isochrones

In order to verify the reliability of the data that had been compiled and test the accuracy of the parameters used for SED fitting, isochrones were produced and overlaid onto the finalised H–R diagrams from Chapter 2.

4.1 Introduction to isochrones

An isochrone is a snapshot of a stellar population at a given time. A population of stars, all of the same age and with identical metallicities, etc., will vary in their current position on the H–R diagram based on their initial mass. Models compute the temperature and luminosity for a range of masses, producing an isochrone. Examples of isochrones, and how they vary with metallicity and age, can be seen in Figure 4.1.

It can be seen that the younger population reaches a higher MS luminosity and temperature, as in the modern era it has retained more massive stars. The equivalent-mass stars for the older population have already passed the MS, and have likely already become a stellar remnant, leaving less-luminous and cooler stars on its MS. It remains hotter than the equivalent-metallicity 12 Gyr popula-

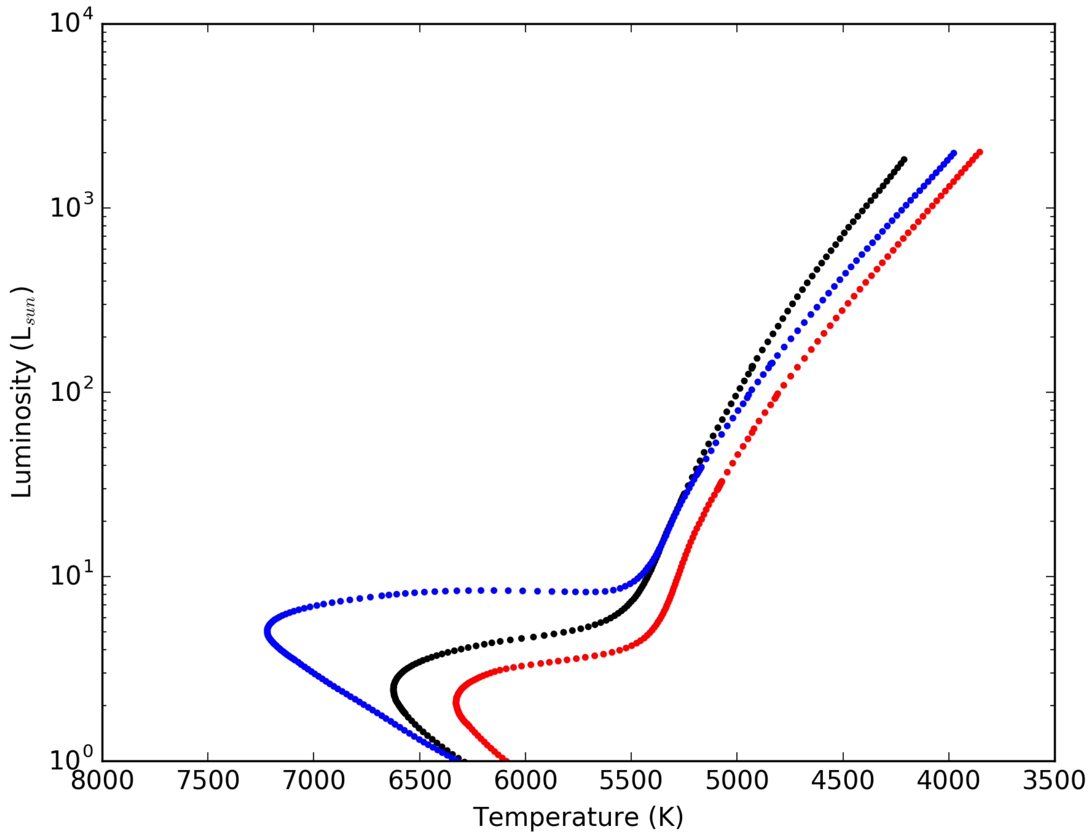

Figure 4.1: An example of three isochrones. The black points represent stars with age 12 Gyr and [Fe/Z] = −2.00 dex, the blue points represent stars with age 5 Gyr and [Fe/Z] = −1.35 dex, and the red points represent stars with age 12 Gyr and [Fe/Z] = −1.35 dex.

tion throughout the RGB. The effects of metallicity can be seen by comparing the two 12 Gyr isochrones. Over the range of luminosities displayed, the metal-poor population is hotter than its counterpart with higher metallicity. This is due to the lower opacity in the stellar atmospheres.

4.2 Selection of an isochrone set

Several sets of isochrones exist, with a comprehensive overview of the advantages and disadvantages of each discussed in McDonald and Zijlstra (2015). The most useful sets for the purposes of this study are the *The Dartmouth stellar evolution database* (Dotter et al. 2008), which allows for variation of [α/Fe] in steps from –0.2 to 0.8 dex, and the PARSEC isochrones from *The Padova database of stellar evolutionary tracks and isochrones* (Bressan et al. 2012), which allows for the fine-tuning of mass-loss rates by adjusting Reimers' η. The ability to change [α/Fe] was considered more important, as metal-poor stars can be significantly α-enhanced compared to solar values, meaning a significant fraction of their overall metallicity is not represented by [Fe/H]. For that reason, the Dartmouth isochrone set was chosen for the analysis of our data.

A disadvantage of the Dartmouth isochrone set is that populations are only modelled up to the RGB tip, and the data in the H–R diagrams from this study tends to be limited to only slightly below this point. However, the overlap in most cases remains sufficient to test the accuracy of the SED fitting and literature parameters. Several isochrone sets continue to model evolution up through the AGB. However, our understanding of the TP-AGB is limited, to the extent that any poor fits to this region could be successfully explained away by a number of possible hypotheses.

4.3 Isochrone fitting

Isochrones were produced for known stellar populations > 1 Gyr old for each galaxy, based on the literature discussed in Section 1.6 and summarised in Table 4.1. The youngest populations were not included as they typically (from the

Dartmouth models) would contain no stars towards the RGB tip in the modern era, so are of no use in this example. These isochrones were then overlaid on the final versions of the H–R diagrams from Section 2.2, allowing for comparisons to be made. The Dartmouth isochrones were produced using cubic interpolation and using helium mass fraction, $Y = 0.245 + \frac{3Z}{2}$.

Table 4.1: A list of parameters used to produce the isochrone fits in this Section. All values are summarised from Section 1.6 and references therein. These literature values were obtained via a variety of methods, and are discussed in detail in the source papers (the typical method is to fit an isochrone to a CMD). Values for [α/Fe] were rounded up to the nearest 0.2 dex, as the input to produce Dartmouth isochrones only allowed steps of this size. Where data was not available, isochrones were fit by eye to the data, assuming that [α/Fe] = 0.4 dex, considered reasonable for metal-poor populations. If a globular cluster is part of the stellar population, the cluster's name is listed.

Galaxy	GC	Age	[Fe/H]	[α/Fe]	Reference
Sex B	—	13	–1.6	0.4	Bellazzini et al. (2014a)
	Unnamed GC	2	–1.35	0.0	Sharina et al. (2007)
Sex A	—	14	–2.2	0.4	Battaglia et al. (2011)
	—	11	–1.4	0.4	Battaglia et al. (2011)
	—	2	–1	0.0	Kaufer et al. (2004)
IC 1613	—	10	–2.00	0.4	Cole et al. (1999)
	—	5	-1.35	0.4	Cole et al. (1999)
Sag DIG	—	6	–2.2	0.4	Gullieuszik et al. (2007)
	—	6	–1.6	0.4	This work
Peg DIG	—	3	–1.4	0.4	Gallagher et al. (1998)
WLM	—	10	–2.18	0.4	Dolphin (2000)
	—	8	–1.34	0.4	Dolphin (2000)
	—	6	–1.25	0.4	Dolphin (2000)

Galaxy	GC	Age (Gyr)	[Fe/H]	[α/Fe]	Reference
	—	4	–1.20	0.4	Dolphin (2000)
	—	2	–1.13	0.4	Dolphin (2000)
	WLM GC	13	–1.96	0.4	Larsen et al. (2014)
NGC 6822	—	8	–1.0	0.4	Tolstoy et al. (2001)
	—	2	–0.8	0.4	Tolstoy et al. (2001)
	Hubble-VII	12	–1.14	0.4	Veljanoski et al. (2015)
	SC1	10	–2.00	0.4	Hwang et al. (2014)
	SC2	12	–0.84	0.4	Veljanoski et al. (2015)
	SC3	12	–1.34	0.4	Veljanoski et al. (2015)
	SC4	12	–0.75	0.4	Veljanoski et al. (2015)
	SC6	12	–1.40	0.4	Veljanoski et al. (2015)
	SC7	12	–0.61	0.4	Veljanoski et al. (2015)
LGS 3	—	11.5	–1.5	0.4	Hidalgo et al. (2011)
Phoenix	—	12	–1.37	0.4	Martínez-Delgado et al. (1999b)
	—	8	–1.37	0.4	Martínez-Delgado et al. (1999b)
	—	3	–1.37	0.4	Martínez-Delgado et al. (1999b)
	—	12	–1.85	0.4	Held et al. (1999); Hidalgo et al. (2009)
	—	8	–1.85	0.4	Held et al. (1999); Hidalgo et al. (2009)

Galaxy	GC	Age (Gyr)	[Fe/H]	[α/Fe]	Reference
	—	3	–1.85	0.4	Held et al. (1999); Hidalgo et al. (2009)
Leo A	—	10	–1.4	0.4	Cole et al. (2007)
	—	8	–1.4	0.4	Cole et al. (2007)
	—	8	–1.9	0.4	This work
	—	3	–1.4	0.4	Cole et al. (2007)
And IX	—	12	–2.2	0.4	Collins et al. (2010)
	—	12	–1.4	0.4	This work
NGC 185	—	10	–1.1	0.4	Crnojević et al. (2014)
	FJJI	9	–1.2	0.4	Sharina et al. (2006)
	FJJIII	10	–1.6	0.2	Sharina et al. (2006)
	FJJIV	9	–2.0	0.0	Sharina et al. (2006)
	FJJV	9	–1.5	0.0	Sharina et al. (2006)
	FJJVII	7	–0.8	0.0	Sharina et al. (2006)
	FJJVIII	8	–1.5	0.0	Sharina et al. (2006)
NGC 147	—	10	–0.95	0.4	Crnojević et al. (2014)
	HodgeI	9	–1.2	0.2	Sharina et al. (2006)
	HodgeII	8	–1.8	0.2	Sharina et al. (2006)
	HodgeIII	10	–1.5	0.6	Sharina et al. (2006)

4.3.1 Sextans B

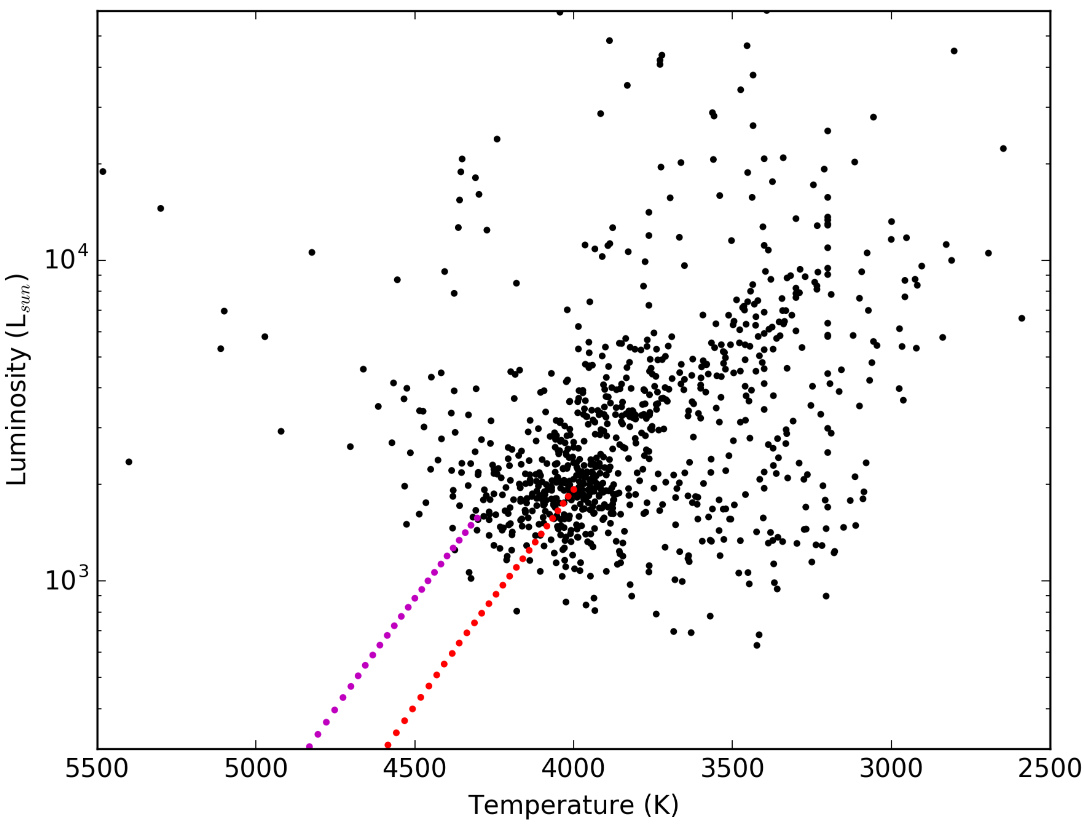

Figure 4.2: H–R diagram and isochrones of the stellar population of Sextans B. Black points are observed objects. The red line is the isochrone of the 13 Gyr population, and the magenta is of the globular cluster.

Although there is only an overlap of $\sim$ 1000 K between the isochrones and observed data (Figure 4.2), it is enough to make several comparisons. It can be seen that the 13 Gyr population is an excellent fit to the data, passing through the centre of the RGB tip and appearing to contain the majority of the stars. The RGB tip extends to a slightly higher luminosity than the isochrone predicts, perhaps due to a slight overestimation of the distance to this galaxy during the SED fitting. This is discussed in more detail in Section 5.1.

The 2 Gyr population fits less well, although there is still a slight overlap with the RGB tip. This is to be expected, as this population only contains a small fraction of the stars in the galaxy. It may also be that the metallicity of this population has been underestimated.

4.3.2 Sextans A

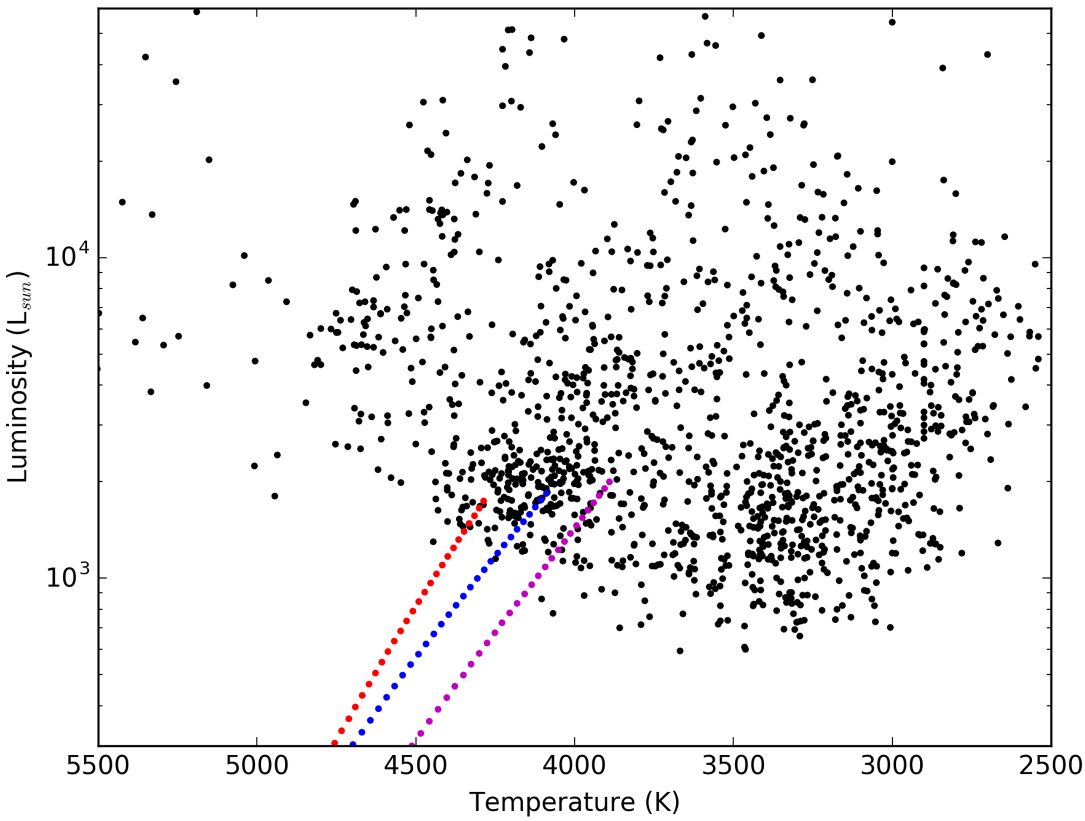

Figure 4.3: H–R diagram and isochrones of the stellar population of Sextans A. Black points are observed objects. The red line is the isochrone of the 14 Gyr population, the magenta is of the 11 Gyr population, and the blue of the 2 Gyr population.

Similar to Sex B, there is only a small overlap of the RGB tip and isochrones in luminosity (Figure 4.3). The 14 Gyr and 2 Gyr populations appear well fit, with the 11 Gyr population (the underlying population of the galactic centre) slightly cooler than the RGB tip. This could be due to an overestimation of the average metallicity of the galactic centre. Again, from the position of the RGB tip there may have been a small overestimation of the distance to Sex A.

4.3.3 IC 1613

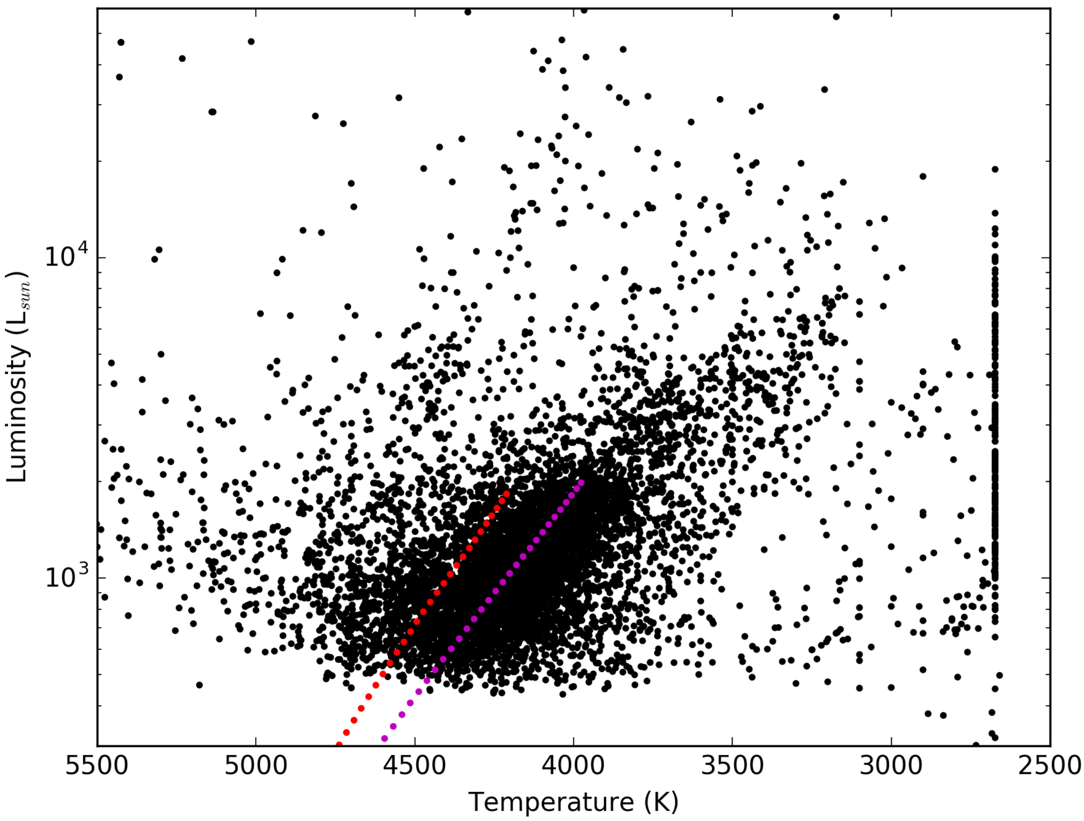

Figure 4.4: H–R diagram and isochrones of the stellar population of IC 1613. Black points are observed objects. The red line is the isochrone of the 12 Gyr population, and the magenta is of the 5 Gyr population.

There is an excellent fit between the isochrones and observed data for IC 1613, in Figure 4.4. The 5 Gyr population is almost perfectly fit in both temperature and luminosity through the centre of the RGB. The 12 Gyr isochrone fits well, considering the small population it represents (Cole et al. 1999). There appears to be a good constraint on distance as the isochrones end very close to the peak of the RGB tip.

4.3.4 Sag DIG

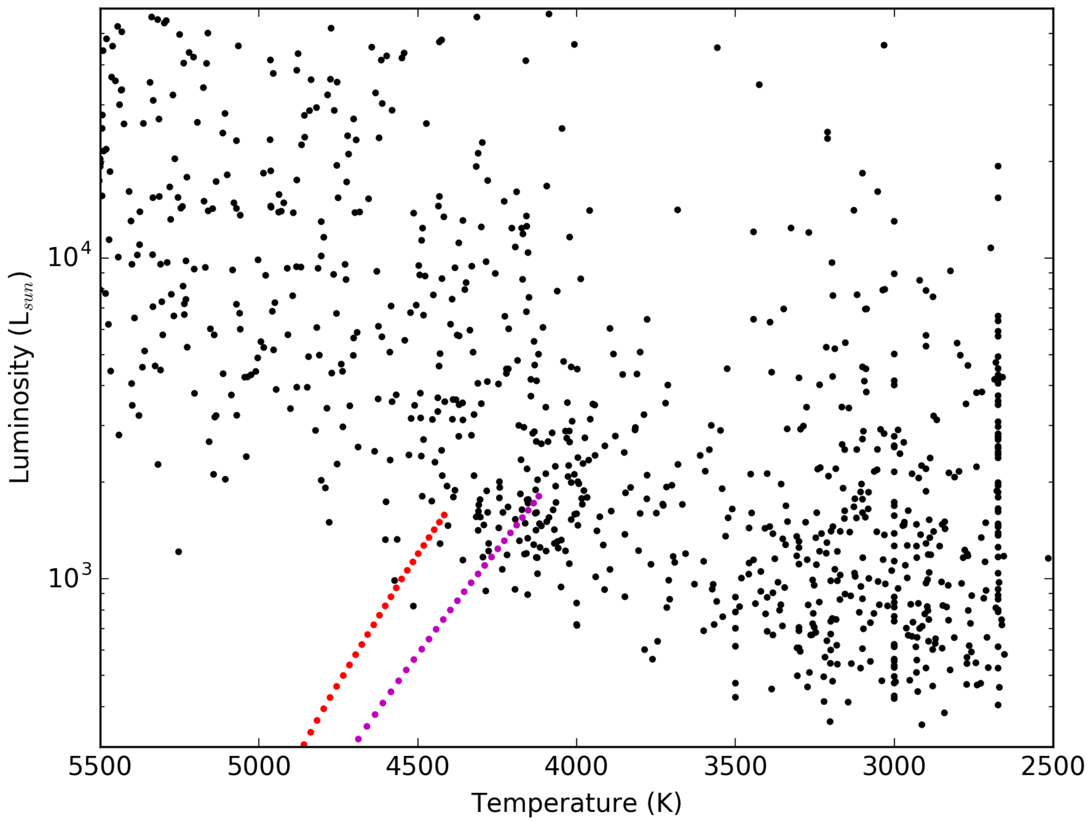

Figure 4.5: H–R diagram and isochrones of the stellar population of Sag DIG. Black points are observed objects. The red line is the isochrone of the 6 Gyr population, while the magenta is that of a 6 Gyr population with [Fe/H] = −1.6 dex and [α/Fe] = 0.4 dex, fit by eye.

Figure 4.5 shows that the 6 Gyr, [Fe/H] = −2.2 dex isochrone, based on data from Gullieuszik et al. (2007), is $\sim$ 300 K hotter than the RGB tip. Increasing the metallicity to [Fe/H] = −1.6 dex produces an isochrone that is a much better fit to the H–R diagram. This is the metallicity estimate for the youngest population of stars in Sag DIG from Gullieuszik et al. (2007). However, due to the very small sample of objects from the RGB, it is difficult to determine if there is any systematic bias towards this temperature, such as those caused by reaching a photometric limit.

4.3.5 Peg DIG

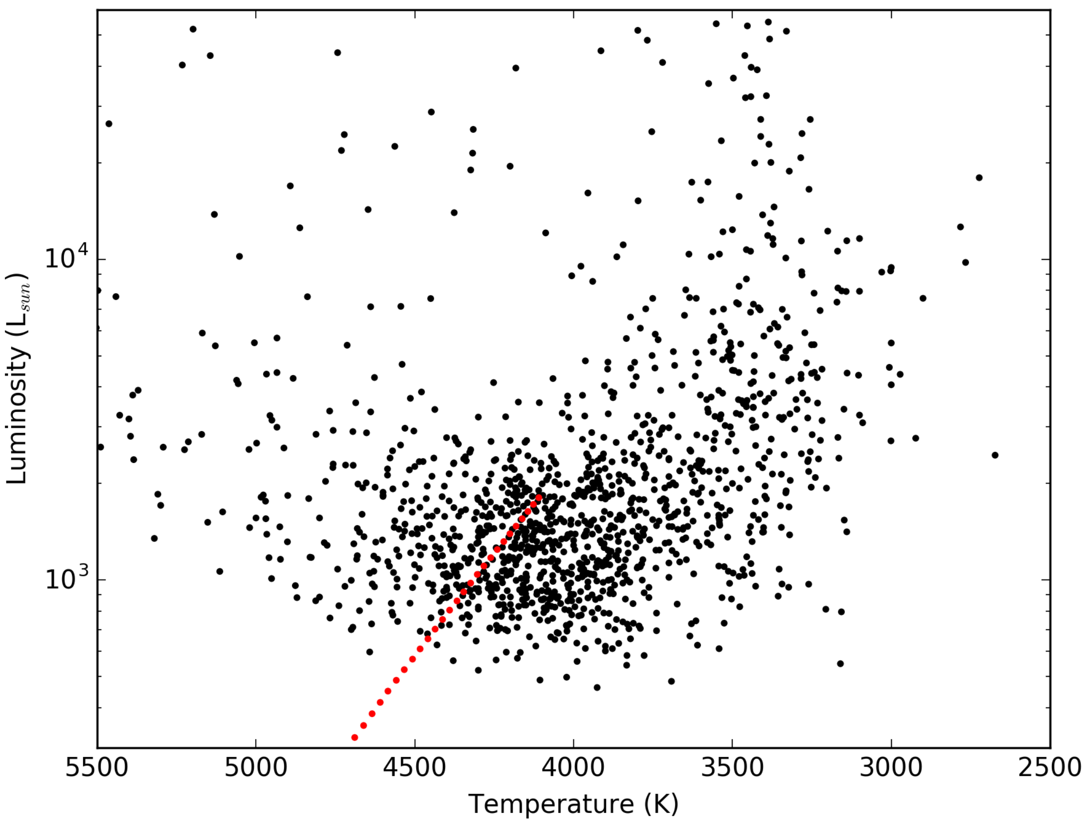

Figure 4.6: H–R diagram and isochrone of the stellar population of Pegasus. Black points are observed objects and the red line is the isochrone of the 3 Gyr population.

Figure 4.6 shows good agreement between observations and the isochrone. The isochrone is slightly hotter than the centre of the RGB tip (perhaps caused by a slight underestimation of metallicity during the assumption made in Section 1.6.5), and peaks at a luminosity ~ 50 $L_\odot$ lower, although is a good fit overall. There is significant scatter in temperature, perhaps indicating a wider range of star-forming epochs than previously expected, or that the photometry is of a low precision or suffers from blending.

4.3.6 WLM

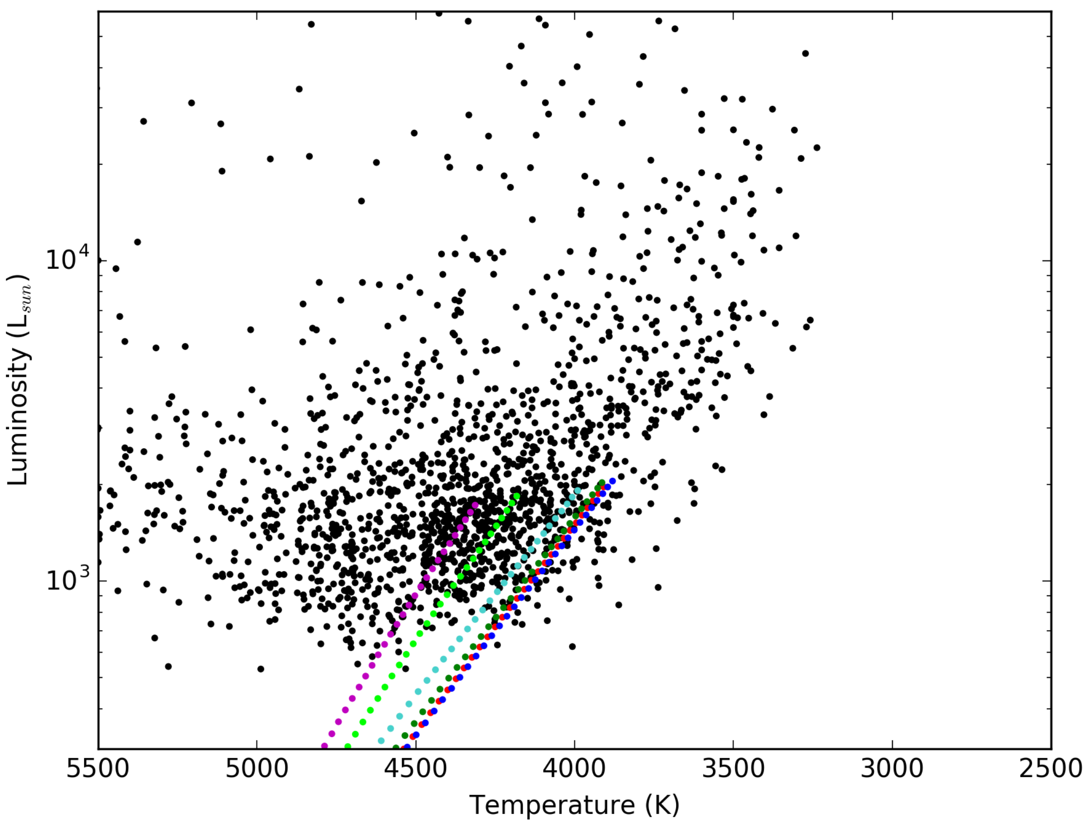

Figure 4.7: H–R diagram and isochrones of the stellar population of WLM. Black points are observed objects. The red line is the isochrone of the 10 Gyr population, the magenta of the 8 Gyr population, the blue of the 6 Gyr population, the green of the 4 Gyr population, the teal of the 2 Gyr population, and the lime of the globular cluster.

Observations of WLM are in good agreement with isochrones (Figure 4.7). In particular, the 8 Gyr and globular cluster isochrones pass close to the centre of the RGB tip, and peak at a very similar luminosity. They also predict the width of the RGB quite well. The remainder of the isochrones lie within the scatter on the cool side of the RGB tip. There are several possible causes of this. It may be that the literature values for [Fe/H] and estimates for [α/Fe] are incorrect. However, these would have to be off by a significant factor to explain the > 100 K offset seen here. Another more likely possibility is that the photometry suffers from completeness issues, suggested by the diagonal cut-off towards the right of the plot. Problems can be caused by an upward bias in the magnitude of detected objects close to the detection limit, which can artificially increase temperatures and luminosities. This would have the effect of shifting the RGB tip to a higher temperature, and increasing scatter at higher temperatures, which can be seen.

4.3.7 NGC 6822

Figure 4.8 shows that while several of the isochrones pass through a portion of the RGB tip, although none pass through its centre. The 2 and 8 Gyr populations, along with the GCs Hubble-VII, SC3, and SC6 are all fit closely together on the cool edge of the RGB tip. The remainder of the GC isochrones are cooler, with the possible exception of SC1 which appears much hotter. The metallicity of SC1 is much lower than that of the other GCs and populations, and was derived by a different method from a different study. For that reason, the position of its isochrone is not of particular concern. The offset seen for the other isochrones may be caused by completeness issues (as a photometric cut-off can be seen), or perhaps due to the lack of mid-IR data for this galaxy.

4.3.8 LGS 3

The scarcity of data points and significant scatter in the H–R diagram of LGS 3 means that it is difficult to conclude much from Figure 4.9. However, the

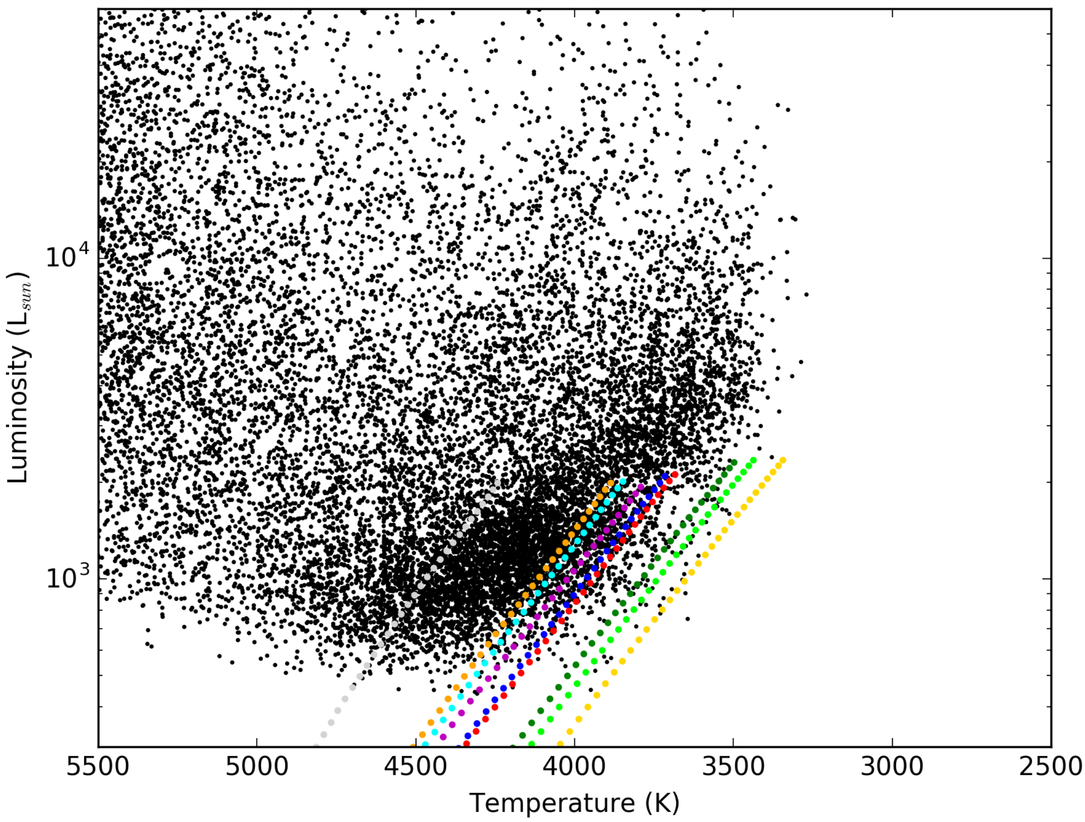

Figure 4.8: H–R diagram and isochrones of the stellar population of NGC 6822. Black points are observed objects. The red line is the isochrone of the 8 Gyr population, the magenta of the 2 Gyr population, the blue of Hubble-VII, the grey of SC1, the green of SC2, the teal of SC3, the lime of SC4, the orange of SC6 and the gold of SC7.

isochrone passes through the centre of the scatter of points that appears to be the RGB tip, and ends around the same luminosity. This suggests that although observations have provided only limited data, the isochrone is a good fit to it.

4.3.9 Phoenix

There are conflicting values of [Fe/H] for Phoenix, as discussed in Section 1.6.9. A value of –1.37 dex was chosen for the SED fitting; this parameter does not have a large impact on the final temperature. However, [Fe/H] does have a significant

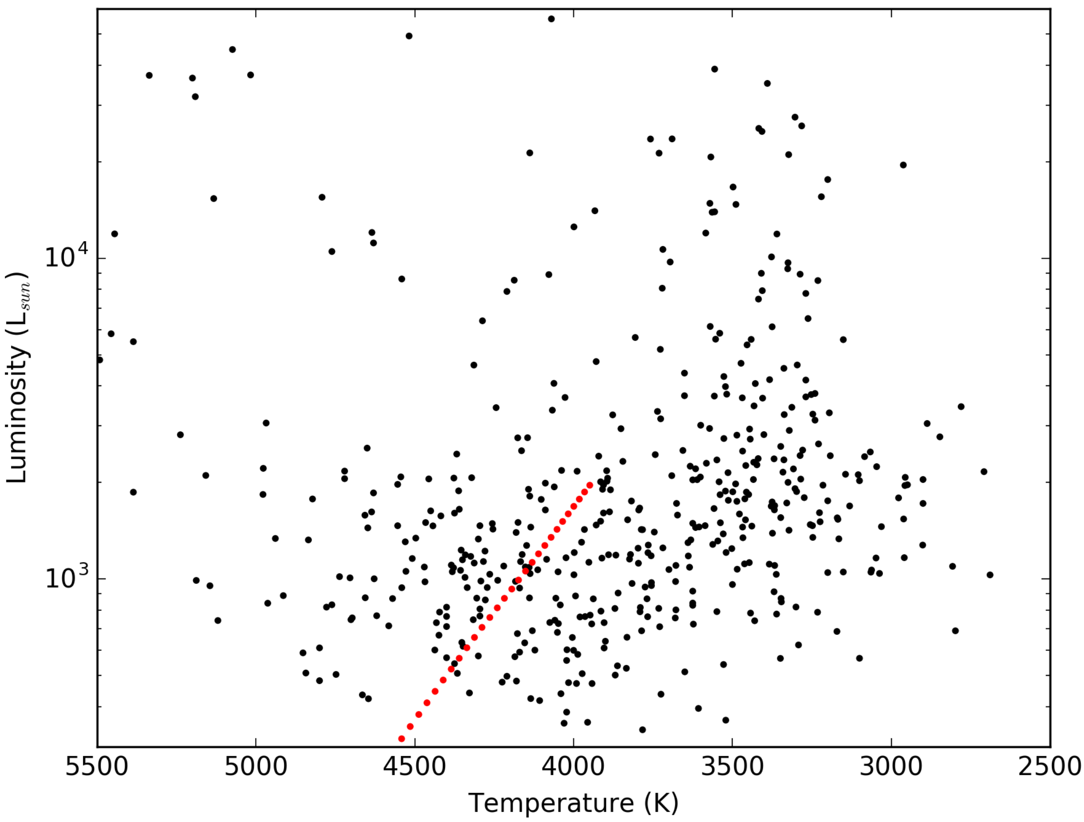

Figure 4.9: H–R diagram and isochrone of the stellar population of LGS 3. Black points are observed objects and the red line is the isochrone of the 11.5 Gyr population.

impact on the temperature of objects in isochrones. At first, the value of –1.85 dex was chosen for the isochrones, in agreement with Held et al. (1999) and Hidalgo et al. (2009). However, these isochrones were found to be $\sim$ 200 K too hot for the RGB (much more of which is visible for this galaxy). Changing the isochrones to [Fe/H] $= -1.37$ dex gave a near perfect fit to the data, agreeing with the RGB in temperature, luminosity, and shape, hence in good agreement with Martínez-Delgado et al. (1999b). The oldest and youngest population isochrones act as constraints to the observed points, which further emphasise the success of the fits. The reliability of the fit begins to break down at $\sim$ 400 $L_{\odot}$, as it is likely

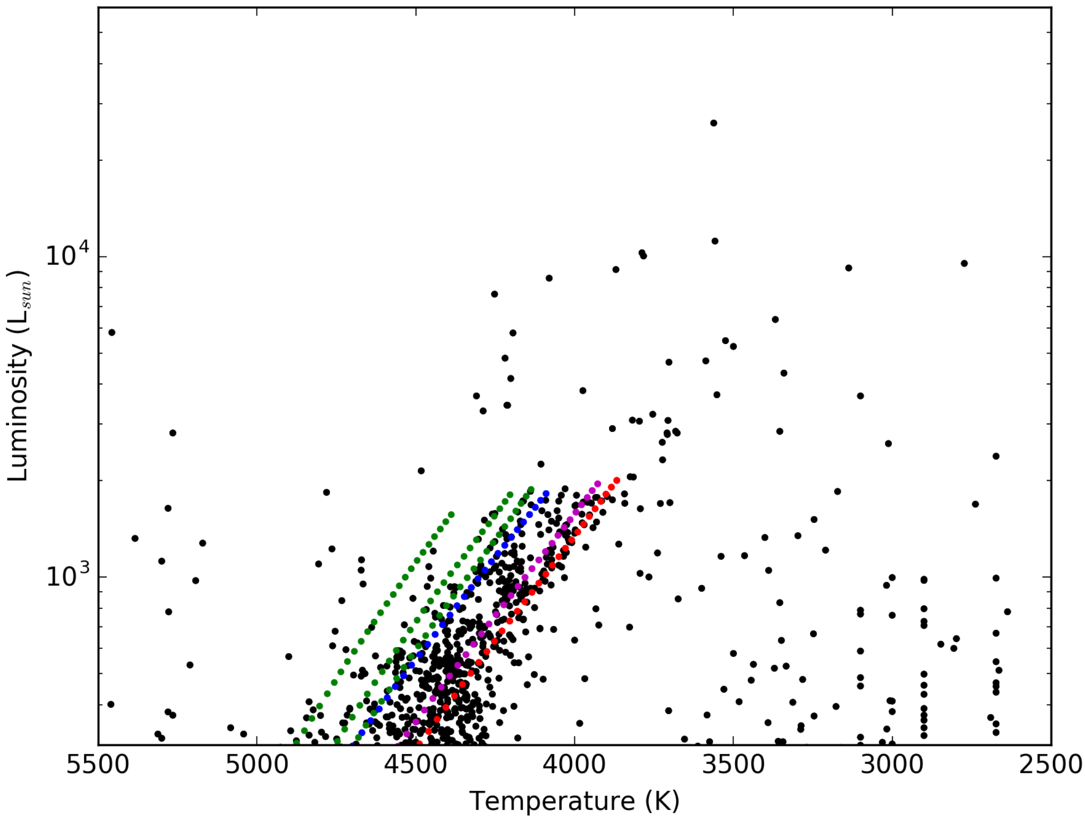

Figure 4.10: H–R diagram of the stellar population of Phoenix, with isochrones using [Fe/H] = −1.37 dex. Black points are observed objects. The red line is the isochrone of the 12 Gyr population, the magenta is of the 8 Gyr population, and the blue is of the 3 Gyr population. Green lines refer to the same age isochrones with [Fe/H] = −1.85 dex.

close to the photometric limit.

4.3.10 Leo A

Figure 4.11 shows that although the 3 Gyr population isochrone is well fit to the H–R diagram, the isochrones of the older populations are cooler than expected. However, all isochrones are of a similar shape and luminosity to the observed RGB tip. The ancient population is tiny (Cole et al. 2007), so the poor fit is not surprising. When performing the SED fitting, it had been assumed that

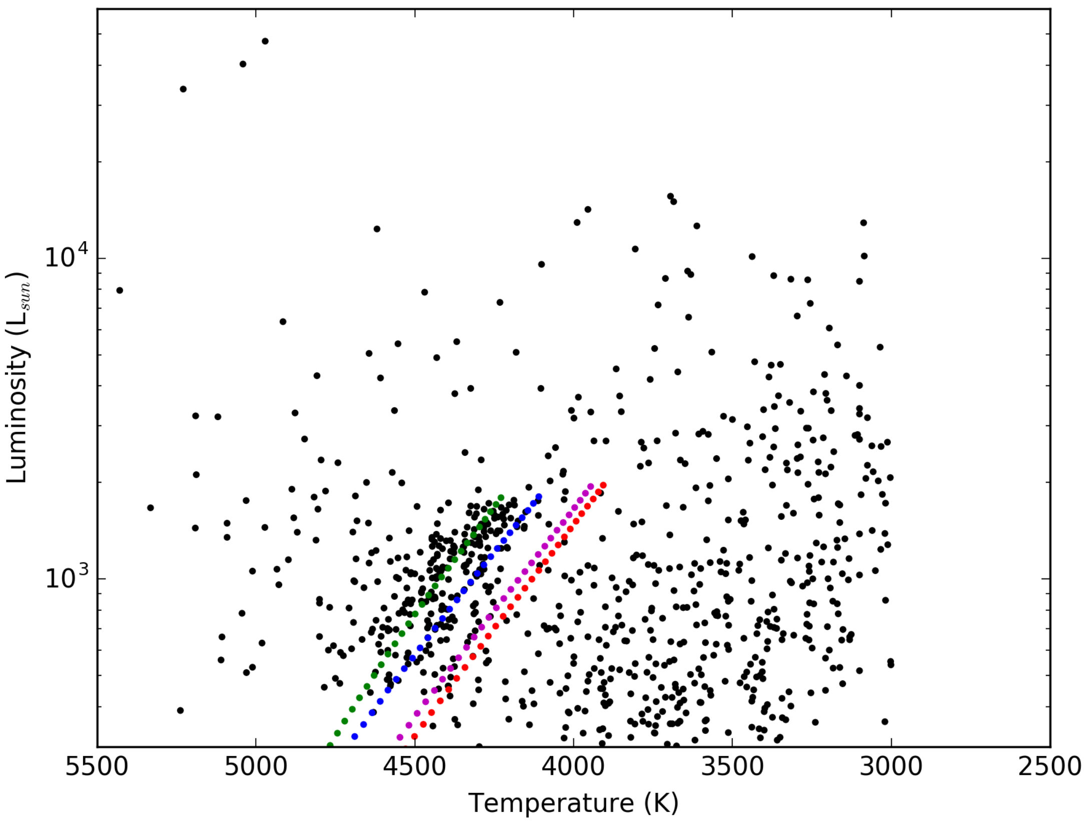

Figure 4.11: H–R diagram and isochrones of the stellar population of Leo A. Black points are observed objects. The red line is the isochrone of the 10 Gyr population, the magenta is of the 8 Gyr population, and the blue of the 3 Gyr population. The green line represents an 8 Gyr population with [Fe/H] = −1.9 dex and [α/Fe] = 0.4 dex, fit by eye.

metallicity has not changed significantly over the lifetime of the galaxy (Cole et al. 2007), so the modern value of [Fe/H] = −1.4 dex has been used for all isochrones. If this assumption is disregarded, it is found that an 8 Gyr isochrone can be well fit to the H–R diagram if [Fe/H] = −1.9 dex.

4.3.11 And IX

The diffuse and poorly studied And IX galaxy has a poor fit to the isochrone (Figure 4.12). It is difficult to determine exactly where the RGB tip is, although

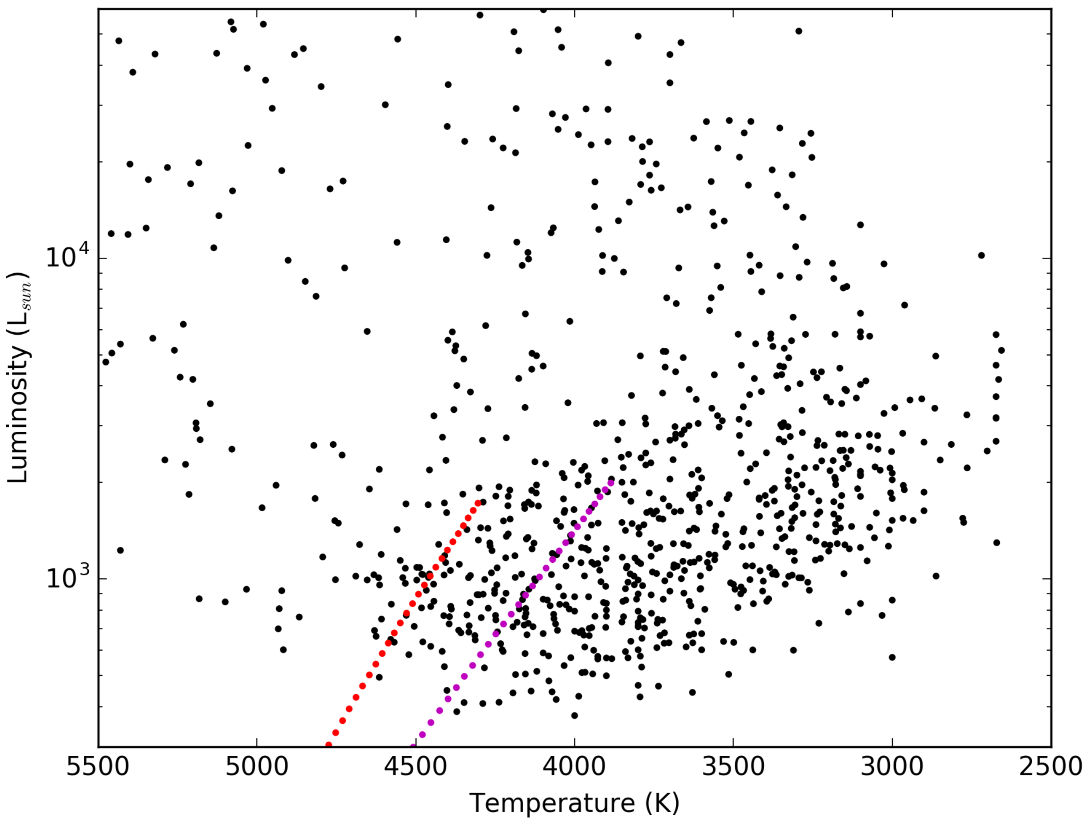

Figure 4.12: H–R diagram and isochrones of the stellar population of And IX. Black points are observed objects. The red line is the isochrone of the 12 Gyr population, and the magenta that of a hypothetical 12 Gyr population with [Fe/H]$= -1.4$ dex and [α/Fe] $= 0.4$ dex, fit by eye.

it is clear that the isochrone is far from its centre. It appears that the metallicity is higher than the literature value of [Fe/H] $= -2.2$ dex (Collins et al. 2010). The magenta line shows an isochrone with identical parameters other than [Fe/H] $= -1.4$ dex, which appears to be a much better fit to the data. The literature value for distance appears to be broadly accurate.

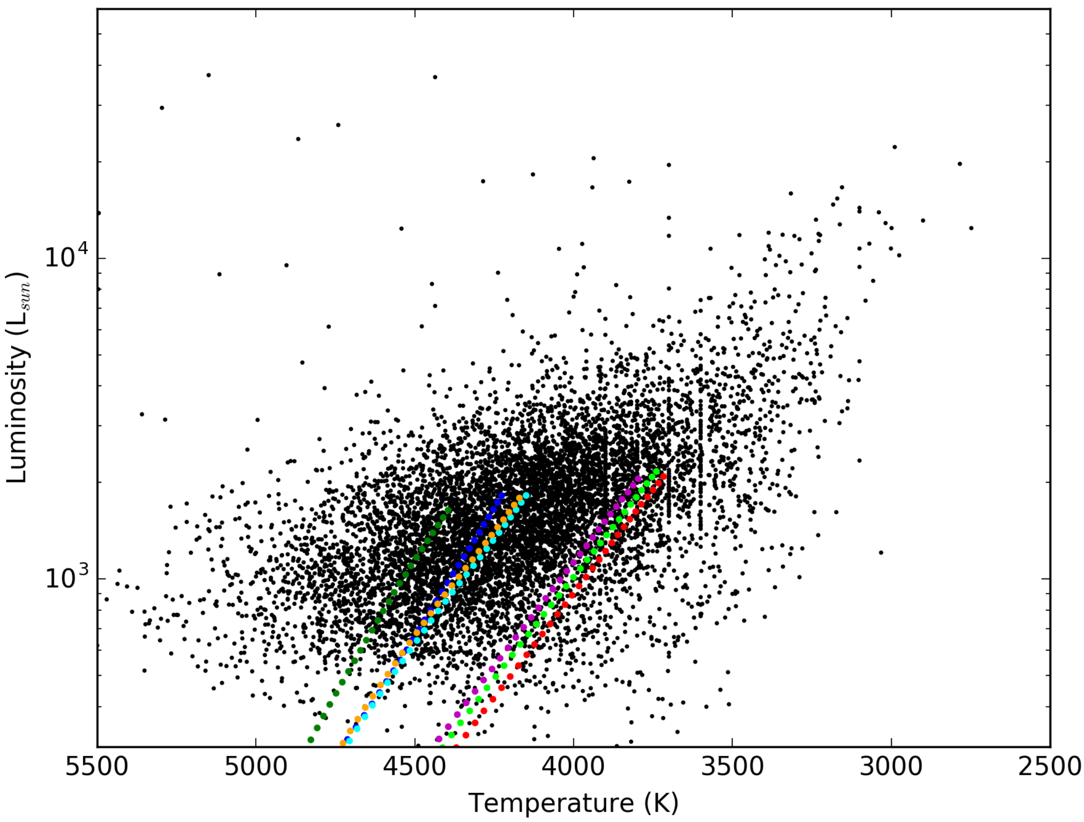

Figure 4.13: H–R diagram and isochrones of the stellar population of NGC 185. Black points are observed objects. The red line is the isochrone of the 10 Gyr population, the magenta of FJJI, the blue of FJJIII, the green of FJJIV, the teal of FJJV, the lime of FJJVII and the orange of FJJVIII.

4.3.12 NGC 185

Figure 4.13 shows that much of the scatter seen in the RGB tip for this galaxy can be explained by multiple stellar populations (indicated by the number of GCs), and their range of ages and metallicities. There may be some completeness issues, however, as the 10 Gyr isochrone, representing the bulk of the stars of the galaxy, appears towards the edge of the RGB tip. However, the lack of scatter (i.e. background galaxies) at lower temperatures may be due to the restricted field of view. It is unclear whether distance has been overestimated, or if the points above the peaks of the isochrones are part of natural scatter. This is discussed further in Section 5.1.

4.3.13 NGC 147

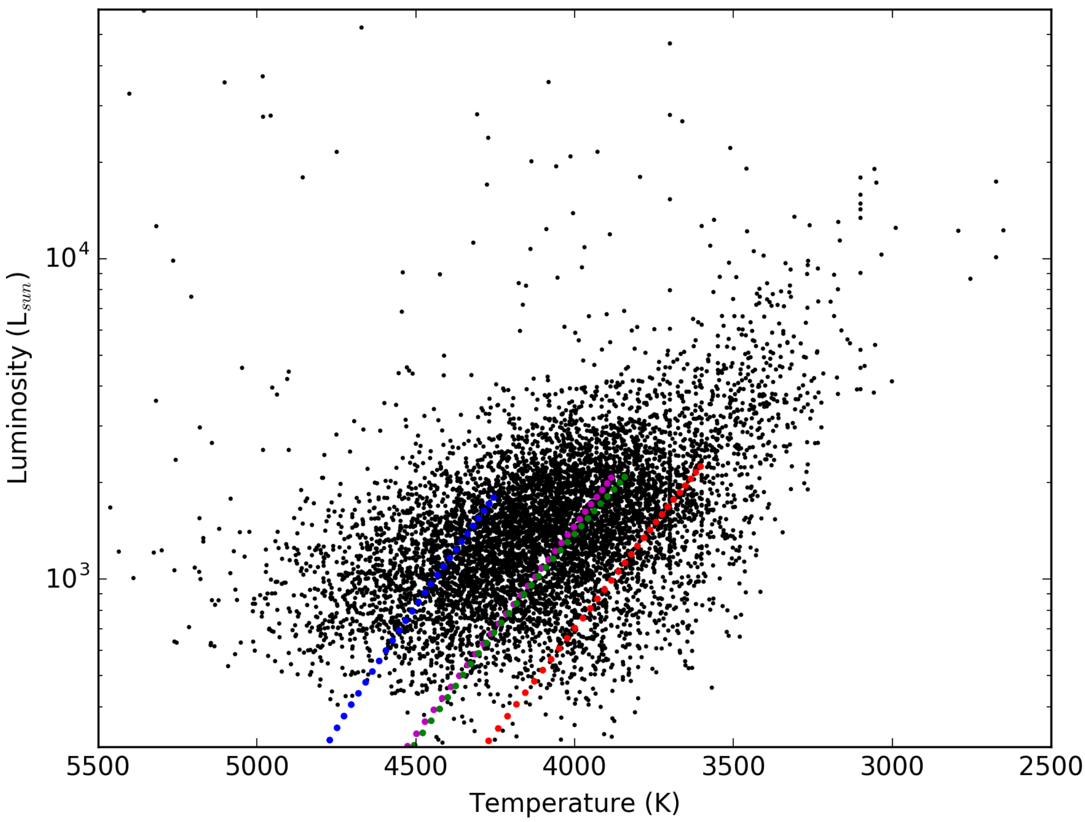

Figure 4.14: H–R diagram and isochrones of the stellar population of NGC 147. Black points are observed objects. The red line is the isochrone of the 10 Gyr population, the magenta of HodgeI, the blue of HodgeII and the green of HodgeIII.

Figure 4.14 shows a very similar plot to NGC 185, as expected due to the similar photometry and histories of the galaxies. The RGB tip appears slightly less broad, likely a consequence of a narrower range of stellar populations, indicated by the reduced number of GCs. Similarly, there appears to be an underestimate of distance.

Chapter 5

Discussion

5.1 Quantification of uncertainties

In order to determine uncertainty in T and L for individual objects in the sample, an analysis was carried out on the RGB tip of each galaxy. A worked example of this process is provided below for IC 1613, as it contains a large number of objects with little variation in the parameters of its population. This is then followed by the results for the remaining 12 galaxies in the sample.

The first step is to determine the maximum luminosity of the RGB tip. A histogram was produced plotting the luminosity of objects in IC 1613, limited to a range of temperatures around the discernible RGB tip in the final H–R diagrams from Section 2.2 (typically $3500 - 5000$ K, although this varied for galaxies with particularly broad or narrow RGB tips). This can be seen in Figure 5.1.

This Figure shows a clear drop in the number of points at ~ 2000 L$_{\odot}$. This is the RGB tip. The point half way along this slope (shown as a solid red line) is chosen to be the upper limit of L, allowing for photometric scatter above and below. In this example, the upper limit, $L_{RGB} = 2000$ L$_{\odot}$ to the nearest 50

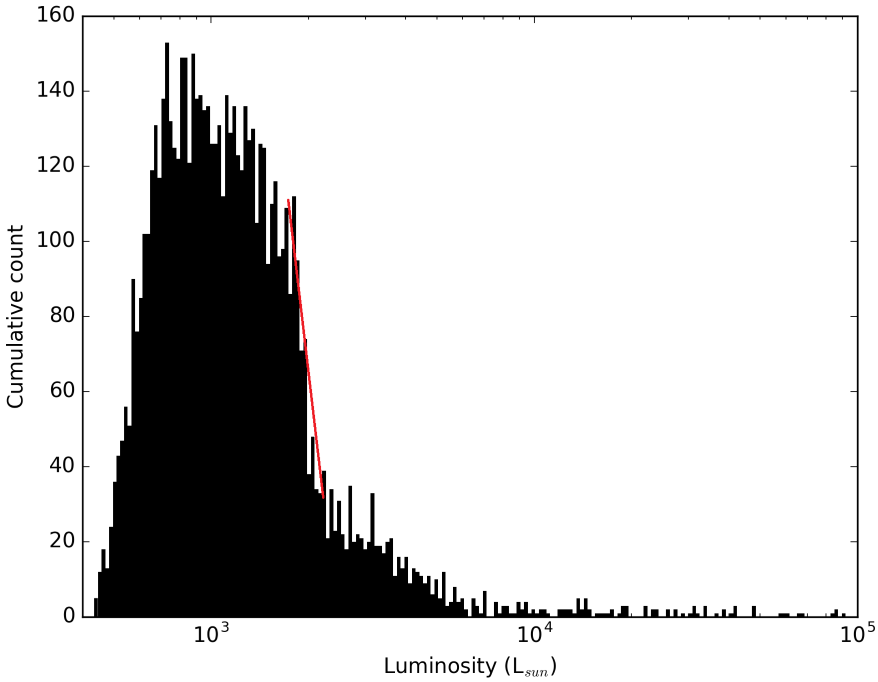

Figure 5.1: A histogram demonstrating the variation in L around the RGB tip in IC 1613. The slope showing the upper luminosity of the RGB tip is approximated in red.

$L_\odot$. Note that L_{RGB} is expected to vary between galaxies, from $\sim$ 1600 $L_\odot$ for the oldest, most metal-poor populations, to $\sim$ 2500 $L_\odot$ for younger, metal-rich populations (Dotter et al. 2008; McDonald et al. 2010b). The effect of [Fe/H] on L_{RGB} and T_{RGB} can be seen in the isochrones in Figure 5.2. L_{RGB} can be predicted with a degree of confidence by stellar isochrones. The isochrone-predicted RGB tip luminosity, L_{iso}, is (in this Section) taken from the most-luminous point of any isochrone on the corresponding Figure in Chapter 4. For IC 1613, the isochrone of the 5 Gyr population (Figure 4.4) predicts $L_{iso} = 1990$ $L_\odot$. This is very similar to the estimate using the method above, implying that our estimate of the distance to this galaxy (755 kpc) is accurate.

The mean temperature of the RGB tip, T_{RGB}, was also estimated by produc-

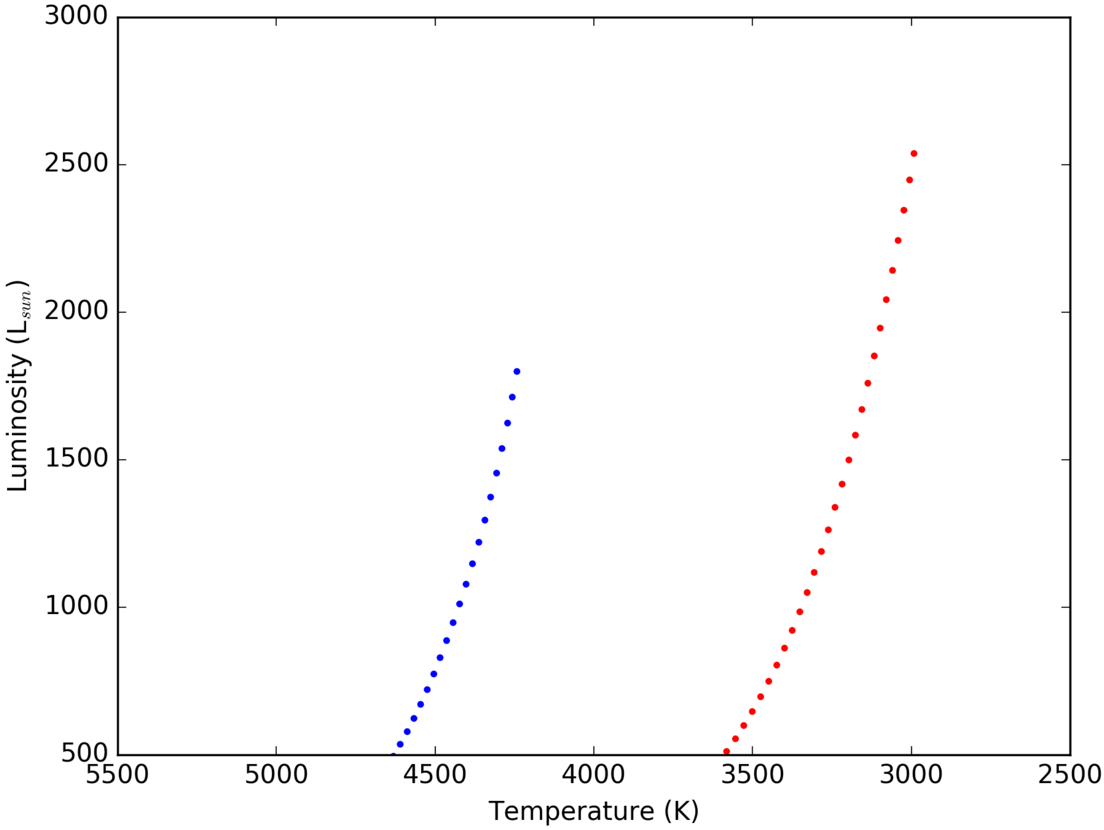

Figure 5.2: An example of two isochrones of age 10 Gyr. The blue points represent a population with [Fe/H] = −2.00 dex, and the red points represent a population with [Fe/H] = 0.00 dex (solar metallicity).

ing a histogram, this time plotting T (in the same temperature range as above) for objects with 1500 $L_{\odot} < L < L_{RGB}$ (Figure 5.3).

T_{RGB} is defined as the central point of the peak, defined by eye. For IC 1613, T_{RGB} = 4000 K, to the nearest 50 K. This compares to 3980 K from the 5 Gyr isochrone (T_{iso}, the temperature of the most-luminous point of the most-luminous isochrone), another successful fit, suggesting that our other input parameters to the SED fitter were correct. The sample of objects shown in Figure 5.3 was also used to estimate the uncertainty in T of an individual star, σ_T. This was calcu-

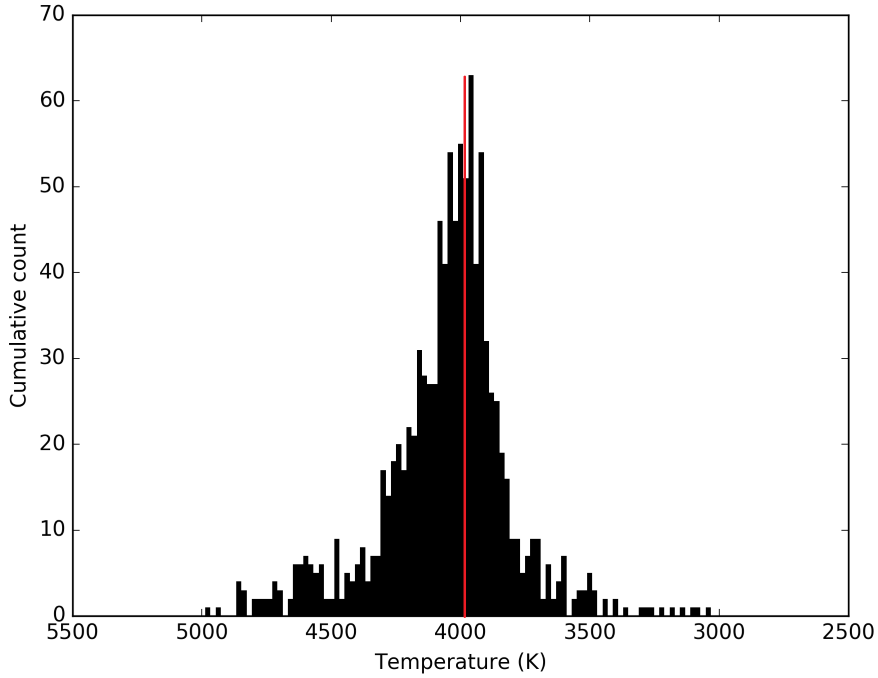

Figure 5.3: A histogram demonstrating the variation in T around the RGB tip. The red line represents the midpoint of the peak.

lated using the same method used to find the deviation in IR excess in Section 3.2. The list of objects were sorted by temperature, and the central 68.3% found. Half of this range between the upper and lower bounds was defined as σ_T. In this example, $\sigma_T = 190$ K. A similar value for the uncertainty of L for an individual star, σ_L, is calculated using $\sigma_L = 4\sigma_T$, as $L \propto T^4$. For IC 1613, $\sigma_L = 760$ L$_\odot$. These values of uncertainty are conservative estimates, since they do not account for any variation in the stellar population of the galaxy.

For the remaining galaxies, L_{RGB} and T_{RGB} are given to the nearest 50 K and 50 L$_\odot$ respectively, unless otherwise stated.

5.1.1 Galaxy parameters and systematic uncertainties

Results from the thirteen galaxies in the sample are presented in Table 5.1. In all cases but WLM, NGC 6822, and Leo A, $T_{RGB} - T_{iso}$ was found to be greater than the reduced σ_L displayed in Figure 5.4, suggesting that one or more parameters used in the SED-fitting process were inaccurate.

Table 5.1: Overview of the temperatures and luminosities of the RGB tips for the sampled dIrrs.

Galaxy	L_{RGB} (L$_\odot$)	T_{RGB} (K)	σ_T (K)	σ_L (L$_\odot$)	L_{iso} (L$_\odot$)	T_{iso} (K)
Sextans B	2300	4000	148	590	1930	4000
Sextans A	2400	4100	194	774	2000	3900-4300
IC 1613	2000	4000	148	590	1990	3980
Sag DIG	2100	4150	246	984	1810	4100
Peg DIG	2300	4000	253	1012	1810	4110
WLM	2100	4200	297	1188	2050	3880-4310
NGC 6822	1600	4100	207	828	2350	3440-3890
LGS 3	1800	4000	402	1608	1960	3950
Phoenix	1600	4100	109	436	2000	3870-4090
Leo A	1800	4200	89	356	1800	4230
And IX	2400	—	—	—	1990	3890
NGC 185	2700	4050	289	154	2160	3720-4400
NGC 147	2350	4050	235	590	2250	3600-4250

As discussed above, L_{RGB} is expected to increase with metallicity. In order to test this, the bulk metallicity of each of the galaxies in the sample (using the values derived in Chapter 4 where necessary) was plotted against the estimated L_{RGB}. This is presented in Figure 5.4. Although [Fe/H] is an input parameter to the SED fitting code, it only has a minimal impact on L, making this a meaningful test.

It can be seen that if we ignore the data point from NGC 6822 ([Fe/H] $= -1.0$ dex, $L_{RGB} = 1600$ L$_\odot$), which is unreliable due to missing mid-IR data, there is a general trend of increasing L_{RGB} with the derived metallicity, agreeing with

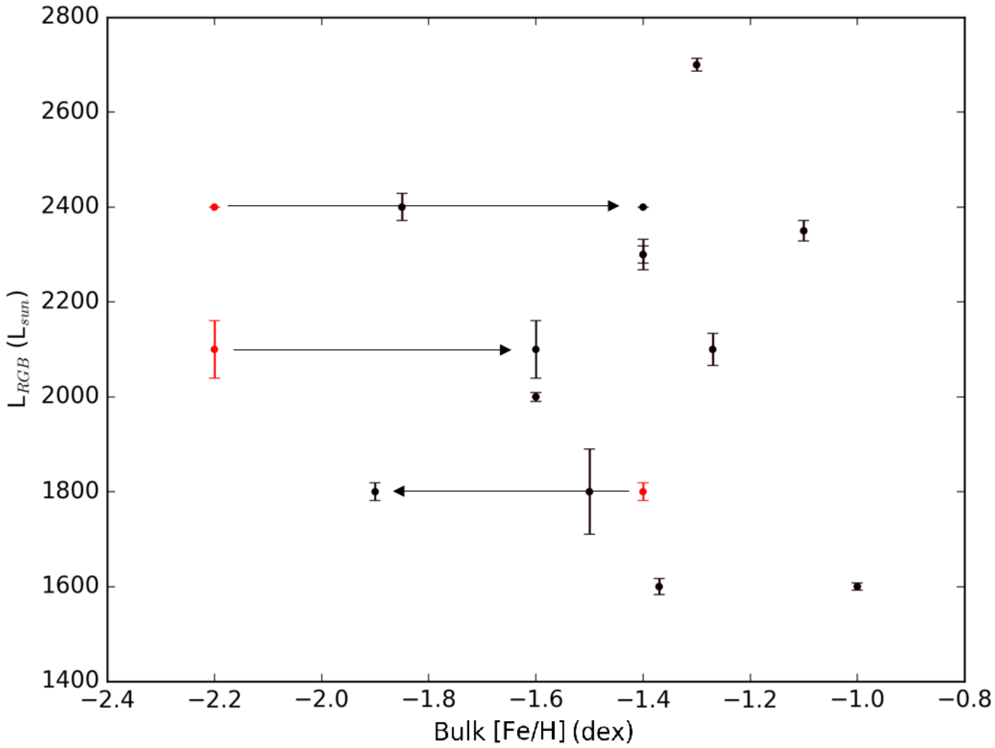

Figure 5.4: Plot relating L_{RGB} for each of the galaxies in this sample to their bulk metallicity, [Fe/H]. Red points indicate literature values of metallicity, and black indicate those either derived in this work or found to be agreement with this study. Arrows indicate which literature values correspond to each newly-derived value. Error bars are calculated using $\sigma_L/\sqrt{N-1}$, where N is the number of points used to calculate σ_L. Error bars are not included for And IX, as σ_L could not be calculated.

the prediction. The fit is much stronger using the three derived values from this study, rather than the literature values, suggesting that those from this work are more accurate. More accurate distance estimates would likely have produced a better fit. An exception to this trend is the data point for Sextans A (–1.85 dex, 2400 $L_{\odot}$). This suggests that the literature value of distance for this galaxy, or the value of [Fe/H] is lower than expected. Other possibilities are a global problem with the photometry, or an over-estimation of reddening. Issues were also encountered when attempting to fit the temperature of the isochrone of the underlying stellar population of this galaxy, although this suggests there had been

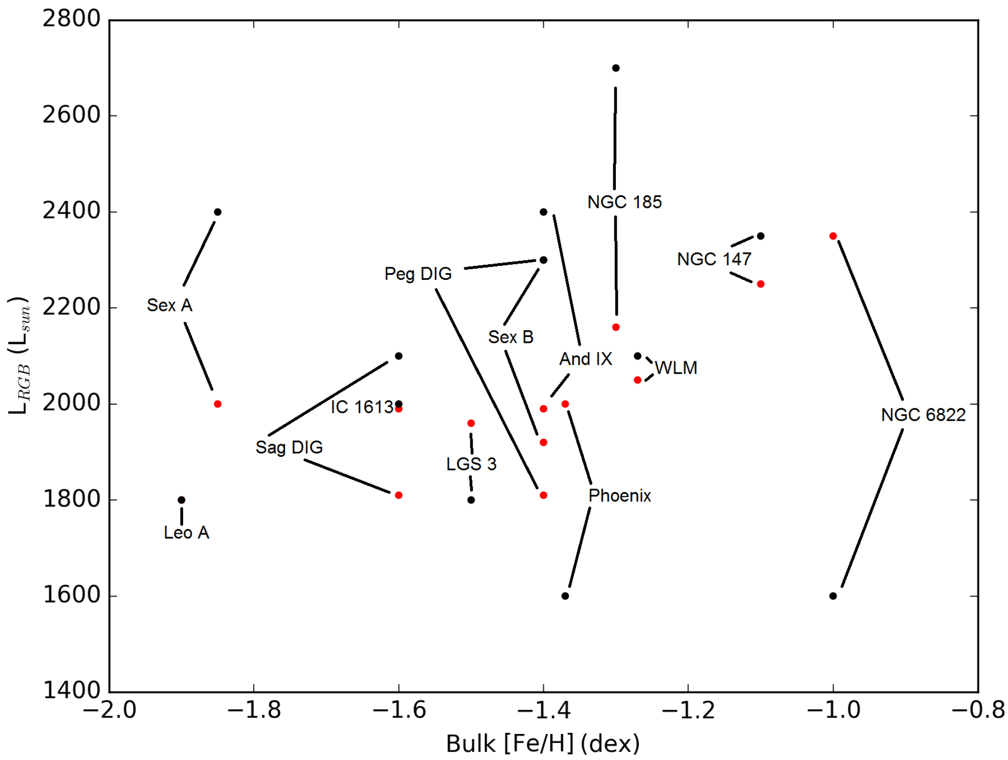

Figure 5.5: Comparison of SED-derived (black) and theoretically-derived (red) RGB tip luminosities. Error bars are not included as they could not be estimated for the isochrone-derived values. The SED-derived L_{RGB} for Leo A matched with its isochrone-derived value perfectly, so there is only one data point for that galaxy. There are two points at –1.4 dex, 2300 $L_{\odot}$. These are estimates of the SED-derived L_{RGB} for Sextans B and Peg DIG.

an over-estimation of metallicity (Section 4.3.2).

For comparison, the same plot was produced including the isochrone-derived values (Figure 5.5). It can be seen that there appears to be an overestimation of the SED-derived RGB tip luminosity of several galaxies. This is most likley due to an overestimation of the distance to these galaxies, and this is assumed in the remainder of this work. However, it is possible that there is some difference in the evolution of metal-poor stars that the models do not account for, which may cause this effect.

5.1.2 Systematic uncertainties

In addition to the uncertainties provided above, there are also systematic uncertainties affecting T and L. These are caused by uncertainties in the SED-fitting process and model atmospheres. An exact numerical estimate of these values is difficult to quantify, but previous studies have suggested that these will be significantly smaller than σ_T and σ_L, which have been caused by photometric uncertainties (McDonald et al. 2009). Additionally, systematic errors will be caused by inaccurate input values of distance, interstellar reddening, and metallicity to the SED fitter, which will impact SED-fit values of L and T.

NGC 6822 likely experiences additional systematic errors. Due to the lack of mid-IR photometry for this galaxy, it seems probable that temperatures and luminosities of the stars within it have been systematically decreased and increased respectively compared to other galaxies in this sample. This can be seen by the comparison of the estimates of T_{RGB} and L_{RGB} with those of the isochrones. This could be caused by poor modelling in H, leading to difficulties in modelling K, the only point in the Rayleigh–Jeans tail for many objects in this galaxy (Section 5.2).

5.1.3 Sextans B

The 13 Gyr isochrone (representing the bulk of stars in the galaxy) predicts a luminosity of 1930 $L_\odot$, suggesting that our assumed distance (1426 kpc) is an overestimate. Using $L \propto d^2$, we can calculate that for $L_{RGB} = 1930\ L_\odot$, $d \approx 1310$ kpc. The isochrone also predicts $T_{RGB} = 4000$ K, in excellent agreement with observations.

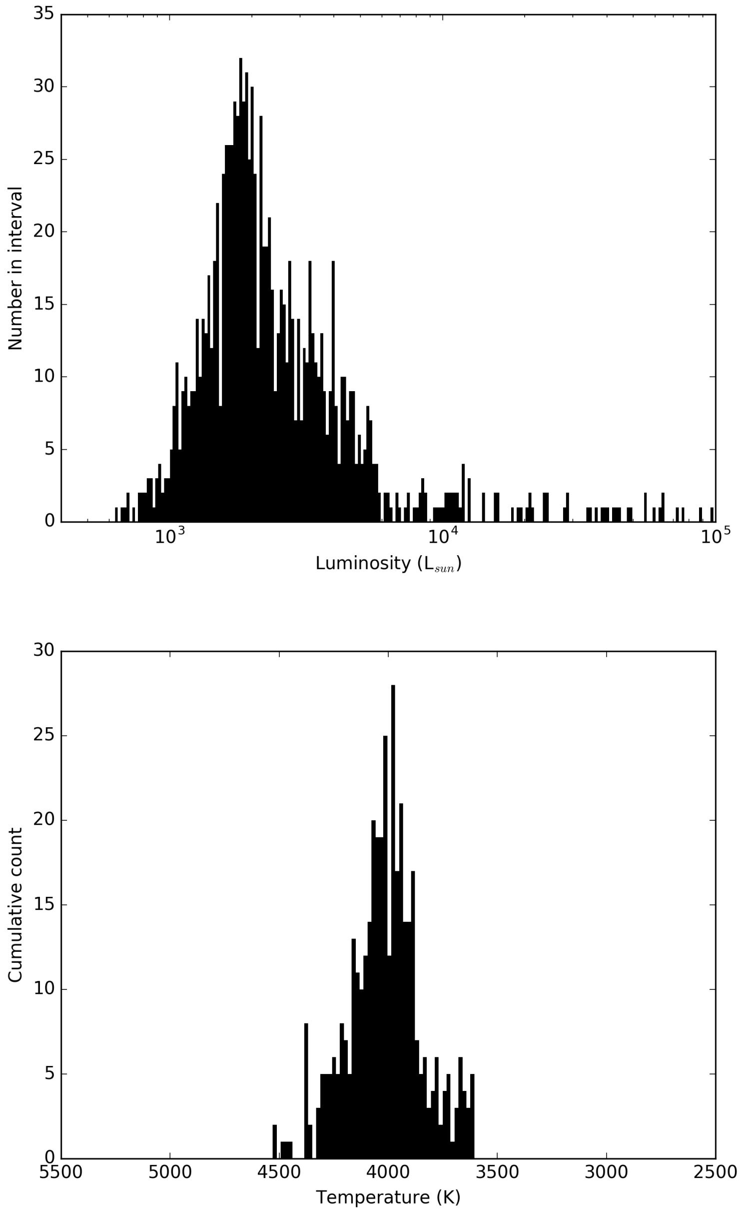

Figure 5.6: (a) Histogram showing the distribution of luminosity for objects in Sextans B at a similar temperature to the RGB tip; (b) Histogram showing the distribution of temperature for objects in Sextans B at a similar luminosity to the RGB tip.

5.1.4 Sextans A

Figure 4.3 shows that the isochrones predict a maximum luminosity of 2000 $L_{\odot}$, suggesting that our assumed distance (1432 kpc) is an overestimate. Using $L \propto$

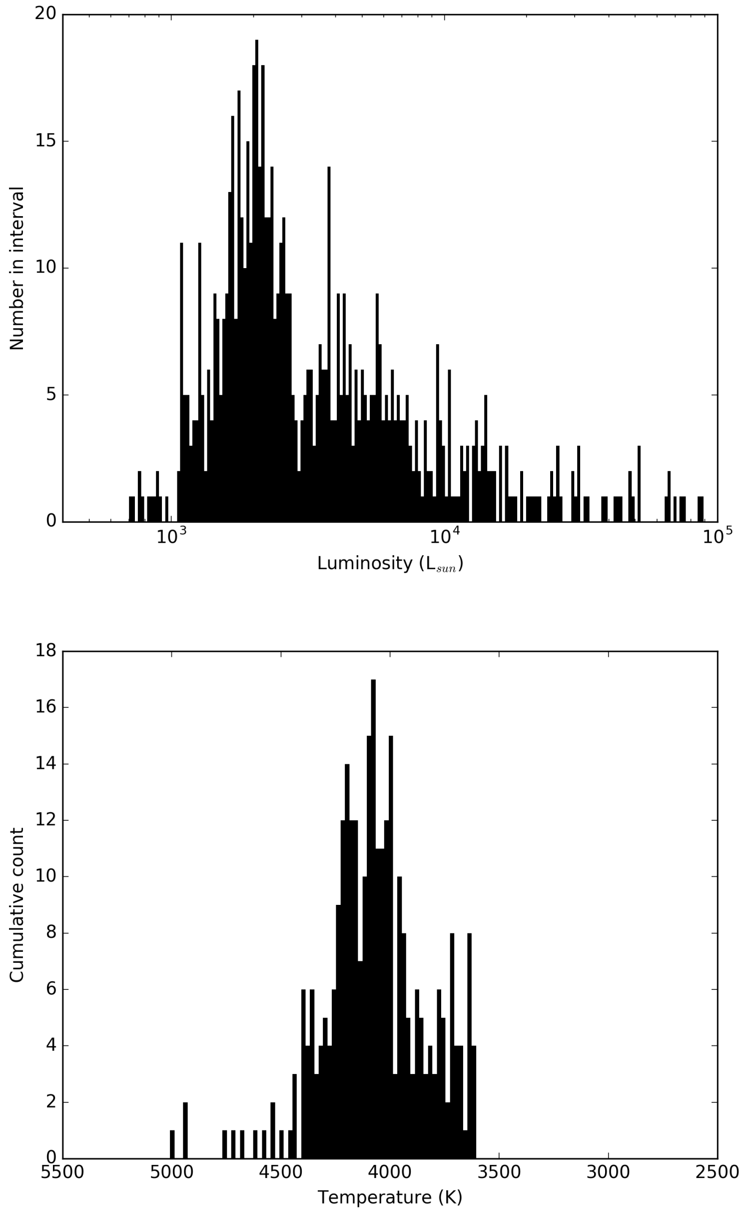

Figure 5.7: (a) Histogram showing the distribution of luminosity for objects in Sextans A at a similar temperature to the RGB tip; (b) Histogram showing the distribution of temperature for objects in Sextans A at a similar luminosity to the RGB tip.

d^2, we can calculate that for $L_{RGB} = 2000$ L$_\odot$, $d \approx 1310$ kpc. The isochrones predict a range of temperatures between 3900 and 4300 K, so the estimate of 4100 K from this method is good.

5.1.5 Sag DIG

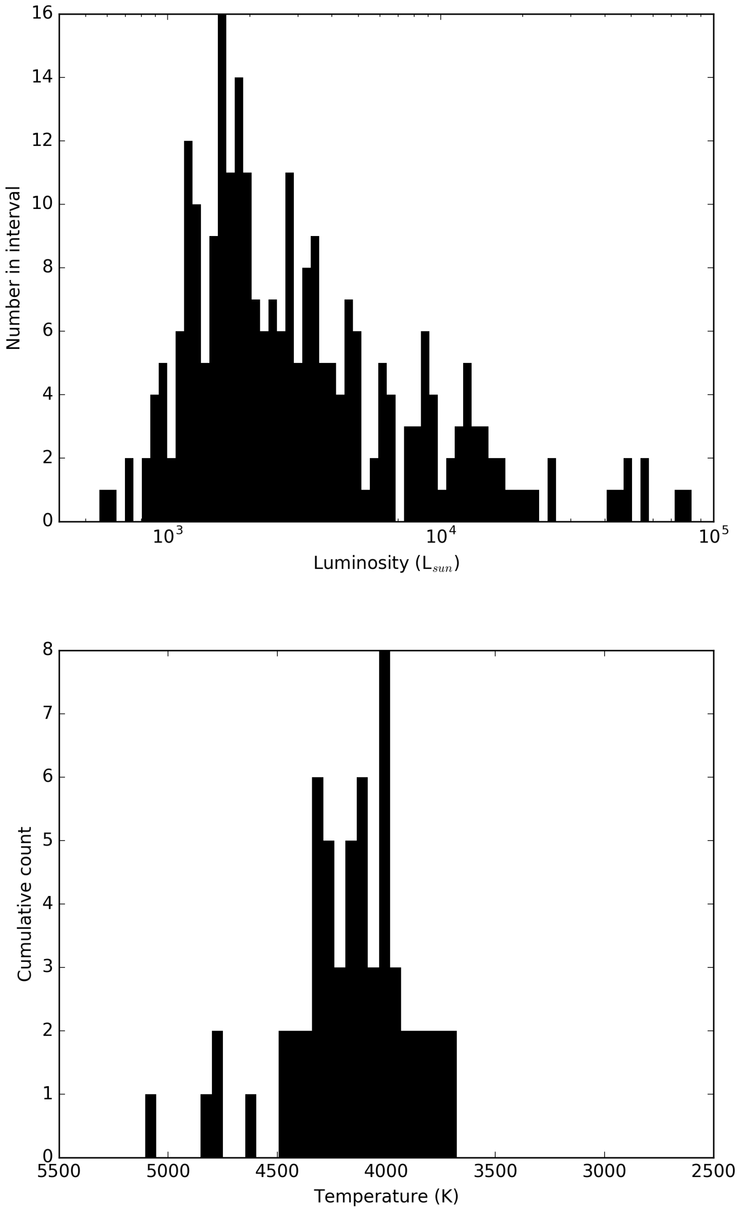

Figure 5.8: (a) Histogram showing the distribution of luminosity for objects in Sag DIG at a similar temperature to the RGB tip; (b) Histogram showing the distribution of temperature for objects in Sag DIG at a similar luminosity to the RGB tip.

The low number of objects present in this galaxy make it difficult to determine

RGB parameters with precision.

The [Fe/H] = −1.6 dex isochrone in Figure 4.5 gives a maximum luminosity of 1810 $L_\odot$, suggesting that our assumed distance (1067 kpc) is a slight overestimate. Using $L \propto d^2$, we can calculate that for $L_{RGB} = 2000\ L_\odot$, $d \approx 990$ kpc. The isochrone also predicts a temperature of 4100 K, similar to this estimate.

5.1.6 Peg DIG

The isochrone in Figure 4.6 gives a maximum luminosity of 1810 $L_\odot$, suggesting that our assumed distance (920 kpc) is an overestimate. Using $L \propto d^2$, we can calculate that for $L_{RGB} = 1810\ L_\odot$, $d \approx 820$ kpc. The isochrone predicts a temperature of 4110 K, showing our estimate is reasonably good.

5.1.7 WLM

The broad distribution of temperatures for the RGB tip is likely due to the presence of a wide range of stellar populations in this galaxy. Uncertainties are therefore likely lower than the values provided.

The isochrones in Figure 4.7 gives a maximum luminosity of 2050 $L_\odot$. Considering the amount of scatter we expect to see with this value of σ_L, this suggests that our estimate for distance is accurate. The isochrones predict a range of temperatures between 3880 and 4310 K, so again, considering σ_T and the range of populations in this galaxy, it is a good estimate.

5.1.8 NGC 6822

The broad distribution of temperatures for the RGB tip is likely due to the presence of a wide range of stellar populations in this galaxy. Uncertainties are

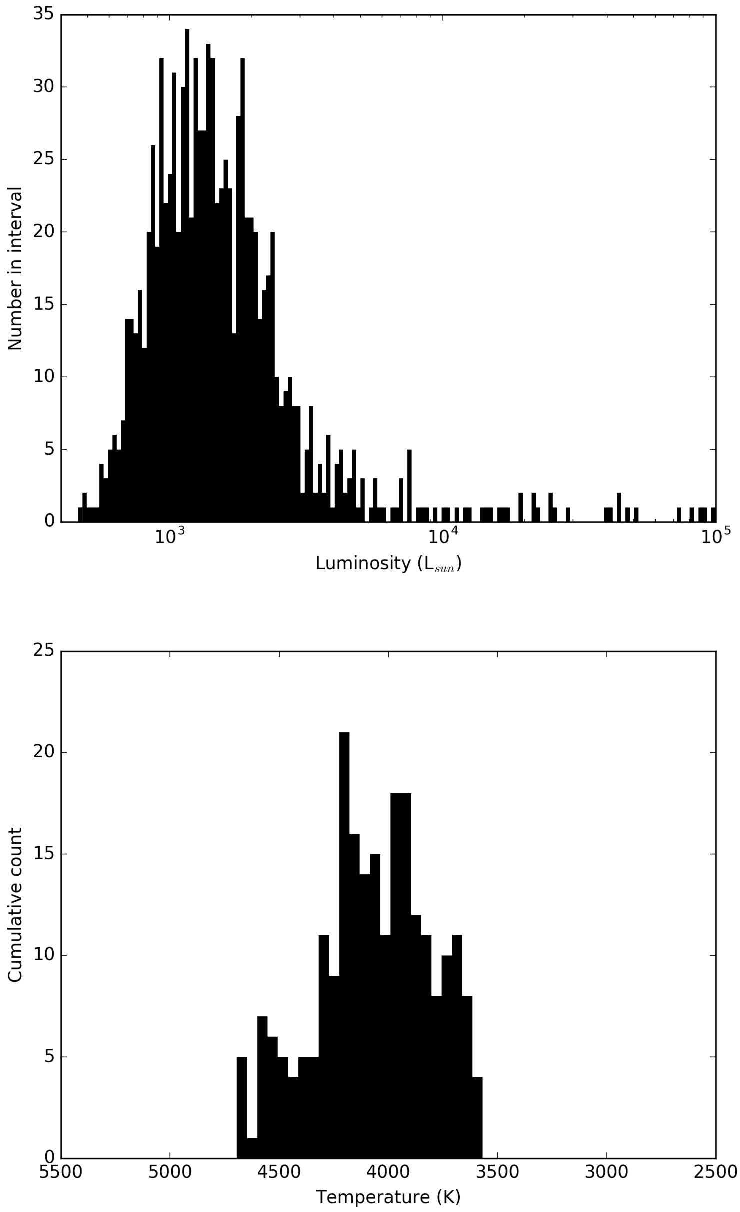

Figure 5.9: (a) Histogram showing the distribution of luminosity for objects in Peg DIG at a similar temperature to the RGB tip; (b) Histogram showing the distribution of temperature for objects in Peg DIG at a similar luminosity to the RGB tip.

therefore likely lower than the values provided.

The isochrones in Figure 4.8 predict a maximum luminosity of 2350 $L_{\odot}$, and

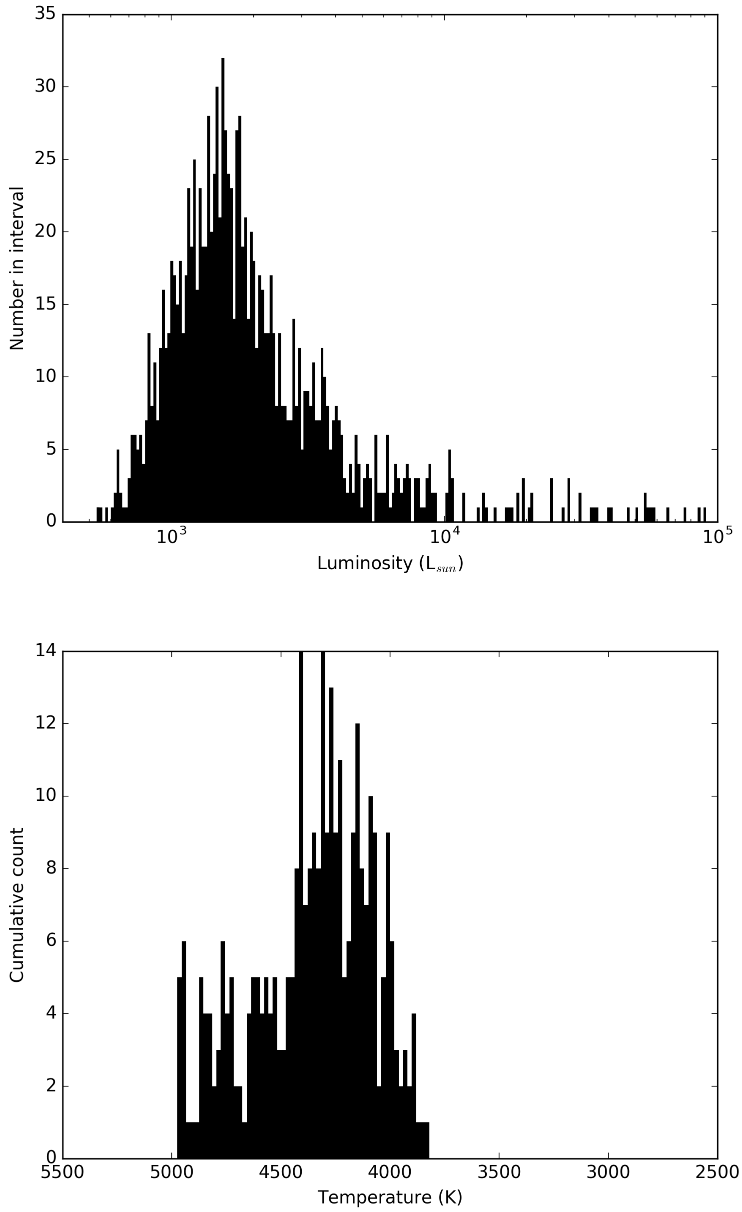

Figure 5.10: (a) Histogram showing the distribution of luminosity for objects in WLM at a similar temperature to the RGB tip; (b) Histogram showing the distribution of temperature for objects in WLM at a similar luminosity to the RGB tip.

a range of temperatures between 3440 and 3890 K. The values differ significantly from the values estimated above. This is likely a systematic error caused by the missing mid-IR data.

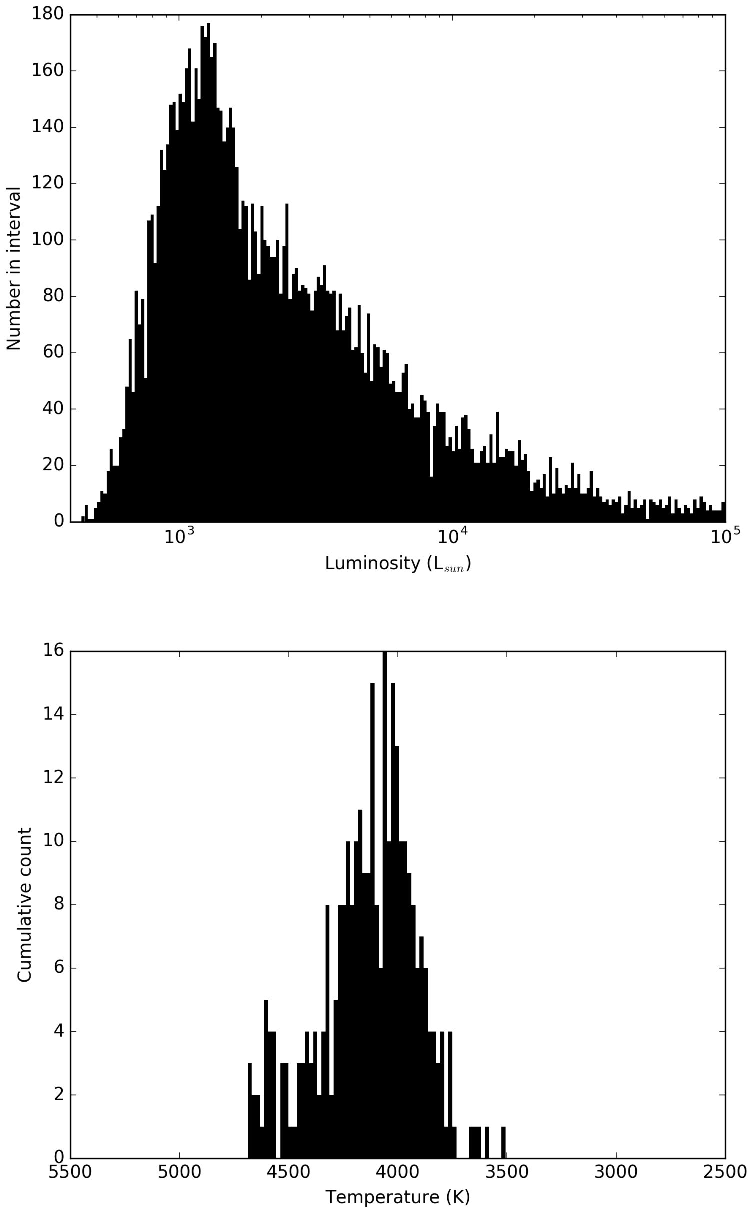

Figure 5.11: (a) Histogram showing the distribution of luminosity for objects in NGC 6822 at a similar temperature to the RGB tip; (b) Histogram showing the distribution of temperature for objects in NGC 6822 at a similar luminosity to the RGB tip.

5.1.9 LGS 3

The lack of data points made determination of RGB parameters more unreliable for this galaxy. L_{RGB} and T_{RGB} are given to the nearest 100 $L_{\odot}$ and K respec-

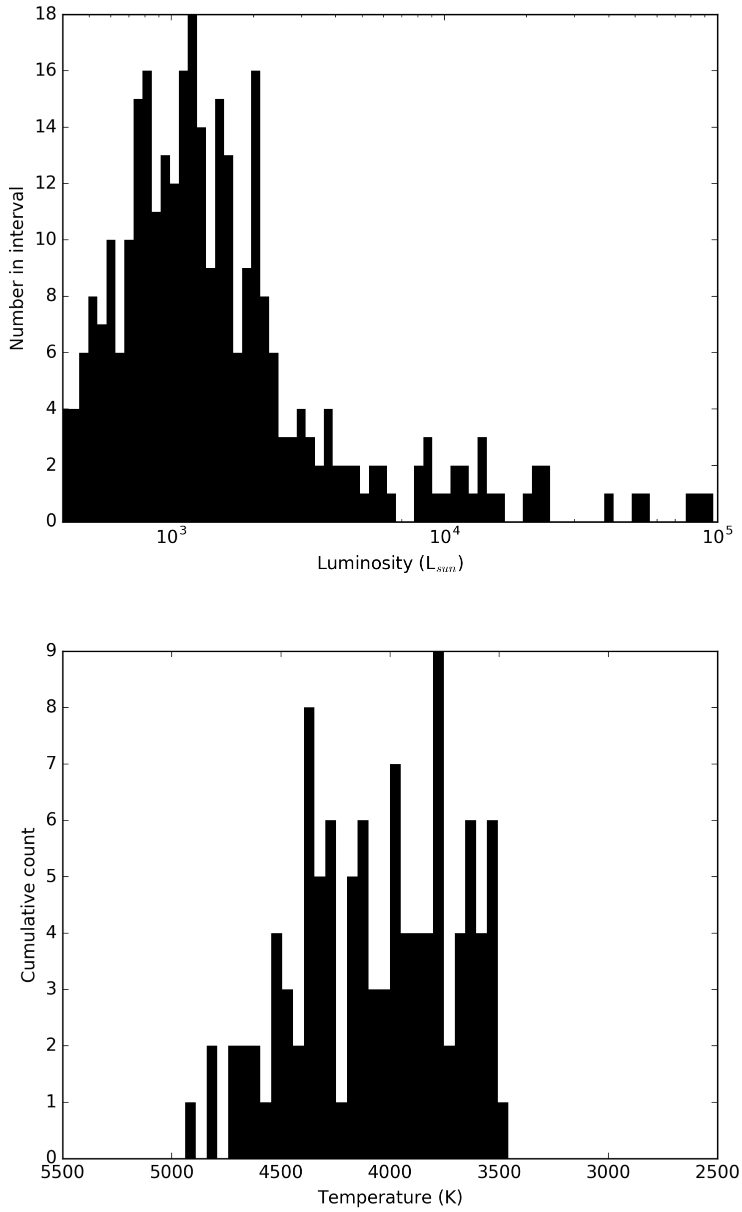

Figure 5.12: (a) Histogram showing the distribution of luminosity for objects in LGS 3 at a similar temperature to the RGB tip; (b) Histogram showing the distribution of temperature for objects in LGS 3 at a similar luminosity to the RGB tip.

tively. 1000 $L_{\odot}$ was used as the lower luminosity limit for calculating T_{RGB} due to the lack of data points above 1500 $L_{\odot}$.

The isochrone in Figure 4.9 gives a maximum luminosity of 1960 $L_{\odot}$, suggesting that our assumed distance (650 kpc) is a small underestimate. The isochrone predicts a temperature of 3950 K, in good agreement with the estimate.

5.1.10 Phoenix

A different technique was used to determine L_{RGB} for this galaxy, as the luminosity of objects extended much lower than the RGB tip due to the galaxy's relative proximity. The slope from 1000 $L_{\odot}$ to where the histogram reaches zero was used to determine L_{RGB}.

The isochrone in Figure 4.9 gives a maximum luminosity of 2000 $L_{\odot}$, suggesting that our assumed distance (415 kpc) is an underestimate. However, this may also be due to the low mass of the galaxy; it may be that there are too few stars above 1600 $L_{\odot}$ to be statistically significant. Assuming that this is caused by an overestimate of the distance to Phoenix, $d \approx 460$ kpc using $L \propto d^2$. The isochrones predict a range of temperatures between 3870 K and 4090 K, slightly below the estimate of 4150 K.

5.1.11 Leo A

The 8 Gyr isochrone in Figure 4.11 gives a maximum luminosity of 1800 $L_{\odot}$, in excellent agreement with the estimate, suggesting the distance estimate is accurate. The isochrones predicts a temperature of 4230 K, in good agreement with the estimate.

5.1.12 And IX

The wide distribution of T and L of the objects made it impossible to accurately determine T_{RGB} and uncertainties for this galaxy. The exact T and L of objects

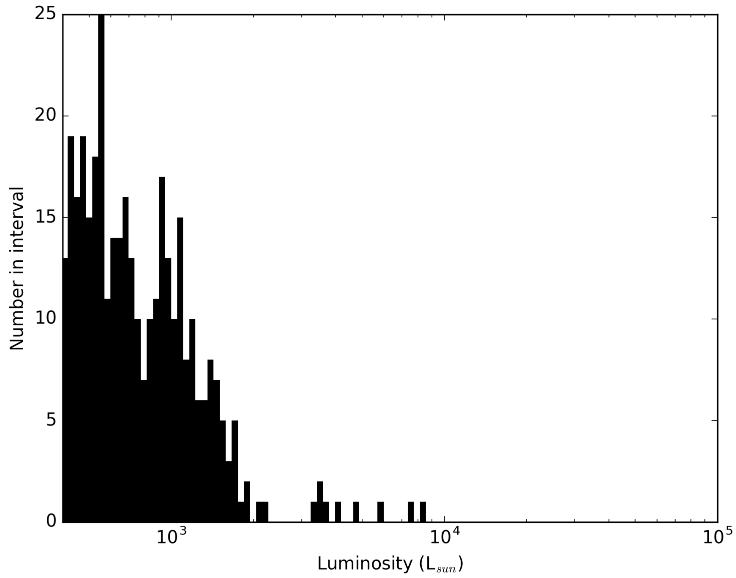

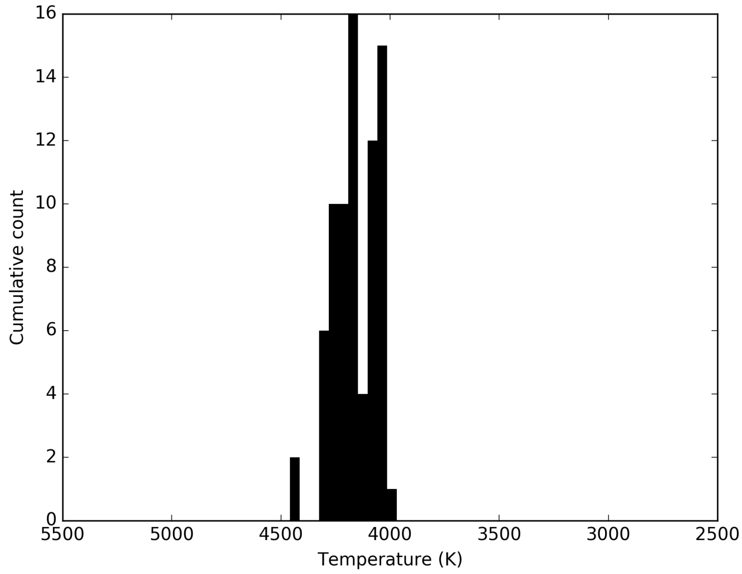

Figure 5.13: (a) Histogram showing the distribution of luminosity for objects in Phoenix at a similar temperature to the RGB tip; (b) Histogram showing the distribution of temperature for objects in Phoenix at a similar luminosity to the RGB tip.

in this galaxy should be therefore treated with scepticism.

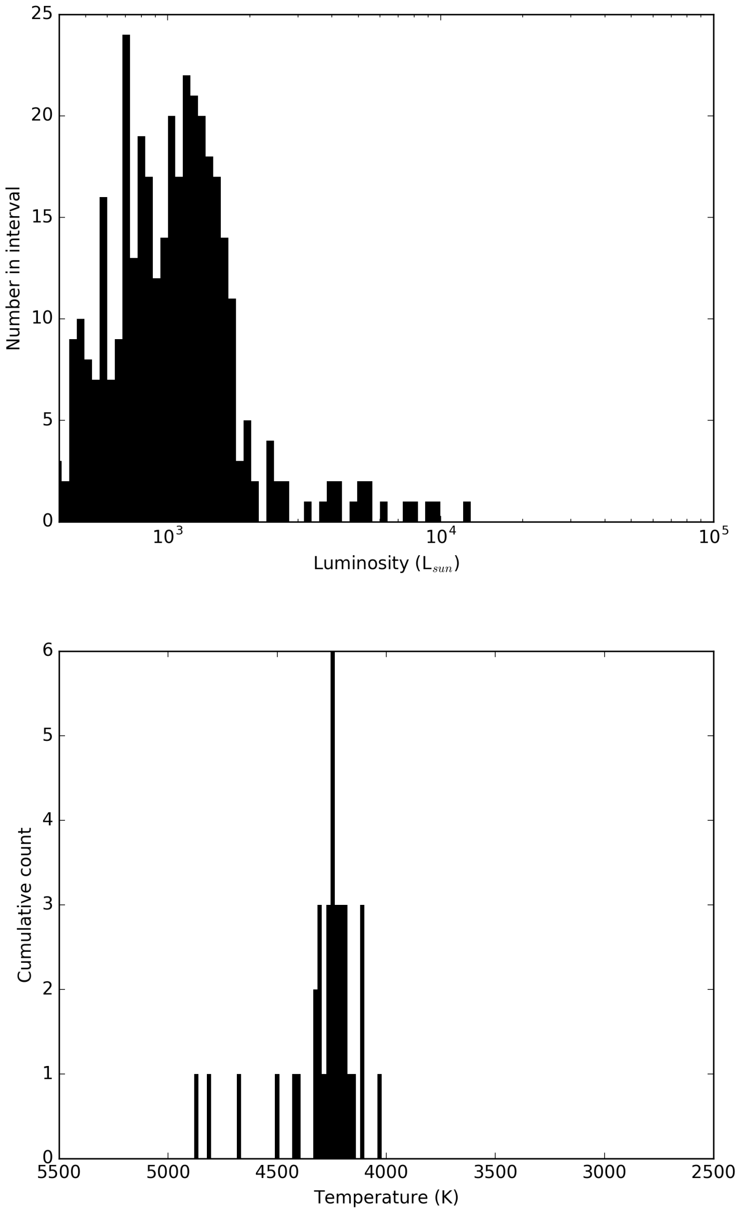

Figure 5.14: (a) Histogram showing the distribution of luminosity for objects in Leo A at a similar temperature to the RGB tip; (b) Histogram showing the distribution of temperature for objects in Leo A at a similar luminosity to the RGB tip.

5.1.13 NGC 185

The wide distribution of temperatures for the RGB tip is likely due to the presence of many stellar populations in this galaxy, indicated by the number of GCs.

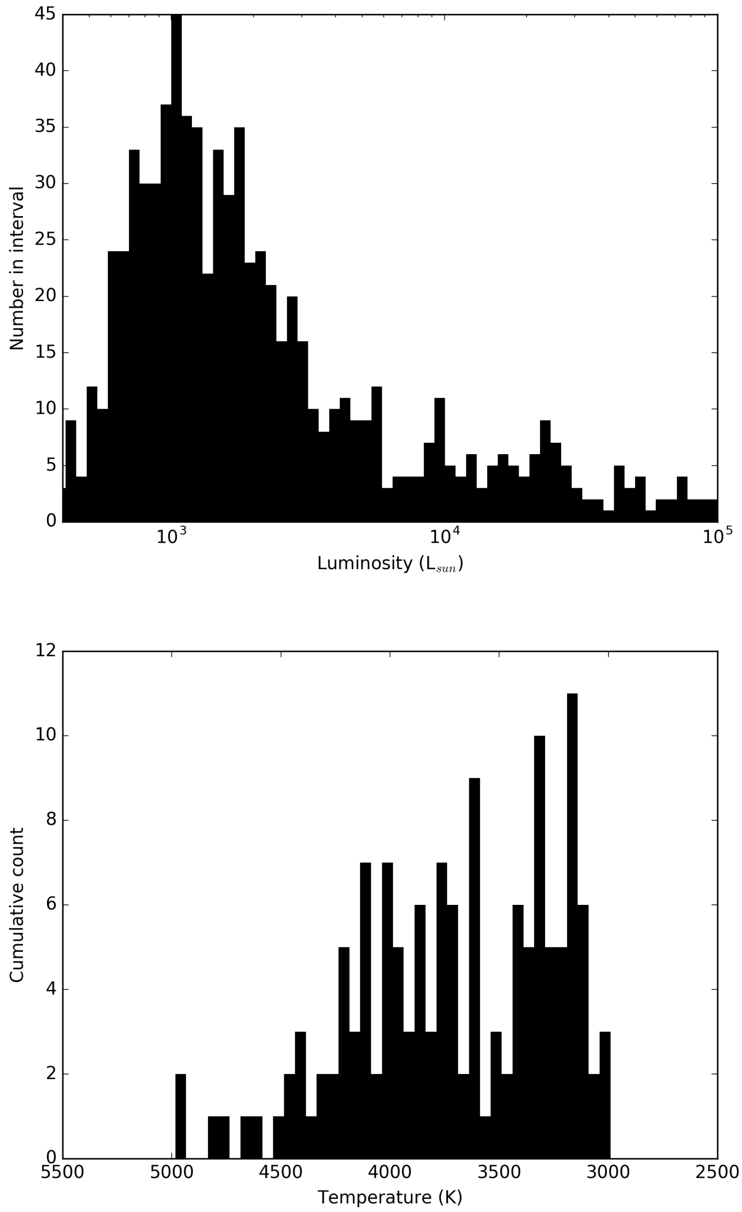

Figure 5.15: (a) Histogram showing the distribution of luminosity for objects in And IX at a similar temperature to the RGB tip; (b) Histogram showing the distribution of temperature for objects in And IX at a similar luminosity to the RGB tip.

Uncertainties are therefore likely lower than the values provided.

The isochrones in Figure 4.13 gives a maximum luminosity of 2160 L$_\odot$, sug-

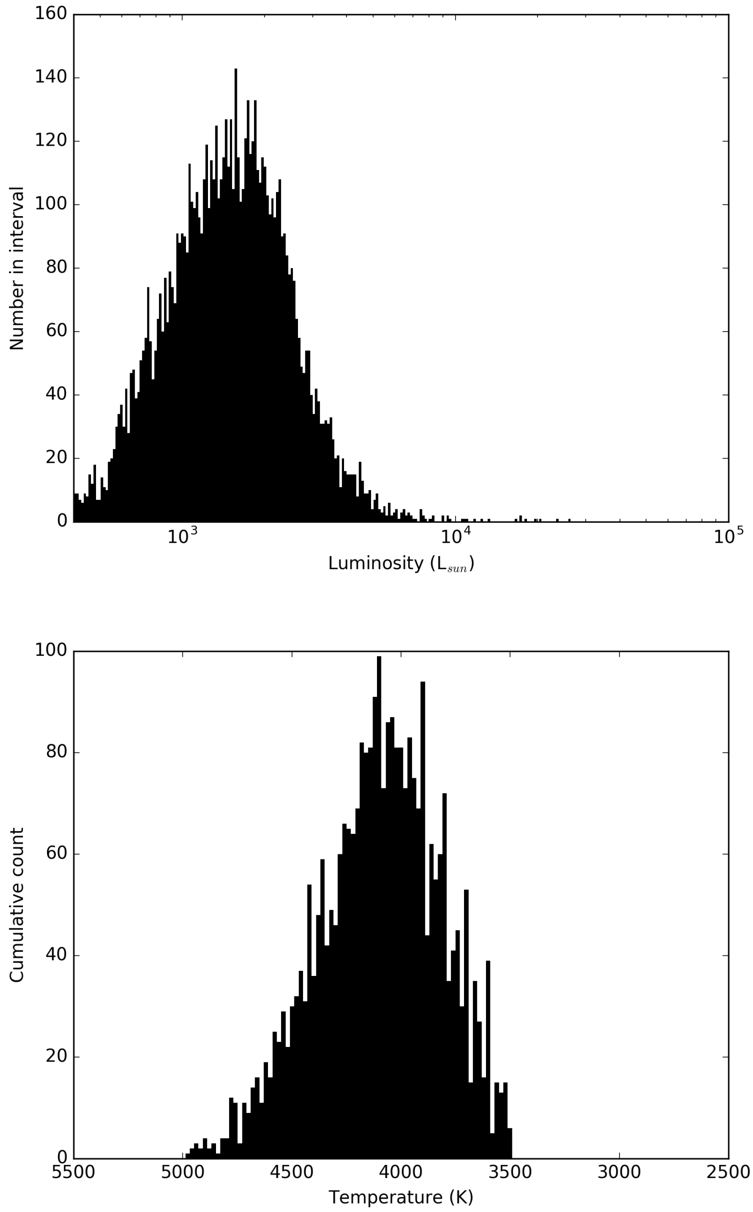

Figure 5.16: (a) Histogram showing the distribution of luminosity for objects in NGC 185 at a similar temperature to the RGB tip; (b) Histogram showing the distribution of temperature for objects in NGC 185 at a similar luminosity to the RGB tip.

gesting that our assumed distance (617 kpc) is an overestimate. Using $L \propto d^2$, we can calculate that for $L_{RGB} = 2160$ L$_\odot$, $d \approx 550$ kpc. The isochrones predict a range of temperatures between 3720 and 4400 K, so the estimate of 4050 K from this method is good.

5.1.14 NGC 147

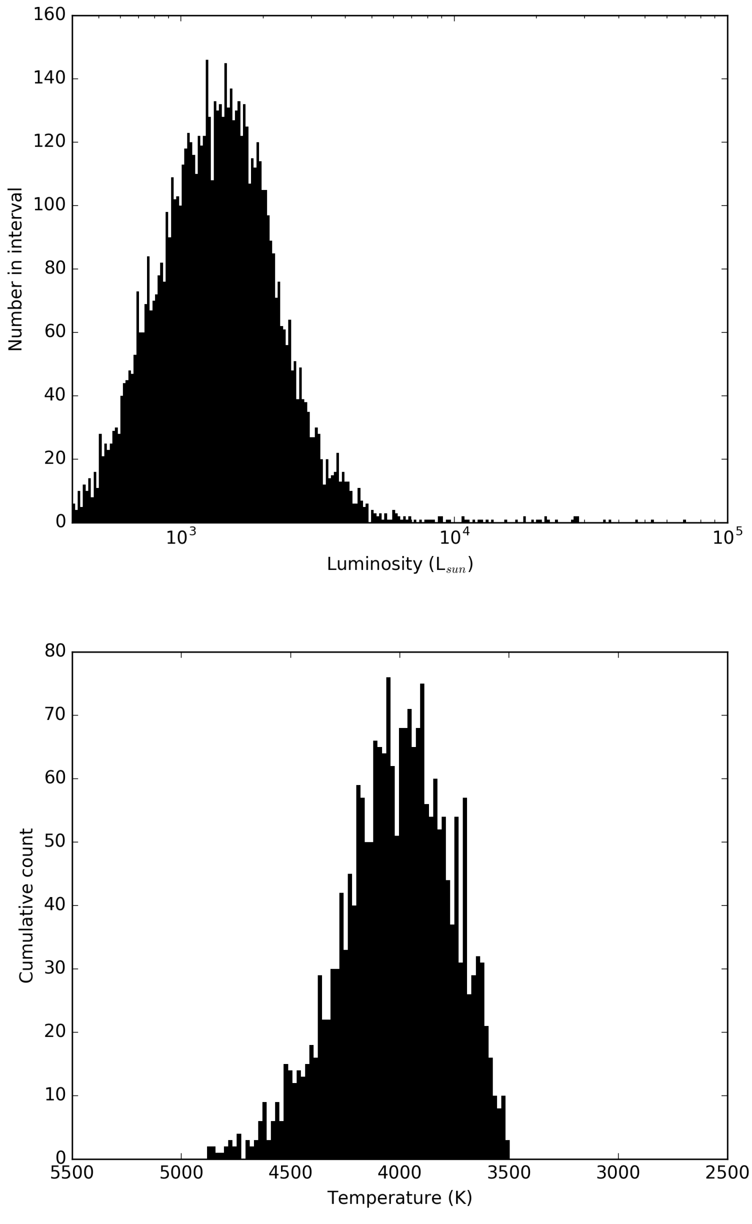

Figure 5.17: (a) Histogram showing the distribution of luminosity for objects in NGC 147 at a similar temperature to the RGB tip; (b) Histogram showing the distribution of temperature for objects in NGC 147 at a similar luminosity to the RGB tip.

The wide distribution of temperatures for the RGB tip is likely due to the presence of several stellar populations in this galaxy, indicated by the number of GCs (σ_T is lower for this galaxy than NGC 185, which contains more GCs). Uncertainties are therefore likely lower than the values provided.

The isochrones in Figure 4.14 give a maximum luminosity of 2250 $L_\odot$, suggesting that our assumed distance (676 kpc) is a slight overestimate. The isochrones predict a range of temperatures between 3600 and 4250 K, so the estimate of 4050 K from this method is good.

5.2 An analysis of supergiants

In order to test the SED-derived temperatures of objects from in this work, comparison with spectroscopically determined values was attempted. Only the brightest objects in this sample of galaxies, such as supergiants, have had their spectroscopic temperature reliably estimated to date, due to the considerable distances involved. These supergiants can therefore be used as a test of the reliability of SED-calculated temperatures derived in this work.

5.2.1 Blue supergiants

Although blue supergiants (BSGs) occur at far higher temperatures ($> 10^4$ K) than the AGB stars that are of interest to this work, spectroscopic temperatures were more readily available for these stars than red supergiants (RSGs). Literature values for these objects were compared with those derived in this study for seven BSGs in IC 1613 (from Bresolin et al. 2007), and eight in WLM (from Urbaneja et al. 2008). These are listed in Table 5.2. It was found that in both of these dIrrs, the SED-fit temperature (T_{SED}) was significantly lower than that spectroscopically determined (T_{spec}), with an average offset of ~ -6000 K in IC 1613, and ~ -4600 K in WLM. For some of the brightest objects, there is an underestimation of T of $\sim 60\%$. The overall inaccuracy in T_{SED}, and the difference in the inaccuracy between to the two galaxies are both primarily caused by the filters available to the GetSED code. In IC 1613, V is the shortest-wavelength band available. This means that hot objects, with spectra that peak in or above this band, will be very poorly fit, as the code requires a good sampling from both the Rayleigh–Jeans and Wien tails to provide an accurate result. In WLM, B is available, allowing for an estimate (albeit a poor one) of the Wien tail in the case of the cooler BSGs, which explains the overall reduced temperature discrepancy. The two hottest BSGs in the WLM sample peak in or above B, and as a result have the worst fit in that galaxy's sample. Photometry in U band would likely improve the fit of these BSGs, but as discussed in Section 3.1, it was removed in the case of WLM to better fit the AGB stars, the focus of this work.

Table 5.2: Comparison between spectroscopically determined and SED fit temperatures for 15 BSGs in IC 1613 and WLM.

Galaxy	Object ID	T_{SED} (K)	T_{spec} (K)	$T_{SED} - T_{spec}$ (K)
IC 1613	A10	16184	25000	–8816
	A12	21522	23000	–1478
	A18	15464	21000	–5536
	B3	17860	24500	–6640
	B11	17160	30000	–12840
	B13	15607	17000	–1393
	B16	14456	21000	–6544
WLM	A6	6796	8750	–1954
	A14	7456	8270	–814
	A16	8730	10650	–1920
	A12	10116	12100	–1984
	A17	10512	13500	–2988
	A9	13737	20000	–6263
	A10	13671	25000	–11329
	A11	19420	29000	–9580

In conclusion, it can be seen that the analysis of the spectroscopic temperature of BSGs is a poor test of the accuracy of the derived temperature of AGB stars, although it does emphasize the need for photometry in a wide range of bands around the spectral peak, and an accurate characterization of interstellar reddening.

5.2.2 Red supergiants

The only values of T_{spec} that could be found for RSGs in this sample of galaxies were for 11 stars in NGC 6822, from Patrick et al. (2015). These values were determined using two different spectroscopic methods. These methods typically provided values that varied by < 50 K. The mean value of T_{spec} from the two methods is presented in Table 5.3. These were compared with T_{SED} for the same stars.

Table 5.3: Comparison between spectroscopically determined and SED fit temperatures for 11 RSGs in NGC 6822.

Object ID	T_{SED} (K)	T_{spec} (K)	$T_{SED} - T_{spec}$ (K)	[Fe/H] (dex)
1	3489	3825	–336	–0.58
2	3850	3830	20	–0.72
4	3558	3880	–322	–0.32
7	3908	3980	–72	–0.57
8	4014	3910	104	–0.58
9	3583	3985	–402	–0.41
10	3742	3875	–133	–0.63
11	3822	3860	–38	–0.51
14	3636	3895	–259	–0.18
17	3585	3890	–305	–0.43
18	3883	3775	108	–0.61

The mean value of $T_{SED} - T_{spec}$ is ~ -150 K. This systematic offset can be explained by several factors. One possibility is that the fits to the SEDs of NGC 6822 are of poor quality due to the lack of mid-IR data, although as discussed in Section 5.1, it appears that this has caused an overestimation of T_{SED} in the RGB tip. However, this may have had a different effect on cooler objects. The

SEDs of the RSGs all peak in the H band, allowing for only one data point in the Rayleigh–Jeans tail (as photometry only extends to K). As a result of this, J and K bands have been fit very poorly; stars with the greatest difference in temperatures tend to have worse fits in these bands. This may also lead to an incorrect estimation of $\log(g)$, providing an incorrect value of the stellar mass. Several of the SED fits predict a mass of < 8 $M_{\odot}$, too low for a supergiant. These effects all cause additional uncertainty in T_{SED}, and may be partly responsible for its general underestimation.

Other factors that could impact T_{SED} are the values of [Fe/H] and [α/Fe] used in the SED fitting. The derived [Fe/H] from Patrick et al. (2015) are found in the range –0.18 to –0.72 dex (Table 5.3, averaged from two values), with the mean ~ -0.5 dex. This is significantly higher than the bulk metallicity of –1.0 dex used for the SED fitting of objects in this galaxy, as these young stars are formed from chemically more-processed matter. Stars with a higher metallicity are, in general, expected to be cooler. Figure 5.18, shows that the RSGs with [Fe/H] closer to the bulk metallicity typically have T_{SED} closer to T_{spec}, although there is significant uncertainty in their [Fe/H]. It appears that for the majority of objects with [Fe/H] < -0.5 dex, $T_{SED} - T_{spec}$ is undergoing only natural scatter (perhaps due to the intrinsic variability of these objects). This suggests that the problem lies only with the more-metal-rich RSGs. However, these stars have an SED-fit temperature that is actually cooler than T_{spec}, the opposite of what is predicted. It is unclear why exactly this has occurred, although it does appear that there is a dependence on metallicity. It is possible that inaccurate [α/Fe] values (not determined by Patrick et al. 2015) could have a similar effect to [Fe/H]. This is another measure of metallicity, and was assumed to be 0.4 dex in these stars. This is expected to decrease in with increasing [Fe/H] (Wheeler et al. 1989), impacting the temperature of the RSG.

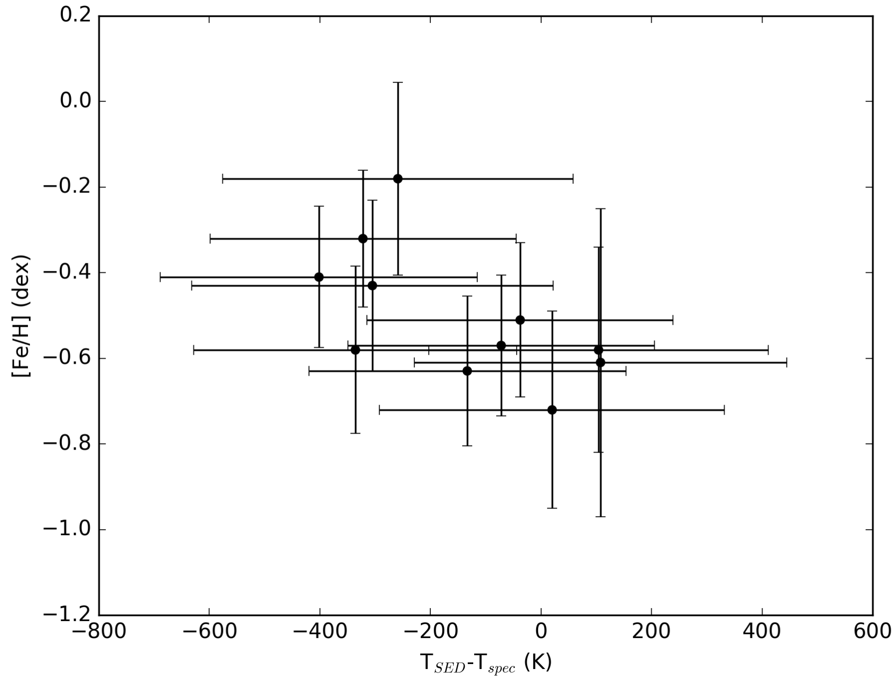

Figure 5.18: Plot relating $T_{SED} - T_{spec}$ to [Fe/H] for 11 RSGs in NGC 6822, as determined by Patrick et al. (2015). Errors in [Fe/H] are taken from the mean of errors in the originating study. Errors in $T_{SED} - T_{spec}$ are taken from the mean of errors in $T_{spec} + \sigma_T$.

Finally, our estimate of interstellar reddening may be incorrect. If overestimated, the SED fit temperatures may be artificially lowered, which could, in part, cause the underestimation of T_{SED}.

Assuming the above effects are the cause of the temperature discrepancies rather than systematic problems in the literature, it would still be incorrect to assume that they would affect the majority of the AGB stars across the sample of dIrrs. The missing mid-IR data is something that affects objects only in this galaxy. Furthermore, the typical dusty AGB star will be older, and therefore likely more-metal-poor than an RSG in the the same galaxy. This means the impact of using bulk metallicity for the SED fitting is reduced, and T_{SED} will be more accurate (although there may be an underestimate of several tens of K for the most luminous AGB stars if the same effect occurs). So although SED fitting has produced marginally inaccurate temperatures for RSGs in NGC 6822, this is not necessarily indicative of an issue affecting the entire AGB sample; rather it actually suggests that the majority of AGB stars will not suffer from the same effects, so are likely much better-fit.

5.3 Determining the typical stellar population of a Local Group dIrr galaxy

A better understanding of the typical dIrr stellar population would allow for better tests of the history of these galaxies, including their formation, SFH, and chemical evolution. In an attempt to determine this typical population, every object from the 13 finalized H–R diagrams from Section 2.2 was plotted on the same axes (Figure 5.19). A shortcoming of this process is that closer galaxies, or those with deeper photometry, may return more stars in the RGB, so bias the plot in their favour.

Figure 5.19 shows that a region is present with a higher density of stars than the surrounding regions, effectively showing the mode RGB tip. This is located at ~ 4000 K and 2000 $L_\odot$. Several poorly fit regions represented by vertical lines can be seen clearly $\lesssim 3100$ K, with other fainter examples spread throughout the displayed region.

A Dartmouth isochrone was fit to the high-density region in order to estimate the age and chemical composition of this typical population. An age of 10 Gyr was chosen, as it is close to the mean of the populations found in Table 4.1. Again, $[\alpha/\mathrm{Fe}] = 0.4$ dex was assumed. [Fe/H] was determined by trial and error, with the best fit found to be at $[\mathrm{Fe/H}] = -1.6$ dex. This isochrone is displayed

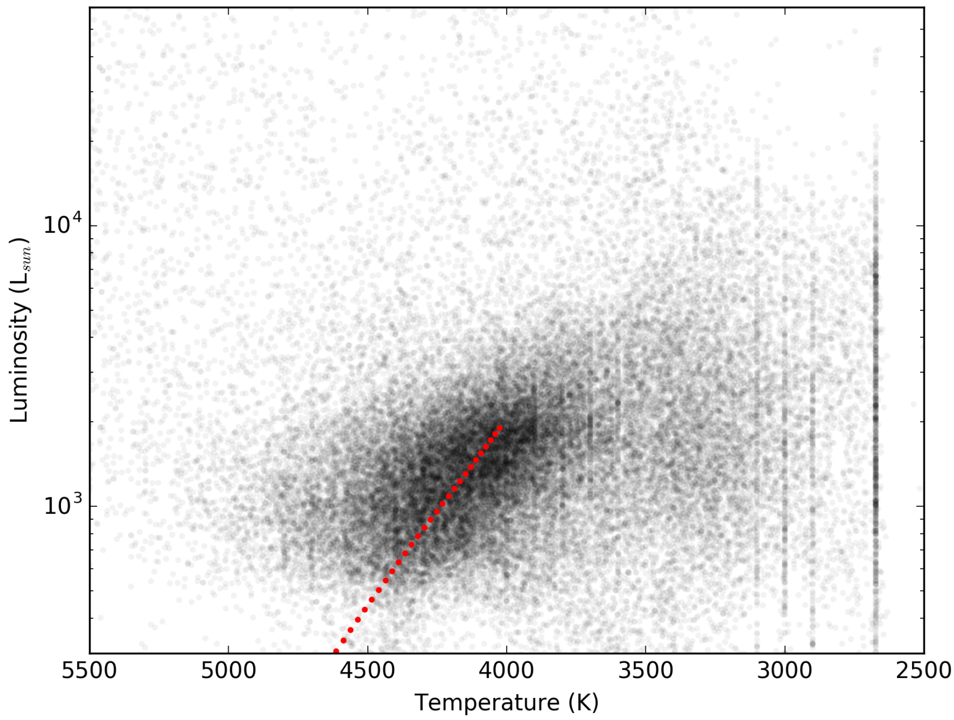

Figure 5.19: An H–R diagram including all points from each finalised H–R diagram in Section 2.2. Darker regions indicate a higher density of data points. The red line shows the position of a best-fit isochrone to the high-density region, of age = 10 Gyr, [Fe/H] = −1.6 dex and [α/Fe] = 0.4 dex.

in Figure 5.19. Assuming that the age and metallicity of this isochrone are that of the typical population, comparison with the populations listed in Table 4.1 shows that Sex B, Sag DIG (based on this work), Phoenix, NGC 185, and NGC 147 contain populations similar to this. These are the predominant populations in Sex B, Sag DIG and Phoenix, suggesting that these galaxies could be used as typical examples of dIrrs in terms of stellar population.

5.4 Properties of dusty objects

The analysis of the galaxies in Chapter 3 identified the IR excess of stars in 12 dIrr galaxies. Objects with an IR excess > median + 3σ were identified, and classed as dusty AGB candidates. Figure 5.20 plots all of these objects.

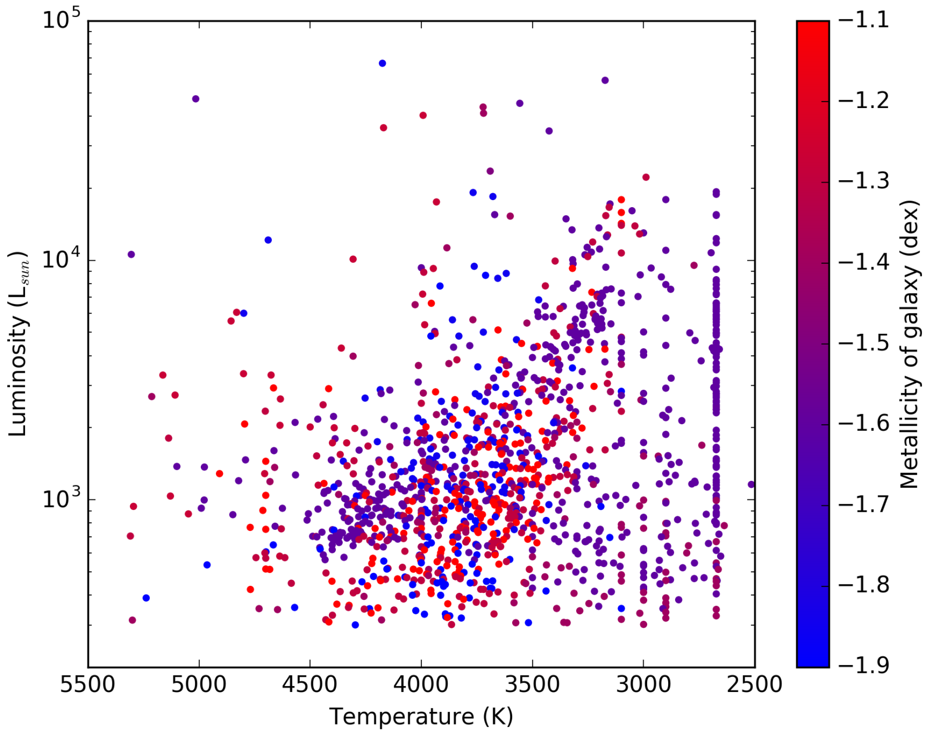

Figure 5.20: H-R diagram showing dusty AGB candidates for 12 of the 13 galaxies in the sample (excluding NGC 6822). Colours represent the bulk metallicity of their galaxy of origin, with values taken from Table 1.1 (with the exceptions of Sag DIG, Leo A, and And IX, which use the derived values from Chapter 4).

The AGB is clearly defined in Figure 5.20, visible as the main group of objects rising from $\sim$ 4000 K and 300 $L_{\odot}$ to a tip at $\sim$ 3100 K and 18,000 $L_{\odot}$. There is no significant change in the density of points beyond the RGB tip (i.e. $>$ 2500 $L_{\odot}$), suggesting that the majority of objects identified here are true AGB stars (as RGB stars are not expected to produce dust). Comparison with Figure 5.19 shows that the general shape of the AGB is cooler than that of the RGB, fitting with theory.

There appears to be a relationship between temperature and bulk metallicity at lower luminosities ($\sim$ 1000 $L_\odot$). AGB stars from more-metal-rich galaxies appear cooler than their metal-poor counterparts, fitting with the theory that metal-rich stars produce more dust, and will therefore appear at lower T. This trend appears to break down at higher L, possibly due to the fewer data points available (as fewer stars are at the higher mass required to reach these luminosities), or that the metallicity of the more-luminous younger objects is greater than that of the bulk metallicity, rendering the colour-scale meaningless. It may also be that the temperatures of the most-luminous objects are less reliable (Section 5.2.2).

Previous studies have suggested that AGB stars can become dusty above $\sim$ 700 $L_\odot$ (McDonald et al. (2012b) and references therein). It can be seen that the density of objects decreases around this luminosity, although this is also around the photometric limit for many of the catalogs used in this work, making it difficult to determine if this is a real effect due to the increased uncertainty.

The AGB appears to have a tip around 3100 K and 18,000 $L_\odot$. This may not be accurate however, as at cooler temperatures the reliability of the model decreases, and objects start to appear in local minima. Additionally, for the more luminous AGB stars, there may be a small underestimate of temperatures, similar to that seen in the RSGs in NGC 6822, Section 5.2.2. Furthermore, cool, red objects may have been excluded due to the difficulty of detecting them in optical bands. A number of the objects in the lower right of the diagram may be dusty O stars, similar to the cool objects ω Cen V6 and V42 described by McDonald et al. (2009).

No consistent trend can be found across the galaxies relating the IR excess to T or L. This may be expected due to the varying sources and quality of photometry used in this work. Stronger conclusions may be drawn from planned future studies with consistent sources of optical and near-IR data.

5.4.1 Analysis of individual objects

An analysis was carried out on 18 luminous objects with a 3σ IR excess that do not fit the AGB slope, highlighted in Figure 5.21. A further 7 objects that appear cooler than the AGB were analysed to confirm their identity, as well as four objects in the AGB. Results are summarized in Table 5.4.

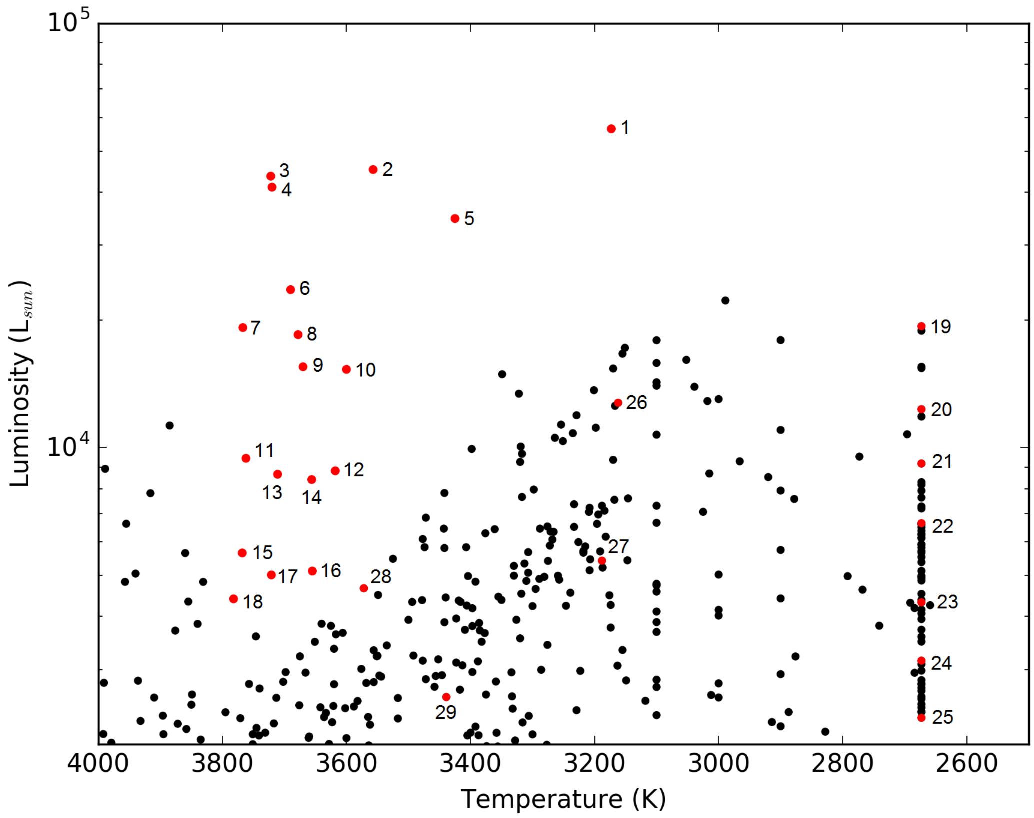

Figure 5.21: H-R diagram highlighting 29 3σ objects (red) for which further a analysis was carried out.

Table 5.4: Summary of the positions and classifications of 29 3σ objects highlighted in Figure 5.21.

Object	RA (HH:MM:SS.ss)	DEC (DD:MM:SS.s)	T (K)	L ($L_\odot$)	Classification
1	01:04:30.32	02:12:45.1	3173	56418	Blended objects
2	19:30:02.02	–17:40:19.3	3557	45223	RSG?
3	10:02:15.84	05:19:58.3	3722	43630	Blended objects?
4	23:28:02.44	14:44:55.9	3720	41105	AGN
5	19:30:03.25	–17:41:33.6	3425	34673	RSG?
6	01:03:43.01	21:50:45.4	3690	23566	Foreground star?
7	10:10:36.27	–04:36:51.9	3767	19182	Foreground star?
8	10:11:27.84	–04:41:06.8	3678	18460	Background galaxy?
9	01:04:35.65	02:06:07.7	3670	15509	RSG?
10	23:28:16.28	14:48:34.6	3600	15289	AGN
11	10:10:57.44	–04:39:14.5	3762	9436	Background galaxy?
12	10:10:56.66	–04:45:22.7	3618	8815	Background galaxy?
13	09:59:31.68	30:45:27.9	3711	8653	PN
14	10:10:51.49	–04:42:52.4	3656	8408	AGB star?
15	09:59:55.59	05:20:40.4	3768	5646	Background galaxy?
16	00:33:11.99	48:30:52.4	3655	5118	AGB star
17	10:10:59.30	–04:42:23.3	3721	5011	Blended objects?
18	01:04:37.24	02:02:16.1	3782	4401	Background galaxy?
19	19:29:55.98	–17:41:36.7	2673	19326	AGB star?
20	01:04:43.94	02:05:48.7	2673	12317	AGB star?
21	01:04:56.51	02:05:30.0	2673	9172	AGB star?
22	01:04:56.16	02:08:02.7	2673	6633	Carbon star
23	19:29:42.37	–17:40:41.3	2673	4320	Background galaxy?
24	01:05:01.44	02:03:43.7	2673	3146	Carbon star
25	01:04:42.45	02:12:21.3	2673	2308	Carbon star
26	00:39:02.83	48:18:45.7	3162	12757	AGB star?
27	01:04:30.32	02:08:57.1	3188	5414	AGB star?
28	10:10:53.05	–04:40:47.4	3572	4661	AGB star?
29	00:33:60.47	48:30:50.3	3439	2583	AGB star?

5.4.1.1 Object 1

Object 1 is in the vicinity of IC 1613. Optical photometry from Ahn et al. (2012) shows what appears to be two objects, a star in front of background galaxy, discernible as they are two different colours. It is likely that flux from both objects were combined in the source catalogs, causing the SED fitter to return a high luminosity.

5.4.1.2 Object 2

Object 2 is a star in Sag DIG, appearing in DSS2 photometry amongst a group of very bright blue objects, likely O or B stars, and several arcsecs away from an H II region (Strobel et al. 1991). For that reason, it is probably a red supergiant.

5.4.1.3 Object 3

Object 3 lies in the outer regions of Sex B, and appears as a blue object in optical photometry from Ahn et al. (2012). It appears in the DSS2 blue survey but not in red. Its SED shows it has been poorly fit. This may have been caused by stellar blending in the source photometry, an incorrect match between catalogs, or if it is a PN.

5.4.1.4 Object 4

Object 4, found near Peg DIG, was identified as a quasar using its spectra by Ahn et al. (2012).

5.4.1.5 Object 5

Object 5 lies towards the edge of Sag DIG. In DSS2 it appears similar to many of the other massive stars in the galaxy. Its well-fit SED implies that these are reasonably accurate values of L and T, suggesting that it is an RSG.

5.4.1.6 Object 6

Object 6 lies near LGS 3. It appears to be a foreground star, as no objects of comparable flux (in photometry from Ahn et al. 2012) are present in the galaxy itself.

5.4.1.7 Object 7

Object 7 lies near Sextans A. Its flux in DSS2, spatial shape, and distance from the galactic centre suggests that it is a foreground star.

5.4.1.8 Object 8

Object 8 lies near Sextans A. Its SED suggests it has been modelled very poorly in optical wavelengths, suggesting an incorrect match between catalogs. A dusty background galaxy may also produce an SED like this, which seems more likely given the low density of objects in this region.

5.4.1.9 Object 9

Object 9 appears as one of the brighter red objects within IC 1613 in the Ahn et al. (2012) photometry. Its SED does not seem significantly different to that of the AGB stars in this galaxy, although it is much brighter than expected in [4.5]. It is most likely an RSG.

5.4.1.10 Object 10

Object 10 lies near Peg DIG. Adelman-McCarthy et al. (2008) identify it as an AGN.

5.4.1.11 Object 11

Object 11 lies near Sex A. It appears to have an extended structure in DSS2 photometry, and its SED increases through the mid-IR, with the highest flux seen at [8.0]. For this reason it is most likely a background galaxy.

5.4.1.12 Object 12

Object 12 appears as a very faint source in the outer regions of Sex A in DSS2 photometry. Its poorly fit SED suggests it is a dusty background galaxy.

5.4.1.13 Object 13

Object 13 is a planetary nebula in Leo A, as described by Magrini et al. (2003). Its SED contains a double-peak, a feature of the SED of post-AGB objects.

5.4.1.14 Object 14

Object 14 is a faint source in the outer regions of Sex A in DSS2 photometry. Although poorly fit to the SED, it appears to be an AGB star. Its proximity to a bright foreground star may have caused problems in certain photometric bands.

5.4.1.15 Object 15

Object 15 is a source in Sex B. No object at its coordinates are immediately obvious in the Ahn et al. (2012) optical photometry. The SED shows that it is very poorly modelled in optical bands, suggesting that this is most likely a background galaxy, or perhaps a very-obscured star.

5.4.1.16 Object 16

Object 16 is a star in NGC 147, listed as an AGB star by Marleau et al. (2010). It is slightly more luminous and hotter than expected, perhaps due to blending. However, its SED seems well-fit, suggesting that this may just be an example of an extremely metal-poor star, which would be hotter and more luminous than the majority of the population in this galaxy. Alternatively, it may be an star beginning its journey onto the post-AGB track.

5.4.1.17 Object 17

Object 17 is a star in the central regions of Sex A. It appears to have been modelled fairly poorly in optical bands. This, along with the high density of stars in this region, suggests that blending or an incorrect match between catalogs could have caused these issues.

5.4.1.18 Object 18

Object 18 appears near IC 1613. Optical photometry from Ahn et al. (2012) shows a background galaxy, albeit a particularly luminous example.

5.4.1.19 Object 19

Object 19 lies in Sag DIG. It does not appear in optical sky surveys, and its SED shows that it is very dim at these wavelengths. Its brightness in mid-IR bands suggests that it is an dusty AGB star.

5.4.1.20 Objects 20 and 21

Objects 20 and 21 lies in IC 1613, both visible as red stars in the Ahn et al. (2012) optical photometry. Their SEDs are similar to Object 19, suggesting they are AGB stars.

5.4.1.21 Object 22

Object 22 was classified as a carbon star in IC 1613 by Albert et al. (2000).

5.4.1.22 Object 23

Object 23 is an object near Sag DIG, not visible in available sky surveys. It is very dim in optical bands, and has a poorly-fit SED. This, combined with its position suggest that it is a background galaxy.

5.4.1.23 Objects 24 and 25

Objects 24 and 25 were classified as carbon stars in IC 1613 by Albert et al. (2000).

5.4.1.24 Objects 26, 27, 28, and 29

Objects 26, 27, 28 and 29 can be found in NGC 185, IC 1613, Sex A and NGC 147 respectively. They all have very similar SEDs, which are poorly fit in mid-IR bands, suggesting they are all AGB stars.

5.4.1.25 Summary

Of the 18 over-luminous objects highlighted in Figure 5.21, only one can be said with certainty to be a well-fit AGB star, Object 16 (which is the closest to the AGB from this sample). Therefore it is reasonable to assume that by ignoring objects that are more luminous than the AGB (for a given temperature), the AGB sample will not be significantly reduced. Seven out of the eight objects sampled from the temperature minimum were also found to be AGB stars, with only one background galaxy in the sample: this may be expected at the lower-end of the temperature and luminosity range. All four objects analysed in the body of the AGB were found to be AGB stars.

5.5 Variability

A catalog of variable, AGB, dust-producing sources was produced by Boyer et al. (2015a), based on the variability between the DUSTiNGS survey and Boyer et al. (2009). The complete catalog contains 710 sources, but restricting to the 12 galaxies with sufficient data to calculate an IR excess leaves 371 objects. Of this remaining catalog, 280 objects were classified as "extreme" AGB (or x-AGB) stars due to their high dust-prodution rates, defined in the originating study by $[3.6] - [4.5] > 0.1$ mag. The majority of these stars are believed to be carbon-rich due to the lack of opacity of O-rich dust at $\lambda \lesssim 10$ μm. All stars in this catalog have a calculated amplitude of pulsation, based on data from two DUSTiNGS epochs ($\sim$ 6 months apart), and in some cases a third epoch from Boyer et al.

(2009). Boyer et al. (2015a) calculated a dust-production rate for each of the x-AGB stars, using a derived relation based on data from Riebel et al. (2012):

$$\log\dot{D}\ [\mathrm{M_\odot\,yr^{-1}}] = -9.5 + [1.4 \times ([3.6] - [4.5])]. \tag{5.1}$$

Objects for which SEDs have been calculated in this work were matched to the variable catalog from Boyer et al. (2015a). Matches were successful for 100 of the 371 objects in the catalog, 73 of which are x-AGBs. Obscuration due to dust may have shifted the colour of the un-matched objects to longer wavelengths, making it difficult to find an optical counterpart. The average temperature of these objects is 3144 K, with many points below 3000 K (the temperatures of which cannot be considered reliable). This has interesting implications for the results of this study. Many of the dusty AGB candidates seen in this study at $T > 3000$ K were not reported by Boyer et al. (2015a), likely because they are variable with a period or amplitude that is difficult to detect based on the limited observations available to that study. Cooler objects (likely to have a higher mass-loss rate), are more difficult to detect in optical bands, meaning many variable objects may not be part of the SED-fit catalog.

Parameters provided by the variable stars catalog, such as the amplitude and rate of dust production, have been related to the IR-excess calculated in this work.

5.5.1 Pulsation amplitude versus IR excess

Figures 5.22, 5.23 and 5.24 display the relationship between the amplitude of pulsation and the IR excess for five galaxies. Note the different scales used. Galaxies which used the same photometry for SED fitting have their data displayed together; displaying galaxies using different photometry sources together may obscure relations due to systematic errors. Galaxies not included in this

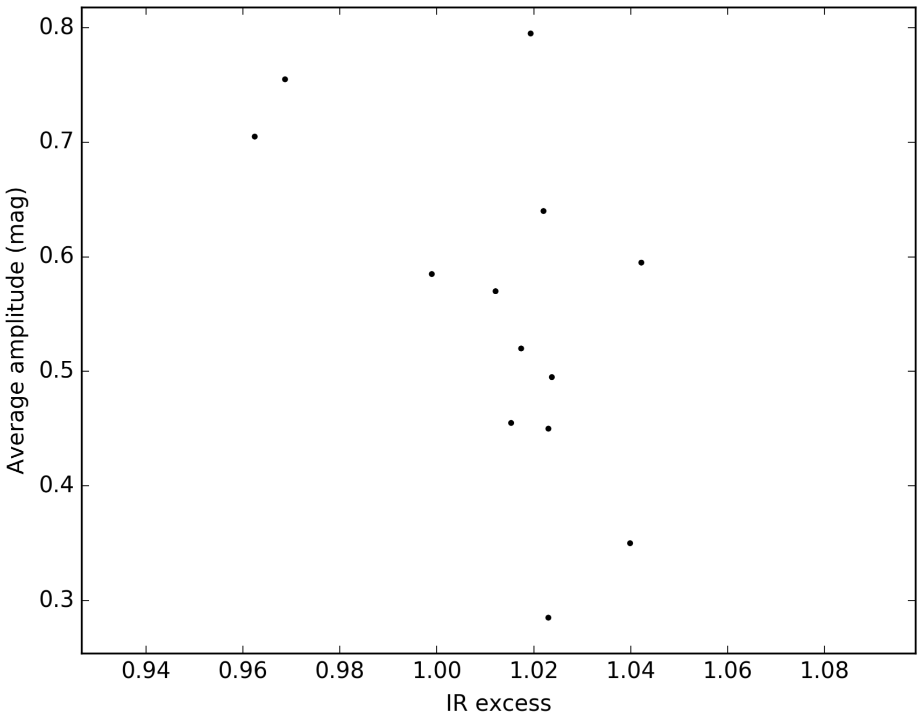

Figure 5.22: Plot showing the relationship between the calculated IR excess and average amplitude variability (both averaged for [3.6] and [4.5]) for variable stars identified by Boyer et al. (2015a) in Sextans A and Sextans B.

selection had insufficient data points to make meaningful statements about this relation.

As these Figures show, there is little relation between the amplitude of pulsation and the IR excess, with perhaps only a weak relation visible in Figure 5.24. This is a surprising result, as it would be expected that the larger stars undergoing high amplitude pulsations would be cooler, and therefore dustier, losing more mass and creating an IR excess.

A possible explanation is the measure of IR excess that is being used in this work. Here, we are calculating this by averaging F_{obs}/F_{model} for [3.6] and [4.5].

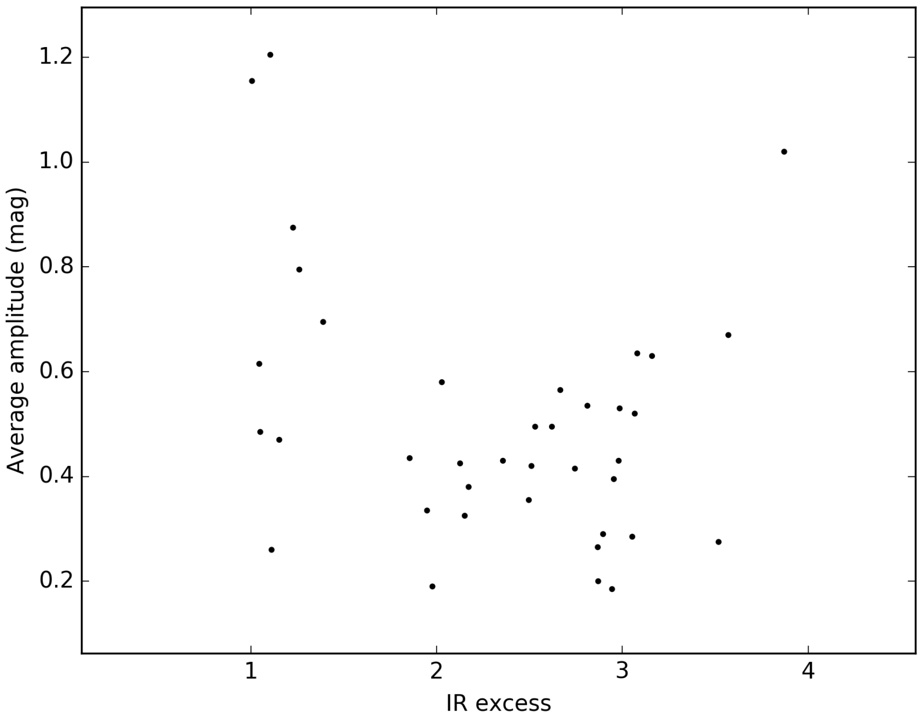

Figure 5.23: Plot showing the relationship between the calculated IR excess and average amplitude variability (both averaged for [3.6] and [4.5]) for variable stars identified by Boyer et al. (2015a) in IC 1613.

These wavelengths are not well-suited for detecting absorption features of O-rich dust (these features are better detected at $\lambda > 10$ μm; Section 1.4.3.3). This means that many O-rich, less-dusty pulsating stars may have been missed, in both this work and in Boyer et al. (2015a). Additionally, the pulsation amplitude has only been calculated from two or three data points, suggesting that these values are unreliable. Pulsation with a period similar to the time between observation epochs would likely be missed entirely, and many given amplitudes would not be representative of the true value.

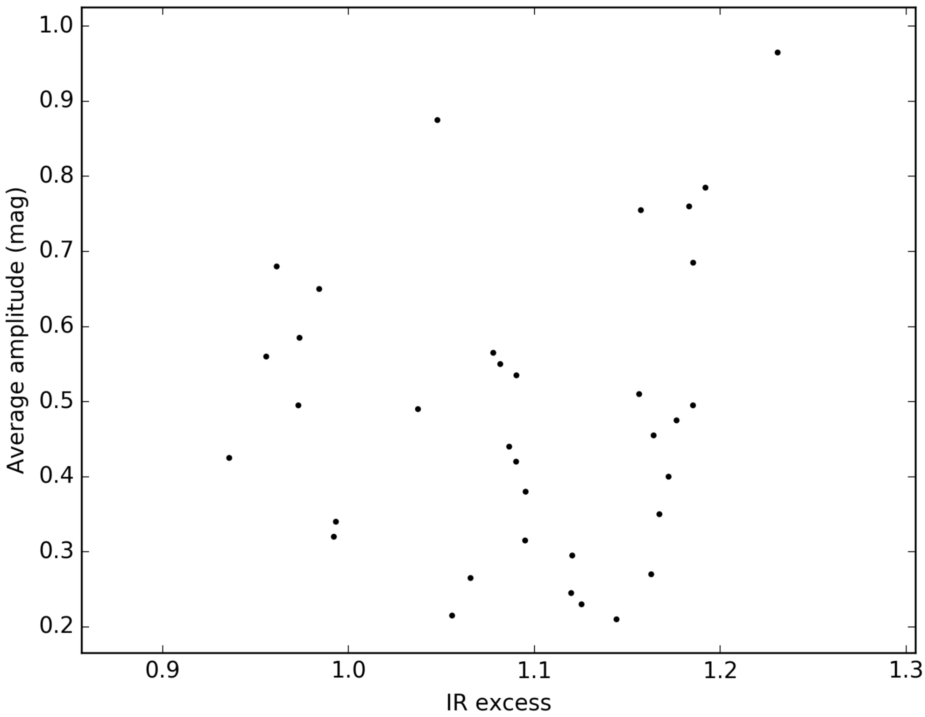

Figure 5.24: Plot showing the relationship between the calculated IR excess and average amplitude variability (both averaged for [3.6] and [4.5]) for variable stars identified by Boyer et al. (2015a) in NGC 185 and NGC 147.

5.5.2 Dust production rate versus IR excess

Figures 5.25, 5.26, and 5.27 display the relationship between IR excess and rate of dust production for five galaxies from the sample, with the same selection criteria as Section 5.5.1.

All three Figures show an increasing level of dust production with IR excess. The relationship is most difficult to determine in Figure 5.25, due to the lack of data points, but is stronger in Figures 5.26 and 5.27. An exact relationship is difficult to determine, however, due to the increased IR excess found for objects seen in IC 1613 (Section 5.4). This result should not be considered surprising, as the dust-production rate and IR excess both involve comparing magnitudes in

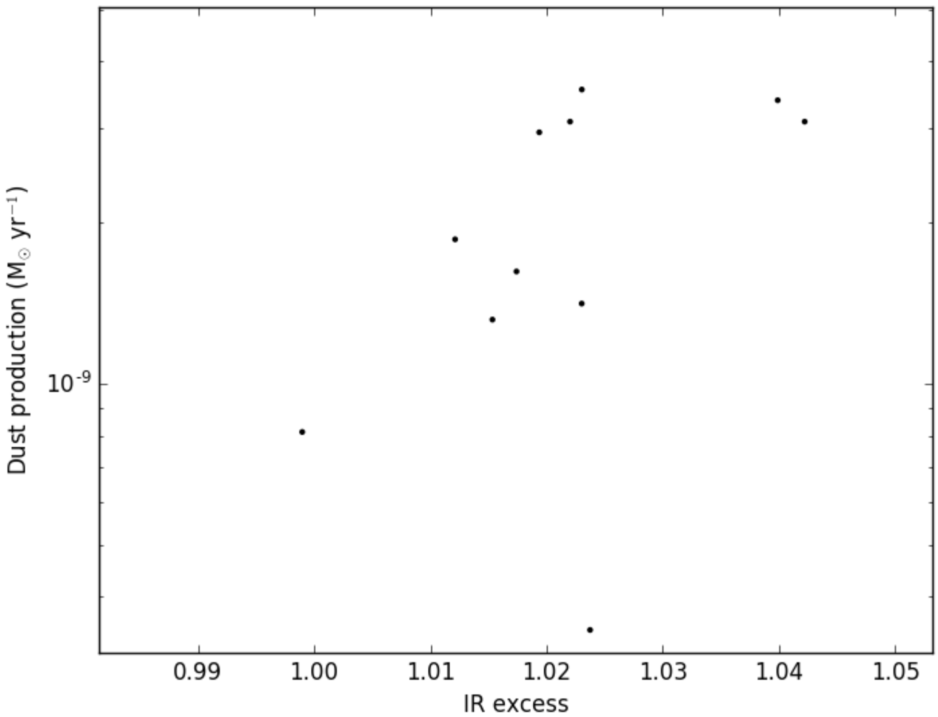

Figure 5.25: Plot showing the relationship between the calculated IR excess (average F_{obs}/F_{model} of [3.6] and [4.5]) and dust-production rate of x-AGB stars identified by Boyer et al. (2015a) in Sextans A and Sextans B.

different filters ([3.6] and [4.5] for dust production versus a wide variety of filters for the SED fitting). However, it does show that results are at least somewhat consistent between the two studies, and is a demonstration of the fact that dust in the stellar atmosphere can cause an IR excess.

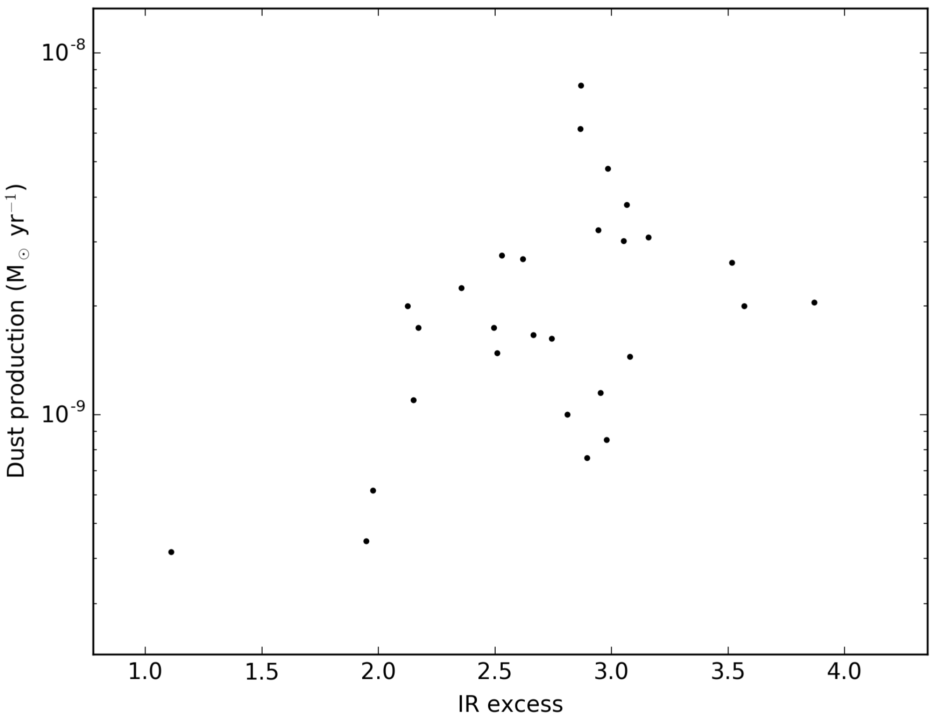

Figure 5.26: Plot showing the relationship between the calculated IR excess (average F_{obs}/F_{model} of [3.6] and [4.5]) and dust-production rate of x-AGB stars identified by Boyer et al. (2015a) in IC 1613.

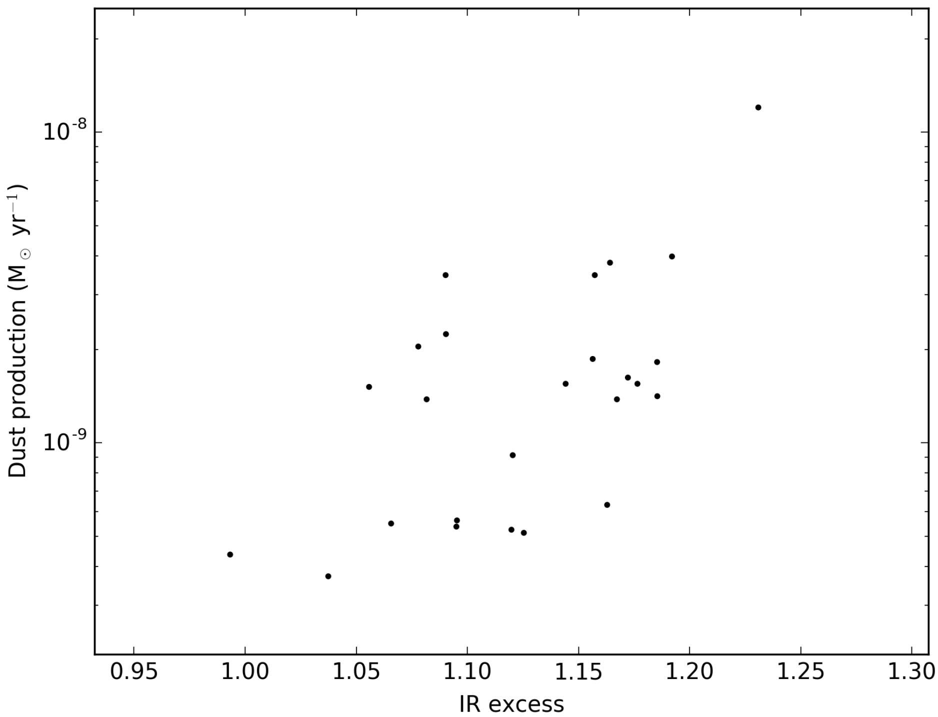

Figure 5.27: Plot showing the relationship between the calculated IR excess (average F_{obs}/F_{model} for [3.6] and [4.5]) and dust-production rate of x-AGB stars identified by Boyer et al. (2015a) in NGC 185 and NGC 147.

5.5.3 Identification of matched variables

Variable stars matched to the catalogue from this work were plotted on the HR diagrams finalised in Section 2.2. Examining Figures 5.28 – 5.37 shows that the identification criteria used by Boyer et al. (2015a) preferentially identified cooler and more luminous objects as variables. Variability is easier to determine and quantify in more-luminous objects as they have a higher signal-to-noise ratio, so this is expected.

5.5.3.1 Sextans B

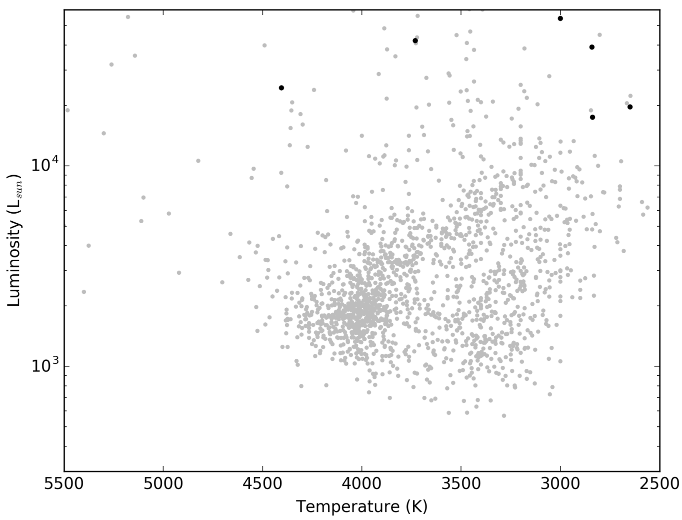

Figure 5.28: H–R diagram of the stellar population Sextans B (grey), with the variable objects identified by Boyer et al. (2015a) highlighted in black.

5.5.3.2 Sextans A

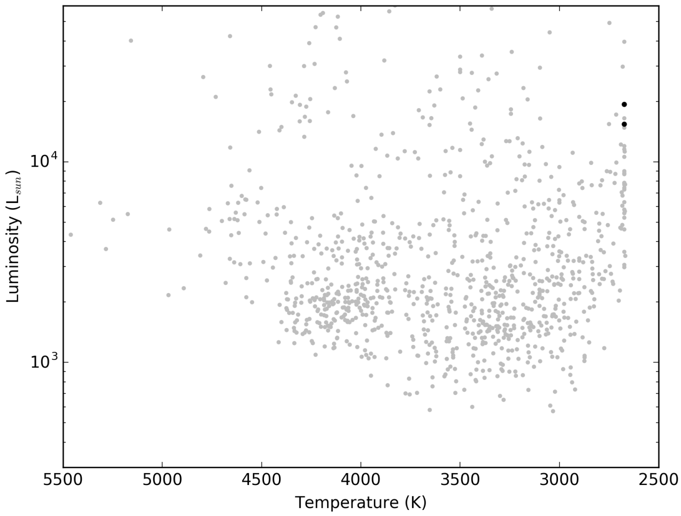

Figure 5.29: H–R diagram of the stellar population Sextans A (grey), with the variable objects identified by Boyer et al. (2015a) highlighted in black.

5.5.3.3 IC 1613

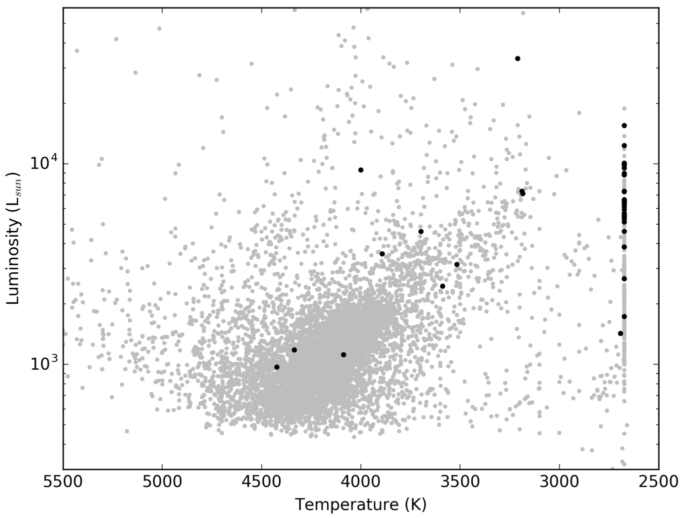

Figure 5.30: H–R diagram of the stellar population IC 1613 (grey), with the variable objects identified by Boyer et al. (2015a) highlighted in black.

5.5.3.4 Sag DIG

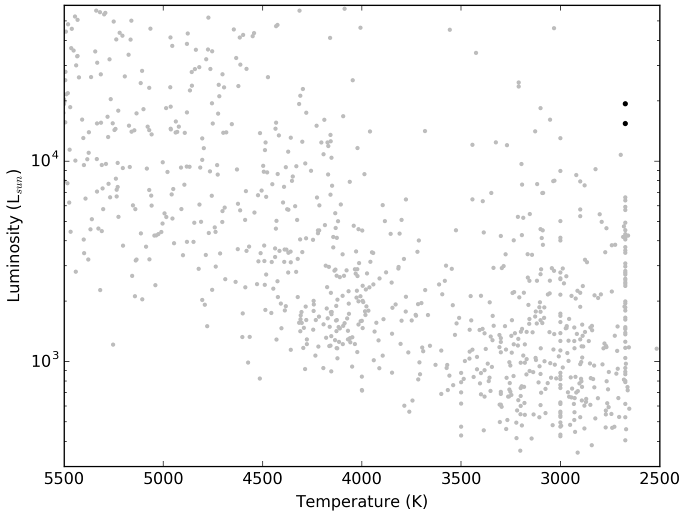

Figure 5.31: H–R diagram of the stellar population Sag DIG (grey), with the variable objects identified by Boyer et al. (2015a) highlighted in black.

5.5.3.5 Peg DIG

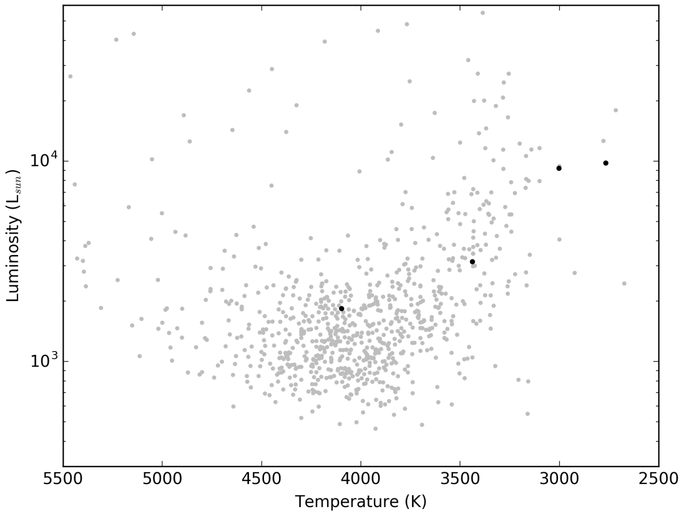

Figure 5.32: H–R diagram of the stellar population Peg DIG (grey), with the variable objects identified by Boyer et al. (2015a) highlighted in black.

5.5.3.6 LGS 3

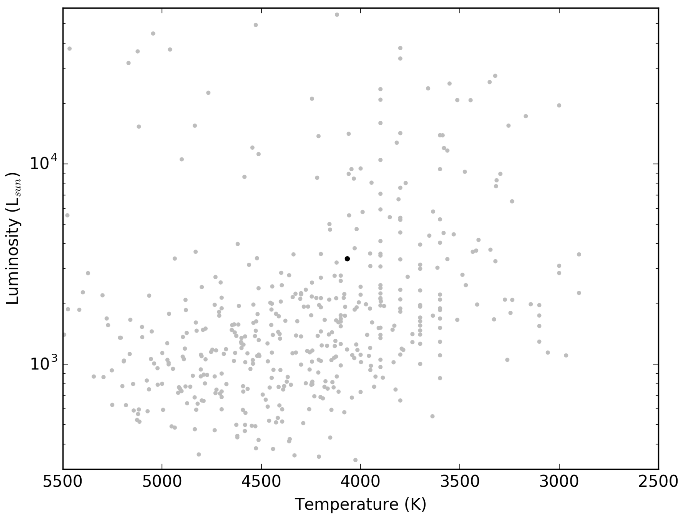

Figure 5.33: H–R diagram of the stellar population LGS 3 (grey), with the variable objects identified by Boyer et al. (2015a) highlighted in black.

5.5.3.7 Leo A

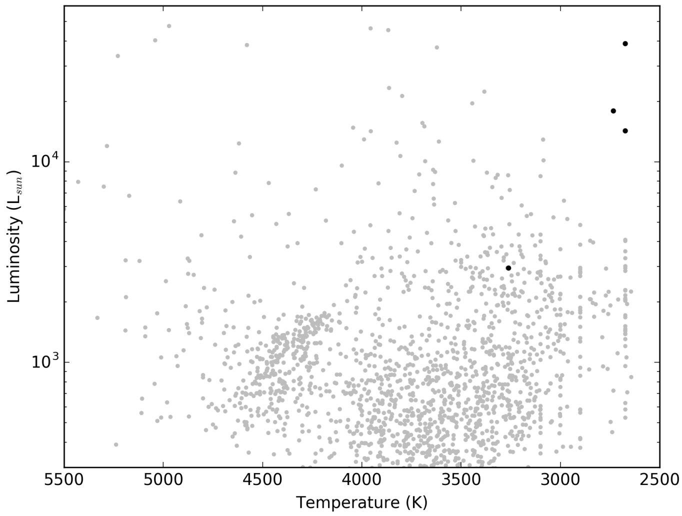

Figure 5.34: H–R diagram of the stellar population Leo A (grey), with the variable objects identified by Boyer et al. (2015a) highlighted in black.

5.5.3.8 And IX

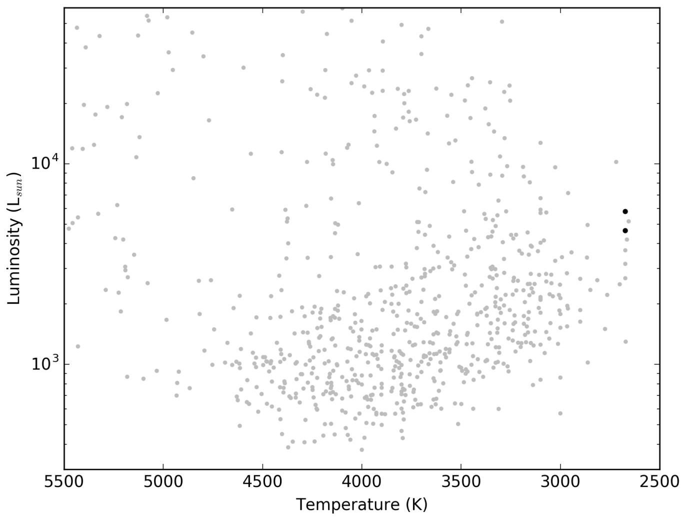

Figure 5.35: H–R diagram of the stellar population And IX (grey), with the variable objects identified by Boyer et al. (2015a) highlighted in black.

5.5.3.9 NGC 185

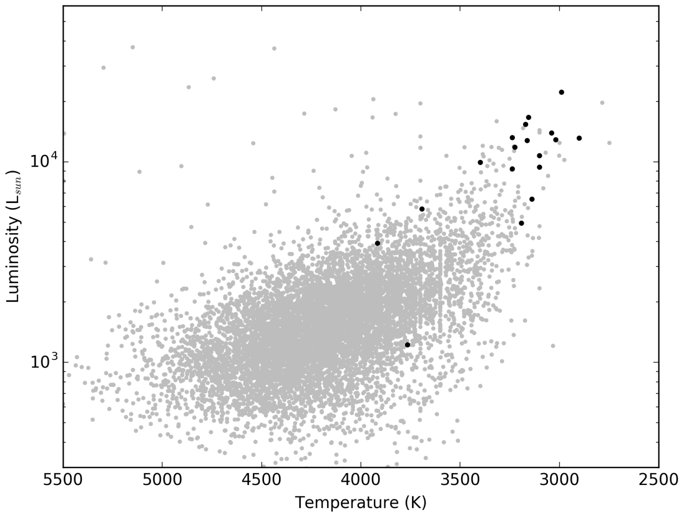

Figure 5.36: H–R diagram of the stellar population NGC 185 (grey), with the variable objects identified by Boyer et al. (2015a) highlighted in black.

5.5.3.10 NGC 147

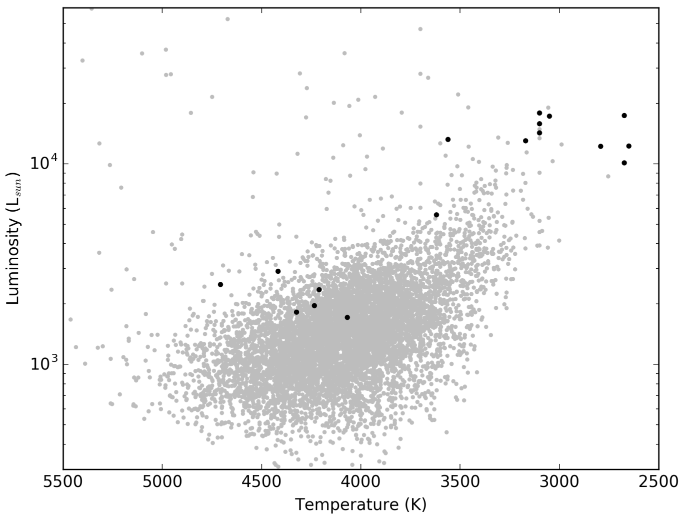

Figure 5.37: H–R diagram of the stellar population NGC 147 (grey), with the variable objects identified by Boyer et al. (2015a) highlighted in black.

5.6 Identification of carbon stars

For a number of the galaxies in the sample, previous studies had carried out carbon star censuses. The known carbon stars were matched to the SED-fit catalogs produced in this work, allowing for a comparison of the properties of C stars to the general AGB population.

5.6.1 IC 1613

Albert et al. (2000) identified 195 carbon stars in IC 1613. This identification is based on the difference in flux in CN and TiO filters, versus $V - I$ (or a scaled equivalent) on a colour–colour diagram, a method first demonstrated by Brewer et al. (1995) and Brewer et al. (1996). Carbon stars contain strong CN bands, while typical O-rich M stars contain strong TiO bands. When the difference between the two is plotted against a temperature discriminant (such as $V - I$), the populations became well-separated. 126 of these C stars were matched to the list of SED-fit objects in IC 1613 (using a tolerance of 1") and plotted on the finalised H–R diagram in Figure 5.38.

Figure 5.38 shows that many of the AGB stars $<$ 3700 K are carbon-rich. It can be seen that the fraction of these objects with a 3σ IR excess increases with decreasing temperature, with the majority of objects $> 3\sigma$ below 3300 K. For the C star population, T_{av} = 3297 K, L_{av} = 5715 $L_{\odot}$, and the average IR excess = 1.434 (compared with a median of 1.084 derived for the majority of the objects in the galaxy).

5.6.2 Sag DIG

Momany et al. (2014) provides a catalog of 22 C and O stars in the vicinity of Sag DIG, although the study suggests that a number of these may lie in the foreground. C stars were identified by the CN–TiO index. Additionally, a number

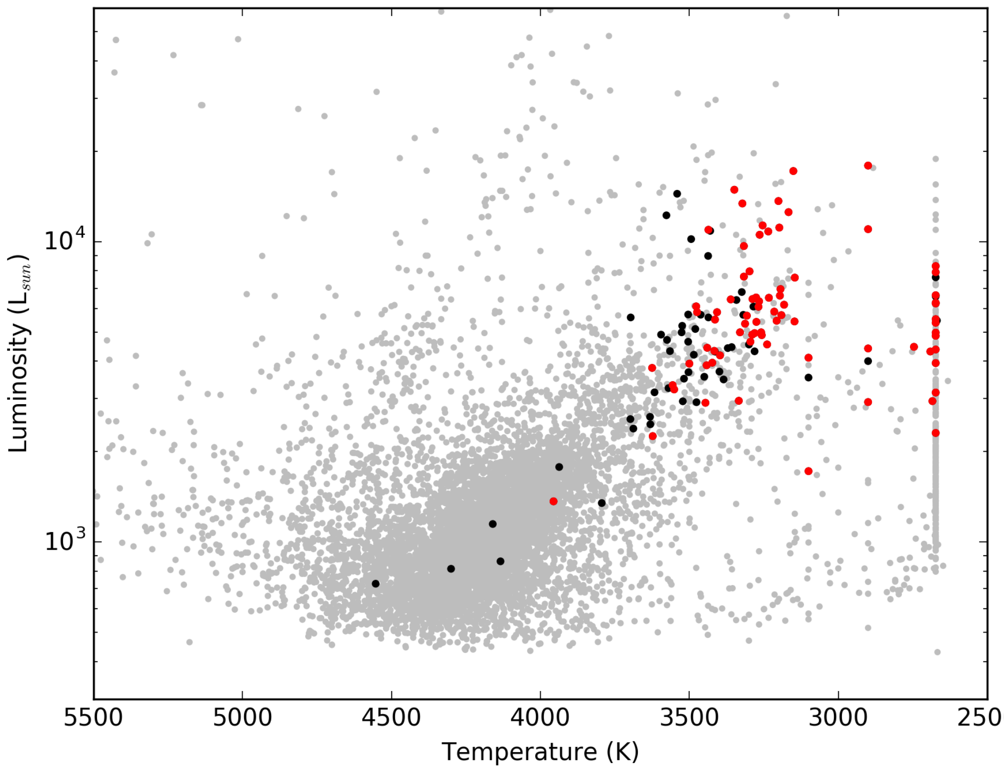

Figure 5.38: H–R diagram of the stellar population IC 1613 (grey), with C stars identified by Albert et al. (2000) highlighted in black and red (if the IR excess exceeds median + 3σ).

of O-rich stars were identified. This catalog was matched to the list of SED-fit objects in Sag DIG using a tolerance of 0.25", providing matches for 17 of the 22 C and O stars identified by Momany et al. (2014). Figure 5.39 shows the position of these objects on a H–R diagram.

Despite the low number of C stars identified in this galaxy, certain features can still be discussed. The two 3σ C stars are amongst the coolest and most-luminous AGB stars on the diagram, which fits with theory, as dustier stars (which would consequently have an IR excess) are expected to be more luminous and cooler. In addition the density of C stars increases with decreasing T. This suggests

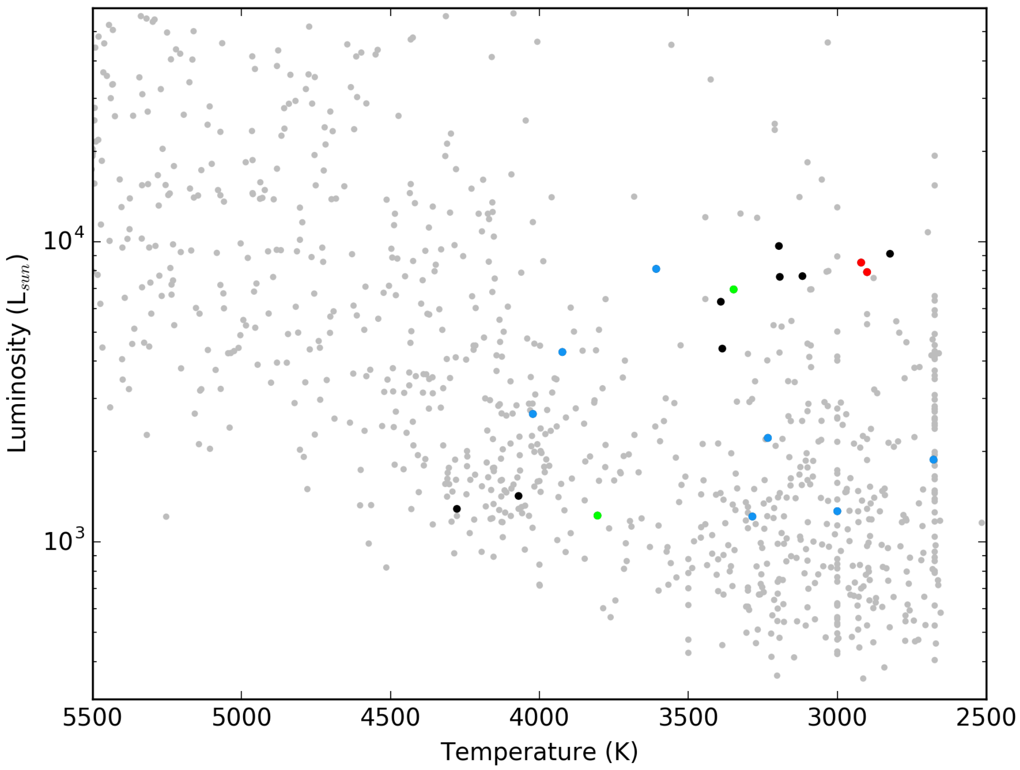

Figure 5.39: H–R diagram of the stellar population Sag DIG (grey), with C stars in the galaxy identified by Momany et al. (2014) highlighted in black and red (if the IR excess exceeds median $+ 3\sigma$). C stars believed to be in the foreground are coloured green, and O stars coloured blue.

that the SED fitting has been broadly successful, as C stars are expected to be cooler due to their higher atmospheric opacity. The four O stars in the region where background galaxies often appear may be correctly fit, as AGB stars of this this temperature and luminosity have been reported previously (McDonald et al. 2009). For the C star population, $T_{av} = 3327$ K, $L_{av} = 6398$ $L_{\odot}$, and average IR excess = 1.092 (compared with a median of 1.041 derived for the majority of the objects in the galaxy).

5.6.3 Peg DIG

A population of 40 C stars were identified in Peg DIG by Battinelli and Demers (2000). These were matched to the SED-fit catalog using a tolerance of 1", and displayed on the H–R diagram in Figure 5.39.

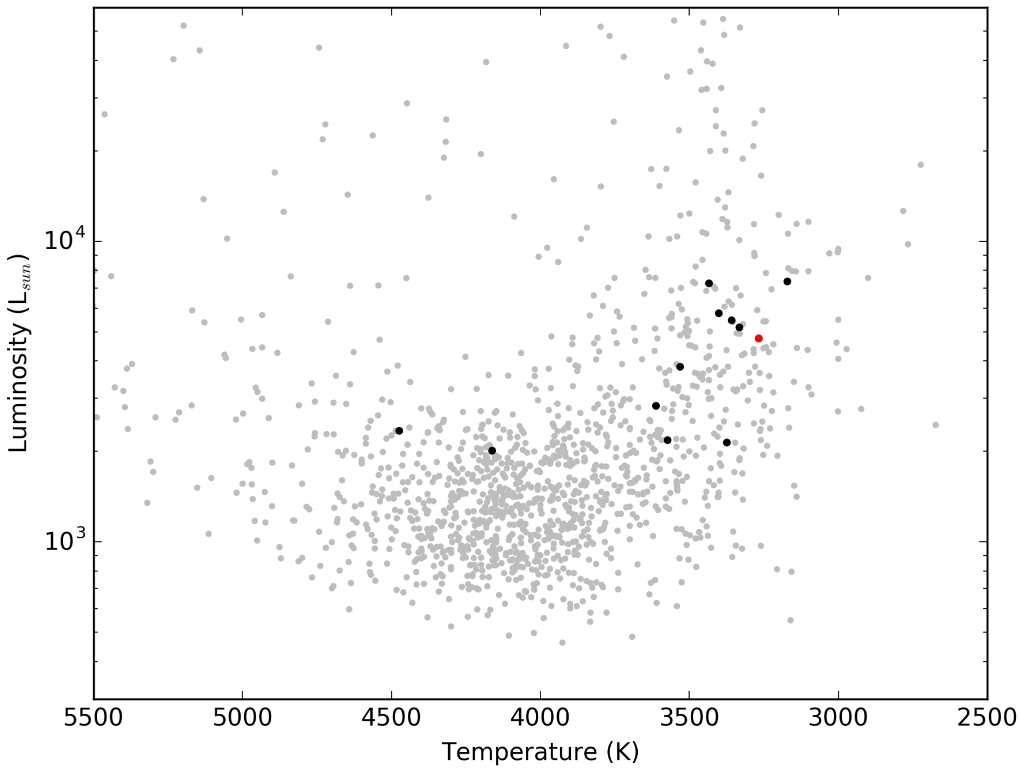

Figure 5.40: H–R diagram of the stellar population Peg DIG (grey), with C stars identified by Battinelli and Demers (2000) highlighted in black and red (if the IR excess exceeds median $+ 3\sigma$).

12 C stars were identified in this galaxy, one of which had a 3σ excess. Up to 28 C stars could not be matched to this work due to the crowding in optical photometry. This is one of the most luminous and coolest C stars in the galaxy. For the C star population, $T_{av} = 3557$ K, $L_{av} = 4257$ $L_{\odot}$, and average IR excess $= 1.124$ (compared with a median of 1.044 derived for the majority of the objects

in the galaxy).

5.6.4 WLM

A catalog of 149 C stars in WLM was produced by Battinelli and Demers (2004c), using the CN–TiO index. Objects with a match in our catalog (using a tolerance of 0.4”) are displayed in Figure 5.41.

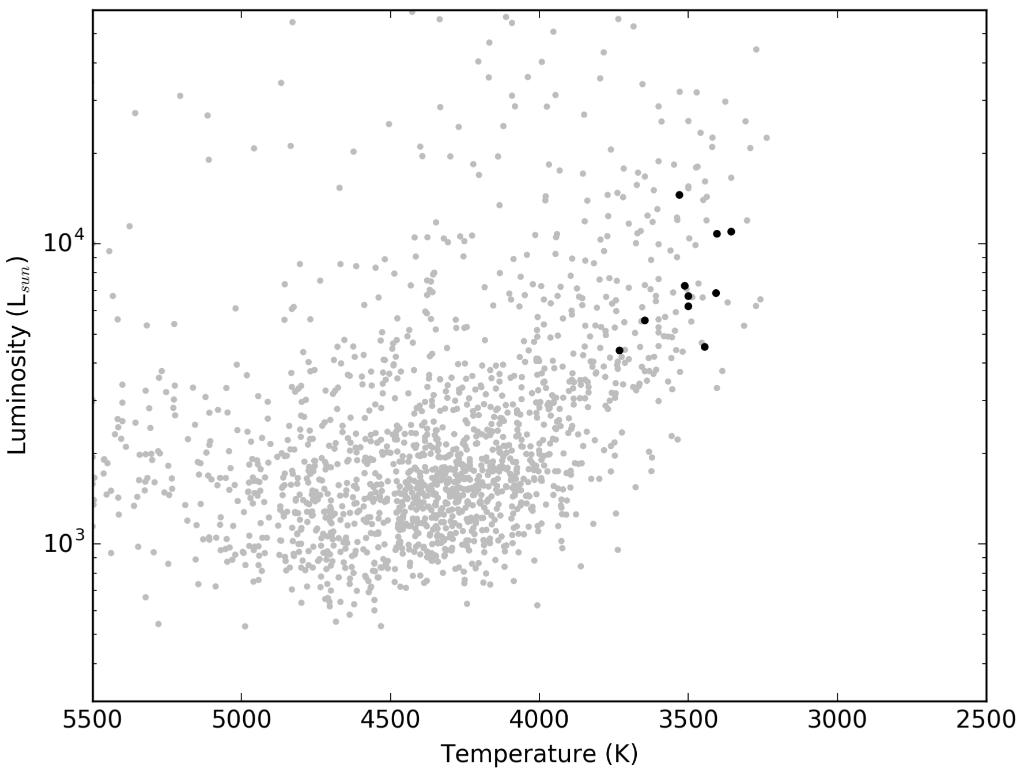

Figure 5.41: H–R diagram of the stellar population WLM (grey), with C stars identified by Battinelli and Demers (2004c) highlighted in black.

Of the 149 identified C stars, only 10 were successfully matched, none of which had a 3σ IR excess. This is likely due to the red photometric sensitivity limit present in this galaxy. Dusty AGB stars (especially C stars) produce a reduced optical flux due to the increased opacity in their atmospheres and of their dust. For this reason, these objects are less likely to be detected in optical observations. The 10 carbon stars seen are all clustered around 3500 K, slightly above the photometric cut-off. They constitute a large fraction of the AGB in this region. For the C star population, $T_{av} = 3503$ K, $L_{av} = 7773$ $L_{\odot}$, and average IR excess = 1.200 (compared with a median of 1.256 derived for the majority of the objects in the galaxy, more evidence that the optical photometry for this galaxy is unreliable).

5.6.5 NGC 6822

Sibbons et al. (2012) produced a list of 698 carbon stars in NGC 6822, as well as identifying 1242 other M-type stars which can be assumed to be oxygen-rich. The separation of the two groups was achieved using $J - K$ magnitudes on a CMD. This photometry was used as part of the catalog produced in this work, so additional matching was not required. The objects identified here were plotted on the H–R diagram in Figure 5.42.

Only 48 C stars and 277 O stars were SED fit, likely for similar reasons as WLM, as this galaxy appears to have a similar cut-off in optical photometry. It is not possible to identify the 3σ sources in this galaxy as it was lacking the necessary mid-IR photometry needed to calculate the IR excess. It can be seen that although the majority of stars are O-rich, the fraction of C stars to O stars increases with decreasing temperature. More C stars than O stars are present ~ 3500 K, a trend expected to continue below this point if the photometry allowed this region to be SED-fit. The scatter of O stars seen above 7000 $L_{\odot}$ are likely predominantly Galactic foreground stars rather than supergiants in this galaxy, as NGC 6822 lies close to the Galactic plane. For the C star population, $T_{av} = 3639$ K, $L_{av} = 4261$ $L_{\odot}$.

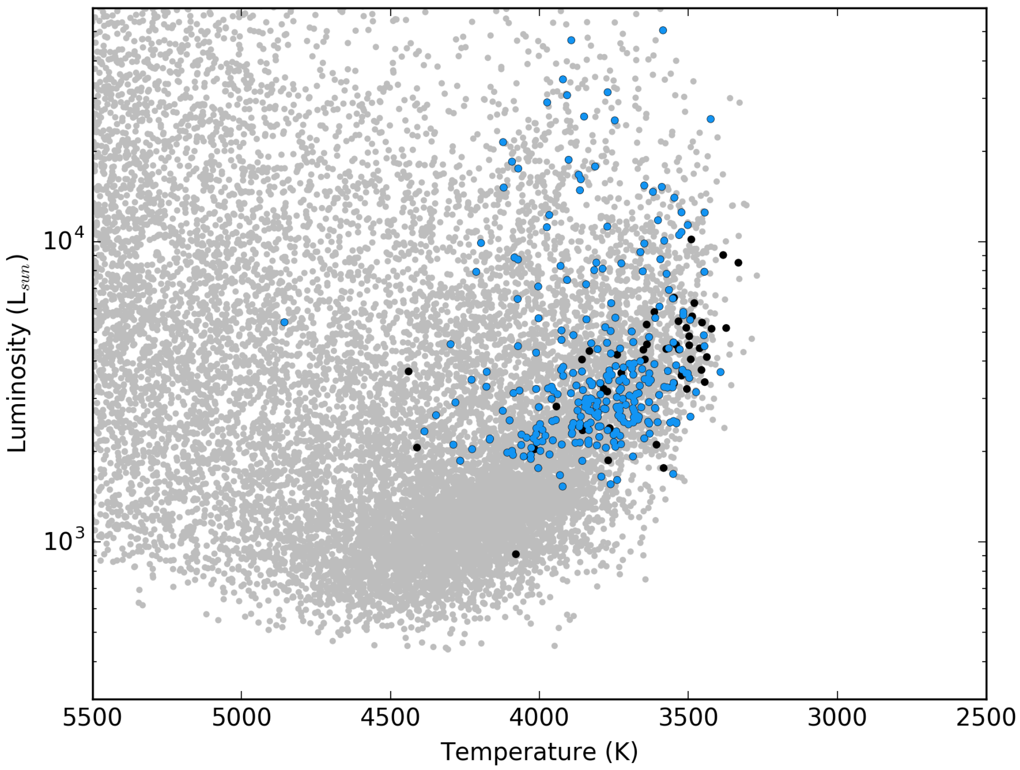

Figure 5.42: H–R diagram of the stellar population NGC 6822 (grey), with C stars identified by Sibbons et al. (2012) highlighted in black and O stars in blue.

5.6.6 NGC 185

Battinelli and Demers (2004b) identified 144 carbon stars in NGC 185 using the CN–TiO index technique. These were matched to the catalog produced in this work using a tolerance of 0.5" and plotted in Figure 5.43.

Only 32 of the 105 C stars in the field of view were matched to the final catalog. Up to 12 C stars were missed from the sample due to the crowding in mid-IR photometry. The majority of the carbon stars can be seen at $T < 3600$ K. Only two of the matched carbon stars have a 3σ IR excess, and they are not near

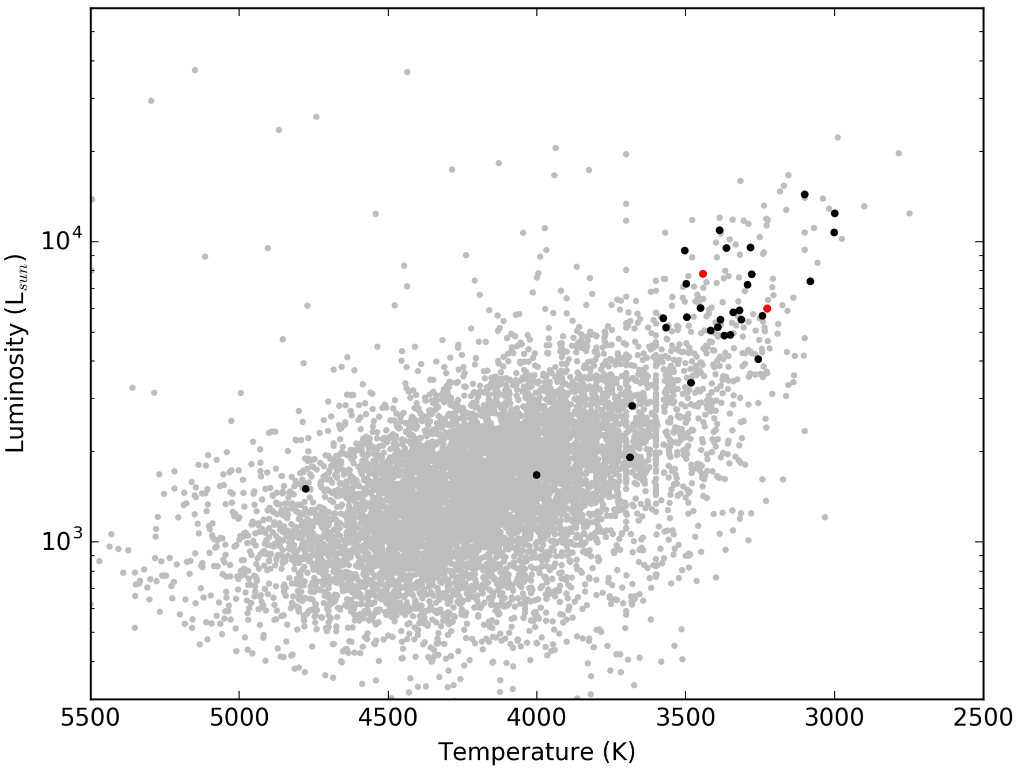

Figure 5.43: H–R diagram of the stellar population NGC 185 (grey), with C stars identified by Battinelli and Demers (2004b) highlighted in black and red (if the IR excess exceeds median + 3σ).

the lower limit of the temperature range. For the C star population, $T_{av} = 3423$ K, $L_{av} = 6449$ $L_{\odot}$, and average IR excess = 1.049 (compared with a median of 0.977 derived for the majority of the objects in the galaxy).

5.6.7 NGC 147

Battinelli and Demers (2004a) identified 288 carbon stars in NGC 147 using the CN–TiO index. These were matched to the catalog produced in this work using a tolerance of 0.55" and plotted in Figure 5.43.

Out of the 288 identified C stars (only 105 of these were in the field of view),

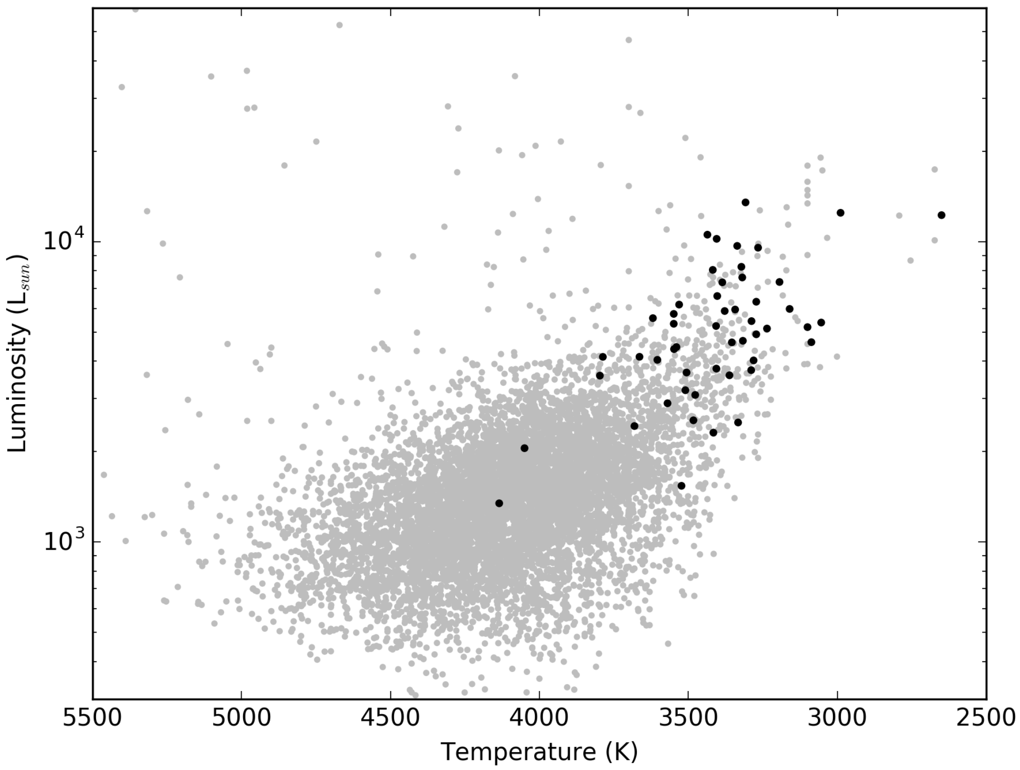

Figure 5.44: H–R diagram of the stellar population NGC 147 (grey), with C stars identified by Battinelli and Demers (2004a) highlighted in black.

51 were matched to the final catalog. Similar to NGC 185, the majority of them are seen at $T < 3600$ K. No C stars have an IR excess greater than 3σ, surprising considering the low variance of this galaxy ($\sigma = 0.047$). For the C star population, $T_{av} = 3411$ K, $L_{av} = 5557$ L$_\odot$, and average IR excess = 1.057 (compared with a median of 1.022 derived for the majority of the objects in the galaxy).

5.7 Constraints on carbon star formation

Following the identification of carbon stars in the dIrr sample (Section 5.6), further analyses were carried out to better constrain the conditions under which they can form.

5.7.1 Less-luminous carbon stars

In the H–R diagrams in Section 5.6, it can be seen that for most of the galaxies, there are one or more C stars identified at a T and L that place it among the RGB. Although this is a location for which the presence of AGB stars is not surprising, the lack of other carbon stars in this region requires further investigation. Some values of σ_T and σ_L may allow the natural scatter of a C star that should be placed towards the AGB tip in the RGB, but these objects appear infrequently and with little scatter between this region and the region in which most dusty stars are found, suggesting this cannot account for all of these objects. A total of 19 of these stars were identified: seven in IC 1613, two in Sag DIG, two in Peg DIG, one in NGC 6822, four in NGC 185, and three in NGC 147.

The SEDs of all these objects were well fit, suggesting that these are in fact broadly correct values of T and L. These are most likely extrinsic C stars, less-evolved objects that have obtained a C-rich atmosphere via mass transfer from a (now WD) companion, (Section 1.4.3.4). Alternatively, these could be misidentifications of M stars as C stars. Regardless, it is unlikely that these objects are intrinsic C stars, and for that reason are not included in the remainder of the C star analysis.

5.7.2 Mass constraints

Paczyński (1970) found a linear relation between the luminosity of an evolved star and its core mass, M_C (L and M all in solar units in this Section):

$$L = 59250(M_C - 0.522). \tag{5.2}$$

It has been shown that although this relation breaks down in > 7 M$_\odot$ models, the core mass-luminosity relation remains valid for objects below this initial mass (Bloecker and Schoenberner 1991). Using the initial–final mass relation (Kalirai et al. 2008):

$$M_{final} = 0.109 M_{initial} + 0.394, \tag{5.3}$$

and approximating $M_C = M_{final}$, Equations 5.2 and 5.3 can be rearranged to give:

$$M_{initial} = 9.17 \left(\frac{L}{59250} + 0.128 \right). \tag{5.4}$$

Equation 5.4 is therefore a guide to find the initial mass of an evolved star using its current luminosity. However, there are several caveats to be considered when using this relation. Firstly, it is likely to suffer from a considerable level of uncertainty. Although not presented in the version in this work, Kalirai et al. (2008) include significant uncertainties for Equation 5.3. Additionally, the approximation of $M_C = M_{final}$ is inexact, and metallicity is not taken into account at any point. Therefore, exact values of $M_{initial}$ are not presented with confidence, but should be considered an approximate value. Secondly, it cannot be assumed that the current luminosity is the final luminosity. L increases over the course of the TP-AGB, so the given $M_{initial}$ is lower limit of initial mass. Additionally, there is intrinsic uncertainty in the photometric measurements, causing additional variation in T and L (Section 5.1). The range of masses calculated here is likely smaller than the true range, suggesting that upper and lower mass limits are artificially increased and decreased respectively. Finally, this method can only provide $M_{initial} > 1.17$ M$_{\odot}$ (occurring when L is set as zero). However, this only rules out a small range of C star stellar masses; objects with $M_{initial} \lesssim 0.9$ M$_{\odot}$ could not yet have evolved to the point where they could become carbon-rich, as it would require an age older than the Universe. Equation 5.4 may therefore artificially increase the mass of the least-luminous evolved sources, though this is unlikely to be an issue for the carbon stars found in this sample.

The luminosity distribution of the intrinsic carbon stars is displayed in Figure 5.45. The distribution appears to peak ~ 5000 $L_{\odot}$, with slopes of equal gradient (in the logartihmic scale) descending on either side.

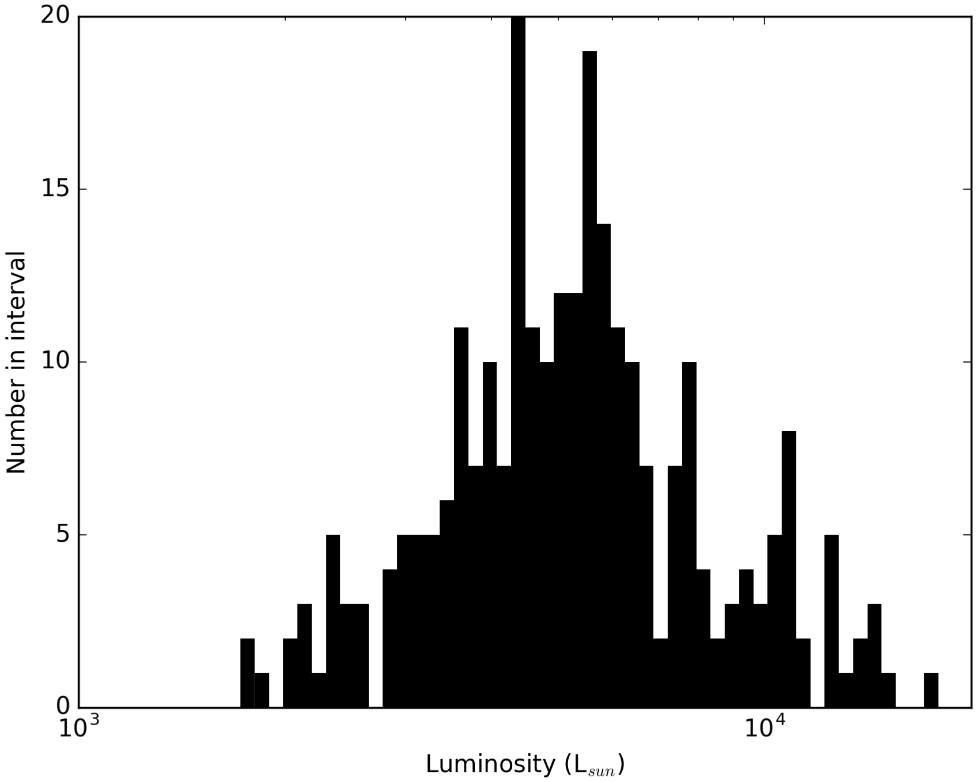

Figure 5.45: Histogram representing the luminosity distribution of a sample of 270 carbon stars from six dIrr galaxies.

$M_{initial}$ was calculated for each of the 270 intrinsic C stars in the sample, with the results displayed in a histogram (Figure 5.46). Also included is a representation of the initial-mass function (IMF), the distribution of initial masses for a stellar population. This is scaled so it intersects with the peak of the histogram, and was produced using the relation $N \propto M_{intial}^{-2.3}$, valid for $M_{intial} > 1$ $M_{\odot}$ (Kroupa 2001).

Figure 5.46 shows that in the sample, there are no carbon stars of $M_{intial} \lesssim 1.4$

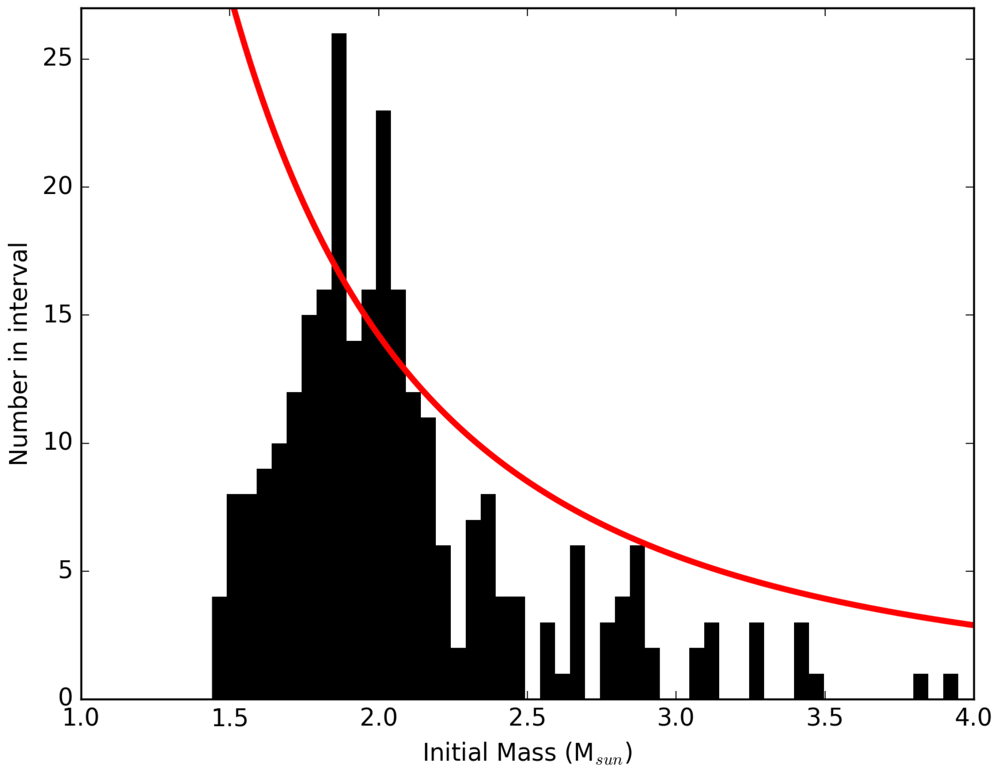

Figure 5.46: Histogram representing the mass distribution of a sample of 270 carbon stars from six dIrr galaxies. The red line is a representation of the IMF.

M$_\odot$. This lower limit with a sharp cut-off compares to model values (at comparable metallicity) of 0.9 M$_\odot$ from Marigo and Girardi (2007) and 1.0 M$_\odot$ from Fishlock et al. (2014). There are two peaks in the C star abundance, at $\sim$ 1.8 and $\sim$ 2.0 M$_\odot$. Few C stars can be seen above 3 M$_\odot$, with only two C stars with M_{intial} > 3.5 M$_\odot$. It is difficult to say with certainty whether this represents the upper limit at which carbon stars can form (due to HBB; Karakas and Lattanzio 2014), or whether there are simply too few stars above this mass to be sampled due to the IMF. It is clear that independently to the IMF, the C star formation "efficiency" decreases at masses greater than the peak. This may be due to the fact that lower-mass stars spend a longer time as in the TP-AGB, allowing for more time for dredge-up to occur (Dell'Agli et al. 2016). They are also younger, so likely at a higher metallicity, and therefore requiring more-powerful dredge-up events to become a C star. From this work, it appears probable that the upper limit of C star formation is $3.5 - 5.0$ M$_\odot$. This compares to model values of $\sim$ 5 M$_\odot$ from Marigo and Girardi (2007), 7.0 M$_\odot$ from Fishlock et al. (2014), and $2.5 - 3.0$ M$_\odot$ from Ventura et al. (2016).

Four galaxies in the sample contained a C star population numerous enough for an individual analysis of their mass distribution.

5.7.2.1 IC 1613

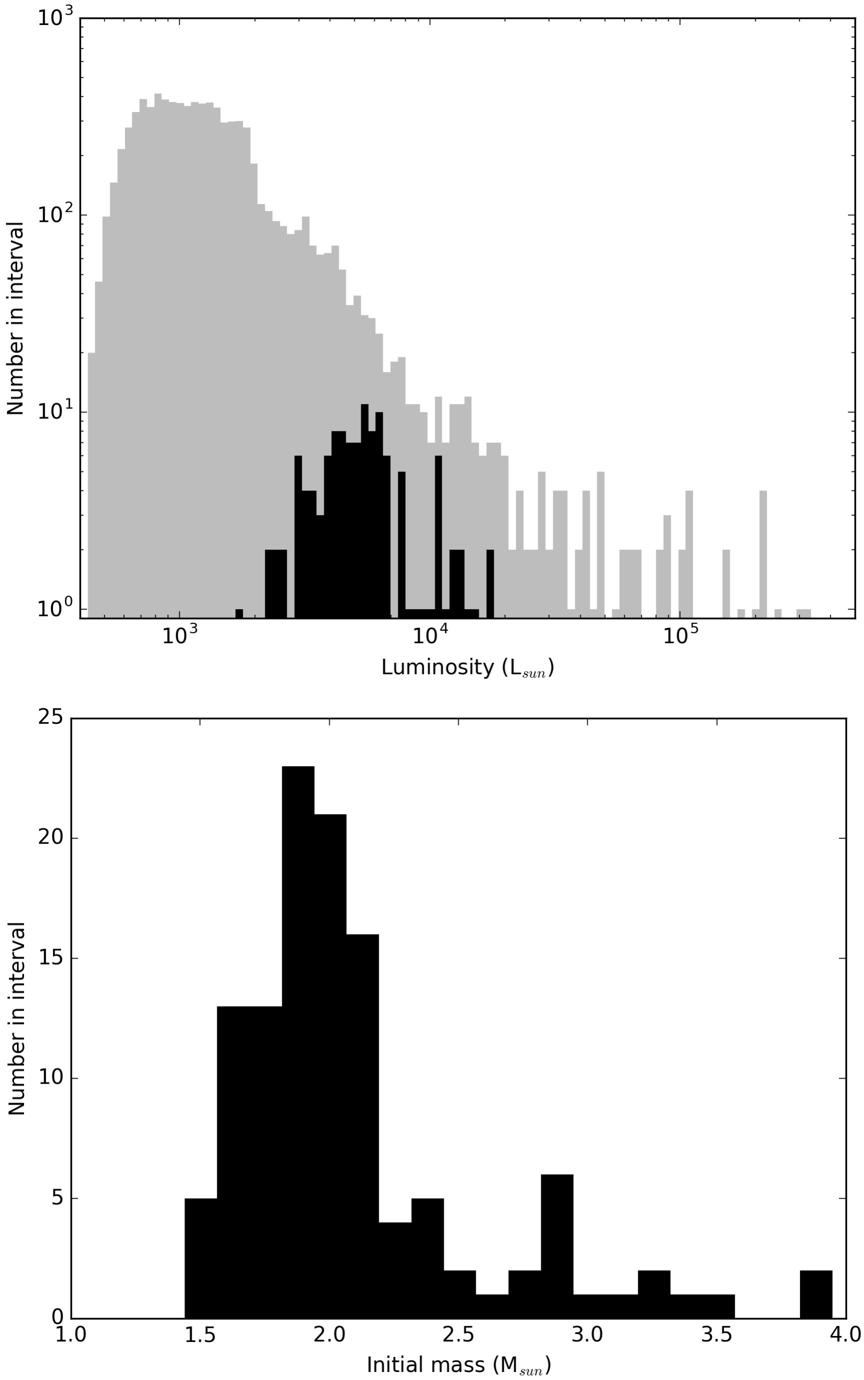

Figure 5.47: (a) Histogram showing the luminosity of C stars (black) and the general SED-fit population (grey) in IC 1613; (b) Histogram showing the range of masses of the C star population of IC 1613.

5.7.2.2 NGC 6822

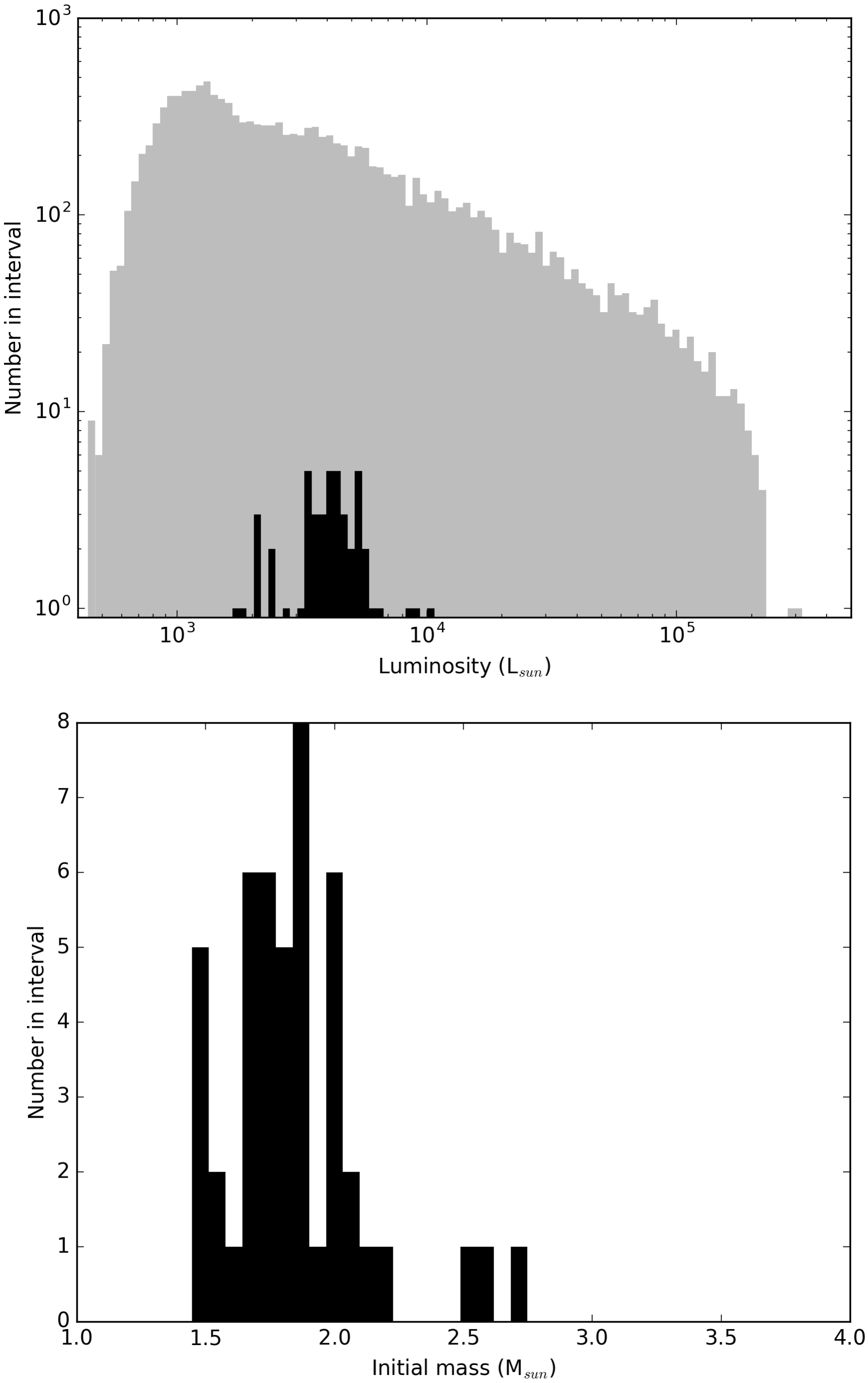

Figure 5.48: (a) Histogram showing the luminosity of C stars (black) and the general SED-fit population (grey) in NGC 6822; (b) Histogram showing the range of masses of the C star population of NGC 6822.

The addition of matched O stars in the sample allows for additional comparisons to be made. Figure 5.49 shows how the relative abundances of C and O stars vary with L. The C/O star ratio is only greater than unity in the luminosity range $4000 \lesssim L \lesssim 4500$ L$_\odot$, corresponding to masses ~ 1.8 M$_\odot$ (around the peak of Figure 5.48 (b)). The relatively high bulk metallicity ([Fe/H] = -1.0 dex), making it more difficult for C stars to form, likely prevents this from occurring at a wider range of metallicities.

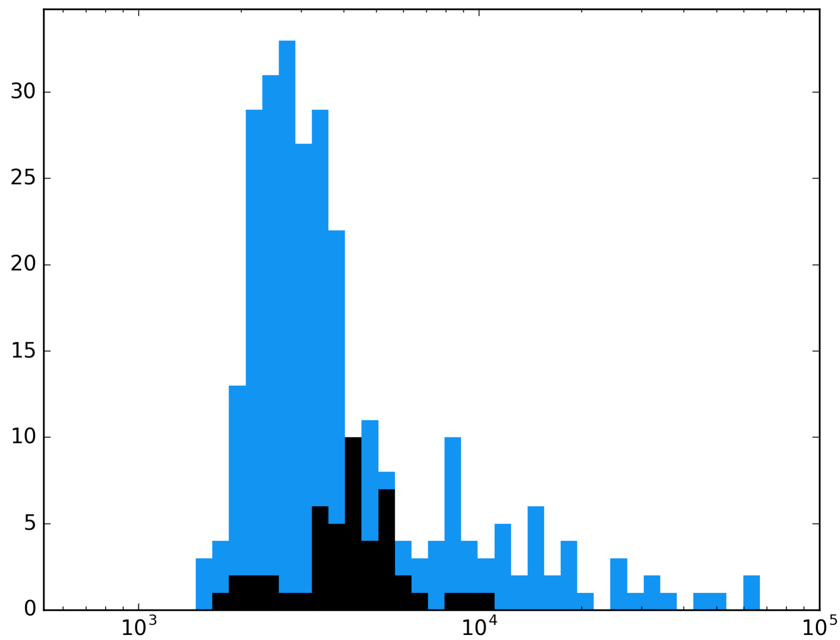

Figure 5.49: Histogram showing the populations of C stars (black) and O stars (blue) in NGC 6822 at a range of luminosities.

5.7.2.3 NGC 185

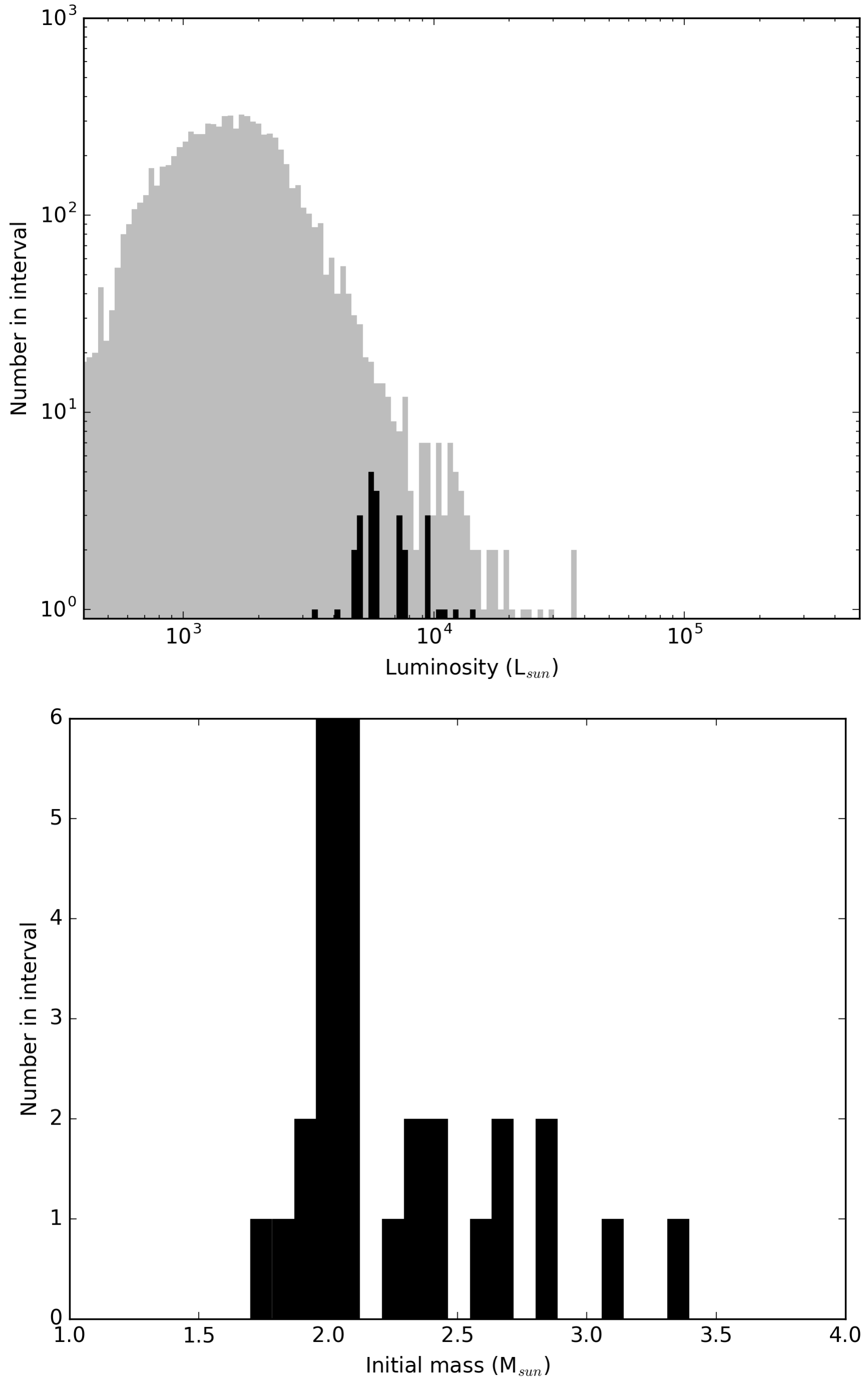

Figure 5.50: (a) Histogram showing the luminosity of C stars (black) and the general SED-fit population (grey) in NGC 185; (b) Histogram showing the range of masses of the C star population of NGC 185.

5.7.2.4 NGC 147

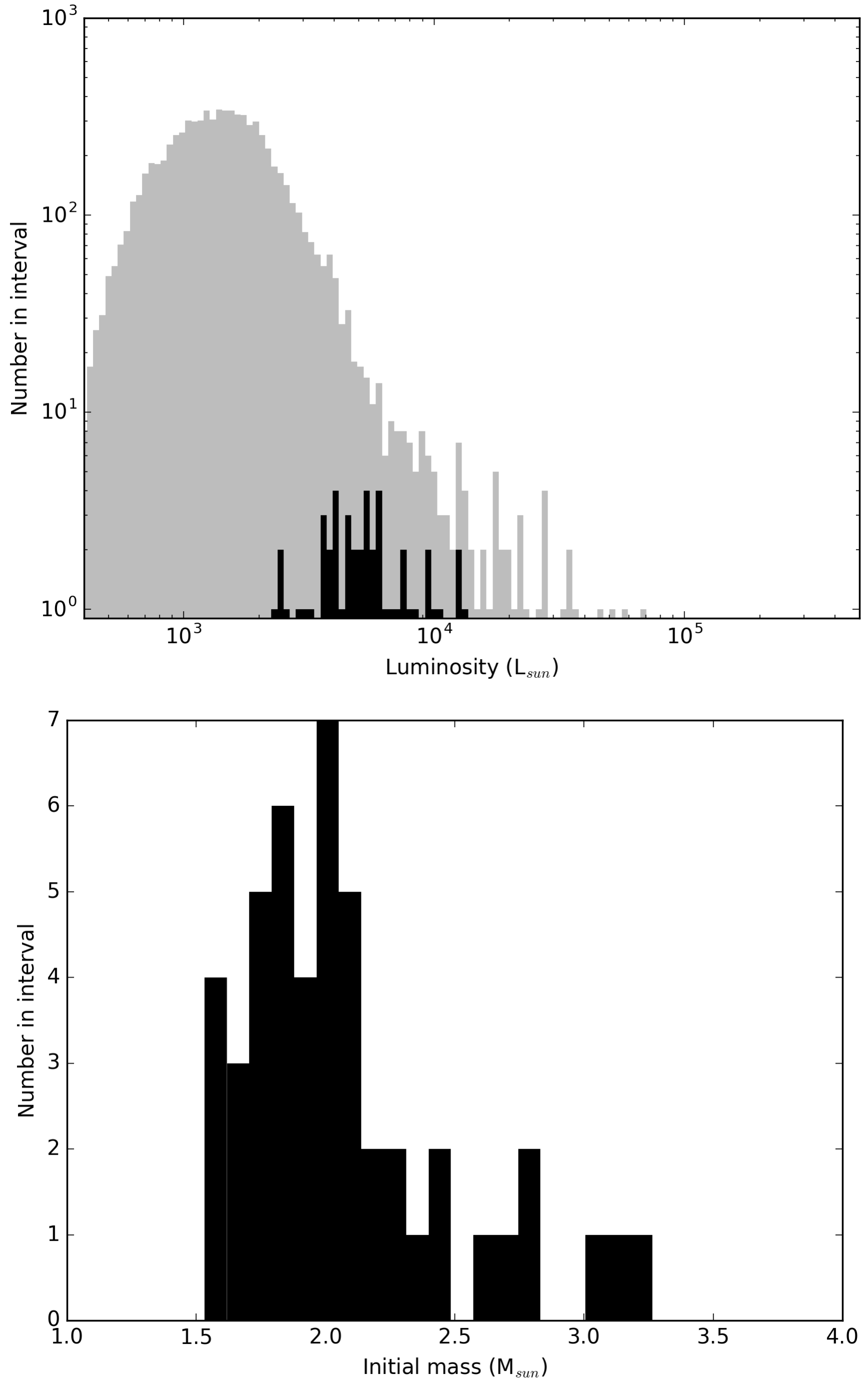

Figure 5.51: (a) Histogram showing the luminosity of C stars (black) and the general SED-fit population (grey) in NGC 147; (b) Histogram showing the range of masses of the C star population of NGC 185.

5.7.2.5 Overview

The histograms of the general galactic population are approximately the same shape in three galaxies, with the exception of NGC 6822, which could be caused by the systematically offset SED fitting, due to lack of mid-IR data and photometric limitations (Section 5.1). Similarly, the distribution of C star luminosity is broadly constant across the sample. Converting these luminosities to $M_{initial}$ shows that the C star abundance of NGC 6822 peaks at around 1.8 $M_{\odot}$, lower than the other galaxies and causing the corresponding peak in Figure 5.46, likely caused by the missing mid-IR data. The location of the C star peak should probably be closer to the $\sim$ 2 $M_{\odot}$ seen in the other galaxies. The lower mass of the C star distribution is broadly consistent across the four galaxies, although the upper limit varies considerably. Due to the lack of stars around this mass range it is impossible to confidently define an upper limit to C star mass (beyond that discussed in Section 5.7) and determine any variation with metallicity. For the same reason, it is difficult to determine any relation between upper and lower mass-limits of C stars with metallicity. More precise observations from the *James Webb Space Telescope* will provide deeper and more accurate photometry, allowing for further constraints to be made.

5.8 Further research

The work carried out in this study suggests several avenues of further research that could improve and build upon the results presented here.

A relatively simple improvement would be the inclusion of mid-IR *Spitzer* photometry for NGC 6822. This galaxy has a large number of stars (both oxygen- and carbon-rich) and has excellent photometry in optical and near-IR bands. The addition of mid-IR photometry would allow for more reliable comparisons between this galaxy and the rest of the sample. This photometry has already been taken, but had not been reduced at the time of writing. More *Spitzer* photometry of the entire dIrr sample at varying epoch divisions would provide more accurate values of the period and amplitude of the variable AGB population, removing many of the limitations encountered in this work and Boyer et al. (2015a) when trying to study these features. This additional data would have the added improvement of reducing the impact of variability on the [3.6] and [4.5] photometry used in the SED fitting process, returning more accurate temperatures and luminosities of variable objects.

Observations of CN and TiO spectral lines would allow for the identification of carbon stars in more dIrrs in this sample. An SED-fit analysis on larger populations of C stars would allow for a better determination of their mass limits (particularly at the upper limit) and a better understanding of the relationship between T, L and the IR excess. This is expected soon in a study by Boyer et al. (in preparation).

A significant improvement would be more consistent and reliable sources of optical and near-IR photometry, such as the data coming from a scheduled project on the VLT. Firstly, this would allow for more accurate and consistent values of the IR excess from the SED-fit [3.6] and [4.5] bands, allowing for better comparison between galaxies. Additionally, this superior photometry could extend our sample to include a number of dIrrs that could not be studied in this work, namely Aquarius, NGC 3109, IC 10, NGC 5, UGCA 438, and Antlia. This would allow for an analysis of dusty AGB stars in a wider variety of stellar environments. Of the sample studied in this work, deep near-IR photometry should be a priority for all galaxies with the exception of NGC 6822. Deep optical photometry would be most useful for Peg DIG, WLM, LGS 3, and And IX. Identification of interesting objects using this VLT data will provide targets for observation with the *James Webb Space Telescope* (*JWST*). As well as producing far more accurate and deeper photometry than is currently available, a spectroscopic study from *JWST* will improve our understanding of dust composition, and lead to improved models of AGB mass-loss and the evolution of dust in the ISM.

JWST will also be able to return photometry in mid-IR bands, at wavelengths of > 5 μm. This will allow for the detection of far more O-rich objects and allow for better characterization of the IR-excess. Additionally, the point spread function of the telescope's photometry will be comparable to that of *HST*, allowing for source matching between datasets at a far higher precision than is currently possible, producing more accurate SEDs.

Chapter 6

Conclusion

An investigation of the resolved stellar populations of 13 nearby (< 1.5 Mpc) dIrr galaxies was carried out, as their metal-poor evolved stars present an opportunity to study stellar evolution in the early Universe. In order to do this, catalogs comprising photometry in a wide range of wavelengths were compiled, and used to produce the SEDs of objects in the sample of galaxies. From this, the temperature, luminosity, and IR excess of each object could be calculated.

New distance estimates to a number of these dIrrs were produced by comparing the luminosity of the RGB tip with isochrones. These new findings are presented in Table 6.1. Additionally, the metallicities of some of the least-studied dIrrs ware suggested to be significantly different than literature values. These new findings are presented in Table 6.2.

By combining the H–R diagrams of every dIrr in the sample, the "typical" dIrr population was determined. By fitting an isochrone to this diagram, it can be seen that it is comparable to a population of age 10 Gyr, with [Fe/H] $= -1.6$ dex. This is akin to the predominant stellar populations in Sex B, Sag DIG, and Phoenix. These galaxies may therefore be considered archetypal dIrrs.

Table 6.1: Table presenting new estimates of the distance to several dIrrs. All distances are given in kpc.

Galaxy	Literature distance	Newly-derived distance
Sextans B	1426	1310
Sextans A	1432	1310
Sag DIG	1067	990
Peg DIG	920	820
Phoenix	415	460
NGC 185	617	550

Table 6.2: Table presenting new estimates of the metallicity of the bulk stellar population of several dIrrs. All metallicities are given in dex.

Galaxy	Literature [Fe/H]	Newly-derived [Fe/H]
Sag DIG	-2.2	-1.6
Leo A	-1.4	-1.9
And IX	-2.2	-1.4

A comparison between the IR excess calculated in this work and the variability data from Boyer et al. (2015a) found very little relation between the strength of the IR excess and the amplitude of pulsation. This may be due to the imprecise variability data from the originating study, with only two epochs of data for most stars, and the fact that the bands used to calculate the IR excess only reliably measure carbon dust. This means that many oxygen-rich stars will not have been detected as dusty. A correlation between the strength of the IR excess and an indicator of dust production was found, but this is to be expected, as both measures used the same sources of photometry.

Finally, known carbon stars were compared to the catalogs produced in this work for the seven galaxies for which C star surveys had been carried out. It was found that with several exceptions (likely extrinsic C stars), these stars were generally among the coolest and most-luminous objects in the dIrrs, as expected. Estimates of the initial mass of these objects were approximated using the core mass–luminosity relation and the initial–final mass relation. It was found that there was a strong cut-off at the lower limit of ~ 1.4 M$_\odot$, higher than theoretical predictions at the range of metallicities found in the dIrrs (although this may be somewhat systematically inflated). The upper limit of $3.5 - 5.0$ M$_\odot$, although more difficult to define due to the lack of stars at this mass range, was more in line with theoretical predictions (Marigo and Girardi 2007; Fishlock et al. 2014; Ventura et al. 2016). The abundance of carbon stars was found to peak at ~ 2.0 M$_\odot$.

A scheduled study using the VLT will improve on the work presented here by providing a more consistent source of optical and near-IR photometry. Looking further ahead, studies using *JWST* will likely revolutionise our understanding of AGB stars, producing photometry and spectra significantly more accurate than anything available presently.

Bibliography

AAVSO (2012). Types of variables. http://www.aavso.org/types-variables.

Adelman-McCarthy, J. K., Agüeros, M. A., Allam, S. S., Allende Prieto, C., Anderson, K. S. J., Anderson, S. F., Annis, J., Bahcall, N. A., Bailer-Jones, C. A. L., Baldry, I. K., Barentine, J. C., Bassett, B. A., Becker, A. C., Beers, T. C., Bell, E. F., Berlind, A. A., Bernardi, M., Blanton, M. R., Bochanski, J. J., Boroski, W. N., Brinchmann, J., Brinkmann, J., Brunner, R. J., Budavári, T., Carliles, S., Carr, M. A., Castander, F. J., Cinabro, D., Cool, R. J., Covey, K. R., Csabai, I., Cunha, C. E., Davenport, J. R. A., Dilday, B., Doi, M., Eisenstein, D. J., Evans, M. L., Fan, X., Finkbeiner, D. P., Friedman, S. D., Frieman, J. A., Fukugita, M., Gänsicke, B. T., Gates, E., Gillespie, B., Glazebrook, K., Gray, J., Grebel, E. K., Gunn, J. E., Gurbani, V. K., Hall, P. B., Harding, P., Harvanek, M., Hawley, S. L., Hayes, J., Heckman, T. M., Hendry, J. S., Hindsley, R. B., Hirata, C. M., Hogan, C. J., Hogg, D. W., Hyde, J. B., Ichikawa, S.-i., Ivezić, Ž., Jester, S., Johnson, J. A., Jorgensen, A. M., Jurić, M., Kent, S. M., Kessler, R., Kleinman, S. J., Knapp, G. R., Kron, R. G., Krzesinski, J., Kuropatkin, N., Lamb, D. Q., Lampeitl, H., Lebedeva, S., Lee, Y. S., French Leger, R., Lépine, S., Lima, M., Lin, H., Long, D. C., Loomis, C. P., Loveday, J., Lupton, R. H., Malanushenko, O., Malanushenko, V., Mandelbaum, R., Margon, B., Marriner, J. P., Martínez-Delgado, D., Matsubara, T., McGehee, P. M., McKay, T. A., Meiksin, A., Morrison, H. L., Munn, J. A., Nakajima, R., Neilsen, Jr., E. H., Newberg, H. J., Nichol, R. C., Nicinski, T., Nieto-Santisteban, M., Nitta, A., Okamura, S., Owen, R., Oyaizu, H., Padmanabhan, N., Pan, K., Park, C., Peoples, Jr., J., Pier, J. R., Pope, A. C., Purger, N., Raddick, M. J., Re Fiorentin, P., Richards, G. T., Richmond, M. W., Riess, A. G., Rix, H.-W., Rockosi, C. M., Sako, M., Schlegel, D. J., Schneider, D. P., Schreiber, M. R., Schwope, A. D., Seljak, U., Sesar, B., Sheldon, E., Shimasaku, K., Sivarani, T., Allyn Smith, J., Snedden, S. A., Steinmetz, M., Strauss, M. A., SubbaRao, M., Suto, Y., Szalay, A. S., Szapudi, I., Szkody, P., Tegmark, M., Thakar, A. R., Tremonti, C. A., Tucker, D. L., Uomoto, A., Vanden Berk, D. E., Vandenberg, J., Vidrih, S., Vogeley, M. S., Voges, W., Vogt, N. P., Wadadekar, Y., Weinberg, D. H., West, A. A., White, S. D. M., Wilhite, B. C., Yanny, B., Yocum, D. R., York, D. G., Zehavi, I., and Zucker, D. B. (2008). The Sixth Data Release of the Sloan Digital Sky Survey. *ApJS*, 175:297–313.

Ahn, C. P., Alexandroff, R., Allende Prieto, C., Anderson, S. F., Anderton, T., Andrews, B. H., Aubourg, É., Bailey, S., Balbinot, E., Barnes, R., and et al. (2012). The Ninth Data Release of the Sloan Digital Sky Survey: First Spectroscopic Data from the SDSS-III Baryon Oscillation Spectroscopic Survey. *ApJS*, 203:21.

Albert, L., Demers, S., and Kunkel, W. E. (2000). A Carbon Star Survey of the Local Group Dwarf Galaxies. I. IC 1613. *AJ*, 119:2780–2788.

Allard, F., Guillot, T., Ludwig, H.-G., Hauschildt, P. H., Schweitzer, A., Alexander, D. R., and Ferguson, J. W. (2003). Model Atmospheres and Spectra: The Role of Dust. In Martín, E., editor, *Brown Dwarfs*, volume 211 of *IAU Symposium*, page 325.

Allard, F., Homeier, D., and Freytag, B. (2012). Models of very-low-mass stars, brown dwarfs and exoplanets. *Philosophical Transactions of the Royal Society of London Series A*, 370:2765–2777.

Aoki, W., Beers, T. C., Christlieb, N., Norris, J. E., Ryan, S. G., and Tsangarides, S. (2007). Carbon-enhanced Metal-poor Stars. I. Chemical Compositions of 26 Stars. *ApJ*, 655:492–521.

Aparicio, A. and Gallart, C. (1995). The Stellar Content of the Pegasus Dwarf Irregular Galaxy. *AJ*, 110:2105.

Aparicio, A., Gallart, C., and Bertelli, G. (1997a). The Star Formation History of the Pegasus Dwarf Irregular Galaxy. *AJ*, 114:669–679.

Aparicio, A., Gallart, C., and Bertelli, G. (1997b). The Stellar Content and the Star Formation History of the Local Group Dwarf Galaxy LGS 3. *AJ*, 114:680–693.

Asplund, M., Grevesse, N., Sauval, A. J., and Scott, P. (2009). The Chemical Composition of the Sun. *Annual Review of Astron and Astrophys*, 47:481–522.

Battaglia, G., Rejkuba, M., Tolstoy, E., Irwin, M. J., and Beccari, G. (2012). A wide-area view of the Phoenix dwarf galaxy from Very Large Telescope/FORS imaging. *MNRAS*, 424:1113–1131.

Battaglia, G., Tolstoy, E., Helmi, A., Irwin, M., Parisi, P., Hill, V., and Jablonka, P. (2011). VizieR Online Data Catalog: CaII triplet in Sextans dSph galaxy (Battaglia+, 2011). *VizieR Online Data Catalog*, 741.

Battinelli, P. and Demers, S. (2000). A Carbon Star Survey of the Local Group Dwarf Galaxies. II. Pegasus, DDO 210, and Tucana. *AJ*, 120:1801–1807.

Battinelli, P. and Demers, S. (2004a). Carbon star survey in the Local Group. VIII. Probing the stellar halo of NGC 147. *A&A*, 418:33–40.

Battinelli, P. and Demers, S. (2004b). Carbon star survey of Local Group galaxies. IX. The spheroidal galaxy NGC 185. *A&A*, 417:479–486.

Battinelli, P. and Demers, S. (2004c). Carbon star survey of Local Group galaxies. X. Wolf-Lundmark-Melotte a galaxy with an extreme C/M ratio. *A&A*, 416:111–118.

Beccari, G., Bellazzini, M., Fraternali, F., Battaglia, G., Perina, S., Sollima, A., Oosterloo, T. A., Testa, V., and Galleti, S. (2014). The extended structure of the dwarf irregular galaxy Sagittarius. *A&A*, 570:A78.

Bellazzini, M., Beccari, G., Fraternali, F., Oosterloo, T. A., Sollima, A., Testa, V., Galleti, S., Perina, S., Faccini, M., and Cusano, F. (2014a). The extended structure of the dwarf irregular galaxies Sextans A and Sextans B. Signatures of tidal distortion in the outskirts of the Local Group. *A&A*, 566:A44.

Bellazzini, M., Beccari, G., Fraternali, F., Oosterloo, T. A., Sollima, A., Testa, V., Galleti, S., Perina, S., Faccini, M., and Cusano, F. (2014b). VizieR Online Data Catalog: gr photometry of Sextans A and Sextans B (Bellazzini+, 2014). *VizieR Online Data Catalog*, 356.

Bensby, T., Feltzing, S., and Lundström, I. (2004). Oxygen trends in the Galactic thin and thick disks. *A&A*, 415:155–170.

Bernard, E. J., Monelli, M., Gallart, C., Fiorentino, G., Cassisi, S., Aparicio, A., Cole, A. A., Drozdovsky, I., Hidalgo, S. L., Skillman, E. D., Stetson, P. B., and Tolstoy, E. (2013). The ACS LCID Project - VIII. The short-period Cepheids of Leo A. *MNRAS*, 432:3047–3061.

Bertolli, M. G., Herwig, F., Pignatari, M., and Kawano, T. (2013). Systematic and correlated nuclear uncertainties in the i-process at the neutron shell closure N = 82. *ArXiv e-prints*.

Bianchi, L., Efremova, B., Hodge, P., Massey, P., and Olsen, K. A. G. (2012). A Treasury Study of Star-forming Regions in the Local Group. I. HST Photometry of Young Populations in Six Dwarf Galaxies. *AJ*, 143:74.

Bianchi, L. and Efremova, B. V. (2006). The Recent Star Formation in NGC 6822 from Hubble Space Telescope Imaging. *AJ*, 132:378–392.

Bladh, S. and Höfner, S. (2012). Exploring wind-driving dust species in cool luminous giants. I. Basic criteria and dynamical models of M-type AGB stars. *A&A*, 546:A76.

Bloecker, T. (1995). Stellar evolution of low- and intermediate-mass stars. II. Post-AGB evolution. *A&A*, 299:755.

Bloecker, T. and Schoenberner, D. (1991). A 7-solar-mass AGB model sequence not complying with the core mass-luminosity relation. *A&A*, 244:L43–L46.

Blommaert, J. A. D. L., Vanhollebeke, E., Cami, J., Groenewegen, M. A. T., Habing, H. J., Markwick-Kemper, F., Omont, A., Schultheis, M., Tielens, A. G. G. M., Waters, L. B. F. M., and Wood, P. R. (2007). The Dust Sequence along the AGB. In Kerschbaum, F., Charbonnel, C., and Wing, R. F., editors, *Why Galaxies Care About AGB Stars: Their Importance as Actors and Probes*, volume 378 of *Astronomical Society of the Pacific Conference Series*, page 164.

Boothroyd, A. I. and Sackmann, I.-J. (1999). The cno isotopes: deep circulation in red giants and first and second dredge-up. *The Astrophysical Journal*, 510(1):232.

Boothroyd, A. I., Sackmann, I.-J., and Ahern, S. C. (1993). Prevention of High-Luminosity Carbon Stars by Hot Bottom Burning. *ApJ*, 416:762.

Boyer, M. L., Girardi, L., Marigo, P., Williams, B. F., Aringer, B., Nowotny, W., Rosenfield, P., Dorman, C. E., Guhathakurta, P., Dalcanton, J. J., Melbourne, J. L., Olsen, K. A. G., and Weisz, D. R. (2013). Is There a Metallicity Ceiling to Form Carbon Stars?A Novel Technique Reveals a Scarcity of C stars in the Inner M31 Disk. *ApJ*, 774:83.

Boyer, M. L., McQuinn, K. B. W., Barmby, P., Bonanos, A. Z., Gehrz, R. D., Gordon, K. D., Groenewegen, M. A. T., Lagadec, E., Lennon, D., Marengo, M., McDonald, I., Meixner, M., Skillman, E., Sloan, G. C., Sonneborn, G., van Loon, J. T., and Zijlstra, A. (2015a). An Infrared Census of DUST in Nearby Galaxies with Spitzer (DUSTiNGS). II. Discovery of Metal-poor Dusty AGB Stars. *ApJ*, 800:51.

Boyer, M. L., McQuinn, K. B. W., Barmby, P., Bonanos, A. Z., Gehrz, R. D., Gordon, K. D., Groenewegen, M. A. T., Lagadec, E., Lennon, D., Marengo, M., Meixner, M., Skillman, E., Sloan, G. C., Sonneborn, G., van Loon, J. T., and Zijlstra, A. (2015b). An Infrared Census of Dust in nearby Galaxies with Spitzer (DUSTiNGS). I. Overview. *ApJS*, 216:10.

Boyer, M. L., Skillman, E. D., van Loon, J. T., Gehrz, R. D., and Woodward, C. E. (2009). A Spitzer Study of Asymptotic Giant Branch Stars. III. Dust Production and Gas Return in Local Group Dwarf Irregular Galaxies. *ApJ*, 697:1993–2014.

Bresolin, F., Urbaneja, M. A., Gieren, W., Pietrzyński, G., and Kudritzki, R.-P. (2007). VLT Spectroscopy of Blue Supergiants in IC 1613. *ApJ*, 671:2028–2039.

Bressan, A., Marigo, P., Girardi, L., Salasnich, B., Dal Cero, C., Rubele, S., and Nanni, A. (2012). PARSEC: stellar tracks and isochrones with the PAdova and TRieste Stellar Evolution Code. *MNRAS*, 427:127–145.

Brewer, J. P., Richer, H. B., and Crabtree, D. R. (1995). Late-Type Stars in M31. I. Photometric Study of AGB Stars and Metallicity Gradients. *AJ*, 109:2480.

Brewer, J. P., Richer, H. B., and Crabtree, D. R. (1996). Late-Type Stars in M31. II. C-, S-, and M-Star Spectra. *AJ*, 112:491.

Britavskiy, N. E., Bonanos, A. Z., Mehner, A., Boyer, M. L., and McQuinn, K. B. W. (2015). Identification of dusty massive stars in star-forming dwarf irregular galaxies in the Local Group with mid-IR photometry. *A&A*, 584:A33.

Brown, W. R., Geller, M. J., Kenyon, S. J., and Kurtz, M. J. (2007). Stellar Velocity Dispersion of the Leo A Dwarf Galaxy. *ApJ*, 666:231–235.

Burbidge, E. M., Burbidge, G. R., Fowler, W. A., and Hoyle, F. (1957). Synthesis of the Elements in Stars. *Reviews of Modern Physics*, 29:547–650.

Busso, M., Palmerini, S., Maiorca, E., Cristallo, S., Straniero, O., Abia, C., Gallino, R., and La Cognata, M. (2010). On the Need for Deep-mixing in

Asymptotic Giant Branch Stars of Low Mass. *ApJL*, 717:L47–L51.

Carroll, B. W. and Ostlie, D. A. (2007). *An Introduction to Modern Astrophysics*. Pearson, 2nd Edition, 2nd (international) edition.

Cherchneff, I. (2012). The inner wind of IRC+10216 revisited: new exotic chemistry and diagnostic for dust condensation in carbon stars. *A&A*, 545:A12.

Cole, A. A., Skillman, E. D., Tolstoy, E., Gallagher, III, J. S., Aparicio, A., Dolphin, A. E., Gallart, C., Hidalgo, S. L., Saha, A., Stetson, P. B., and Weisz, D. R. (2007). Leo A: A Late-blooming Survivor of the Epoch of Reionization in the Local Group. *ApJL*, 659:L17–L20.

Cole, A. A., Tolstoy, E., Gallagher, III, J. S., Hoessel, J. G., Mould, J. R., Holtzman, J. A., Saha, A., Ballester, G. E., Burrows, C. J., Clarke, J. T., Crisp, D., Griffiths, R. E., Grillmair, C. J., Hester, J. J., Krist, J. E., Meadows, V., Scowen, P. A., Stapelfeldt, K. R., Trauger, J. T., Watson, A. M., and Westphal, J. R. (1999). Stellar Populations at the Center of IC 1613. *AJ*, 118:1657–1670.

Collins, M. L. M., Chapman, S. C., Irwin, M. J., Martin, N. F., Ibata, R. A., Zucker, D. B., Blain, A., Ferguson, A. M. N., Lewis, G. F., McConnachie, A. W., and Peñarrubia, J. (2010). A Keck/DEIMOS spectroscopic survey of the faint M31 satellites AndIX, AndXI, AndXII and AndXIII. *MNRAS*, 407:2411–2433.

Conn, A. R., Ibata, R. A., Lewis, G. F., Parker, Q. A., Zucker, D. B., Martin, N. F., McConnachie, A. W., Irwin, M. J., Tanvir, N., Fardal, M. A., et al. (2012). A bayesian approach to locating the red giant branch tip magnitude. ii. distances to the satellites of m31. *The Astrophysical Journal*, 758(1):11.

Corradi, R. L. M., Magrini, L., Greimel, R., Irwin, M., Leisy, P., Lennon, D. J., Mampaso, A., Perinotto, M., Pollacco, D. L., Walsh, J. R., Walton, N. A., and Zijlstra, A. A. (2005). The Local Group Census: planetary nebulae in the spheroidal galaxies NGC 147, NGC 185 and NGC 205. *A&A*, 431:555–563.

Crnojević, D., Ferguson, A. M. N., Irwin, M. J., McConnachie, A. W., Bernard, E. J., Fardal, M. A., Ibata, R. A., Lewis, G. F., Martin, N. F., Navarro, J. F., Noël, N. E. D., and Pasetto, S. (2014). A PAndAS view of M31 dwarf elliptical satellites: NGC 147 and NGC 185. *MNRAS*, 445:3862–3877.

De Rijcke, S., Prugniel, P., Simien, F., and Dejonghe, H. (2006). The internal dynamics of the Local Group dwarf elliptical galaxies NGC 147, 185 and 205.

MNRAS, 369:1321–1333.

Decin, L., Justtanont, K., De Beck, E., Lombaert, R., de Koter, A., Waters, L. B. F. M., Marston, A. P., Teyssier, D., Schöier, F. L., Bujarrabal, V., Alcolea, J., Cernicharo, J., Dominik, C., Melnick, G., Menten, K., Neufeld, D. A., Olofsson, H., Planesas, P., Schmidt, M., Szczerba, R., de Graauw, T., Helmich, F., Roelfsema, P., Dieleman, P., Morris, P., Gallego, J. D., Díez-González, M. C., and Caux, E. (2010). Water content and wind acceleration in the envelope around the oxygen-rich AGB star IK Tauri as seen by Herschel/HIFI. *A&A*, 521:L4.

Dell'Agli, F., Di Criscienzo, M., Boyer, M. L., and García-Hernández, D. A. (2016). Evolved stars in the Local Group galaxies - I. AGB evolution and dust production in IC 1613. *MNRAS*, 460:4230–4241.

Dell'Agli, F., García-Hernández, D. A., Rossi, C., Ventura, P., Di Criscienzo, M., and Schneider, R. (2014). On the alumina dust production in the winds of O-rich asymptotic giant branch stars. *MNRAS*, 441:1115–1125.

Dolphin, A. E. (2000). Hubble Space Telescope Studies of the WLM Galaxy. II. The Star Formation History from Field Stars. *ApJ*, 531:804–812.

Dolphin, A. E., Saha, A., Claver, J., Skillman, E. D., Cole, A. A., Gallagher, J. S., Tolstoy, E., Dohm-Palmer, R. C., and Mateo, M. (2002). Variable Stars in Leo A: RR Lyrae Stars, Short-Period Cepheids, and Implications for Stellar Content. *AJ*, 123:3154–3198.

Dolphin, A. E., Saha, A., Skillman, E. D., Dohm-Palmer, R. C., Tolstoy, E., Cole, A. A., Gallagher, J. S., Hoessel, J. G., and Mateo, M. (2003). Deep Hubble Space Telescope Imaging of Sextans A. II. Cepheids and Distance. *AJ*, 125:1261–1290.

Dolphin, A. E., Saha, A., Skillman, E. D., Tolstoy, E., Cole, A. A., Dohm-Palmer, R. C., Gallagher, J. S., Mateo, M., and Hoessel, J. G. (2001). Deep Hubble Space Telescope Imaging of IC 1613. I. Variable Stars and Distance. *ApJ*, 550:554–569.

Dotter, A., Chaboyer, B., Jevremović, D., Kostov, V., Baron, E., and Ferguson, J. W. (2008). The Dartmouth Stellar Evolution Database. *ApJS*, 178:89–101.

Draine, B. T. (2010). *Physics of the interstellar and intergalactic medium*. Princeton University Press.

Dupree, A. K., Hartmann, L., and Avrett, E. H. (1984). Chromospheres and mass loss in metal-deficient giant stars. *ApJL*, 281:L37–L39.

Falceta-Gonçalves, D. and Jatenco-Pereira, V. (2002). The Effects of Alfvén Waves and Radiation Pressure in Dust Winds of Late-Type Stars. *ApJ*, 576:976–981.

Fishlock, C. K., Karakas, A. I., Lugaro, M., and Yong, D. (2014). Evolution and Nucleosynthesis of Asymptotic Giant Branch Stellar Models of Low Metallicity. *ApJ*, 797:44.

Freedman, W. L., Rigby, J., Madore, B. F., Persson, S. E., Sturch, L., and Mager, V. (2009). The Cepheid Period-Luminosity Relation (The Leavitt Law) at Mid-Infrared Wavelengths. IV. Cepheids in IC 1613. *ApJ*, 695:996–998.

Gallagher, J. S., Tolstoy, E., Dohm-Palmer, R. C., Skillman, E. D., Cole, A. A., Hoessel, J. G., Saha, A., and Mateo, M. (1998). A Wide Field Planetary Camera 2 Study of the Resolved Stellar Population of the Pegasus Dwarf Irregular Galaxy (DDO 216). *AJ*, 115:1869–1887.

García-Rojas, J., Peña, M., Flores-Durán, S., and Hernández-Martínez, L. (2016). The planetary nebulae and H II regions in NGC 6822 revisited. Clues to AGB nucleosynthesis. *A&A*, 586:A59.

Gautschy, A. and Saio, H. (1996). Stellar Pulsations Across the HR Diagram: Part 2. *Annual Review of Astron and Astrophys*, 34:551–606.

Gieren, W., Pietrzyński, G., Szewczyk, O., Soszyński, I., Bresolin, F., Kudritzki, R.-P., Urbaneja, M. A., Storm, J., and Minniti, D. (2008). The Araucaria Project: The Distance to the Local Group Galaxy WLM from Near-Infrared Photometry of Cepheid Variables. *ApJ*, 683:611–619.

Goodwin, S. (2013). Star formation. In Oswalt, T. and Barstow, M., editors, *Planets, Stars and Stellar Systems, Volume 4: Stellar Structure and Evolution*. Springer Reference, Springer Publishing Company, 11 West 42nd Street, 15th Floor, New York, NY 10036.

Górski, M., Pietrzyński, G., and Gieren, W. (2011). The Araucaria Project. Infrared Tip of the Red Giant Branch Distances to Five Dwarf Galaxies in the Local Group. *AJ*, 141:194.

Grebel, E. K., Gallagher III, J. S., and Harbeck, D. (2003). The progenitors of dwarf spheroidal galaxies. *The Astronomical Journal*, 125(4):1926.

Gritschneder, M., Lin, D. N. C., Murray, S. D., and Burkert, A. (2011). Ionization and Triggered Star Formation. In Qain, S., Leung, K., Zhu, L., and Kwok, S., editors, *9th Pacific Rim Conference on Stellar Astrophysics*, volume 451 of *Astronomical Society of the Pacific Conference Series*, page 199.

Groenewegen, M. A. T. (2014). First detection of rotational CO line emission in a red giant branch star. *A&A*, 561:L11.

Gullieuszik, M., Rejkuba, M., Cioni, M. R., Habing, H. J., and Held, E. V. (2007). Near-infrared photometry of carbon stars in the Sagittarius dwarf irregular galaxy and DDO 210. *A&A*, 475:467–477.

Gustafsson, B., Bell, R. A., Eriksson, K., and Nordlund, A. (1975). A grid of model atmospheres for metal-deficient giant stars. I. *A&A*, 42:407–432.

Gustafsson, B., Edvardsson, B., Eriksson, K., Jørgensen, U. G., Nordlund, Å., and Plez, B. (2008). A grid of MARCS model atmospheres for late-type stars. I. Methods and general properties. *A&A*, 486:951–970.

Habing, H. J. (1996). Circumstellar envelopes and Asymptotic Giant Branch stars. *A&AR*, 7:97–207.

Habing, H. J. and Olofsson, H., editors (2003). *Asymptotic giant branch stars*. Springer Reference, Springer Publishing Company, 11 West 42nd Street, 15th Floor, New York, NY 10036.

Hansen, C. J., Kawaler, S. D., and Trimble, V. (2012). *Stellar interiors: physical principles, structure, and evolution*. Springer Science & Business Media.

Harbeck, D., Gallagher, J. S., Grebel, E. K., Koch, A., and Zucker, D. B. (2005). Andromeda IX: Properties of the Faintest M31 Dwarf Satellite Galaxy. *ApJ*, 623:159–163.

Held, E. V., Saviane, I., and Momany, Y. (1999). Stellar populations in the PHOENIX dwarf galaxy. *A&A*, 345:747–759.

Herwig, F. (2000). The evolution of AGB stars with convective overshoot. *A&A*, 360:952–968.

Herwig, F. (2013). Evolution of solar and intermediate-mass stars. In Oswalt, T. and Barstow, M., editors, *Planets, Stars and Stellar Systems, Volume 4: Stellar Structure and Evolution*. Springer Reference, Springer Publishing Company, 11 West 42nd Street, 15th Floor, New York, NY 10036.

Hidalgo, S. L., Aparicio, A., Martínez-Delgado, D., and Gallart, C. (2009). On the Extended Structure of the Phoenix Dwarf Galaxy. *ApJ*, 705:704–716.

Hidalgo, S. L., Aparicio, A., Skillman, E., Monelli, M., Gallart, C., Cole, A., Dolphin, A., Weisz, D., Bernard, E. J., Cassisi, S., Mayer, L., Stetson, P., Tolstoy, E., and Ferguson, H. (2011). The ACS LCID Project. V. The Star Formation History of the Dwarf Galaxy LGS-3: Clues to Cosmic Reionization and Feedback. *ApJ*, 730:14.

Ho, L. C., Filippenko, A. V., and Sargent, W. L. W. (1997). A Search for "Dwarf" Seyfert Nuclei. III. Spectroscopic Parameters and Properties of the Host Galaxies. *ApJS*, 112:315–390.

Höfner, S. (2008). Winds of M-type AGB stars driven by micron-sized grains. *A&A*, 491:L1–L4.

Höfner, S. (2011). Starlight and Sandstorms: Mass Loss Mechanisms on the AGB. In Kerschbaum, F., Lebzelter, T., and Wing, R. F., editors, *Why Galaxies Care about AGB Stars II: Shining Examples and Common Inhabitants*, volume 445 of *Astronomical Society of the Pacific Conference Series*, page 193.

Hwang, N., Park, H. S., Lee, M. G., Lim, S., Hodge, P. W., Kim, S. C., Miller, B., and Weisz, D. (2014). Spectroscopic Study of Extended Star Clusters in Dwarf Galaxy NGC 6822. *ApJ*, 783:49.

Iben, Jr., I. (1975). Thermal pulses; p-capture, alpha-capture, s-process nucleosynthesis; and convective mixing in a star of intermediate mass. *ApJ*, 196:525–547.

Ita, Y., Tanabé, T., Matsunaga, N., Nakajima, Y., Nagashima, C., Nagayama, T., Kato, D., Kurita, M., Nagata, T., Sato, S., Tamura, M., Nakaya, H., and Nakada, Y. (2004). Variable stars in the Magellanic Clouds: results from OGLE and SIRIUS. *MNRAS*, 347:720–728.

Jacoby, G. H. and Lesser, M. P. (1981). Distances to nearby galaxies derived from planetary nebulae. *AJ*, 86:185–192.

Johnson, C. I. and Pilachowski, C. A. (2012). Oxygen and Sodium Abundances in M13 (NGC 6205) Giants: Linking Globular Cluster Formation Scenarios, Deep Mixing, and Post-RGB Evolution. *ApJL*, 754:L38.

Jones, O. C., Kemper, F., Sargent, B. A., McDonald, I., Gielen, C., Woods, P. M., Sloan, G. C., Boyer, M. L., Zijlstra, A. A., Clayton, G. C., Kraemer, K. E., Srinivasan, S., and Ruffle, P. M. E. (2012). On the metallicity dependence of crystalline silicates in oxygen-rich asymptotic giant branch stars and red supergiants. *MNRAS*, 427:3209–3229.

Jones, O. C., Kemper, F., Srinivasan, S., McDonald, I., Sloan, G. C., and Zijlstra, A. A. (2014). Modelling the alumina abundance of oxygen-rich evolved stars in the Large Magellanic Cloud. *MNRAS*, 440:631–651.

Kalirai, J., Richer, H., Reitzel, D., Hansen, B., Rich, R. M., Fahlman, G., Gibson, B., and von Hippel, T. (2004). The Initial-Final Mass Relation and the DA/DB White Dwarf Ratio. In *American Astronomical Society Meeting Abstracts*, volume 36 of *Bulletin of the American Astronomical Society*, page 170.02.

Kalirai, J. S., Hansen, B. M. S., Kelson, D. D., Reitzel, D. B., Rich, R. M., and Richer, H. B. (2008). The Initial-Final Mass Relation: Direct Constraints at the Low-Mass End. *ApJ*, 676:594–609.

Kamath, D., Karakas, A. I., and Wood, P. R. (2012). Evolution and Nucleosynthesis of Asymptotic Giant Branch Stars in Three Magellanic Cloud Clusters. *ApJ*, 746:20.

Karachentsev, I., Aparicio, A., and Makarova, L. (1999). The Sagittarius dwarf irregular galaxy (SagDIG): distance and star formation history. *A&A*, 352:363–370.

Karakas, A. I. (2014). Helium enrichment and carbon-star production in metal-rich populations. *MNRAS*, 445:347–358.

Karakas, A. I. and Lattanzio, J. C. (2014). The Dawes Review 2: Nucleosynthesis and Stellar Yields of Low- and Intermediate-Mass Single Stars. *Publications of the Astronomical Society of Australia*, 31:30.

Karakas, A. I., Lattanzio, J. C., and Pols, O. R. (2002). Parameterising the Third Dredge-up in Asymptotic Giant Branch Stars. *Publications of the Astronomical Society of Australia*, 19:515–526.

Karttunen, H. (2007). *Fundamental astronomy.* Springer Science & Business Media.

Kaufer, A., Venn, K. A., Tolstoy, E., Pinte, C., and Kudritzki, R.-P. (2004). First Stellar Abundances in the Dwarf Irregular Galaxy Sextans A. *AJ*, 127:2723–2737.

Kemper, F., de Koter, A., Waters, L. B. F. M., Bouwman, J., and Tielens, A. G. G. M. (2002). Dust and the spectral energy distribution of the OH/IR star OH 127.8+0.0: Evidence for circumstellar metallic iron. *A&A*, 384:585–593.

Kervella, P., Montargès, M., Lagadec, E., Ridgway, S. T., Haubois, X., Girard, J. H., Ohnaka, K., Perrin, G., and Gallenne, A. (2015). The dust disk and companion of the nearby AGB star L_2 Puppis. SPHERE/ZIMPOL polarimetric imaging at visible wavelengths. *A&A*, 578:A77.

Kirby, E. N., Guhathakurta, P., and Sneden, C. (2008). Metallicity and Alpha-Element Abundance Measurement in Red Giant Stars from Medium-Resolution Spectra. *ApJ*, 682:1217–1233.

Kniazev, A. Y., Brosch, N., Hoffman, G. L., Grebel, E. K., Zucker, D. B., and Pustilnik, S. A. (2009). The faint outer regions of the Pegasus dwarf irregular galaxy: a much larger and undisturbed galaxy. *MNRAS*, 400:2054–2069.

Koester, D. (2013). Evolution of solar and intermediate-mass stars. In Oswalt, T. and Barstow, M., editors, *Planets, Stars and Stellar Systems, Volume 4: Stellar Structure and Evolution*. Springer Reference, Springer Publishing Company, 11 West 42nd Street, 15th Floor, New York, NY 10036.

Kroupa, P. (2001). On the variation of the initial mass function. *MNRAS*, 322:231–246.

Lagadec, E. and Zijlstra, A. A. (2008). The trigger of the asymptotic giant branch superwind: the importance of carbon. *MNRAS*, 390:L59–L63.

Larsen, S. S., Brodie, J. P., Forbes, D. A., and Strader, J. (2014). Chemical composition and constraints on mass loss for globular clusters in dwarf galaxies: WLM and IKN. *A&A*, 565:A98.

Lattanzio, J., Frost, C., Cannon, R., and Wood, P. R. (1996). Hot bottom burning in intermediate mass stars. *Mem. Soc. Astron. Italiana*, 67:729.

Le Bertre, T. (1997). Optical and infrared observations of 23 carbon-rich stars. Modelling of the circumstellar dust shells. *A&A*, 324:1059–1070.

Leaman, R., Venn, K. A., Brooks, A. M., Battaglia, G., Cole, A. A., Ibata, R. A., Irwin, M. J., McConnachie, A. W., Mendel, J. T., and Tolstoy, E. (2012). The Resolved Structure and Dynamics of an Isolated Dwarf Galaxy: A VLT and Keck Spectroscopic Survey of WLM. *ApJ*, 750:33.

Lebzelter, T., Posch, T., Hinkle, K., Wood, P. R., and Bouwman, J. (2006). Tracing the Development of Dust around Evolved Stars: The Case of 47 Tuc.

ApJL, 653:L145–L148.

Lebzelter, T. and Wood, P. R. (2007). The AGB stars of the intermediate-age LMC cluster NGC 1846. Variability and age determination. *A&A*, 475:643–650.

Lee, M. G. (1995). Is the Pegasus Dwarf Galaxy a Member of the Local Group? *Journal of Korean Astronomical Society*, 28:169–175.

Levesque, E. M. (2013). Red Supergiants in the Local Group. In Kervella, P., Le Bertre, T., and Perrin, G., editors, *EAS Publications Series*, volume 60 of *EAS Publications Series*, pages 269–277.

Lind, K., Primas, F., Charbonnel, C., Grundahl, F., and Asplund, M. (2009). Signatures of intrinsic Li depletion and Li-Na anti-correlation in the metal-poor globular cluster NGC 6397. *A&A*, 503:545–557.

Lugaro, M., Karakas, A. I., Stancliffe, R. J., and Rijs, C. (2012). The s-process in Asymptotic Giant Branch Stars of Low Metallicity and the Composition of Carbon-enhanced Metal-poor Stars. *ApJ*, 747:2.

Maas, T., Van Winckel, H., and Lloyd Evans, T. (2005). Depletion in post-AGB stars with a dusty disc. II. *A&A*, 429:297–308.

Madore, B. F., Rigby, J., Freedman, W. L., Persson, S. E., Sturch, L., and Mager, V. (2009). The Cepheid Period-Luminosity Relation (The Leavitt Law) at Mid-Infrared Wavelengths. III. Cepheids in NGC 6822. *ApJ*, 693:936–939.

Magrini, L., Corradi, R. L. M., Greimel, R., Leisy, P., Lennon, D. J., Mampaso, A., Perinotto, M., Pollacco, D. L., Walsh, J. R., Walton, N. A., and Zijlstra, A. A. (2003). The Local Group Census: Planetary nebulae in IC 10, Leo A and Sextans A. *A&A*, 407:51–59.

Magrini, L., Corradi, R. L. M., Greimel, R., Leisy, P., Mampaso, A., Perinotto, M., Walsh, J. R., Walton, N. A., Zijlstra, A. A., Minniti, D., and Mora, M. (2005a). The Local Group Census: searching for planetary nebulae in IC 1613, WLM and GR8. *MNRAS*, 361:517–524.

Magrini, L., Leisy, P., Corradi, R. L. M., Perinotto, M., Mampaso, A., and Vílchez, J. M. (2005b). The chemistry of planetary nebulae and HII regions in the dwarf galaxies Sextans A and B from deep VLT spectra. *A&A*, 443:115–132.

Maraston, C., Daddi, E., Renzini, A., Cimatti, A., Dickinson, M., Papovich, C., Pasquali, A., and Pirzkal, N. (2006). Evidence for TP-AGB Stars in High-Redshift Galaxies, and Their Effect on Deriving Stellar Population Parameters.

ApJ, 652:85–96.

Marigo, P. and Girardi, L. (2007). Evolution of asymptotic giant branch stars. I. Updated synthetic TP-AGB models and their basic calibration. *A&A*, 469:239–263.

Marleau, F. R., Noriega-Crespo, A., and Misselt, K. A. (2010). Dust abundance and properties in the nearby dwarf galaxies ngc 147 and ngc 185. *The Astrophysical Journal*, 713(2):992.

Martínez-Delgado, D. and Aparicio, A. (1998). The Star Formation History of the Local Group Dwarf Elliptical Galaxy NGC 185. I. Stellar Content. *AJ*, 115:1462–1471.

Martínez-Delgado, D., Aparicio, A., and Gallart, C. (1999a). The Star Formation History of the Local Group Dwarf Elliptical Galaxy NGC 185. II. Gradients in the Stellar Population. *AJ*, 118:2229–2244.

Martínez-Delgado, D., Gallart, C., and Aparicio, A. (1999b). The Stellar Content of the Local Group Dwarf Galaxy PHOENIX. *AJ*, 118:862–882.

Martins, L. P., Lanfranchi, G., Gonçalves, D. R., Magrini, L., Teodorescu, A. M., and Quireza, C. (2012). The ionization mechanism of NGC 185: how to fake a Seyfert galaxy? *MNRAS*, 419:3159–3166.

Massey, P., Olsen, K. A. G., Hodge, P. W., Jacoby, G. H., McNeill, R. T., Smith, R. C., and Strong, S. B. (2007). A Survey of Local Group Galaxies Currently Forming Stars. II. UBVRI Photometry of Stars in Seven Dwarfs and a Comparison of the Entire Sample. *AJ*, 133:2393–2417.

Mateo, M. L. (1998). Dwarf Galaxies of the Local Group. *Annual Review of Astron and Astrophys*, 36:435–506.

McClure, R. D. (1985). The carbon and related stars. *Journal of the Royal Astron. Soc. of Canada*, 79:277–293.

McConnachie, A. W. (2012). The Observed Properties of Dwarf Galaxies in and around the Local Group. *AJ*, 144:4.

McConnachie, A. W., Irwin, M. J., Ferguson, A. M. N., Ibata, R. A., Lewis, G. F., and Tanvir, N. (2005). Distances and metallicities for 17 Local Group galaxies. *MNRAS*, 356:979–997.

McDonald, I. (2009). *Stellar Mass Loss in Globular Clusters*. PhD thesis, Keele University.

McDonald, I., Boyer, M. L., van Loon, J. T., and Zijlstra, A. A. (2011). Dust Production and Mass Loss in the Galactic Globular Cluster 47 Tucanae. *ApJ*, 730:71.

McDonald, I., Sloan, G. C., Zijlstra, A. A., Matsunaga, N., Matsuura, M., Kraemer, K. E., Bernard-Salas, J., and Markwick, A. J. (2010a). Rusty Old Stars: A Source of the Missing Interstellar Iron? *ApJL*, 717:L92–L97.

McDonald, I. and van Loon, J. T. (2007). Dust, pulsation, chromospheres and their rôle in driving mass loss from red giants in Galactic globular clusters. *A&A*, 476:1261–1282.

McDonald, I., van Loon, J. T., Decin, L., Boyer, M. L., Dupree, A. K., Evans, A., Gehrz, R. D., and Woodward, C. E. (2009). Giants in the globular cluster ω Centauri: dust production, mass-loss and distance. *MNRAS*, 394:831–856.

McDonald, I., van Loon, J. T., Dupree, A. K., and Boyer, M. L. (2010b). Discovery of long-period variable stars in the very metal-poor globular cluster M15. *MNRAS*, 405:1711–1722.

McDonald, I., White, J. R., Zijlstra, A. A., Guzman Ramirez, L., Szyszka, C., van Loon, J. T., Lagadec, E., and Jones, O. C. (2012a). Carbon enrichment of the evolved stars in the Sagittarius dwarf spheroidal. *MNRAS*, 427:2647–2659.

McDonald, I. and Zijlstra, A. A. (2015). Mass-loss on the red giant branch: the value and metallicity dependence of Reimers' η in globular clusters. *MNRAS*, 448:502–521.

McDonald, I., Zijlstra, A. A., and Boyer, M. L. (2012b). Fundamental parameters and infrared excesses of Hipparcos stars. *MNRAS*, 427:343–357.

McDonald, I., Zijlstra, A. A., Rajoelimanana, A. F., and Johnson, C. I. (2013). On the impossible NGC 4372 V1 and V2: an extended AGB to the [Fe/H] = -2.2 cluster. *MNRAS*, 429:L65–L69.

McDonald, I., Zijlstra, A. A., Sloan, G. C., Kerins, E., Lagadec, E., and Minniti, D. (2014). VISTA variables in the Sagittarius dwarf spheroidal galaxy: pulsation-versus dust-driven winds on the giant branches. *MNRAS*, 439:2618–2637.

McDonald, I., Zijlstra, A. A., Sloan, G. C., Lagadec, E., Johnson, C. I., Uttenthaler, S., Jones, O. C., and Smith, C. L. (2016). EU Del: exploring the onset of pulsation-driven winds in giant stars. *MNRAS*, 456:4542–4550.

Meschin, I., Gallart, C., Cassisi, S., Aparicio, A., and Rosenberg, A. (2008). The Cepheid Variable Population in the Local Group Dwarf Irregular Galaxy Pegasus. In Knapen, J. H., Mahoney, T. J., and Vazdekis, A., editors, *Pathways Through an Eclectic Universe*, volume 390 of *Astronomical Society of the Pacific Conference Series*, page 306.

Mestel, L. and Ruderman, M. (1967). The energy content of a white dwarf and its rate of cooling. *Monthly Notices of the Royal Astronomical Society*, 136(1):27–38.

Meyer, M. R., Calvet, N., and Hillenbrand, L. A. (1997). Intrinsic Near-Infrared Excesses of T Tauri Stars: Understanding the Classical T Tauri Star Locus. *AJ*, 114:288–300.

Miller, B. W., Dolphin, A. E., Lee, M. G., Kim, S. C., and Hodge, P. (2001). The Star Formation History of LGS 3. *ApJ*, 562:713–726.

Molster, F. J., Waters, L. B. F. M., and Tielens, A. G. G. M. (2002). Crystalline silicate dust around evolved stars. II. The crystalline silicate complexes. *A&A*, 382:222–240.

Momany, Y., Clemens, M., Bedin, L. R., Gullieuszik, M., Held, E. V., Saviane, I., Zaggia, S., Monaco, L., Montalto, M., Rich, R. M., and Rizzi, L. (2014). The H I hole and AGB stellar population of the Sagittarius dwarf irregular galaxy. HST proper-motion decontamination. *A&A*, 572:A42.

Momany, Y., Held, E. V., Saviane, I., Bedin, L. R., Gullieuszik, M., Clemens, M., Rizzi, L., Rich, M. R., and Kuijken, K. (2005). HST/ACS observations of the old and metal-poor Sagittarius dwarf irregular galaxy. *A&A*, 439:111–127.

Momany, Y., Held, E. V., Saviane, I., and Rizzi, L. (2002). The Sagittarius dwarf irregular galaxy: Metallicity and stellar populations. *A&A*, 384:393–402.

Monet, D. G., Levine, S. E., Canzian, B., Ables, H. D., Bird, A. R., Dahn, C. C., Guetter, H. H., Harris, H. C., Henden, A. A., Leggett, S. K., Levison, H. F., Luginbuhl, C. B., Martini, J., Monet, A. K. B., Munn, J. A., Pier, J. R., Rhodes, A. R., Riepe, B., Sell, S., Stone, R. C., Vrba, F. J., Walker, R. L., Westerhout, G., Brucato, R. J., Reid, I. N., Schoening, W., Hartley, M., Read, M. A., and Tritton, S. B. (2003). The USNO-B Catalog. *AJ*, 125:984–993.

Nomoto, K., Kobayashi, C., and Tominaga, N. (2013). Nucleosynthesis in Stars and the Chemical Enrichment of Galaxies. *Annual Review of Astron and As-*

trophys, 51:457–509.

Norris, B. R. M., Tuthill, P. G., Ireland, M. J., Lacour, S., Zijlstra, A. A., Lykou, F., Evans, T. M., Stewart, P., and Bedding, T. R. (2012). A close halo of large transparent grains around extreme red giant stars. *Nature*, 484:220–222.

Nowotny, W., Kerschbaum, F., Olofsson, H., and Schwarz, H. E. (2003). A census of AGB stars in Local Group galaxies. II. NGC 185 and NGC 147. *A&A*, 403:93–103.

Owocki, S. (2013). Stellar winds. In Oswalt, T. and Barstow, M., editors, *Planets, Stars and Stellar Systems, Volume 4: Stellar Structure and Evolution*. Springer Reference, Springer Publishing Company, 11 West 42nd Street, 15th Floor, New York, NY 10036.

Paczyński, B. (1970). Evolution of Single Stars. I. Stellar Evolution from Main Sequence to White Dwarf or Carbon Ignition. *Acta Informatica*, 20:47.

Palmerini, S., La Cognata, M., Cristallo, S., and Busso, M. (2011). Deep Mixing in Evolved Stars. I. The Effect of Reaction Rate Revisions from C to Al. *ApJ*, 729:3.

Patrick, L. R., Evans, C. J., Davies, B., Kudritzki, R.-P., Gazak, J. Z., Bergemann, M., Plez, B., and Ferguson, A. M. N. (2015). Red Supergiant Stars as Cosmic Abundance Probes: KMOS Observations in NGC 6822. *ApJ*, 803:14.

Pilyugin, L. S. (2001). On the oxygen abundance determination in HII regions. High-metallicity regions. *A&A*, 369:594–604.

Pogge, R. (2015). The evolution of low-mass stars. http://www.astronomy.ohio-state.edu/ pogge/Ast162/Unit2/lowmass.html.

Reimers, D. (1975). Circumstellar absorption lines and mass loss from red giants. *Memoires of the Societe Royale des Sciences de Liege*, 8:369–382.

Riebel, D., Srinivasan, S., Sargent, B., and Meixner, M. (2012). The Mass-loss Return from Evolved Stars to the Large Magellanic Cloud. VI. Luminosities and Mass-loss Rates on Population Scales. *ApJ*, 753:71.

Riello, M., Piotto, G., Recio-Blanco, A., Cassisi, S., and Salaris, M. (2003). The Red Giant Branch Bump. In Piotto, G., Meylan, G., Djorgovski, S. G., and Riello, M., editors, *New Horizons in Globular Cluster Astronomy*, volume 296 of *Astronomical Society of the Pacific Conference Series*, page 232.

Sakai, S., Madore, B. F., and Freedman, W. L. (1996). Tip of the Red Giant

Branch Distances to Galaxies. III. The Dwarf Galaxy Sextans A. *ApJ*, 461:713.

Sakai, S., Madore, B. F., and Freedman, W. L. (1997). Tip of the Red Giant Branch Distances to Galaxies. IV. Sextans B. *ApJ*, 480:589–595.

Sandage, A. and Carlson, G. (1985). The brightest stars in nearby galaxies. V - Cepheids and the brightest stars in the dwarf galaxy Sextans B compared with those in Sextans A. *AJ*, 90:1019–1026.

Sandage, A. and Carlson, G. A. (1984). Cepheids in the Dwarf Galaxies Sextans A, Sextans B and WLM. In *Bulletin of the American Astronomical Society*, volume 16 of *Bulletin of the AAS*, page 880.

Saviane, I., Exter, K., Tsamis, Y., Gallart, C., and Péquignot, D. (2009). VLT/FORS1 spectrophotometry of the first planetary nebula discovered in the Phoenix dwarf galaxy. *A&A*, 494:515–525.

Scalo, J. M., Despain, K. H., and Ulrich, R. K. (1975). Studies of evolved stars. V - Nucleosynthesis in hot-bottom convective envelopes. *ApJ*, 196:805–817.

Schöier, F. L., Ryde, N., and Olofsson, H. (2002). Probing the mass loss history of carbon stars using CO line and dust continuum emission. *A&A*, 391:577–586.

Schröder, K.-P. and Cuntz, M. (2005). A New Version of Reimers' Law of Mass Loss Based on a Physical Approach. *ApJL*, 630:L73–L76.

Sharina, M. E., Afanasiev, V. L., and Puzia, T. H. (2006). Ages, metallicities and [α/Fe] ratios of globular clusters in NGC 147, 185 and 205. *MNRAS*, 372:1259–1274.

Sharina, M. E., Puzia, T. H., and Krylatyh, A. S. (2007). A globular cluster in the dwarf galaxy Sextans B. *Astrophysical Bulletin*, 62:209–216.

Sharina, M. E., Puzia, T. H., and Makarov, D. I. (2005). Hubble Space Telescope imaging of globular cluster candidates in low surface brightness dwarf galaxies. *A&A*, 442:85–95.

Sibbons, L. F., Ryan, S. G., Cioni, M.-R. L., Irwin, M., and Napiwotzki, R. (2012). The AGB population of NGC 6822: distribution and the C/M ratio from JHK photometry. *A&A*, 540:A135.

Sibbons, L. F., Ryan, S. G., Irwin, M., and Napiwotzki, R. (2015). The AGB population in IC 1613 using JHK photometry. *A&A*, 573:A84.

Simon, J. D. and Geha, M. (2007). The Kinematics of the Ultra-faint Milky Way Satellites: Solving the Missing Satellite Problem. *ApJ*, 670:313–331.

Sloan, G., Matsuura, M., Lagadec, E., Van Loon, J. T., Kraemer, K., McDonald, I., Groenewegen, M., Wood, P., Bernard-Salas, J., and Zijlstra, A. (2012). Carbon-rich dust production in metal-poor galaxies in the local group. *The Astrophysical Journal*, 752(2):140.

Soszynski, I., Udalski, A., Kubiak, M., Szymanski, M., Pietrzynski, G., Zebrun, K., Szewczyk, O., and Wyrzykowski, L. (2004). The Optical Gravitational Lensing Experiment. Small Amplitude Variable Red Giants in the Magellanic Clouds. *Acta Informatica*, 54:129–152.

Stonkutė, R., Arimoto, N., Hasegawa, T., Narbutis, D., Tamura, N., and Vansevičius, V. (2014). Dwarf Irregular Galaxy Leo A: Suprime-Cam Wide-field Stellar Photometry. *ApJS*, 214:19.

Strobel, N. V., Hodge, P., and Kennicutt, Jr., R. C. (1991). H II regions in seven dwarf irregular galaxies. *ApJ*, 383:148–163.

Tammann, G. A., Reindl, B., and Sandage, A. (2011). New period-luminosity and period-color relations of classical Cepheids. IV. The low-metallicity galaxies IC 1613, WLM, Pegasus, Sextans A and B, and Leo A in comparison to SMC. *A&A*, 531:A134.

Tikhonov, N. A., Galazutdinova, O. A., and Drozdovsky, I. O. (2005). Thick disks and halos of spiral galaxies M 81, NGC 55 and NGC 300. *A&A*, 431:127–142.

Tolstoy, E., Hill, V., and Tosi, M. (2009). Star-Formation Histories, Abundances, and Kinematics of Dwarf Galaxies in the Local Group. *Annual Review of Astron and Astrophys*, 47:371–425.

Tolstoy, E., Irwin, M. J., Cole, A. A., Pasquini, L., Gilmozzi, R., and Gallagher, J. S. (2001). Using the Ca ii triplet to trace abundance variations in individual red giant branch stars in three nearby galaxies. *MNRAS*, 327:918–938.

Torrealba, G., Koposov, S. E., Belokurov, V., and Irwin, M. (2016). The feeble giant. Discovery of a large and diffuse Milky Way dwarf galaxy in the constellation of Crater. *MNRAS*, 459:2370–2378.

Tosi, M., Greggio, L., Marconi, G., and Focardi, P. (1991). Star formation in dwarf irregular galaxies - Sextans B. *AJ*, 102:951–974.

Tully, R. B., Rizzi, L., Dolphin, A. E., Karachentsev, I. D., Karachentseva, V. E., Makarov, D. I., Makarova, L., Sakai, S., and Shaya, E. J. (2006). Associations of Dwarf Galaxies. *AJ*, 132:729–748.

Udalski, A., Wyrzykowski, L., Pietrzynski, G., Szewczyk, O., Szymanski, M., Kubiak, M., Soszynski, I., and Zebrun, K. (2001). The Optical Gravitational Lensing Experiment. Cepheids in the Galaxy IC1613: No Dependence of the Period-Luminosity Relation on Metallicity. *Acta Informatica*, 51:221–245.

Urbaneja, M. A., Kudritzki, R.-P., Bresolin, F., Przybilla, N., Gieren, W., and Pietrzyński, G. (2008). The Araucaria Project: The Local Group Galaxy WLMDistance and Metallicity from Quantitative Spectroscopy of Blue Supergiants. *ApJ*, 684:118–135.

van den Bergh, S. (2000). *The Galaxies of the Local Group*, volume 35. Cambridge University Press.

van den Bergh, S. (2000). Updated Information on the Local Group. *Public. of the Astron. Soc. Pac.*, 112:529–536.

Veljanoski, J., Ferguson, A. M. N., Huxor, A. P., Mackey, A. D., Fishlock, C. K., Irwin, M. J., Tanvir, N., Chapman, S. C., Ibata, R. A., Lewis, G. F., and McConnachie, A. (2013). Newly discovered globular clusters in NGC 147 and NGC 185 from PAndAS. *MNRAS*, 435:3654–3666.

Veljanoski, J., Ferguson, A. M. N., Mackey, A. D., Huxor, A. P., Hurley, J. R., Bernard, E. J., Côté, P., Irwin, M. J., Martin, N. F., Burgett, W. S., Chambers, K. C., Flewelling, H., Kudritzki, R., and Waters, C. (2015). The globular cluster system of NGC 6822. *MNRAS*, 452:320–332.

Ventura, P. and D'Antona, F. (2005). Full computation of massive AGB evolution. I. The large impact of convection on nucleosynthesis. *A&A*, 431:279–288.

Ventura, P., Di Criscienzo, M., Carini, R., and D'Antona, F. (2013). Yields of AGB and SAGB models with chemistry of low- and high-metallicity globular clusters. *MNRAS*, 431:3642–3653.

Ventura, P., Karakas, A. I., Dell'Agli, F., García-Hernández, D. A., Boyer, M. L., and Di Criscienzo, M. (2016). On the nature of the most obscured C-rich AGB stars in the Magellanic Clouds. *MNRAS*, 457:1456–1467.

Vlemmings, W. H. T. (2014). Magnetic fields around AGB stars and Planetary Nebulae. In Petit, P., Jardine, M., and Spruit, H. C., editors, *IAU Symposium*, volume 302 of *IAU Symposium*, pages 389–397.

Walch, S., Wünsch, R., Burkert, A., Glover, S., and Whitworth, A. (2011). The Turbulent Fragmentation of the Interstellar Medium: The Impact of Metallicity on Global Star Formation. *ApJ*, 733:47.

Wallerstein, G., Iben, Jr., I., Parker, P., Boesgaard, A. M., Hale, G. M., Champagne, A. E., Barnes, C. A., Käppeler, F., Smith, V. V., Hoffman, R. D., Timmes, F. X., Sneden, C., Boyd, R. N., Meyer, B. S., and Lambert, D. L. (1997). Synthesis of the elements in stars: forty years of progress. *Reviews of Modern Physics*, 69:995–1084.

Wallerstein, G. and Knapp, G. R. (1998). Carbon Stars. *Annual Review of Astron and Astrophys*, 36:369–434.

Weisz, D. R., Dolphin, A. E., Skillman, E. D., Holtzman, J., Gilbert, K. M., Dalcanton, J. J., and Williams, B. F. (2014). The Star Formation Histories of Local Group Dwarf Galaxies. I. Hubble Space Telescope/Wide Field Planetary Camera 2 Observations. *ApJ*, 789:147.

Wheeler, J. C., Sneden, C., and Truran, Jr., J. W. (1989). Abundance ratios as a function of metallicity. *Annual Review of Astron and Astrophys*, 27:279–349.

Williams, S. J. and Bonanos, A. Z. (2016). Spitzer mid-infrared point sources in the fields of nearby galaxies$\star$. $A\&A, 587 : A121$.

Willson, L. A. (2000). Mass Loss From Cool Stars: Impact on the Evolution of Stars and Stellar Populations. *Annual Review of Astron and Astrophys*, 38:573–611.

Woitke, P. (2006). Too little radiation pressure on dust in the winds of oxygen-rich AGB stars. *A&A*, 460:L9–L12.

Wood, P. R. (2000). Variable Red Giants in the LMC: Pulsating Stars and Binaries? *Publications of the Astronomical Society of Australia*, 17:18–21.

Zacharias, N., Monet, D. G., Levine, S. E., Urban, S. E., Gaume, R., and Wycoff, G. L. (2004). The Naval Observatory Merged Astrometric Dataset (NOMAD). In *American Astronomical Society Meeting Abstracts*, volume 36 of *Bulletin of the American Astronomical Society*, page 1418.

Zucker, D. B., Kniazev, A. Y., Bell, E. F., Martínez-Delgado, D., Grebel, E. K., Rix, H.-W., Rockosi, C. M., Holtzman, J. A., Walterbos, R. A. M., Annis, J., York, D. G., Ivezić, Ž., Brinkmann, J., Brewington, H., Harvanek, M., Hennessy, G., Kleinman, S. J., Krzesinski, J., Long, D., Newman, P. R., Nitta, A., and Snedden, S. A. (2004). Andromeda IX: A New Dwarf Spheroidal Satellite of M31. *ApJL*, 612:L121–L124.

The End